Search for Spatial Extra Dimensions in the Two Muon Final State with the CMS Experiment at $\sqrt{s} = 13\,\text{TeV}$

Von der Fakultät für Mathematik, Informatik und Naturwissenschaften der RWTH Aachen University zur Erlangung des akademischen Grades eines Doktors der Naturwissenschaften genehmigte Dissertation

vorgelegt von

Markus Radziej, Master of Science

aus

Velbert, Deutschland

Berichter:
Prof. Dr. Thomas Hebbeker
Prof. Dr. Michael Krämer

Tag der Mündlichen Prüfung: 4. Februar 2019

"Wohin der Weg? — Kein Weg ins Unbetretene."

Johann Wolfgang von Goethe, Faust

Kurzfassung

Suche nach zusätzlichen Raumdimensionen in einem Entzustand mit zwei Myonen mit dem CMS Experiment bei $\sqrt{s} = 13\,\text{TeV}$

von Markus Radziej

Im Rahmen dieser Dissertation wird eine Suche nach großen, zusätzlichen Raumdimensionen im Spektrum der invarianten Masse von Myonenpaaren durchgeführt. Sowohl das ursprüngliche Szenario, welches Arkani-Hamed, Dimopoulos und Dvali (ADD) konzipiert haben, als auch das asymptotisch sichere (AS) Szenario für die Quantengravitation werden untersucht. Die Suche basiert auf Proton-Proton Kollisionen welche einer integrierten Luminosität von $36.3\,\text{fb}^{-1}$ entsprechen, vom Large Hadron Collider bei einer Schwerpunktsenergie von $\sqrt{s} = 13\,\text{TeV}$ produziert wurden und mit dem Compact Muon Solenoid Experiment während der Datennahme im Jahre 2016 aufgezeichnet wurden.

Da die untersuchten Modelle einen nicht-resonanten Überschuss zu großen invarianten Massen hin vorhersagen, werden dedizierte Rekonstruktionsalgorithmen und Selektionskriterien für den entsprechenden Phasenraum verwendet. Durch die Verwendung von Resultaten detaillierter Studien des dominanten Drell–Yan Prozesses wird eine akkurate Beschreibung des Standardmodelluntergrunds sichergestellt. Um die systematische Unsicherheit in der Vorhersage der Ereigniszahlen zu quantifizieren wurden mehrere theoretische und experimentelle Quellen ausgewertet.

Da kein Überschuss im Verhältnis zur Vorhersage gemessen wurde, werden Ausschlussgrenzen auf die jeweiligen Modellparameter gesetzt. Werte des ultravioletten Grenzparameters des ADD Szenarios für das Modell großer, zusätzlicher Raumdimensionen oberhalb von $M_S > 8.2$–$5.5\,\text{TeV}$ für 2 bis 7 zusätzliche Dimensionen werden bis zum 95 % Kredibilitätsniveau ausgeschlossen. Durch Kombination der Ergebnisse dieser Analyse mit denen der komplementären Analysen der CMS Kollaboration der Elektronen- und Photonenpaar Kanäle wird der ausgeschlossene Parameterbereich bis zu $M_S > 9.3$–$6.1\,\text{TeV}$ erweitert. Die 95 % Kredibilitätsniveau Ausschlussgrenze für die Übergangsskala zwischen dem infraroten und ultravioletten Energiebereich $\Lambda_{\text{Transition}}$ des AS Szenarios für die Quantengravitation befindet sich unterhalb der fundamentalen Skala der Gravitation M_D für Werte von $M_D = 5$–$6.5\,\text{TeV}$ für 2 bis 7 zusätzliche Dimensionen.

Abstract

Search for Spatial Extra Dimensions in the Two Muon Final State with the CMS Experiment at $\sqrt{s} = 13\,\text{TeV}$

by Markus Radziej

Within the scope of this dissertation, a search for large extra dimensions is performed in the invariant mass spectrum of muon pairs. Both the original scenario devised by Arkani-Hamed, Dimopoulos and Dvali (ADD) and the asymptotically safe (AS) scenario for quantum gravity are investigated. The search is based on proton-proton collisions corresponding to an integrated luminosity of $36.3\,\text{fb}^{-1}$, which have been provided by the Large Hadron Collider at a center-of-mass energy of $\sqrt{s} = 13\,\text{TeV}$ and recorded with the Compact Muon Solenoid experiment during the data-taking period of 2016.

As the investigated models predict a nonresonant excess toward large invariant masses, dedicated reconstruction algorithms and selection criteria for the corresponding phase space are utilized. By applying the results obtained in detailed studies of the dominant Drell–Yan process, an accurate description of the standard model background is ensured. In order to quantify the systematic uncertainty in the predicted event yields, multiple theoretical and experimental sources are evaluated.

Having measured no excess with respect to the prediction, exclusion bounds are set on the respective model parameters. In the ADD scenario for the model of large extra dimensions, the 95 % credibility level exclusion limits on the ultraviolet cutoff parameter range from $M_S > 8.2$–$5.5\,\text{TeV}$ for 2 to 7 additional dimensions. By combining the results of this analysis with those of the complementary electron and photon pair channel analyses of the CMS Collaboration, the excluded parameter space is extended to $M_S > 9.3$–$6.1\,\text{TeV}$. The 95 % credibility level exclusion limit on the transition scale between the infrared and the ultraviolet energy regimes $\Lambda_{\text{Transition}}$ of the AS scenario for quantum gravity is found to be smaller than the fundamental scale of gravity M_D up to values of $M_D = 5$–$6.5\,\text{TeV}$ for 2 to 7 additional dimensions.

Acknowledgements

I would like to express my sincere gratitude to the people who supported me during my time as a doctoral student. First, I want to thank Professor Thomas Hebbeker for the opportunity to be part of the Physics Institute III A of the RWTH Aachen University. Under his guidance as the head of the institute, I obtained both my Bachelor as well as Master of Science and was able to visit many conferences and schools while working toward my doctorate. I thank my long-time advisor Arnd Meyer, who has supported me during all three of the aforementioned theses, for his encyclopedic knowledge of useful publications and procedures within the CMS Collaboration. I am also grateful to Professor Michael Krämer for the time he invested as the second reviewer of this dissertation.

My sincere thanks go to all past and present colleagues and friends in the institute. This includes members of the administrative staff who have helped to reduce the bureaucratic overhead and the IT team which has ensured a smooth operation of the computing resources. In the institute, a relaxed yet motivating atmosphere has always been emphasized and lead to many productive hours spent on many different projects. Among the research groups, I particularly want to thank the CMS data analysis team of which I have been a part of. For questions which arose during my search for large extra dimensions, there was always somebody available in this group with whom I could debate potential answers and settle on appropriate solutions. Special thanks go to Sebastian Thüer for the numerous discussions about limit setting and Tobias Pook for the expertise on large extra dimensions and related topics.

I am also grateful to the members of the High Energy & Particle Theory Group of the Technical University Dortmund who have been instrumental for the analysis of the asymptotically safe scenario for quantum gravity. Without their technical implementation, the simulation and subsequent evaluation of this model would not have been possible. Special thanks go to Magdalena Zenglein who has been my contact from the aforementioned institute and has talked me through the dependencies which govern the asymptotically safe scenario.

I express my gratitude to the CMS Collaboration for their meticulous measurement and preparation of the data sets with which the presented analysis has been performed. Managing the enormous associated workload and the necessary attention to detail is only possible thanks to a multitude of individual contributions by fellow scientists from all over the world. Of the collaboration's members, I would particularly like to thank the group of co-authors with whom I have worked through many iterations of the publication detailing the results of this dissertation.

During the final months of writing, many members of various institutes have read different parts of this document to enhance the clarity of its statements. I appreciate the time they have invested to provide critiques from an outside perspective.

Last but not least, I want to thank my family: My brother and sister-in-law, my two grandmothers and most importantly my parents who have been a continuous pillar of support throughout the entirety of my studies and life in general.

Contents

Chapter 1

Introduction

In the standard model of particle physics [1–5], three of the four known fundamental forces and the generation of particle masses are described using the mathematical framework provided by quantum field theory. The description of gravity, the exception to the rule, is instead given by Albert Einstein's general theory of relativity [6]. Attempts to formulate a consistent model of quantum gravity have not yet been met with success, however, some descriptions via effective field theories yield predictions that can be tested at the Large Hadron Collider. One such effective field theory, the model of large extra dimensions [7, 8], proposes that spacetime contains additional spatial dimensions hidden via compactification. These extra dimensions are further assumed to be the cause of the substantial difference between the coupling strength of gravity compared to those corresponding to the other three fundamental forces.

Historically, Theodor Kaluza [9] and Oskar Klein [10, 11] pioneered the concept of additional compactified spatial dimensions in the first half of the 20th century. They developed this concept in an attempt to describe general relativity and electromagnetism in a unified theoretical framework where the photon field originates from the fifth dimension. With the advent of the standard model and its quantum field theoretical description of electromagnetism in the 1960s, the multidimensional approach lost traction. Interest resurged around the 1980s alongside new developments in the field of string theory [e.g. 12] which requires additional spatial dimensions for a mathematically consistent formulation. This eventually led to the inception of the model of large extra dimensions by Nima Arkani-Hamed, Savas Dimopoulos and Gia Dvali [7, 8] at the turn of the century. While the predictions of their theory are only valid up to a given energy scale, this restriction could be removed by the asymptotically safe scenario for quantum gravity [13]. First suggested by Steven Weinberg around the same time as the aforementioned resurgence of interest in extra dimensions, this scenario attempts to unify the description of all fundamental forces. While it is not the only approach being pursued to achieve unification, asymptotic safety remains one of the most frequently studied.

Using proton-proton collisions provided by the Large Hadron Collider at a center-of-mass energy of $\sqrt{s} = 13\,\text{TeV}$, recorded by the CMS detector during the data-taking period of 2016, a search for large extra dimensions is performed in the presented analysis. Assuming the existence of extra dimensions, both an emission and a virtual exchange of gravitons lead to a distinct type of signature in the detector. While the graviton is produced alongside a standard model particle and evades detection for the former process, it decays into pairs of particles for the latter one. This analysis focuses on the *virtual exchange of gravitons decaying to muon pairs*, which allows for a direct measurement of all resulting particles. Choosing the dimuon channel is further motivated by the CMS Collaboration's robust identification of muons and precise measurement of their properties [14].

Although not always feasible, the structure of this document aims to allow the reader to comprehend a given chapter requiring only the knowledge of the preceding ones. In chapters 2 and 3, the respective theoretical foundations of the standard model and its extension by additional spatial dimensions are laid. This is followed by an overview of the experimental setup in chapter 4 and a discussion of the reconstruction of muon trajectories in chapter 5. The data sets recorded by the CMS experiment and those of the corresponding simulated processes are given in chapter 6. In the last section of this chapter, the properties of the simulated signal models are discussed. A detailed overview of the selection criteria as well as their impact on the event yields is provided in chapter 7. The following chapter, number 8, is concerned with corrections applied to the simulated backgrounds and the data-driven description of backgrounds where at least one of the two muons does not originate from the primary interaction. An estimation of the systematic uncertainties affecting the event yields as well as the shapes of the final dimuon invariant mass distributions are given in chapters 9 and 10, respectively. The statistical analysis of the aforementioned distributions and subsequent interpretation of the results can be found in chapter 11 while the potential for future analyses is discussed in the concluding chapter 12.

Chapter 2

Physics of the Standard Model

The standard model (SM) is formulated as a relativistic gauge quantum field theory aiming to classify particles and describe their interactions in a unified mathematical framework. While a comprehensive discussion of the full theory and its inevitable complexity is beyond the scope of this document, a brief review of selected aspects will be given in this chapter. These aspects are chosen to serve as the basis for the discussion of physics beyond the SM.

As a reference for the upcoming sections, if not otherwise specified, both the "Introduction to Elementary Particles" by David Griffiths [15] as well as Francis Halzen and Alan D. Martin's "Quarks and Leptons" [16] have been used.

2.1 Structure & Lagrangian Formalism

In the SM, individual particles are modeled as excitations of the respective underlying field. Their dynamics are determined by the corresponding Lagrangian density $\mathcal{L}$, which is often just referred to as a Lagrangian. Interactions between matter (fermions) are incorporated into the theory by requiring the Lagrangian to remain invariant under local gauge transformations for the product of groups

$$U(1)_Y \times SU(2)_L \times SU(3)_C. \tag{2.1}$$

The resulting description of the strong interaction for quark spinors q, given by the Lagrangian of quantum chromodynamics (QCD), reads

$$\mathcal{L}_{\text{QCD}} = \underbrace{i\bar{q}\gamma^\mu\partial_\mu q}_{\text{Kinetic term}} - \underbrace{m_q\bar{q}q}_{\text{Mass term}} - \underbrace{ig_3\bar{q}\gamma^\mu G^c_\mu T^c q}_{\text{Quark-gluon interaction}} - \underbrace{\frac{1}{4}G^{\mu\nu}_c G^c_{\mu\nu}}_{\text{Gluon-gluon interaction}}. \tag{2.2}$$

A similarly structured expression describes the electroweak (EW) interaction, i.e., both the electromagnetic and weak force. For a Dirac fermion ψ, it is given by

$$\mathcal{L}_{\text{EW}} = \bar{\psi}\gamma^\mu\left(i\partial_\mu - g_1\frac{1}{2}Y_W B_\mu - g_2\frac{1}{2}\vec{\tau}_L\cdot\vec{W}_\mu\right)\psi - \frac{1}{4}B^{\mu\nu}B_{\mu\nu} - \frac{1}{4}W^{\mu\nu}_a W^a_{\mu\nu}. \tag{2.3}$$

The aforementioned invariance under local gauge transformations implies that the respective groups correspond to (internal) symmetries of the theory. A conserved quantity exists for each of these symmetries as dictated by Noether's theorem. They are given by the $SU(3)_C$ color charge corresponding to T^a ($a = 1, 2, \ldots, 8$), the $SU(2)_L$ weak isospin generated by the three-component $\vec{\tau}_L$ with the index L indicating that this interaction couples only to left-handed particles, and the $SU(1)_Y$ weak hypercharge of the Y_W generator. Every interaction also has its respective gauge coupling parameter g_1, g_2 and

g_3 where the indices relate to the dimension of the generator. These couplings govern the "strength" of the interaction. Whereas the gluon fields G^c_μ directly correspond to their particles, the mass eigenstates $W^\pm$, Z and γ are superpositions of the $\vec{W}_\mu$ and B_μ fields. In particular, the latter two mass eigenstates are obtained via a mixing of the third component W^3_μ and B_μ. The associated mixing of the weak hypercharge and the third component of the weak isospin yields the commonly used electric charge $Q = \frac{Y_W}{2} + \tau^3_L$.

Cross sections can be calculated based on this foundation by following the set of rules for creating interaction diagrams and evaluating their scattering amplitudes introduced by the eponymous Richard Feynman [17].

2.2 Scale Dependence of Coupling Parameters

The values of the gauge coupling parameters g_1, g_2 and g_3, introduced in the previous section, depend on the energy scale of the interaction. This behavior can be understood as a polarization of the vacuum depending on the distance to the charged particle. Interactions at higher energies translate to shorter distances between the interacting particles, which alters the impact of the polarized vacuum.

For a given Feynman diagram, this results in the introduction of closed particle loops corresponding to the respective gauge coupling parameter g_i. While the exchanged momentum Q^2 between initial- and final-state particles of an interaction is fixed, such loops of particles have no momentum restrictions. In order to account for all possible momenta (up to infinite values), the coupling parameters are expressed perturbatively with respect to loop contributions given sufficiently large Q^2. The resulting scale-dependent description is formulated in relation to an experimentally determined value of the parameter itself at a reference energy scale μ. Allowing for up to one loop, the expression for what is often referred to as the "running coupling constant" of QCD α_s reads

$$\alpha_s(Q^2) = \frac{g_3}{4\pi} = \alpha_s(\mu^2) \cdot \left(1 + \frac{\alpha_s(\mu^2)}{12\pi}(33 - 2n_f)\log\frac{Q^2}{\mu^2}\right)^{-1}. \tag{2.4}$$

Here, n_f denotes the number of quark flavors that contribute at the given interaction scale. This systematic treatment of infinite contributions by closed particle loops allows for extrapolating the value of coupling parameters to arbitrary energy scales. Its general application in the context of quantum field theories is termed *renormalization*.

Examining the denominator of equation (2.4) reveals two decisive characteristics of g_3. The coupling decreases for rising values of Q^2 (given the maximum of $n_f = 6$ in the SM) resulting in what is called the "asymptotic freedom" of QCD. On the other hand, quarks and gluons become strongly coupled for small exchanges of momenta $Q^2 = \Lambda^2_{\mathrm{QCD}} \simeq (200\,\mathrm{MeV})^2$. This necessitates a nonperturbative description for the low-energy regime of QCD.

2.3 Parton Distribution Functions

A particular aspect of determining the cross sections of processes at hadron colliders, aside from calculating the matrix elements for the involved constituents, is estimating the composition of the colliding hadrons. Following the discussion in section 2.2, the determination can be divided into a perturbative description of the high-energy or "hard" interaction and a nonperturbative one to describe the structure of the hadron. According to the QCD factorization theorem [18], one can express the total cross section for two inelastically colliding hadrons A, B producing two particles M, N and other

hadronic remnants X as

$$\begin{aligned}\sigma_{AB\to MN+X} = \sum_{a,b} \int \mathrm{d}x_1\, f_{a/A}(x_1, \mu_F^2) \int \mathrm{d}x_2\, f_{b/B}(x_2, \mu_F^2) \\ \times \hat{\sigma}_{ab\to MN}(x_1, x_2, Q^2, \alpha_s(\mu_R^2), \mu_R^2, \mu_F^2).\end{aligned} \tag{2.5}$$

Here, the *parton distribution function* (PDF) for parton a in hadron A is denoted by $f_{a/A}$ with an analogous naming scheme for b, B and $f_{b/B}$. Both PDFs depend on the respective hadron momentum fraction $x_i \in [0, 1)$ and the scale of the factorization μ_F. The hard scattering cross section $\hat{\sigma}$ can be interpreted as the parton cross section of a and b producing the desired particles M, N. In addition to dependencies on the hadron momentum fractions x_i as well as the exchanged momentum Q^2, it also depends on the strong coupling constant α_s and the renormalization and factorization scales μ_R and μ_F, respectively. The factorization is often evaluated at the energy scale $Q = \mu_R = \mu_F$ and is accurate up to corrections power-suppressed by Q^2.

For the nonperturbative description of PDFs, empirical input is required. Modern sets of PDFs, e.g., NNPDF 3.0 [19], are generally based on complementary data from deep inelastic scattering and collider experiments including the LHC. Their evolution with respect to the interaction scale Q^2 is described by the DGLAP equations [20–22], which in turn allow for extrapolations beyond what has been measured. Naturally, these extrapolations are necessary for analyses probing unexplored regions of phase space, but they may also entail substantial uncertainties. These uncertainties depend on the available measurements of the PDF at or close to the respective value of Q^2.

2.4 Production of Lepton Pairs

As declared in the title of this analysis, the considered decay products of the final state are two muons. The primary channel for the production of lepton pairs in the SM is the (neutral) Drell–Yan (DY) process $q\bar{q} \to \gamma^*/Z \to \ell\ell$ [23]. One can structure the corresponding differential cross section with respect to its angular variables, as done by the CMS Collaboration in their measurement of the angular coefficients A_i [24], like

$$\begin{aligned}\frac{\mathrm{d}\sigma}{\mathrm{d}p_\mathrm{T}\,\mathrm{d}y\,\mathrm{d}m\,\mathrm{d}\Omega} = &\frac{3}{16\pi}\frac{\mathrm{d}\sigma^{U+L}}{\mathrm{d}p_\mathrm{T}\,\mathrm{d}y\,\mathrm{d}m}\Big\{(1+\cos^2\theta^*) + A_0\frac{1}{2}(1-3\cos^2\theta^*) \\ &+ A_1 \sin 2\theta^* \cos\phi^* + A_2\frac{1}{2}\cos 2\theta^* \cos\phi^* + A_3 \sin\theta^* \cos\phi^* \\ &+ A_4 \cos\theta^* \\ &+ A_5 \sin^2\theta^* \sin 2\theta^* + A_6 \sin 2\theta^* \sin\phi^* + A_7 \sin\theta^* \sin\phi^*\Big\}.\end{aligned} \tag{2.6}$$

Here, θ^* and ϕ^* denote the respective polar and azimuth angle of the negatively charged lepton and are defined in the center-of-mass frame of the boson (or dilepton system). The chosen implementation of this frame, illustrated in figure 2.1, is known as the Collins–Soper (CS) frame [25]. It aims to minimize the impact of nonvanishing parton transverse momenta. Following the most commonly used convention when adopting the CS frame, the angle θ^* is measured between the negatively charged lepton and the z axis defined as the line bisecting the angle between the two momenta of the protons,

which results in

$$\cos\theta^* = \frac{p_z(\ell\ell)}{|p_z(\ell\ell)|}\frac{2(p_1^+p_2^- - p_1^-p_2^+)}{m(\ell\ell)\sqrt{m(\ell\ell)^2 + p_\mathrm{T}(\ell\ell)^2}} \quad \text{with} \quad p_i^\pm = \frac{1}{\sqrt{2}}(E_i \pm p_{i,z}). \tag{2.7}$$

The momentum of the boson determines the direction of the z axis and the numeric indices 1 and 2 refer to the negatively and positively charged lepton, respectively.

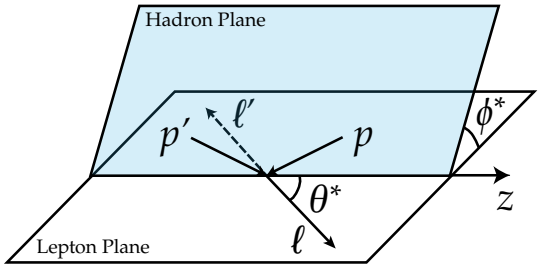

FIGURE 2.1: Illustration of the Collins–Soper frame showing the intersecting lepton and hadron planes. Of particular interest are the polar angle θ^* and azimuth angle ϕ^*.

Dependencies on the boson mass m, transverse momentum p_T and rapidity y are contained within the unpolarized cross section σ^{U+L} [26] and angular coefficients A_i. The kinematic distributions of the particles produced in the interaction depend on these coefficients. At leading order (LO) in perturbative QCD, all coefficients other than A_4 vanish. Dependencies on ϕ^* are introduced at next-to-leading order (NLO) in QCD where A_0, A_1, A_2 and A_3 are different from 0. While the first three coefficients A_{0-2} are related to the polarization of the Z boson, A_3 and A_4 depend on the vector and axial-vector coupling between the boson and leptons and are therefore responsible for the forward-backward asymmetry A_FB of the DY process. Studies of the latter have also been conducted by the CMS collaboration [27, 28]. Even more precise next-to-next-to-leading order (NNLO) calculations in QCD introduce the A_{5-7} terms for gluon loops whose contributions are comparatively small.

2.5 Electroweak Symmetry Breaking

What has been tacitly implied when quoting the Lagrangians of the QCD and EW theory in equations (2.2) and (2.3), respectively, is that a gauge invariant formulation of the Lagrangian is possible for both massless and massive (mediator) particles. While utilizing the covariant derivative is sufficient to ensure local gauge invariance for massless particles such as gluons, generating the $W^\pm$ and Z boson mass requires *electroweak symmetry breaking*. In the SM, this is achieved through the Brout–Englert–Higgs mechanism [29–34].

The mechanism introduces a suitable potential whose symmetry can be *spontaneously broken* by entering its energy ground state. This scenario is most commonly discussed in the form of the "Mexican hat potential"

$$V(\phi) = \mu^2\left(\phi^\dagger\phi\right) + \lambda\left(\phi^\dagger\phi\right) \quad \text{with} \quad \mu^2 < 0, \lambda > 0 \quad \text{and} \quad \phi = \frac{1}{\sqrt{2}}\begin{pmatrix}\phi_1 + i\phi_2\\ \phi_3 + i\phi_4\end{pmatrix}. \tag{2.8}$$

Here, ϕ is given by a $SU(2)$ doublet of four scalar fields ϕ_i. Using a particular (but otherwise equivalent) choice for the vacuum expectation value where ϕ_3 is the only one of the four fields different from 0 and is given by $v \equiv \pm\sqrt{-\mu^2/\lambda}$ allows for identifying the

gauge bosons mass terms. In addition to a massless photon and massive vector bosons $W^{\pm}$, Z, one receives a massive scalar boson known as the Higgs boson H. The fermion masses are also generated through their coupling to the Higgs boson. For quarks and leptons, the Lagrangian for left-handed doublets L and right-handed singlets R is of the form

$$\mathcal{L}_{\text{Yukawa}} = -g\bar{L}\phi R + \text{Hermitian conjugate.} \tag{2.9}$$

This results in masses proportional to the vacuum expectation value of the Higgs field ϕ and the Yukawa coupling g corresponding to the particle in question.

The minimal version of the SM Brout–Englert–Higgs mechanism presented here leads to a *single* massive scalar boson H. Using proton-proton collisions produced by the LHC during the data-taking period of 2012, both the CMS [35] and ATLAS [36] experiments were able to observe a boson compatible with this prediction. Further tests of the particle properties, e.g., its couplings to SM particles [37] and spin-parity measurements [38], have shown no significant deviation from the SM prediction. The current best measurement of the Higgs boson mass has been performed by the CMS Collaboration in the four-lepton decay channel [39] which yielded

$$m_H = 125.26 \pm 0.20\,(\text{stat}) \pm 0.08\,(\text{syst})\ \text{GeV}. \tag{2.10}$$

By expressing the mass in terms of its dominant loop corrections [40], larger rest masses implying a stronger coupling to the Higgs boson, one arrives at

$$m_H^2 = m_{H,\text{bare}}^2 + \frac{3\Lambda^2}{8\pi^2 v^2}\left(m_H^2 + 2m_W^2 + m_Z^2 - 4m_t^2\right). \tag{2.11}$$

The contributing momenta of the loops are regularized by the ultraviolet (UV) cutoff scale Λ. If one associates this scale with the advent of physics beyond the standard model (BSM) the value of Λ might be very large. For contributions by gravitational processes, it may be as large as the Planck mass $M_{\text{Planck}} \simeq 1.2 \times 10^{19}\,\text{GeV}$. To compensate for Λ in this scenario, a precise arrangement of at least 15 digits of the Higgs boson bare mass $m_{H,\text{bare}}$ would be necessary. This "fine-tuning" or "hierarchy problem" (with respect to the coupling strengths of gravity and the other fundamental forces) and discussions about its "naturalness" serve as motivation to many BSM theories proposing different kinds of solutions. The model of large extra dimensions is one such theoretical approach and the main topic of this analysis.

Chapter 3

Spatial Dimensions beyond the Standard Model

Extending spacetime by additional spatial dimensions while remaining compatible with observations of SM physics necessitates a mechanism to suppress the new physical phenomena. Kaluza and Klein have pioneered the concept of compactified dimensions [9–11] where the impact of new phenomena is related to the scale of the compactification. For sufficiently small scales this relation may serve as a suppression mechanism.

The theoretical framework of string theory [e.g. 12] provides a general motivation for the search of additional spatial dimensions. Its applications aim for a unified description of all four fundamental interactions and require additional dimensions for a mathematically consistent formulation. Taking M-theory [41, 42] as an example, the required number of dimensions would amount to 11 in total. The most commonly discussed models which can provide this extension of spacetime are universal extra dimensions, warped extra dimensions and large extra dimensions. All of them build on the foundation of the Kaluza-Klein (KK) theory and are further motivated by addressing questions left unanswered by the SM. In the *brane* terminology used in this context, a p-brane has $p+1$ dimensions while the *bulk* encompasses all dimensions. The common three dimensions of space and one dimension of time then correspond to a 3-brane.

Conceptually, *universal extra dimensions* [43] offer the most straightforward approach. The introduced spatial extra dimensions are flat and compactified on an orbifold, with all SM fields being able to propagate through the entire bulk. In its most simple implementation, there is only one additional dimension that is compactified on an S^1/Z_2 orbifold. Here, S^1 denotes the symmetric group of order 1 (a circle) while Z_2 denotes the cylic group of order 2 (two cyclic values). The periodic boundary conditions of the compactification result in KK excitations (see Sec. 3.2) for every particle; as the lightest excitations are stable (because of a Z_2 parity), the ones that do not carry charge become candidates for dark matter. Similar to the aforementioned scenario with one additional dimension, the model of *warped extra dimensions* [44] also proposes a five-dimensional spacetime and a compactification on an S^1/Z_2 orbifold of the fifth dimension but introduces an additional "warp factor" into the metric. Its corresponding exponential suppression of the Higgs vacuum expectation value may result in a "natural" solution of the hierarchy problem. In the original model developed by Lisa Randall and Raman Sundrum (RS) [44] SM fields were confined to the 3-brane and only gravity could propagate through the bulk. A common signature for experimental searches are dilepton resonances produced by the KK excitations of RS gravitons. Scenarios with large extra dimensions are discussed in the remainder of this chapter.

Both introductory material [45, 46] and the publications which have laid the theoretical foundation [7, 8, 47–49] have been used as references for the following sections on model of large extra dimensions. The review of the asymptotically safe scenario

for quantum gravity takes inspiration from pedagogical material [50] as well as both general [51] and extra dimension specific studies [52] on this topic.

3.1 The Fundamental Scale of Gravity

Nima Arkani-Hamed, Savas Dimopoulos and Gia Dvali suggested a model with *large extra dimensions* [7, 8]—titled the ADD scenario for the model of LED, or just ADD model—possessing the following features. The common four-dimensional spacetime is extended by an arbitrary number n of additional flat spatial dimensions which are orthogonal to the 3-brane. These additional dimensions are compactified; an n-dimensional torus $T^n = S^1 \times S^1 \times \cdots \times S^1$ of uniform radius R is the chosen geometry for the compactification in the following discussion[1]. All SM fields are confined to the 3-brane while gravity propagates through the bulk.

A naive, geometric understanding of the concept of compactified dimensions is conveyed by the illustration shown in figure 3.1. While movement on a rope is effectively restricted to one dimensions for humans, ants, living on a much smaller scale, are able to experience additional circular degrees of freedom. With smaller distances translating to higher energies in interactions of particles, this figure illustrates how a collider experiment may probe additional dimensions whose presence is otherwise hidden because of their compactification.

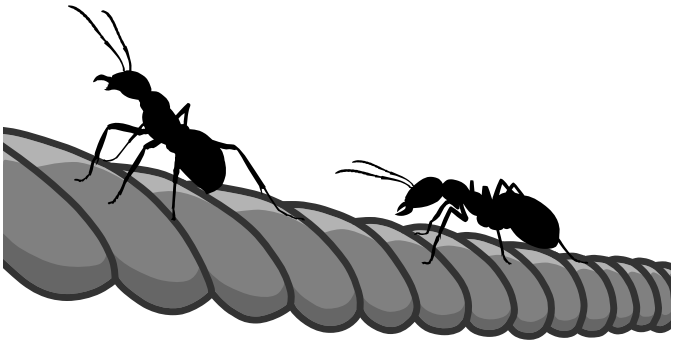

FIGURE 3.1: Illustration of ants on a rope conveying a naive, geometric understanding of the concept of compactified dimensions. The difference in size between humans and ants allows the latter to move both along and around the rope, thus in two dimensions, while the former is limited to the longitudinal degree of freedom.

Examining the homogeneous Einstein–Hilbert action S_{EH} under these conditions, using the sign convention $(+,-,-,-,\dots)$, yields

$$S_{\mathrm{EH}} = \frac{1}{2}\overline{M}_D^{2+n} \int \mathrm{d}^{4+n}x \, \sqrt{\det g^{(4+n)}} R^{(4+n)}, \tag{3.1}$$

where $\overline{M}_D$ is the reduced Planck mass in $D = 4 + n$ dimensions. The generalized, higher-dimensional metric tensor and Ricci scalar are denoted by $g^{(4+n)}$ and $R^{(4+n)}$, respectively. As the additional dimensions are assumed to be flat and orthogonal to the ordinary four, their integral can be calculated independently and $\sqrt{\det g^{(4+n)}}$ becomes $\sqrt{\det g^{(4)}}$. For SM fields confined to the 3-brane, the stress-energy tensor T_{MN} vanishes in the higher dimensions. In this context, capital Roman letters (mostly M, N) are used

[1] Other geometries are possible and are not prohibited by theory. Choosing a torus of uniform radius simplifies the calculation.

to represent the $4 + n$-dimensional indices. By examining the Einstein field equations

$$R_{MN}^{(4+n)} - \frac{1}{2} R^{(4+n)} g_{MN}^{(4+n)} = -\frac{1}{M_D^{2+n}} T_{MN}^{(4+n)}, \tag{3.2}$$

one can see that $R^{(4+n)}$ therefore reduces to $R^{(4)}$. These two relations allow for an independent integration over the volume of the n-dimensional torus:

$$S_{\mathrm{EH}} = \frac{1}{2} \overline{M}_D^{2+n} \int \mathrm{d}V^{(n)} \int \mathrm{d}^4x \sqrt{\det g^{(4)}} R^{(4)} \tag{3.3}$$

$$= \frac{1}{2} \overline{M}_D^{2+n} V^{(n)} \int \mathrm{d}^4x \sqrt{\det g^{(4)}} R^{(4)} \tag{3.4}$$

$$= \frac{1}{2} \overline{M}_{\mathrm{Pl}}^2 \int \mathrm{d}^4x \sqrt{\det g^{(4)}} R^{(4)}. \tag{3.5}$$

In the last step, the equation has been identified with the ordinary four-dimensional form of the Einstein–Hilbert action with the reduced Planck mass $\overline{M}_{\mathrm{Pl}} = M_{\mathrm{Pl}}/\sqrt{8\pi}$. This yields the prefactor relation

$$\overline{M}_{\mathrm{Pl}}^2 = V^{(n)} \overline{M}_D^{2+n} = (2\pi R)^n \overline{M}_D^{2+n} \equiv R^n M_D^{2+n}. \tag{3.6}$$

Should the model of LED describe nature, the quantity known as the Planck mass would thus be derived from a *fundamental scale of gravity*[2] M_D based on the volume of the extra dimensions. Furthermore, the apparent relative weakness of gravity becomes a consequence of the asymmetric spacetime propagation of the four fundamental interactions. Given low numbers of extra dimensions n with large radii R, it might be possible to probe the a priori unknown fundamental scale of gravity at the LHC. If one assumes that M_D is experimentally accessible, its value would be comparatively close to electroweak scale. The terms contributing to the Higgs mass, discussed in section 2.5, would consequently require significantly less fine-tuned values to produce the measured physical mass (Eq. 2.10).

Equation (3.6) also allows for estimating the size of the compactification radii for different numbers of extra dimensions n at a given M_D. Table 3.1 provides an overview of this relation for two values of M_D. The first one represents the considered parameter space prior to the construction of the LHC while the second one characterizes radii closer to the current experimental reach. Focusing on the latter results, the radius is comparable to distances within the solar system for a single extra dimension and is thus ruled out by astrophysical observations. Scenarios with $n = 2$ could be probed through tests of the Newtonian force while even smaller radii require a different approach. One of them is given by the indirect detection of graviton mediators at collider experiments.

n	1	2	3	4	5	6
$R_{1\,\mathrm{TeV}}$ / m	1×10^{12}	5×10^{-4}	4×10^{-9}	1×10^{-11}	3×10^{-13}	3×10^{-14}
$R_{10\,\mathrm{TeV}}$ / m	1×10^{9}	5×10^{-6}	8×10^{-11}	3×10^{-13}	1×10^{-14}	1×10^{-15}

TABLE 3.1: Compactification radii R for different numbers of additional spatial dimensions n in the ADD scenario for the model of LED for two values of the fundamental scale of gravity M_D.

[2]Different definitions of the fundamental scale of gravity with various factors of 2 and π are used in literature. It is also referred to as the fundamental Planck mass.

3.2 Virtual Exchange of Gravitons

To derive a description for the exchange of gravitons at colliders, one can express the metric $g_{MN}^{(4+n)}$ perturbatively for small fluctuations of the graviton field h_{MN} around a flat spacetime metric η_{MN}, resulting in

$$g_{MN}^{(4+n)} = \eta_{MN} + \frac{1}{2M_D^{n/2+1}} h_{MN}. \tag{3.7}$$

Given the periodic boundary conditions of the toroidal extra dimensions, h_{MN} can be expressed as a Fourier series. By defining the coordinates $z_M = (x_\mu, y_i)$, the periodicity implying $y_i \to y_i + 2\pi R$, the series can be written as

$$h_{MN}(x, y) = \sum_{k_1=-\infty}^{+\infty} \cdots \sum_{k_n=-\infty}^{+\infty} \frac{h_{MN}^{\vec{k}}(x)}{\sqrt{V^{(n)}}} \exp\left(i \frac{k^j y_j}{R}\right). \tag{3.8}$$

Here, Greek letters have been introduced to denote four-dimensional indices. A schematic evaluation of an action S for the Fierz–Pauli Lagrangian [48], obtained by linearizing the integrand of equation (3.1) with respect to the graviton field h_{MN} that has been introduced in equation (3.7), reads

$$S = \frac{1}{2} \int \mathrm{d}^{4+n} z \, \partial^A h^{MN} \partial_A h_{MN} \tag{3.9}$$

$$= \frac{1}{2} \sum_{\vec{k},\vec{l}} \int \mathrm{d}^n y \, \frac{1}{V^{(n)}} e^{i \frac{\vec{k}+\vec{l}}{R} \cdot \vec{y}} \int \mathrm{d}^4 x \, \partial_\mu h_{MN}^{\vec{k}} \partial^\mu h^{MN\,\vec{l}} + \frac{\vec{k} \cdot \vec{l}}{R^2} h_{MN}^{\vec{k}} h^{MN\,\vec{l}} \tag{3.10}$$

$$= \frac{1}{2} \sum_{\vec{k}} \int \mathrm{d}^4 x \, \partial_\mu h_{MN}^{\vec{k}} \partial^\mu h^{MN\,-\vec{k}} - \frac{k^2}{R^2} h_{MN}^{\vec{k}} h^{MN\,-\vec{k}}. \tag{3.11}$$

Thus, integration over the extra dimensions yields a tower of (infinite) graviton KK modes with their respective mass given by $m_{\vec{k}}^2 = \vec{k}^2/R^2$. One massless mode is retained, $\vec{k} = 0$, which corresponds to the four-dimensional graviton. It should be emphasized that this is only a partial evaluation of the Fierz–Pauli Lagrangian with a focus on the $(\partial h)^2$ term. To comprehensively study the tensorial structure of the graviton, all terms of the Lagrangian need to be taken into account.

At this point one might expect to measure resonances but examining the mass splitting of the modes

$$\Delta m \sim \frac{1}{R} = M_D \left(\frac{M_D}{\overline{M}_{\mathrm{Pl}}}\right)^{2/n} \tag{3.12}$$

suggests otherwise. Even for $M_D = 10\,\mathrm{TeV}$ and large numbers of extra dimensions $n = 4, 6, 8$ the splitting is only of the order of 640 keV, 0.2 GeV and 2.5 GeV, respectively. Considering that a continuous excitation of additional KK modes with rising interaction scales would result in measurements most sensitive toward the tail end of the energy spectrum, resolving the individual modes is not feasible.

Focusing on the s-channel graviton exchange, the scattering amplitude $\mathcal{A}$ can be written as

$$\mathcal{A} = \mathcal{S}(s) \left(T_{\mu\nu} T^{\mu\nu} - \frac{T_\mu{}^\mu T_\nu{}^\nu}{n+2}\right), \tag{3.13}$$

where $\mathcal{S}$ would be obtained by summing over all gravitons of the KK tower. Given the inability to resolve individual graviton resonances, the sum over all propagators can be replaced by an integral to obtain an effective description with [53]

$$\mathcal{S}(s) = \frac{1}{\overline{M}_{\mathrm{Pl}}} \sum_{\vec{k}} \frac{1}{\hat{s} - m_{\vec{k}}^2 - i m_{\vec{k}} \Gamma_G(m_{\vec{k}})} \rightarrow \frac{2\pi^{n/2}}{\Gamma(n/2) M_D^{2+n}} \int_o^{\Lambda} \mathrm{d}m \, \frac{m^{n-1}}{\hat{s} - m^2 - i m \Gamma_G(m)}. \quad (3.14)$$

Using the narrow-width approximation, an explicit expression for F_n given in [47], one arrives at

$$\mathcal{S}(s) = \frac{2\pi^{n/2} \Lambda^{n-2}}{\Gamma(n/2) M_D^{2+n}} F_n \left(\frac{\hat{s}}{\Lambda^2} \right). \quad (3.15)$$

Here, Λ is an arbitrary UV cutoff regularizing the otherwise divergent integral by only including graviton mass eigenstates of the KK tower with $m < \Lambda$. The still unknown underlying theory of quantum gravity is assumed to account for the divergences while the predictions of the effective field theory describing the ADD model are limited by them. As discussed by Gian F. Guidice, Riccardo Rattazzi and James D. Wells (GRW) [47], unitarity may still allow for values of $\hat{s}$ slightly larger than the cutoff parameter, but one would expect the regulatory influence of the underlying theory to be significant well before the effective field theory breaks down. To maintain the predictive power of the effective approach, contributions by the ADD model where $\hat{s}$ is larger than the (respective) cutoff parameter will be truncated. Should large extra dimensions exist in the *asymptotically safe* scenario for quantum gravity—discussed in sections 3.3 and 3.4—the predictions of the resulting model could be accurate at any energy scale.

Examining equation (3.15) for energy scales well below the cutoff motivates the choice of Λ_T as the parameter of interest in the GRW convention.

$$\mathcal{S}(s \ll \Lambda^2) = \begin{cases} \dfrac{2\pi^{n/2}}{(1-n/2)\Gamma(n/2)} \dfrac{\Lambda^{n-2}}{M_D^{2+n}} \equiv \dfrac{4\pi}{\Lambda_T^4} & \text{for } n > 2 \\ \dfrac{\pi}{M_D^4} \ln \dfrac{\hat{s}}{\Lambda^2} & \text{for } n = 2 \end{cases} \quad (3.16)$$

A different parametrization of the form factor by Tao Han, Joseph D. Lykken and Ren-Jie Zhang (HLZ) [48] retains the number of extra dimensions n as a free parameter. One can translate from Λ_T to the UV cutoff parameter M_S of the HLZ convention as follows:

$$M_S^4 = \frac{2}{2-n} \Lambda_T^4 \qquad \text{for} \quad n > 2 \quad (3.17)$$

$$M_S^4 = \log\left(\frac{M_S^2}{\hat{s}} \right) \Lambda_T^4 \quad \text{for} \quad n = 2 \quad (3.18)$$

The third commonly used parameter convention, developed by JoAnne L. Hewett [49], allows for contributions from the DY interference term (Fig. 3.2) to be negative through its sign parameter $\lambda = \pm 1$. Translation between the GRW and Hewett convention can be achieved through

$$M_S^4 = \frac{\lambda \pi}{2} \Lambda_T^4. \quad (3.19)$$

As outlined in the publication, the impact of the sign of λ on the dilepton invariant mass spectrum is only minor to the point of being statistically indistinguishable at large

interaction scales. For this reason, only the positive interference scenario $\lambda = +1$ will be considered when converting between parameter conventions in this analysis.

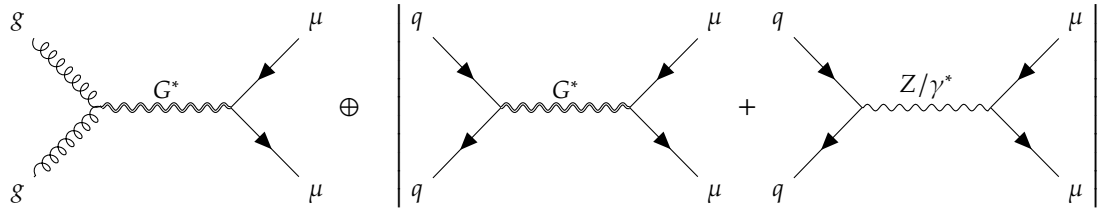

FIGURE 3.2: Tree-level Feynman diagrams for the virtual exchange of gravitons and its interference with the Drell–Yan process.

As illustrated in the Feynman diagrams shown in figure 3.2, quark annihilation is only one of two production channels for the virtual exchange of gravitons at tree-level while no other option exists for the DY process. A comparison of the primary angular dependencies corresponding to the respective LO cross sections is given in table 3.2. The different spin quantum numbers of the mediating particles and corresponding vectorial and tensorial couplings result in distinct angular distributions [54, 55]. Quark annihilation processes in proton-proton collisions also require at least one of the two partons to be a sea-quark while no such asymmetry is necessary in gluon fusion processes. With the tensorial coupling favoring more orthogonal angles θ^* in the CS frame and the gluon fusion production channel not being biased toward longitudinally boosted initial states, the decay products of the virtual graviton exchange process are expected to be more central with respect to the detector frame than those of the DY process. As the resulting discriminatory power of these differences in the angular distributions evolves with respect to the energy scale, their impact has to be evaluated for the phase space in question.

Process	Angular density for $\cos\theta'$
$q\bar{q} \to Z/\gamma^* \to f\bar{f}$	$3/8\ (1 + \cos^2\theta')$
$q\bar{q} \to G^* \to f\bar{f}$	$5/8\ (1 - 3\cos^2\theta' + 4\cos^4\theta')$
$gg \to G^* \to f\bar{f}$	$5/8\ (1 + \cos^4\theta')$

TABLE 3.2: Comparison of the primary angular dependencies given by terms with even powers of $\cos\theta$ in the dilepton center-of-mass frame [54]. The angle θ' is measured between the negatively charged lepton and incident quark or gluon. Measurements of θ^* in the Collins–Soper frame are considered the best approximation of θ' given partons with nonvanishing transverse momenta [54].

To summarize the discussion of LED with respect to collider experiments, searches are motivated by the potential reduction of the otherwise unreachable fundamental scale of gravity immanent to this theory. Providing a first glance at quantum gravitational processes, tightly packed graviton KK modes result in a quasi-continuous enhancement of the lepton pair production rate toward high energies and therefore a distinct final-state signature for analyses. Additionally, the angular distributions of the decay products differ between the graviton and SM background processes, providing further discriminatory power.

3.3 Renormalizing Quantum Gravity

Beginning with a general discussion of quantum gravity in D dimensions and deferring the implications of large extra dimensions to section 3.4, the following observations can be made. The construction of a canonical quantum field theory for gravity by perturbative expansion around the flat metric η_{MN} for small fluctuations of h_{MN}, as done in equation (3.7), is possible and yields the desired degrees of freedom for a massless, spin-2 scalar graviton field [56]. However, the result is not perturbatively renormalizable. Dimensional analysis hints at this issue as the gravitational coupling G_N^{2-D} in D dimensions has a negative mass (or energy) dimension for $D > 2$. Thus, every vertex involving a graviton requires an appropriate power of momenta to offset the negative mass dimension, which leads to divergent terms when approaching the Planck scale. In the SM, the dimensionless coupling parameters allow for redefining a finite number of parameters (e.g., mass and charge of the electron in quantum electrodynamics) to prevent divergences when calculating loop diagrams. However, in gravitational interactions the corresponding divergences require independent counterterms and therefore undetermined parameters at every order. To renormalize quantum gravity in this fashion, one would ultimately need to determine an infinite amount of parameters. The first of these counterterms are already introduced for single loops given the presence of matter fields [57] and for two loops in the absence of them [58].

To solve this issue and construct a UV complete theory of quantum gravity, various models such as string theory and loop quantum gravity are being pursued. Another one of these models, originally proposed by Steven Weinberg [13], is the *asymptotically safe* (AS) *scenario for quantum gravity*. Instead of requiring the (dimensionless) couplings to be sufficiently small for perturbative renormalization, asymptotic safety only necessitates them to approach finite values allowing for a *nonperturbative renormalization*. This requirement can also be formulated mathematically using the effective average action Γ_μ representing the theory at a given energy scale μ. Asymptotic safety dictates that the action has to approach a fixed point $\Gamma_\star$ under the renormalization group flow for $\mu \to \infty$ at which the beta functions for the couplings vanish.

Introducing quantum fluctuations to the theory of gravity implies a scale-dependent evolution of its coupling parameter. Using Newton's coupling constant $G_N^{(D)}$ in D dimensions as the experimental reference value, one can construct

$$G(\mu) = G_N^{(D)} Z^{-1}(\mu), \tag{3.20}$$

where the scale dependence is determined by the wave function renormalization factor $Z(\mu)$. This factor is of the form

$$Z^{-1}(\mu) = Z^{-1}(\mu_0) \exp\left(\int_{\mu_0}^{\mu} \mathrm{d}k \, \eta(k) \right), \tag{3.21}$$

and has to evolve like $Z^{-1}(\mu) \to 1$ when $\mu \to 0$ for the coupling parameter to return the expected low energy value of $G_N^{(D)}$. The anomalous dimension of the graviton $\eta(\mu)$, a function of the couplings corresponding to the theory, is given by

$$\eta(\mu) = -\frac{\mathrm{d} \ln Z}{\mathrm{d} \ln \mu}. \tag{3.22}$$

By defining the dimensionless gravitational coupling as $g(\mu) = \mu^{D-2} G(\mu)$, based on both equation (3.20) and the discussed dimensional analysis, the evolution of $g(\mu)$ with

respect to the energy scale reads

$$\beta(g) = \frac{\mathrm{d}g(\mu)}{\mathrm{d}\ln\mu} = \left[D - 2 + \eta(\mu)\right] g(\mu). \tag{3.23}$$

To satisfy the precondition for the existence of a fixed point, the beta function has to vanish. This is achieved in two scenarios. The Gaussian (G) or noninteracting fixed point $g(\mu_\star)_G = g_G = 0$ corresponds to a negligible anomalous dimension η and therefore a static coupling $G(\mu) = G_N^{(D)}$. It dictates the behavior of the theory for classical general relativity. In the second, non-Gaussian (NG) scenario, the mass dimension has to be compensated by $\eta_\star = 2 - D$ while $g_{\mathrm{NG}} \neq 0$. That such a fixed point could be approached in the UV regime was first shown for the Euclidean Einstein–Hilbert truncation[3] [59] using exact renormalization group equations [60, 61]. Subsequent, more advanced calculations (e.g., taking polynomials of R into account [62]) were able to show the same behavior. These promising results motivate searching for such a non-Gaussian fixed point.

3.4 Approximate Renormalization Group Flow

Within the Einstein–Hilbert truncation, an expression for the anomalous dimension has been determined to be [51]

$$\eta(\bar{g}) = \frac{(D-2)(D+2)\bar{g}}{(D-2)\bar{g} - 2(\lambda - 1/2)^2}, \tag{3.24}$$

where λ denotes the dimensionless cosmological constant and the coupling parameter has been rescaled to $\bar{g} = g/c_d$ with $c_d = \Gamma(D/2+2)(4\pi)^{D/2-1}$. For a vanishing cosmological constant, the evolution of $\bar{g}$ is then given by

$$\beta(\bar{g}) = \frac{(1 - 4D\bar{g})(D-2)\bar{g}}{1 + 2(2-D)\bar{g}}. \tag{3.25}$$

The two fixed points of this beta function correspond to $\bar{g}_{\mathrm{G}} = 0$ and $\bar{g}_{\mathrm{NG}} = 1/(4D)$. Integrating this equation analytically for an arbitrary scale μ yields

$$\frac{\mu}{\mu_0} = \left(\frac{\bar{g}(\mu)}{\bar{g}_0}\right)^{-1/\theta_{\mathrm{G}}} \left(\frac{\bar{g}_{\mathrm{NG}} - \bar{g}(\mu)}{\bar{g}_{\mathrm{NG}} - \bar{g}_0}\right)^{-1/\theta_{\mathrm{NG}}}, \tag{3.26}$$

with $g_0 = g(\mu_0)$ and the respective Gaussian and non-Gaussian critical exponents

$$\theta_{\mathrm{G}} = 2 - D \quad \text{and} \quad \theta_{\mathrm{NG}} = 2D\frac{D-2}{D+2}. \tag{3.27}$$

Starting from the classical infrared (IR) regime, these exponents determine how rapid the transition to the fixed point UV regime is as a function of the logarithmic energy scale $\ln\mu$. Both absolute values of the exponents increase for larger numbers of dimensions D, leading to more compact windows in which the transition takes place. In particular, the ratio $\theta_{\mathrm{NG}}/\theta_{\mathrm{G}}$ always remains within $[-4/3, -2]$ for numbers of dimensions between $D = 4$ and $D = \infty$.

[3] In the Euclidean Einstein–Hilbert truncation, the action is primarily determined by the scale-dependent coupling $g(\mu)$ and the two terms $\sqrt{\det g_{MN}}(R + 2\lambda)$ with the dimensionless cosmological constant $\lambda = \mu^{-2}\Lambda$.

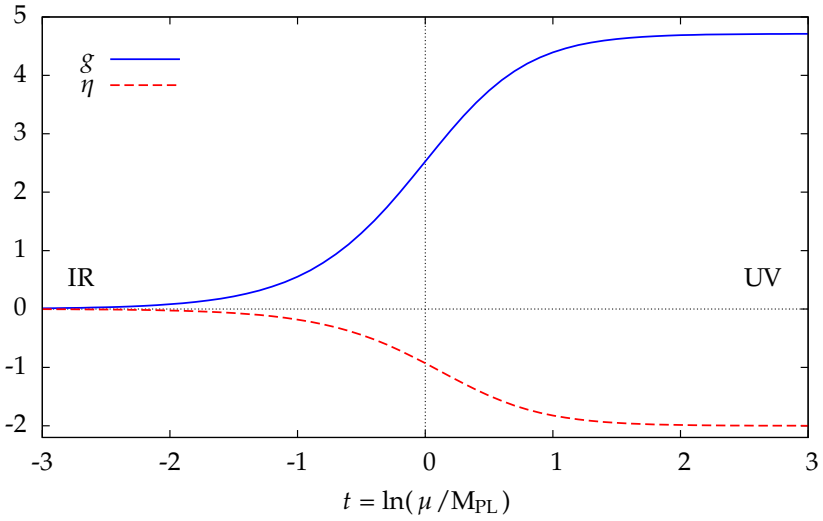

FIGURE 3.3: Scale dependence of the anomalous dimension η and the dimensionless coupling parameter g in four dimensions [51, 63].

The scale dependence of the anomalous dimension (with $\lambda = 0$) and coupling parameter are shown in figure 3.3 for four dimensions. Here, the characteristic scale for the crossover region between the IR and UV regime, referred to as the transition scale[4] $\Lambda_{\text{Transition}}$ (shortened to Λ_{Tr} in formulas), has been identified with the Planck mass M_{Pl}. With the introduction of additional spatial dimensions by the ADD scenario for the model of LED, the order of magnitude associated with the transition scale is instead given by the significantly lower fundamental scale of gravity M_D as motivated in section 3.1. Returning to the dimensionless coupling g and rearranging its expression to $G(\mu) = g/\mu^{D-2}$ shows that, while g remains finite, G approaches 0 in the UV regime. This behavior is often compared to the asymptotic freedom of QCD discussed in section 2.2. With the virtual exchange of gravitons governed by the gravitational coupling parameter, a reduction of the latter implies decreasing contributions by graviton mediated processes. As a consequence for the ADD model, the predicted increase of the lepton pair production rate is progressively suppressed toward higher interaction scales. Serving as a regularization mechanism, this behavior renders the model UV complete as it removes the dependence on the UV cutoff parameter. As a corollary to the suppression of graviton interactions, bounds on the model parameters would also be overestimated.

The preceding discussion of the AS scenario is specific to the Einstein–Hilbert truncation and can therefore only yield approximate descriptions. Nonetheless, it is possible to formulate effective expressions for $G(\mu)$ through Z and η within the truncation [52]. These expressions are given with respect to the transition scale $\Lambda_{\text{Transition}}$, which remains a free parameter to be determined experimentally unless otherwise matched to quantities of an underlying theory. As the critical exponents characterize the rapidity of the transition (Eq. 3.27), studies often differentiate between three approximations which serve as boundary cases.

Quenched approximation To reflect that the crossover region between the IR and UV regime becomes narrower for larger D, a benchmark scenario with an instantaneous transition can be implemented via an anomalous dimension $\eta =$

[4] While Λ_T is frequently used for both quantities in literature, the transition scale is not to be confused with the UV cutoff parameter associated with the GRW parameter convention of the ADD model.

$(2-D)\Theta(\mu-\Lambda_{\mathrm{Tr}})$ with the Heaviside function Θ. In this quenched scenario, the wave function renormalization factor has the following structure:

$$Z_{(0)}^{-1}(\mu,\Lambda_{\mathrm{Tr}}) = \begin{cases} 1 & \text{if } \mu < \Lambda_{\mathrm{Tr}} \\ (\Lambda_{\mathrm{Tr}}/\mu)^{D-2} & \text{if } \mu \leq \Lambda_{\mathrm{Tr}} \end{cases} \tag{3.28}$$

Linear approximation A lower bound on the rapidity of the transition for a continuous crossover can be derived by demanding $\theta_{\mathrm{NG}}/\theta_{\mathrm{G}} = -1$ (while approximating $g_0 \ll g_\star$ and $\mu_0 \ll \Lambda_{\mathrm{Tr}}$). The two quantities then read

$$Z_{(1)}^{-1}(\mu,\Lambda_{\mathrm{Tr}}) = \left[1+\left(\frac{\mu}{\Lambda_{\mathrm{Tr}}}\right)^{D-2}\right]^{-1}, \quad \eta = (2-D)\left(1-Z^{-1}\right). \tag{3.29}$$

Quadratic approximation Proceeding analogously to the derivation of the linear approximation for a transition twice as rapid, $\theta_{\mathrm{NG}}/\theta_{\mathrm{G}} = -2$, one receives the upper bound given by

$$Z_{(2)}^{-1}(\mu,\Lambda_{\mathrm{Tr}}) = \sqrt{1+\left[\frac{1}{2}\left(\frac{\mu}{\Lambda_{\mathrm{Tr}}}\right)^{D-2}\right]^2} - \frac{1}{2}\left(\frac{\mu}{\Lambda_{\mathrm{Tr}}}\right)^{D-2}, \quad \eta = (2-D)\frac{Z^2-1}{Z^2+1}. \tag{3.30}$$

It should be noted that the transition scales of the different approximations are a priori not identical. An energy scale at which to match the instances of $\Lambda_{\mathrm{Transition}}$ can be defined to allow for comparisons between the approximations. For example, all wave function renormalization factors $Z_{(i)}$ converge on $Z^{-1}(\mu\to\infty,\Lambda_{\mathrm{Tr}}) \simeq \left(\Lambda_{\mathrm{Tr}}/\mu\right)^{D-2}$ in the UV limit.

The evolution for all approximations of $Z_{(i)}$ and their corresponding η are exemplarily shown for $D = 6$ in figure 3.4. Matching the expectation formulated in the preceding discussions, the low energy scales of classical general relativity correspond to $Z_{(i)} = 1$. For increasing energies, both continuous approximations approach their value at the fixed point $Z_{(i)} \to 0$ with the quadratic one doing so more rapidly than the linear one. This behavior of $Z_{(i)}$ allows for the dimensionless coupling g to remain finite as it compensates the dependence on μ^{D-2}.

For experimental searches, two essential features have been discussed in this review of the AS scenario for quantum gravity. If it describes reality, the predictions of the ADD model for graviton contributions are rendered UV complete. Consequently, the associated virtual exchange process is no longer restricted by an high-energy cutoff. However, the cross sections of gravitational contributions also decrease as the corresponding coupling parameter becomes suppressed toward and beyond the transition scale $\Lambda_{\mathrm{Transition}}$. This would imply that the current bounds on LED are overestimated.

3.5 Current Experimental Bounds

Given that LED affect both observables of general relativity and quantum field theory, the sources for experimental constraints are varied. This section aims to give a concise overview of the current bounds on the model parameters and (mostly) follows the summary provided by the Particle Data Group [64]. Results from searches for quantum black holes are omitted as they require additional assumptions about the behavior of these objects.

Gravitational force As shown in table 3.1, small numbers of extra dimensions n allow for large compactification radii with respect to M_D. Tests of the classical Newtonian force at distances comparable to these radii, below which LED would give rise to deviations, can be translated into constraints on M_D. With the $n = 1$ scenario ruled out, current torsion balance experiments allow for tests of distances below the millimeter scale [65] corresponding to compactification radii for $n = 2$. Modifications to the gravitational potential are usually parametrized as

$$V(r) = -G_N \frac{m_1 m_2}{r} \left[1 + \alpha e^{-r/\lambda}\right], \tag{3.31}$$

where $\alpha = 8n/3 = 16/3$ and $\lambda = R$ for a 2-torus. The most stringent limits exclude values of $R > 37\,\mu\text{m}$ at 95 % credibility level (CL), translating to $M_D > 3.6\,\text{TeV}$ for $n = 2$ [65].

Astrophysical sources To remain compatible with models of stellar objects, the production and emission of gravitons has to be severely limited for small numbers of extra dimensions. The introduction of gravitons, contributing to the cooling process of supernovae by carrying away energy in a similar fashion to neutrinos, would lead to a significant change of the expected neutrino flux. Measurements of this flux emitted by the supernova SN1978A put very strict bounds on scenarios with $n = 2$ (3) extra dimensions of $M_D > 27$ (2.4) TeV [66]. However, the strongest limits derived from measurements of astrophysical observables are given by studies of neutron stars. Gravitons produced in a supernova, gravitationally bound to the remaining neutron star and decaying to photon pairs, would heat the surface of the neutron star. Bounds from surface temperature measurements require $M_D > 1700$ (76) TeV for $n = 2$ (3) [67].

Cosmological sources Considerations of nucleosynthesis pose constraints on contributions by gravitons to cosmological observables [68]. With respect to the density parameter of the universe, the addition of relic gravitons must not lead to an overclosure[5] to remain compatible with measurements, thus restricting the fundamental Planck mass to $M_D > 7\,\text{TeV}$ for $n = 2$. The same relic gravitons decaying to photons would alter the cosmic diffuse gamma radiation. Deriving bounds based on this relation yields $M_D > 100\,\text{TeV}$ for $n = 2$.

Graviton emission While section 3.2 focuses on the virtual exchange of gravitons, their emission and noninteracting traversal through the detector results in final states with missing transverse momentum[6]. Prominent final states are jet + p_T^miss and $\gamma + p_\text{T}^\text{miss}$. The most stringent limits are given by results of the CMS Collaboration quoting $M_D > 9.9$–$5.3\,\text{TeV}$ [69] for 2 to 6 extra dimensions based on $35.9\,\text{fb}^{-1}$ of data recorded in 2016 at a center-of-mass energy of $\sqrt{s} = 13\,\text{TeV}$. In the same data-taking period, the ATLAS experiment has recorded an integrated luminosity of $36.1\,\text{fb}^{-1}$ and have published comparable limits of $M_D > 7.7$–$4.8\,\text{TeV}$ for the same numbers of extra dimensions [70].

Virtual graviton exchange The virtual production and decay of gravitons offers multiple final-state signatures; each requires a dedicated analysis. As discussed in section 3.2, the fundamental scale of gravity M_D cannot be directly inferred from

[5] A closed universe implies a positive curvature of space and a density parameter of $\Omega > 1$.

[6] Missing transverse momentum is defined as the projection of the negative vector sum of all momenta reconstructed in an event onto a plane orthongonal to the beam axis.

measurements in this scenario. Instead, limits are set on the UV cutoff parameters associated to the respective conventions. For the sake of brevity while still allowing for direct comparisons, only the limits on Λ_T of the GRW parameter convention for LO cross sections are given in this paragraph. The current, most stringent bound of $\Lambda_T > 10.1\,\text{TeV}$ [71] has been determined by the CMS Collaboration with $35.9\,\text{fb}^{-1}$ of recorded data in the angular distributions of the dijet final state. With the same amount of data, a search for the decay into two photons by the CMS Collaboration provides the next best limit of $\Lambda_T > 7.8\,\text{TeV}$ [72]. Both measurements correspond to a center-of-mass energy of $\sqrt{s} = 13\,\text{TeV}$. For dilepton signatures, the strictest bound of $\Lambda_T > 4\,\text{TeV}$ has also been determined by the CMS Collaboration [73]. It is based on the combination of both the dielectron and dimuon channels at $\sqrt{s} = 8\,\text{TeV}$. The presented analysis is the first one to explore the dimuon mass spectrum for data recorded at a center-of-mass energy of $\sqrt{s} = 13\,\text{TeV}$ with respect to the ADD scenario for the model of LED.

Asymptotic safety in the presence of extra dimensions A reinterpretation of the results obtained in the search for LED in the dilepton channel at a center-of-mass energy of $\sqrt{s} = 8\,\text{TeV}$ has yielded exclusion limits on the model parameters of LED in the AS scenario for quantum gravity [63]. For each of the three approximations of the transition between the IR and UV energy regime discussed in section 3.4, two-dimensional bounds have been set in the plane spanned by the fundamental scale of gravity M_D and the transition scale $\Lambda_{\text{Transition}}$. These 95 % CL exclusion limits are shown for multiple numbers of extra dimensions $n \geq 2$ in figure 3.5. Each subfigure label indicates the considered approximation of the transition and explicitly mentions the assumed Minkowskonian spacetime as other options have been explored as well.

The motivation for experimental searches using data collected at particle colliders to set limits for $n = 2$, even though astrophysical and cosmological results pose extraordinarily strict limits on them, is twofold. On the one hand, the latter measurements are subject to significantly larger uncertainties compared to the terrestrial ones. On the other hand, as discussed by the original authors of the ADD model, scenarios with a reduced branching fraction for decays into photon pairs are possible [7]. As a consequence, limits derived using photon signatures could potentially be significantly overestimated.

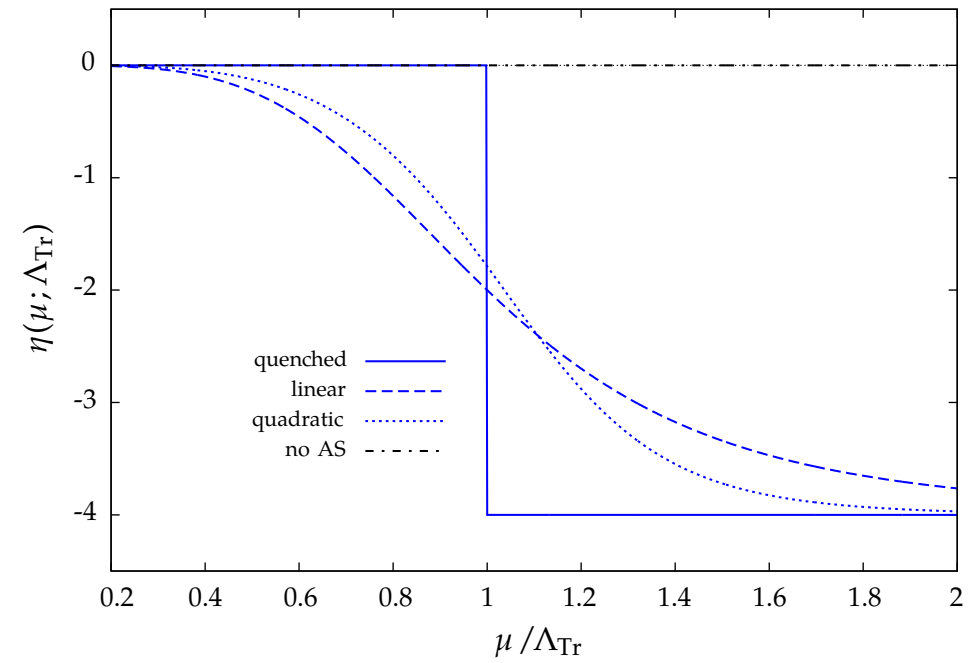

(a)

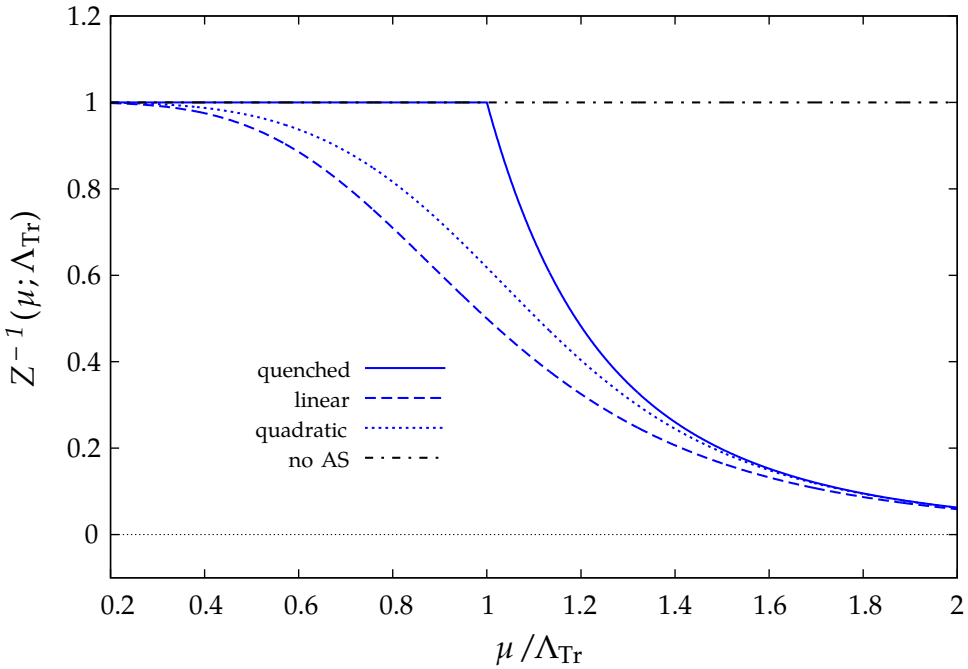

(b)

FIGURE 3.4: Anomalous dimension η in (a) and wave function renormalization factor Z^{-1} in (b) as a function of the energy scale μ with respect to the transition scale $\Lambda_{\rm Transition}$ [Adapted from 63]. Shown are the quenched, linear and quadratic approximations in comparison to a scenario without asymptotic safety in $D = 6$ dimensions.

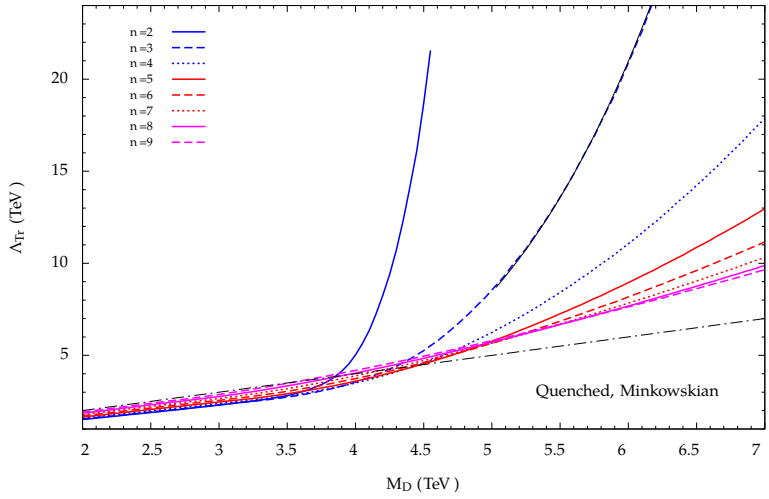

(a)

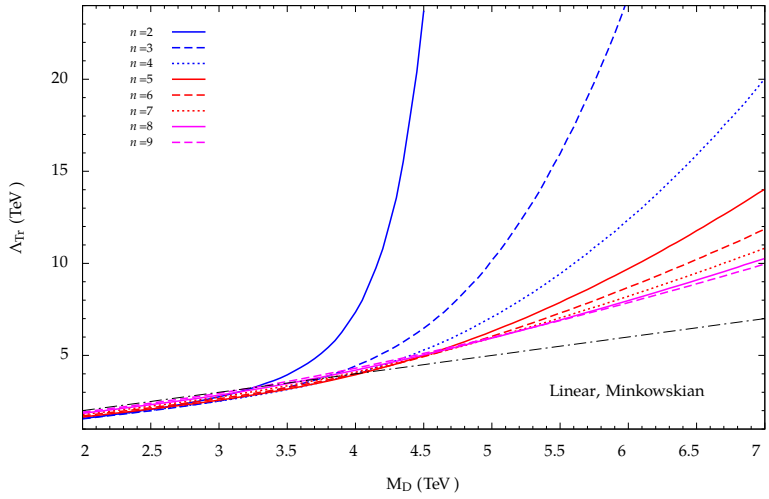

(b)

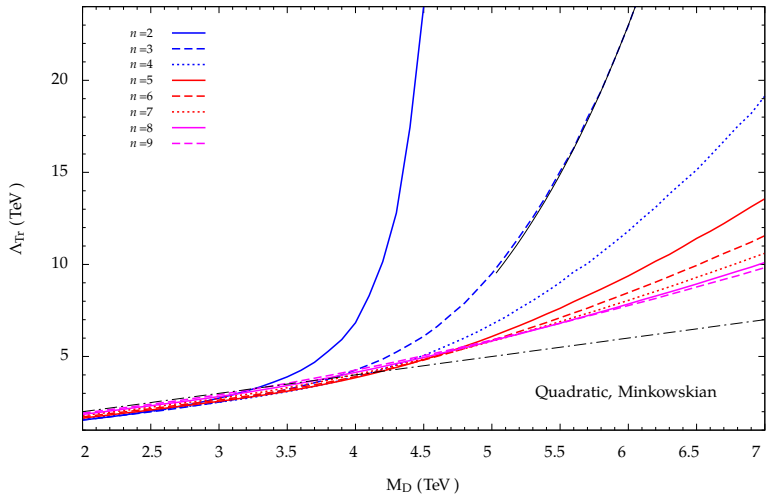

(c)

FIGURE 3.5: Exclusion limits at 95 % CL in the plane spanned by the fundamental scale of gravity M_D and the transition scale Λ_{Tr} [Adapted from 63]. They are based on the analysis of the dilepton channel at $\sqrt{s}$ = 8 TeV [73]. Refer to the text for details.

Chapter 4

Experimental Setup

The experimental basis of this analysis are the proton-proton collisions produced and recorded by the Large Hadron Collider (LHC) and Compact Muon Solenoid (CMS) experiments, respectively, during 2016 at a center-of-mass energy of $\sqrt{s} = 13\,\text{TeV}$. These two facilities are part of the laboratory of the European Organization for Nuclear Research, better known as CERN, located in Switzerland near Geneva. An aerial view of the border region around Geneva with an overlay indicating the tunnel structure of the LHC and the locations of the corresponding particle detectors is shown in figure 4.1.

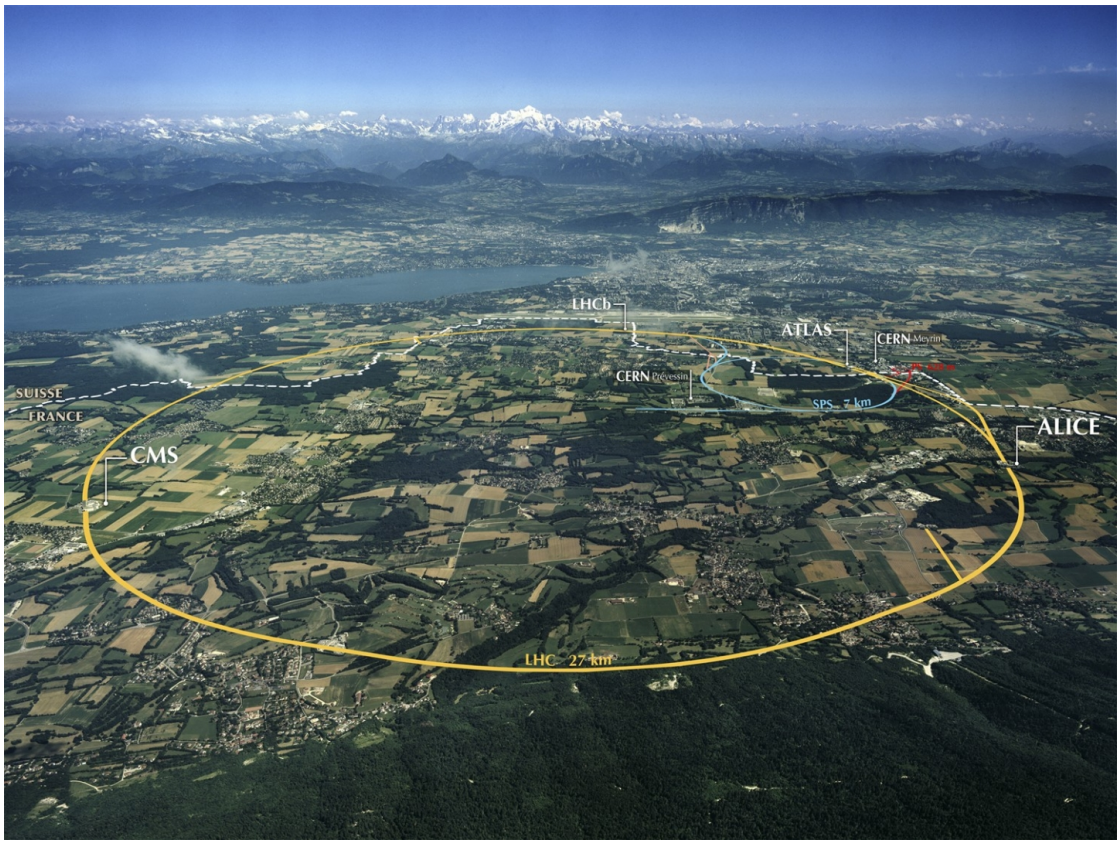

FIGURE 4.1: Aerial view of the Franco–Swiss border near Geneva overlaid by a sketch of the LHC accelerator complex and its particle detectors [74].

4.1 Large Hadron Collider

At the time of writing, the LHC is the most advanced, man-made particle accelerator and collider. Its general design [75] consists of a set of two, bidirectional storage rings

where dipole magnets are used to direct the particle beam, quadrupoles as well as higher order magnets to focus it and radio frequency cavities to accelerate the particles. All components reside in a 27 km long tunnel about 100 m below the earth, previously home to the Large Electron–Positron Collider. The aforementioned design allows for operating with both protons and heavy ions, including asymmetric setups where each beam consists of one of the two particle types. As this analysis is based on proton–proton collisions, the following description of particle acceleration at the LHC will be proton specific.

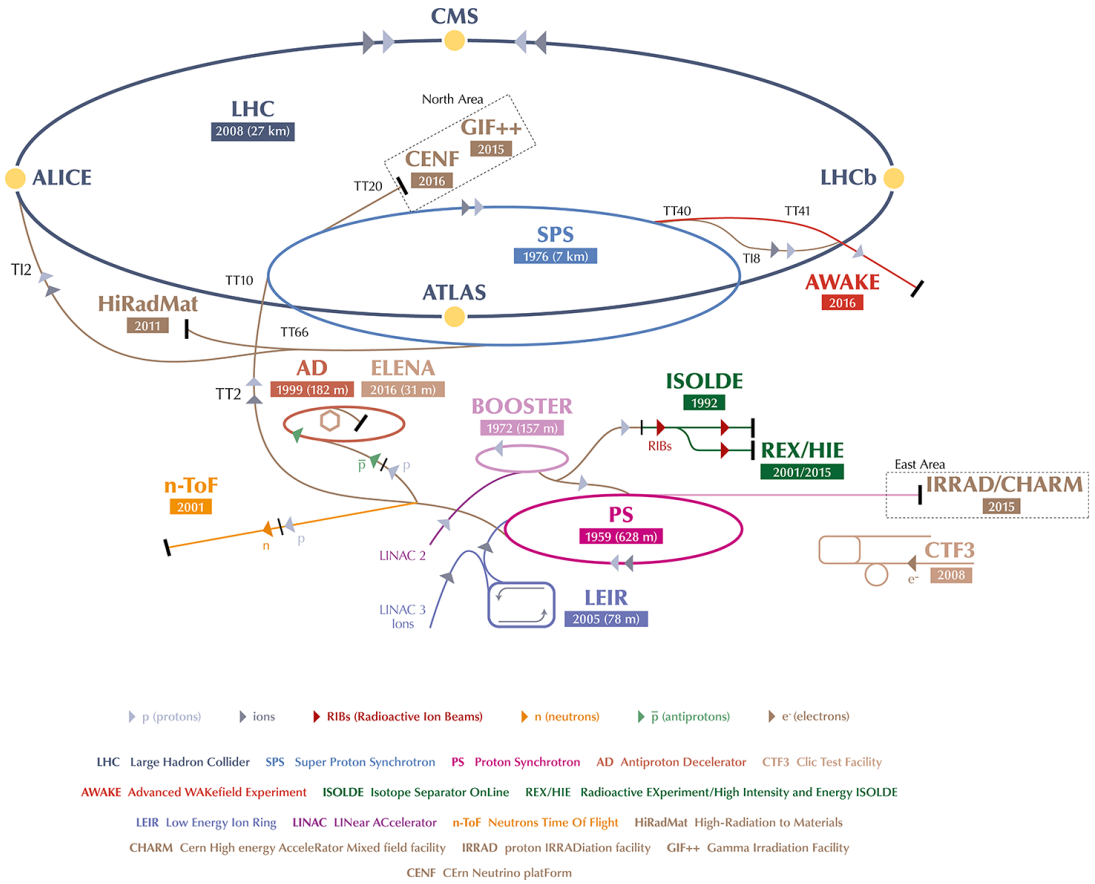

FIGURE 4.2: Schematic overview of the CERN accelerator complex [76].

The multistage injection chain providing bunches of protons to the LHC is schematically depicted as part of the CERN accelerator complex in figure 4.2. Extracted from hydrogen gas via an electric field, the initial protons have an energy of 90 keV. They receive an additional boost by a radio frequency quadrupole and then experience further sequential acceleration by the LINAC2, Proton Synchrotron Booster, Proton Synchrotron and the Super Proton Synchrotron, reaching an energy of 450 GeV. Splitting the resulting beam in half, the proton bunches are then transferred into the two beam pipes of the LHC where the final stage of the acceleration takes place.

Successive passes through the aforementioned radio frequency cavities, made of niobium, enable the protons to reach energies of 6.5 TeV. Given the fixed circumference of the storage ring, the maximum energy of the protons is ultimately limited by the bending power of the magnets directing their trajectory. By utilizing niobium–titanium dipole magnets, high field strengths are generated with values up to 7.7 T during 2016 [77]. Allowing the necessary 11 kA to pass through the material to produce this immense B-field is only possible by rendering the magnets superconductive. For this purpose, they are chilled down to 1.9 K by means of superfluid helium. Compared to the data-taking

period referred to as Run 1 (2009–2012) where the magnets were only trained to handle a maximum of 4 TeV per beam, the proton energies of 6.5 TeV in 2016 were much closer to the design maximum of 7 TeV. Focusing the beam is achieved through quadrupole, sextupole and octupole magnets while collimators are used to cleaning it of divergent particles.

Aside from the center-of-mass energy, the defining quantity of collider experiments is their (integrated) luminosity $\mathcal{L}$. It connects the cross section σ for a given process to the expected, average number of produced events per interaction region N by

$$N = \sigma \int \mathrm{d}t\, \dot{\mathcal{L}} \quad \text{with} \quad \dot{\mathcal{L}} = \frac{\mathrm{d}\mathcal{L}}{\mathrm{d}t} = \frac{N_p^2 n_b}{4\pi\sigma_x\sigma_y}\frac{c}{l}. \tag{4.1}$$

In this context, an event refers to the products of the fundamental interactions occurring at a single bunch crossing. The integrated luminosity is determined by the characteristic parameters of the beam. Here, N_p denotes the number of protons per bunch, n_b the number of bunches and σ_x, σ_y refer to the standard deviations of the normal-distributed beam width in the respective x, y directions at the interaction point. The second fraction represents the rotational frequency of the protons with c denoting the speed of light and l the circumference of the ring. With peak instantaneous luminosities exceeding the original nominal value by up to 50 %, the integrated luminosity recorded by the CMS experiment during the 2016 data-taking period (Fig. 4.3) amounts to 37.76 fb^{-1}.

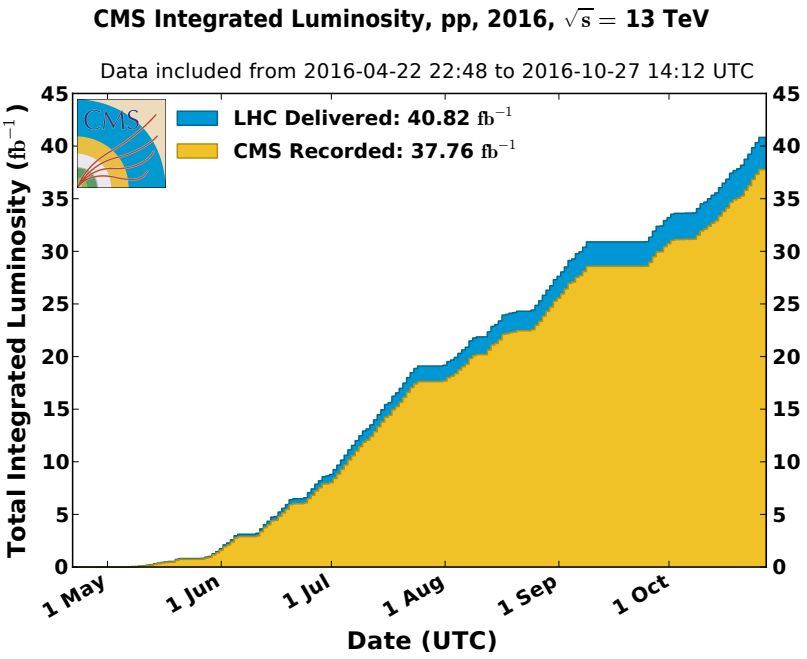

FIGURE 4.3: Integrated luminosity produced by the LHC and recorded by the CMS experiment over the course of the data-taking period of 2016 [78].

Of the four major particle detectors installed at the interaction points of the LHC, the specialized experiments ALICE [79] and LHCb [80] focus on heavy-ion and b-quark physics, respectively. The remaining two, the CMS [81] and ATLAS [82] experiments, are both general-purpose detectors of comparable capability. Their independent measurements serve as a safeguard against statistical fluctuations with respect to discoveries.

4.2 Compact Muon Solenoid

Being designed as a general-purpose particle detector, the CMS experiment [81] consists of multiple calorimetric and trajectory tracking components alongside its central feature, the superconducting solenoid. Its approximately cylindrical shape is structured into two "endcap" disks housing the central "barrel" inbetween them. The apparatus measures 22 m in length, 15 m in diameter, weighs 14 kt and is located at the fifth interaction point of the LHC. An overview of the different components is shown in figure 4.4, where a section is cut away to display the interior layout. Given the chosen final state of this analysis, the following sections will provide a brief description of the calorimetric subsystems and then focus on the reconstruction of high-energy muon tracks.

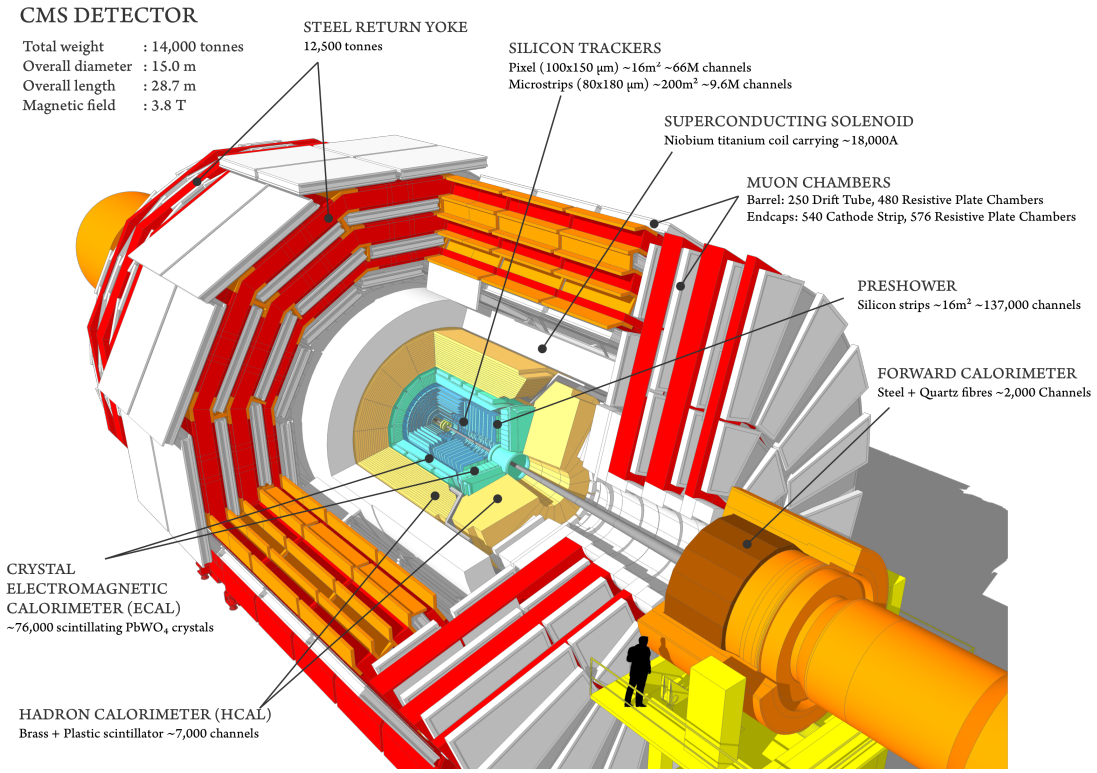

FIGURE 4.4: Cutaway view of the CMS detector [83] showcasing the different components.

The coordinate system chosen by the CMS Collaboration to describe their detector reference frame has its origin at the nominal interaction point of the two incoming beams. Defining the z axis along the beam trajectory and the x axis inwards to the storage ring center results in the y axis facing upward. Using radial coordinates, the distance r is determined with respect to the origin and the azimuth angle ϕ is measured in the x-y plane. Instead of the r-z plane polar angle θ, measurements are usually referring to the pseudorapidity $\eta = -\ln\tan(\theta/2)$ as it remains invariant under longitudinal Lorentz boosts. Angular distances between two objects can thus be defined as

$$\Delta R = \sqrt{(\Delta\phi)^2 + (\Delta\eta)^2}. \tag{4.2}$$

4.2.1 Calorimeters

Particle energy measurements in the CMS detector are performed by the electromagnetic (ECAL) and hadronic calorimeters (HCAL). Both subsystems rely on having a sufficient amount of material in terms of radiation/interaction lengths to ensure that the incoming particles deposits all (or at least most) of their energy. A segmented design allows for extracting directional information, which can be used to infer global characteristics of events.

Electromagnetic Calorimeter

As the name implies, the ECAL is responsible for measuring the energy of electrons and photons. This includes the electromagnetic component of jets[1], which is mostly given by $\pi^0 \to \gamma\gamma$. The material of choice are lead tungstate crystals $PbWO_4$, which provide a good response time and fine granularity in combination with radiation hardness.

Geometrically, the ECAL is split into a barrel component covering up to $|\eta| < 1.479$ and endcap components extending the reach to $1.479 < |\eta| < 3.0$. The former contains the majority of all crystals with 61 200 cells. For reading out and digitizing the scintillation light produced when particles deposit energy in these cells, avalanche photodiodes are used. Each endcap adds an additional 7324 crystals equipped with vacuum phototriodes, which are less efficient but more resistant to radiation damage than avalanche photodiodes. The physical length of all cells corresponds to about 25 radiation lengths X_0, ensuring the capture of most electromagnetically induced showers.

To avoid misidentifying the aforementioned neutral pion decays as single photons, a preshower detector is installed in front of the crystals for $1.653 < |\eta| < 2.6$. It forces electromagnetic showers by means of two lead radiators and measures them with silicon strip sensors.

The overall energy resolution of the ECAL for particles with an energy below 500 GeV can be parametrized as

$$\left(\frac{\sigma_E}{E}\right)^2 = \left(\frac{2.8\,\%}{\sqrt{E/\mathrm{GeV}}}\right)^2 + \left(\frac{12\,\%}{E/\mathrm{GeV}}\right)^2 + (0.3\,\%)^2. \tag{4.3}$$

The terms in this order correspond to stochastic, noise and constant contributions to the total resolution.

Hadronic Calorimeter

As the hadronic interaction length λ_I significantly exceeds the electromagnetic one, a dedicated HCAL is required. Its design as a four component system is driven by the increased radiation dose toward high pseudorapidities and limited volume available within the CMS detector.

The HCAL barrel component covers angles up to $|\eta| < 1.3$ and is positioned between the ECAL and the solenoid. Each top and bottom tile of its 36 wedges are made of steel. The steel tiles are interleaved with layers of brass and scintillating plastic, with the scintillation photons being captured by wavelength-shifting fibers and read out by hybrid photodiodes. Depending on the pseudorapidity, a single wedge has an effective thickness of 5.83 to 10.6 interaction lengths λ_I. The endcap equivalent is structured in the same way and adds coverage up to $1.3 < |\eta| < 3.0$. To capture the remainder of the hadronic activity beyond the solenoid coil, while also using it as absorber material, the

[1] Jets refer to narrow cones of particles produced in the hadronization of quarks or gluons.

"HCAL outer " (not shown in Fig. 4.4) adds an additional 1.2 interaction lengths in the central region.

The radiation intense forward region requires a different design approach. Using grooved steel absorber plates and quartz fibers as its active medium, the HCAL forward captures hadronic activity between $3.0 < |\eta| < 5.0$. While the output of its multi-anode photomultipliers is rarely used directly in analyses, it provides valuable input for the measurement of the missing transverse momentum.

4.2.2 Magnetic Field

With the bending power of the magnet being critical to the resolution of the momentum measurement and ability to differentiate electric charge, its design is instrumental to the reconstruction of muons. For the CMS experiment, the helix shape of the solenoid constitutes four wound layers of reinforced, niobium-titanium, Rutherford-type cables. While this choice implies an increased amount of multiple scattering within the coil, it allows for immense field strengths. Operating close to its maximum design value, the magnet provides a homogeneous B-field of 3.8 T for the inner tracking system. As discussed with respect to the design of the LHC (Sec. 4.1), accommodating the necessary electric current for these field strengths requires superconductivity. For the CMS magnet, this is primarily achieved through liquid helium cooling. Beyond the coil, the inhomogeneous flux of the B-field is mostly contained within and returned by the iron yoke. Interleaved with the layers of this 12 500 t structure, are the muon chambers. With the cold mass of the solenoid coil "only" amounting to 220 t, the yoke accounts for the majority of magnet system material.

4.2.3 Inner Tracking System

The primary trajectory reconstruction (tracking) system for charged particles and the detector subsystem closest to the nominal interaction point, is the inner tracker. Given its proximity, it faces the biggest challenges. Balancing a requirement for high granularity and fast response times with radiation hardness, while also minimizing the amount of material, has led to a design exclusively based on silicon detector technologies.

The semiconductor detection principle is centered around having a charge depletion zone where ionizing radiation can create free charge carriers[2]. To achieve this depletion, one can apply a reverse voltage to a half p- and half n-doted (silicon) diode. Measuring a current generated by the flow of free charge carriers then indicates the passage of a charged particle.

Figure 4.5 shows a cross section of the tracker layout, highlighting the division into silicon pixel and strip components. Demanding the highest granularity, the three innermost layers at radii 4.4, 7.3 and 10.2 cm as well as the corresponding disk on each side consist of pixels $100 \times 150\,\mu m^2$ in size. With an overall amount of 66 million pixels, an area of roughly $1\,m^2$ is covered. Interpolation of the read out charge pulses results in an excellent spatial resolution of 15 to 20 µm. This accurate reconstruction of individual hits[3] translates to precise track estimates but also allows for differentiating between the primary interaction vertex and secondary vertices from delayed decays.

Silicon strip detectors, organized into four subdivisions, surround the pixels. The tracker inner barrel (TIB) and tracker inner disks (TID) add four parallel and three perpendicular layers with respect to the beam direction, respectively. In the central

[2]With an electron transferred from the valence band to the conducting band, both the electron and the vacant bond or "hole" act as free charge carriers.

[3]A "hit" refers to a particle ionization signal in a single detector element, e.g., a pixel or strip.

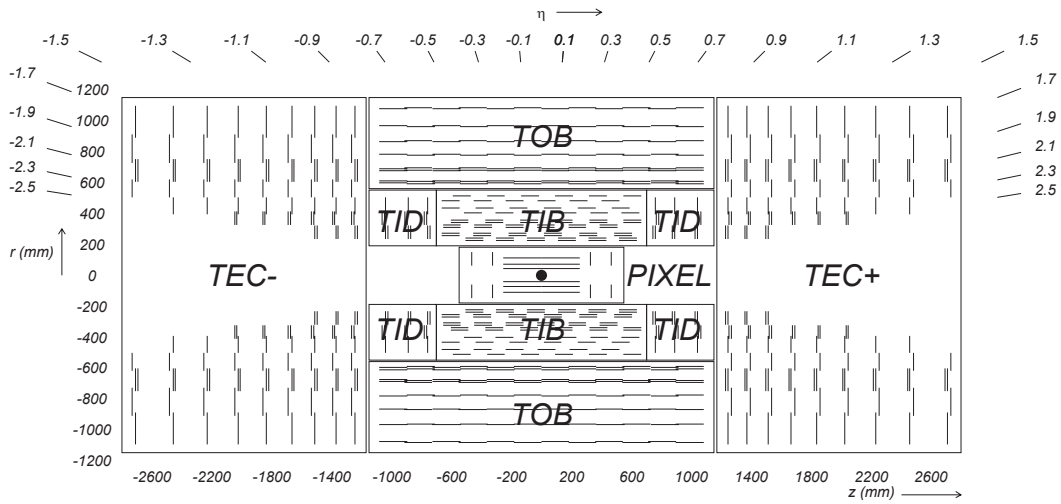

FIGURE 4.5: Layout of the inner tracking system of the CMS experiment [81]. Individual lines represent silicon strips (pixels), whereas double lines indicate an additional micro-strip detector to measure the respective secondary coordinate.

region beyond a radius of 55 cm, the tracker outer barrel (TOB) extends the coverage with an additional six layers. Following this structure, the tracker endcaps (TEC) provide nine more layers in each direction along the z axis. In total, the 9.3 million strips span a surface area of 198 m^2. Being determined by the width and pitch of the strips, the respective spatial resolution varies between 23, 35 and 53 µm with a tendency toward smaller values for strips closer to the interaction point. Attached to the first two layers of the TIB, TID and TOB, are additional micro-strip detectors. Their purpose is to measure the respective secondary coordinate (z in the barrel region and r in the disks) with a stereo angle of 100 mrad.

To ensure a consistently efficient performance of the inner tracking system with respect to leakage currents and radiation damage, it is operated at −20 °C and generally kept below a temperature of 0 °C. This design and careful instrumentation allows for deriving the momenta of high-energy (∼100 GeV) charged particles based on the measurement of the inner tracking system with an uncertainty of only 1 to 2 %. The geometric coverage of the silicon tracker extends up to $|\eta| < 2.5$.

4.2.4 Muon System

Both the subsystem dedicated to their measurement and the incorporation of their name into the title of the experiment emphasize the importance of muons. The aforementioned tracking system is placed behind the solenoid coil and between the return yoke layers, which is possible because of the minimal ionizing nature of relativistic muons. Being the only charged SM particle able to pass through the preceding detector material reliably, muons generate distinct tracks whose signature is used to trigger the recording of events. As this fact also precludes calorimetric measurements, the importance of a precisely reconstructed track to derive the momentum from is raised.

That the system is able to achieve this up to the highest energies, is ensured by three different gas-based detectors to be elaborated on in the next sections. They cover a combined area of 25 000 m^2 and are divided into five wheels in the barrel region and four disks in the endcaps. The layout of the individual muon system components, which, as mentioned before, are interleaved with the layers of the flux return yoke, is shown

in figure 4.6 for one quadrant of the CMS detector. Of particular interest is the angular coverage of $|\eta| < 2.4$, which defines the geometric acceptance of the detector for muons.

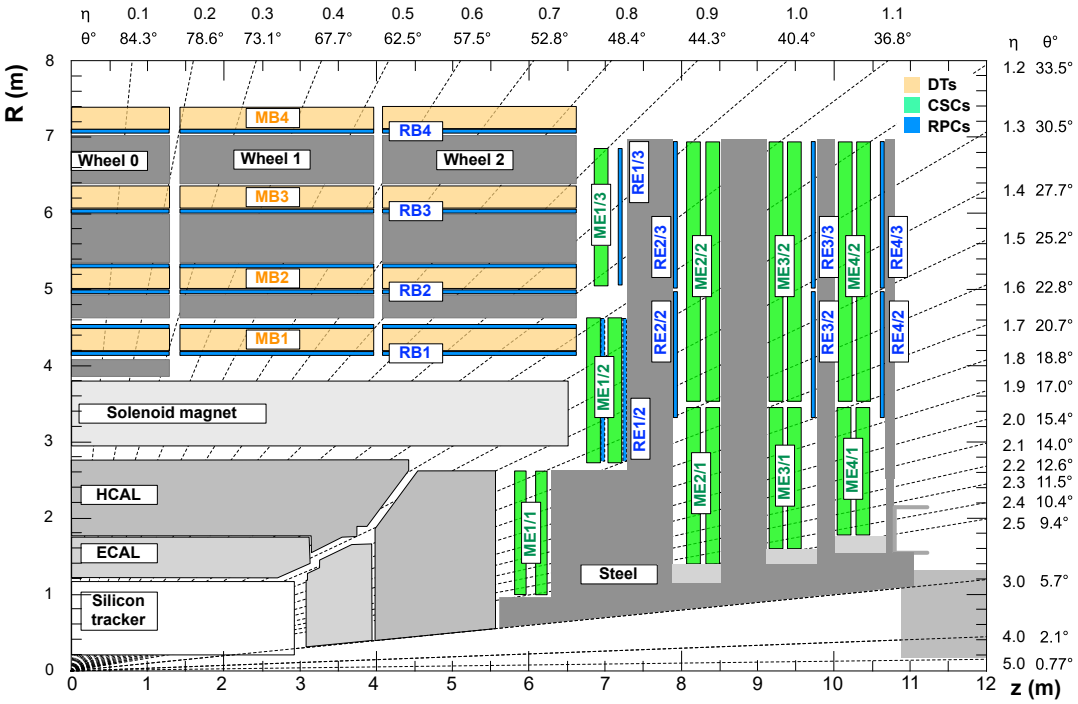

FIGURE 4.6: Quadrant of the CMS detector showcasing the muon system [84]. Individual component types are colored according to the legend.

Drift Tubes

Drift tubes (DTs) are installed in the muon system wheels up to $|\eta| < 1.2$ and are organized into four stations. The first three stations consist of three superlayers each, which are in turn made of four layers of drift cells. While the outer two superlayers measure the r-ϕ coordinates, the middle one is dedicated to the determination of the z component. In the fourth station, there is no central superlayer and therefore it focuses entirely on measurements in the r-ϕ plane.

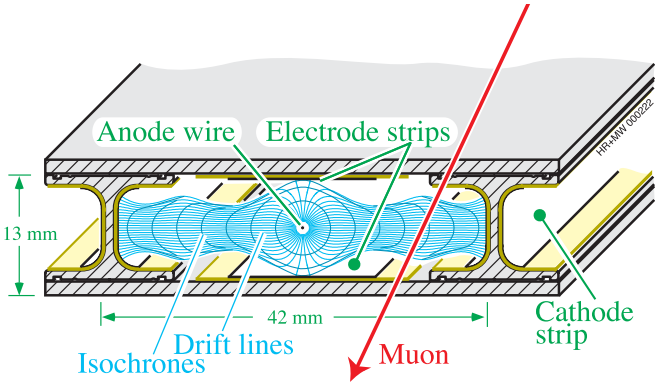

FIGURE 4.7: Schematic view of a single cell in the drift tubes of the muon system [85]. Simulated drift paths and their isochrones give an indication of the charge carrier trajectories.

Even though the physical structure is quite different, the detection principle of gas detectors is comparable to the one of semiconductors. A gold plated steel wire acts as the anode at the center of each 2.4 m long drift cell, with aluminum tape on each wall constituting the cathode counterpart. Figure 4.7 shows a muon traversing the drift cell and ionizing the gas mixture consisting of 85 % argon and 15 % carbon dioxide. Electrons and ions then follow the drift paths toward the anode and cathode, respectively, resulting in a current pulse signal. Isochrone lines indicate positions where primary ionization coincides with identical anode response times.

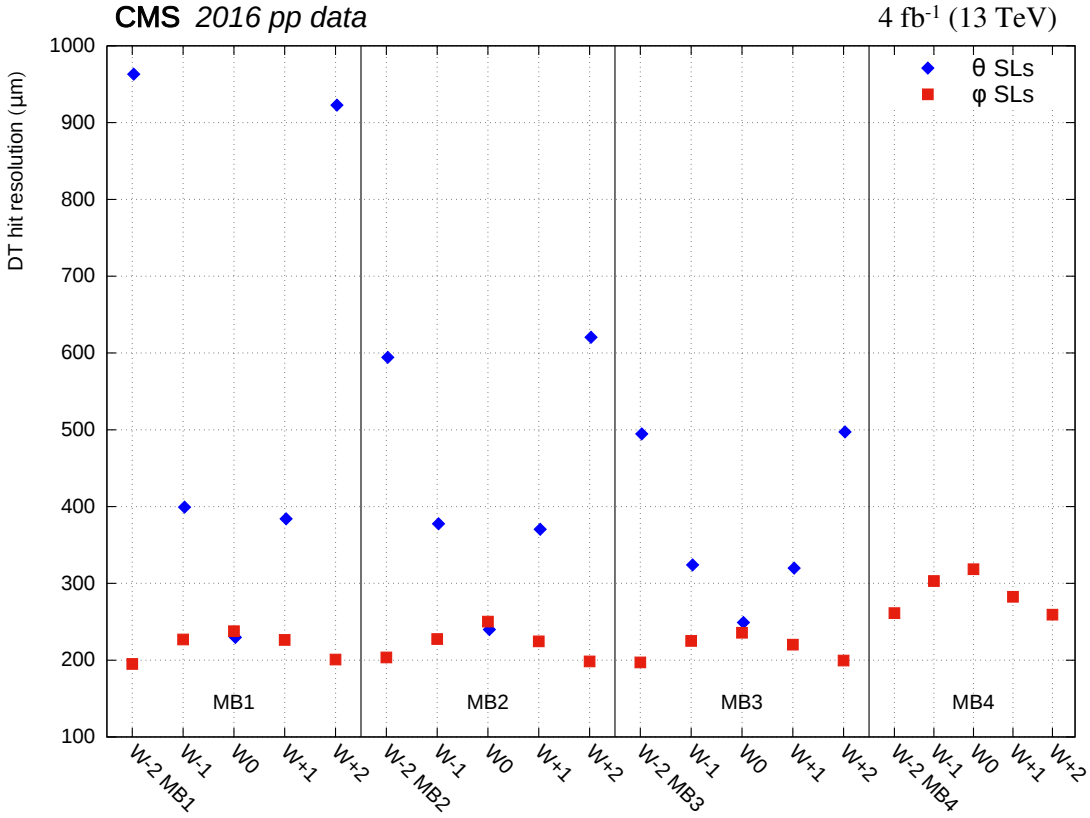

FIGURE 4.8: Spatial resolution of individual hits reconstructed by drift tubes in the respective muon station and wheel during 2016 [14]. Measurements of the ϕ and θ coordinate are denoted by squares and diamonds, respectively. The size of the markers exceeds the uncertainties in the measurements.

The design of the drift tubes allows for covering a large area and is optimized for operating with moderate muon fluxes in a homogeneous magnetic field (here, mostly contained within the yoke). A total of 172 000 tubes are installed in the five wheels of the barrel region. Categorized by muon station, the spatial resolutions of the DTs in a given wheel are visualized in figure 4.8. Matching the detector design, a symmetric dependence on the pseudorapidity is observed. While the resolutions in the ϕ and θ direction are similar in the central wheel as the trajectories are mostly transverse to the layers, they evolve differently with rising inclinations. For larger values of $|\eta|$, the track segment in a ϕ superlayer is elongated, which results in more ionization and thus a better resolution. However, the resolution worsens for θ superlayers as the linearity of the distance-drift time relation is negatively affected. With single-hit spatial resolutions in the ϕ direction below 250 µm (slightly worse in the fourth station without the complementary θ measurement), a station with 2×4 hits is able to meet its goal to resolve differences of 100 µm.

Cathode Strip Chambers

Being faced with an inhomogeneous magnetic field and much higher particle fluxes in the endcaps, a different detection approach is required. The region between $0.9 < |\eta| < 2.4$ has therefore been chosen to be covered by four layers[4] of cathode strip chambers (CSCs). They are designed as multi-wire proportional chambers, where a single CSC consists of seven trapezoidal panels of radially oriented anode wires. A 40 % Ar, 50 % CO_2 and 10 % CF_4 mixture fills the intermediary volume. At the wider end of each trapezoid, cathode strips are placed perpendicularly to the wires.

Station / ring	Spatial resolution / µm		
	Run 1	Run 2	
	2012	2015	2016
ME1/1a	66	48	45
ME1/1b	57	54	52
ME1/2	93	93	90
ME1/3	108	110	105
ME2/1	132	130	125
ME2/2	140	142	134
ME3/1	125	125	120
ME3/2	142	143	135
ME4/1	127	128	123
ME4/2	147	143	134

TABLE 4.1: Transverse spatial resolution per cathode strip chamber station based on six respective hits [14]. The systematic improvement in the 2016 measurement corresponds to a slight increase in the argon fraction of the gas mixture caused by a miscalibration. As it would otherwise impact the longevity of the cathode strip chambers, the gas composition has since been corrected. Values of the fourth column thus represent roughly 65 % of the data recorded in 2016, while the remainder is better represented by the third column.

Utilizing the respective outputs of the anode and cathode allows for a simultaneous measurement of r and ϕ, with a spatial resolution varying between 45 to 143 µm in 2016 (Tab. 4.1). This CSC design maintains a fine segmentation while providing the necessary response times in combination with radiation hardness.

Resistive Plate Chambers

The design of the third and final gas detection technology does not offer a competitive spatial resolution but instead focuses on fast response times. These response times allow for an accurate assignment of measurements to bunch crossings and are therefore ideal for triggering. The resistive plate chambers (RPCs) follow a double-gap design consisting of two parallel plates housing a gas filled volume with a layer of read out strips installed in the middle. By using a segmented central layer, the necessary spatial resolution is ensured. Operating in avalanche mode enables response times of about 2 ns, which are comparable to those of scintillators and much lower than the 25 ns between successive bunch crossings.

To serve their purpose while retaining a high spatial resolution, RPCs are installed in tandem with the other two technologies. One RPC is mounted on the top and bottom of a wheel for the first two DT stations while the outer layers have one RPC each. As shown

[4]The fourth layer has been extended during the upgrade phase preceding Run 2.

in figure 4.6, a large part of the four CSC discs is also accompanied by one respective layer of RPCs. This amounts to a total coverage of roughly $|\eta| \lesssim 1.8$.

4.3 Alignment

A crucial ingredient for the translation from individual position measurements of the detector components to a precise momentum determination is the alignment of the components relative to each other. There are two systems in place to determine the alignment. The first one is based on hardware and, while less precise than the other option, is the only one available after detector disassembly for the purpose of upgrades. At the beginning of a data-taking period, after the detector is commissioned and the magnet has been ramped up to its nominal field strength, optical systems are utilized to measure the relative positions. While the alignment of the silicon tracker and CSCs is primarily determined via lasers and CMOS cameras, LEDs are used for the DTs. Relative positions are then computed by the link system to which all values are forwarded. Despite the invested effort, the initial alignment at the beginning of a data-taking period is not expected to be ideal.

The other system requires a sufficient amount of track data (including measurements of cosmic muons) to be recorded from which the alignment can then be derived. Based on measured hits and expected particle propagation, it is possible to refine the alignment of the inner tracking system. This is achieved through a minimization of the χ^2 test statistic, i.e., the squared residuals of the distance between hits and the reconstructed track relative to the uncertainty in the measured hit position. Outward extrapolation of the tracks from a well aligned silicon tracker, while taking into account energy losses and the inhomogeneous magnetic field, allows for improving the muon system alignment as well. As this procedure scales with increasing amounts of recorded data, the final settings are being referred to as the *asymptotic alignment*.

4.4 Triggering & Data Acquisition

The LHC reached event production rates of 40 MHz with peak instantaneous luminosities of $1.5 \times 10^{34}\,\mathrm{cm}^{-2}\,\mathrm{s}^{-1}$ during 2016 [78]. This number far exceeds current storage capabilities, which are designed to record at a rate of less than 1 kHz. A system to select events of interest is required. For the CMS detector, a two-stage, consecutive triggering architecture has been designed. In anticipation of the increased challenges of Run 2 and beyond, it has received a substantial upgrade [86, 87].

The initial decision whether to keep or discard an event is made by the Level-1 (L1) trigger system. Its rate is constrained by several other electronic components who can operate at a maximum of 100 kHz. In order to maintain this limit, the L1 trigger is designed to reach a decision with a maximum latency of 4 µs with respect to the associated bunch crossing. Figure 4.9 shows the hierarchical flow of data for the upgraded system. Both the calorimetric and muonic trigger paths rely on primitive inputs from subsystems being gathered and evaluated at different layers, with the final decision resting with the global trigger(s). The aforementioned upgrade introduced custom circuit boards equipped with powerful field programmable gate arrays, facilitating sophisticated reconstruction algorithms to be run during data taking. Communication via optical fibers has increased the bandwidth of the boards by a factor of 8.

When the L1 trigger accepts an event, the data buffered in the various subsystems is forwarded to the data acquisition system. With all the digitized information available and a less constrained time budget, a high-level trigger (HLT) then performs a more

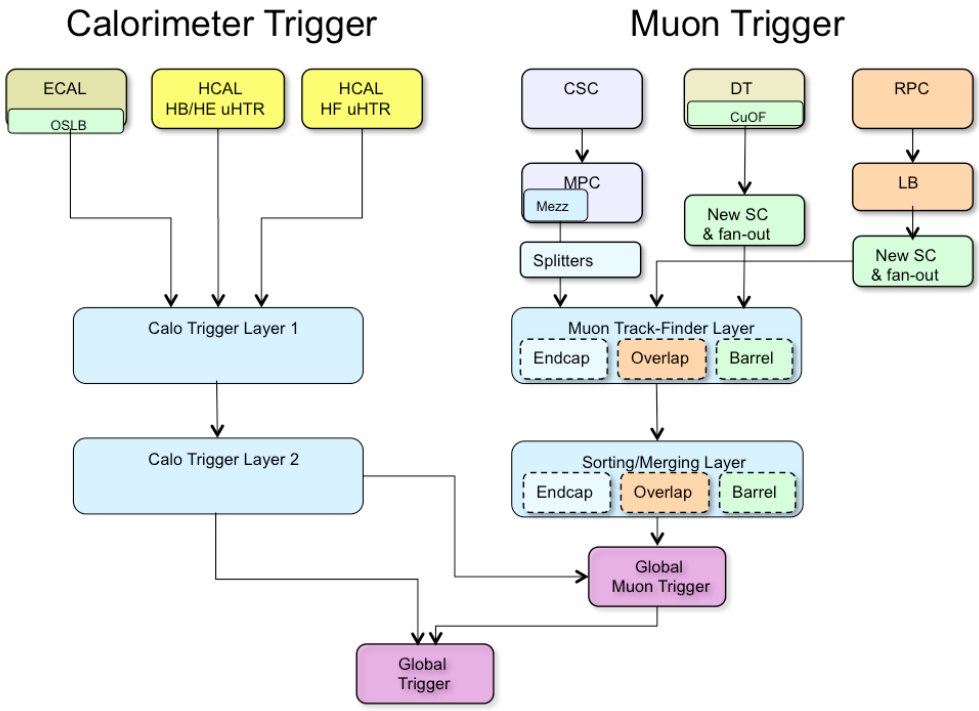

FIGURE 4.9: Hierarchical flow of data for the Level-1 trigger of the CMS experiment [86].

advanced reconstruction. Applying the requirements of the HLT reduces the rate to about 600 Hz and leads to the event being stored on disk as well as its eventual, tiered distribution to computing centers.

4.5 Computing Grid

The four-layer design of the worldwide LHC computing grid [88] serves as a scheme for the distribution and analysis of the recorded events. All data passes through the central hub of CERN referred to as Tier-0. While the hub also performs other computational tasks, its primary purpose is the storage and safe-keeping of data. For that reason, it consists of two physically removed data centers with mirrored content. The 11 large scale computing facilities of the Tier-1 layer share some of the same safe-keeping responsibilities but are primarily utilized for reconstruction tasks and the storage of their results. Typical Tier-2 computing grids are hosted by universities or institutes. Some reconstruction tasks are externalized to these resources, but they are also available for running individual analyses. Local computing resources are usually subsumed under the Tier-3 label.

Chapter 5

Reconstruction of Muon Trajectories

While a few general aspects of particle track reconstruction have been touched upon in the previous chapter, the chosen dimuon final state warrants a more detailed discussion with respect to high-energy muon tracks. For events with this type of signature, virtually all relevant information (most notably momentum, charge and particle type) are derived from the trajectories measured by the two tracking systems. In the CMS Collaboration, a dedicated "Tune-P" algorithm [14] is used for the hit-based reconstruction of high-energy muons. Prior to the review of this algorithm, the general track reconstruction procedure [89] will be briefly discussed.

5.1 Trajectories of Charged Particles

For a free, charged particle passing through a magnetic field, the equations of motion only depend on the Lorentz force. In an ideal, cylindrical detector, this behavior would be described by a helix and its free parameters. An inhomogeneous magnetic field as well as the inclusion of energy loss and multiple scattering while traversing the detector material requires a generalized description with different dependencies

$$\{x, y, z, \alpha, q/p\} \rightarrow \{x, y, x', y', \alpha, q/p\} \,. \tag{5.1}$$

Here, the helix coordinates are denoted by x, y and z, the angle of the trajectory segment with respect to the magnetic field by α and the quotient of electric charge divided by momentum by q over p. The corresponding curvature radius in the x-y plane is then given by $R = p\cos(\alpha)/(qB)$. A generalized form with respect to a reference plane $z = z_r$ for a nonuniform magnetic field $\vec{B}(x, y, z)$ can instead be expressed in dependence of the two coordinates x, y and their derivatives x', y'.

Using the given expression for the curvature radius as an estimate, one can see how the detector-specific parameters impact the measurement of the momentum. Stronger magnetic fields correlate with tighter radii, whose determination has a quadratic dependence on the spatial resolution. The curvature of the particle trajectory is also impacted by the traversal of the detector material, which primarily results in two types of interactions. The first one is given by a stochastic sequence of Coulomb scattering processes (mostly off nuclei) and is therefore referred to as multiple scattering. Given sufficiently thick material, the trajectory deflection angle becomes Gaussian distributed [90]. Mean energy loss of charged particles traversing through material, the second type of interaction, is described by the Bethe–Bloch formula [91, 92]. For muons with momenta above 100 GeV, this consecutive process of ionization becomes nonnegligible. A further aspect to consider is the cascading ionization of muons with sufficiently large momenta, which can also produce showers of secondary particles prompting additional detector responses.

5.2 Track Building

To reconstruct trajectories based on positional information provided by each subdetector, the CMS Collaboration utilizes a procedure constituting four phases [93]: Seeding, trajectory building, trajectory cleaning and trajectory smoothing. These stages are specific to combinatorial Kalman filtering [94]. In its most simple scenario of linear models and Gaussian uncertainties, Kalman filtering is equivalent to maximum likelihood estimation. The combinatorial version draws motivation from physical constraints and consequent attempts to reduce biases by exploring all combinations of hits.

Seeding As a starting point of the track, seeds are generated based on individual hits assuming compatibility with the primary vertex[1]. They can be categorized into hit-based and state-based types, which constitute the ones most commonly used by the CMS Collaboration. Multiple hits (pairs or triplets) in the inner tracking system whose combined trajectory has its origin close to the nominal interaction point are required for the former type. For state-based seeds, all assumptions are based on the initial state-estimates of the momentum and direction derived from the muon system measurements, requiring no hits in the silicon tracker.

Using "standalone" muons, those whose reconstruction is only based on hits in the muon system, as an example, seed candidates are constructed via an initial transverse momentum estimate. This estimate is generally derived from the bending angle $\Delta\phi$ between two detector components with respect to the assumed vertex of origin. Its specific implementation depends on the number of available segments, subsystem and distance to the interaction point. Given hits in the third and fourth CSC muon station, the angle would simply be given by their distance in ϕ. For single segments in the first DT station, $\Delta\phi$ would be determined with respect to the direction of the primary vertex.

Trajectory Building Initiating the track building process based on the positional and directional information of a seed, the trajectory is extrapolated using the Kalman filter. Each iterative extrapolation to find compatible hits uses the full knowledge of track parameters at the given detector layer, including the aforementioned uncertainties due to material effects. In terms of mathematical procedure, this implies evaluating and updating the fit parameters and covariance matrices at each step. The combinatorial approach dictates that all possible trajectories are explored in parallel. Putting constraints on the number of missing or invalid hits and the fit quality of the extrapolations limits the number of trajectories that are ultimately taken into consideration.

Trajectory Cleaning An exploration of all trajectories in the aforementioned manner yields a large amount of tracks. At the cleaning stage, ambiguities between reconstructed trajectories with large fractions of identical hits are resolved. The goal is to retain the maximum number of independent tracks.

Trajectory Smoothing Reversing the fitting direction of tracks allows for the evaluation of the updated covariance matrices at each stage. Based on the final fit parameters, outliers and improbable track candidates can be efficiently rejected. This last stage increases the robustness of the algorithm and yields the final track candidates.

[1] A primary vertex is defined as the reconstructed vertex with the largest sum of squared transverse momenta of physics-objects [95]. These objects are jets, reconstructed using all tracks associated to the vertex, and the corresponding missing transverse momentum, i.e., the negative vector sum of their transverse momenta.

Before choosing the preferred track from the remaining candidates, they are pruned for signatures without sufficient hits in the muon system. Finally, by judging the quality of the track fits and points of closest approach to both the beam line and interaction point via extrapolations, one track is chosen.

5.3 Muons with High Momenta

Following the steps detailed in section 5.2, multiple types of tracks can be reconstructed based on different subdetector inputs and varying filtering constraints. The Tune-P algorithm [14], optimized for the reconstruction of high-energy muon tracks, can be understood as a decision tree for selecting between track types. An overview of these types is given in the following paragraphs before the logic of the decision tree is detailed. The initial three track reconstruction algorithms are motivated by the individual measurements of the two tracking systems as well as their combination, while the subsequent track types aim to reduce specific sources of uncertainty in the reconstruction.

Standalone Standalone muon tracks refer to those which are only based on DT and CSC information. As outlined in section 5.2, seed candidates are chosen based on rough momentum estimates derived from the bending angle between segments. These types of tracks are not directly incorporated into the Tune-P algorithm but are instead indirectly evaluated in combination with spatially matching tracks reconstructed in the inner tracking system.

Global With the aforementioned matching between standalone trajectories to silicon tracker tracks, global muon tracks are constructed. Said matching starts with an outside-in process. Using an extrapolation of the standalone muon track constrained by the requirement to originate close to the interaction point allows for selecting suitable track candidates from a tracker-only reconstruction. An iterative pruning of these candidates is performed via stringent momentum and spatial matching. The latter includes a projection of both tracks onto the same plane and subsequent application of fit constraints. This procedure is accompanied by an inside-out approach where the silicon tracker tracks are extrapolated under consideration of increasing radiative energy losses and Coulomb scattering.

If suitable matches are found, the respective hits of the tracks are used to perform a new global fit. Should more than one suitable match exist, the fit with the best, i.e., lowest quality parameter χ^2 is chosen. It should be noted that individual hits can be discarded in the process of reconstructing the global track.

Tracker Similar to the construction of standalone muon tracks in the muon system, one can perform a reconstruction based on information provided by the inner tracking system. The aptly named tracker muon tracks are seeded by two to three consecutive hits recorded by the pixel and/or strip components. While the track fits themselves only use the measurements of the silicon tracker, compatible hits in the muon chambers are required for the muon to be considered a valid tracker muon. One major advantage, aside from the high granularity of the subsystem, is the minimized impact of interactions with the material. With the inner tracking system being closest to the nominal interaction point, each muon only has to traverse its silicon components which have a comparatively low density. As the trajectories of muons with low momenta are prone to be affected by the substantial increase in the material density beyond the inner tracking system, the best estimate for their momentum is often provided by tracker muon tracks.

Tracker plus first muon station As radiative energy losses become increasingly important toward higher particle energies, the accompanying electromagnetic showers (see Sec. 5.1) can contaminate the positional measurements in a layer. A relatively simplistic approach to address this issue is to discard the information provided by the outer muon system layers. The resulting tracker plus first muon station (TPFMS) track is then given by a refit of the global muon track using only the hits recorded in the tracker and the innermost muon station with measurements.

Picky Evaluating the multiplicity of hits in each chamber the muon passes through facilitates a reconstruction that is more specific to the characteristics of a given trajectory compared to the TPFMS tracks. Once again using the global muon track as its basis, the "picky" algorithm checks for additional hits in a cone around the ones that are part of the fit. Layers with more than one hit are considered to be contaminated. Hits in these chambers are removed from the fit if they deviate too much from the global muon track using the χ^2 test statistic as the criterion. As done for the TPFMS track, this pruned set of global trajectory hits is then refit.

Dynamic truncation By combining the truncation of the TPFMS algorithm with the fine-grained evaluation of hits from the picky one, a dynamically truncated (DYT) track can be constructed. As the global trajectory beyond the inner tracking system is built, the extrapolations to muon system segments are scrutinized for large energy losses. Using the covariance matrix obtained after the propagation through the silicon tracker, the extrapolation estimate is compared to the available hits in the muon system layers in an iterative fashion. Should the compatible segments correspond to a large energy loss of the muon, they are excluded from the Kalman filtering process and the refit only takes the preceding hits into account.

Based on these options, the Tune-P algorithm aims to provide the best track estimate for each muon. The default order in which the reconstructed tracks are considered as candidates is given by the following sequence: The picky, DYT, tracker muon, TPFMS and finally the global muon track. If the fit corresponding to an algorithm did not converge or has a high relative uncertainty in the tranverse momentum, it is removed from the sequence. By default, only tracks with a $\Delta p_\mathrm{T}/p_\mathrm{T} < 25\,\%$ satisfy the latter requirement. However, if this threshold is exceeded in all fit results, a less stringent criterion with $\Delta p_\mathrm{T}/p_\mathrm{T} < \Delta p_\mathrm{T}/p_\mathrm{T}\big|_\mathrm{min} + 15\,\%$ is applied with respect to the lowest relative uncertainty in the transverse momentum of all tracks $\Delta p_\mathrm{T}/p_\mathrm{T}\big|_\mathrm{min}$. Starting with the first of the remaining track candidates, pairwise comparisons with the other ones are performed in the defined order using varying criteria. Should the considered track at a given step provide a better estimate of the muon trajectory, the candidate is updated accordingly.

In a scenario where all trajectory fits have converged and have a sufficiently small relative uncertainty in the transverse momentum, the first pair of tracks to be compared are provided by the picky and DYT algorithm. The criterion to be evaluated is, once again, the relative uncertainty in the momentum measurement $\Delta p_\mathrm{T}/p_\mathrm{T}$ where the track with the lower value is chosen. Using the tail probability of the respective χ^2 distribution[2]

$$\tilde{P}(\chi^2, k) = -\log\left(\int_0^{\chi^2} \mathrm{d}m\, \frac{m^{k/2-1}}{2^{k/2}\Gamma(k/2)} e^{-m/2}\right), \tag{5.2}$$

[2]Using a logarithm in this context has no impact on the sign of the difference. Its primary purpose is to avoid operating with values of vastly different magnitudes.

where k denotes the number of degrees of freedom, the candidate is then successively compared to the tracker muon and TPFMS algorithm. The thresholds above which the candidate is replaced, $\tilde{P}_{\text{Candidate}} - \tilde{P}_{\text{Tracker}} > 17$ and $\tilde{P}_{\text{Candidate}} - \tilde{P}_{\text{TPFMS}} > 40$, have been specifically determined for the two algorithms in question. Following the preceding discussion of muons with low momenta and the impact of the significantly increasing material density beyond the silicon tracker, one last test is performed. Should the transverse momentum estimate of either the candidate or tracker muon track be below 200 GeV at this point, the tracker muon track will be chosen. Seeing how there is no specific test for global muon tracks, they can only become the candidate in the rare scenario where all other track fits yielded poor results. This is of course by design, as one expects the optimized track reconstruction algorithms to perform better than the general global one. With respect to previous iterations of this algorithm, the major addition for analyses at $\sqrt{s} = 13$ TeV is the DYT track.

For about 99 % of all muons produced within the detector acceptance either a tracker muon or global muon track, and consequently a Tune-P track, is reconstructed [14]. By characterizing the relative residuals of the charge over transverse momentum ratio using the root mean square (RMS), the performance of the Tune-P and tracker muon algorithms are compared in figure 5.1. Given that the former incorporates the latter, no (substantial) differences between the two algorithms are observed for transverse momenta below 200 GeV. Beyond this threshold, the Tune-P algorithm does not default to the tracker muon track and shows a progressively better performance as it benefits from the inclusion of measurements in the muon system. At transverse momenta of 1 TeV, the difference in terms of RMS approaches a factor of two.

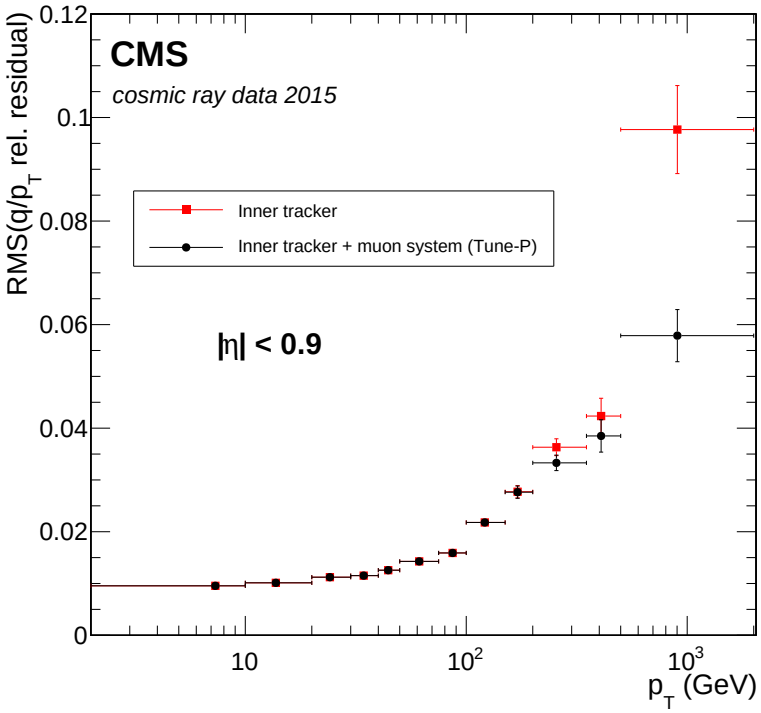

FIGURE 5.1: Root mean square of the relative residuals for the charge over transverse momentum ratio [14]. Compared are the performances of the Tune-P and tracker muon algorithms as a function of the transverse momentum. The measurement is based on muons from cosmic rays recorded during 2015.

Chapter 6

Data Sets

Having defined the final-state signature with a well motivated signal to search for, appropriate data sets with which to perform the analysis need to be selected. This chapter will provide the reasons behind each choice, starting with the experimentally recorded data and then proceeding to the simulated backgrounds of the SM and signals of the virtual graviton exchange process.

Programmatic access to the processed data sets is provided by the software framework developed by the CMS Collaboration, generally abbreviated to CMSSW [96]. Its flexible structure allows for the integration of individual programs and libraries, creating a centralized software stack with many applications. This includes but is not limited to the calibration and alignment of detector components, simulation and reconstruction of events as well as subsequent derivation of high-level physics objects. The level of abstraction in the data formats which are used to store the reconstructed events ranges from RAW to MINIAOD [97]. Here, the former contains the digitized detector and DAQ output on which the object reconstruction of the RECO format is based. Serving as the starting point for most studies, the analysis object data (AOD) format and its slimmed down MINIAOD version provide the aforementioned sophisticated and convenient physics objects.

The presented analysis is based on `CMSSW_8_0_26_patch2` of the recommended `CMSSW_8_0_X` release cycle for analyses pertaining to the 2016 data-taking period [98]. Local processing is performed by the TAPAS software framework [99] developed in a collaborative effort by the members of the Physics Institute III A of the RWTH Aachen University.

6.1 Trigger Options

The data provided within the CMS Collaboration is structured with respect to its trigger paths, i.e., the sequence of triggers culminating in the HLT. For the given dimuon final state, the available options for triggering are either demanding both or at least one of the two muons to be identified. While one would naturally gravitate toward double-muon trigger paths given a signature constituting two muons, the deciding factor are the trigger efficiencies.

With respect to the event selection—to be discussed in chapter 7—the combination of HLT_Mu50 and HLT_TkMu50 reaches an efficiency of more than 99 % as shown in figure 6.1. These two labels represent the single-muon triggers with the lowest kinematic threshold while not requiring any prescaling[1] or spatial isolation. The observed "turn-on" behavior, a steep increase of the efficiency at the beginning of the spectrum before a plateau is reached, corresponds to the momentum threshold of the triggers. As

[1] Prescaling refers to the practice of scaling down the rate of accepted events by only recording every nth event, where n is the prescale factor.

encoded in the nomenclature of the HLT labels, both require a single muon with a transverse momentum larger than 50 GeV. Matching the full detector coverage of the inner tracker in combination with the muon system, the triggers accept muons with $|\eta| < 2.4$. Analyses focusing on intermediate muon momenta often favor lower transverse momentum thresholds over the high efficiency of single-muon triggers. Using the search for Higgs boson pair production [100] as an example, the utilized double-muon trigger requires $p_T(\mu_1) > 17$ GeV and $p_T(\mu_2) > 8$ GeV but only offers an efficiency of 90 to 95 % as a function of the respective muon momenta [101]. As the excess predicted by the signal models is most pronounced toward high invariant masses, lower transverse momentum thresholds are opted against in favor of the more efficient single-muon triggers.

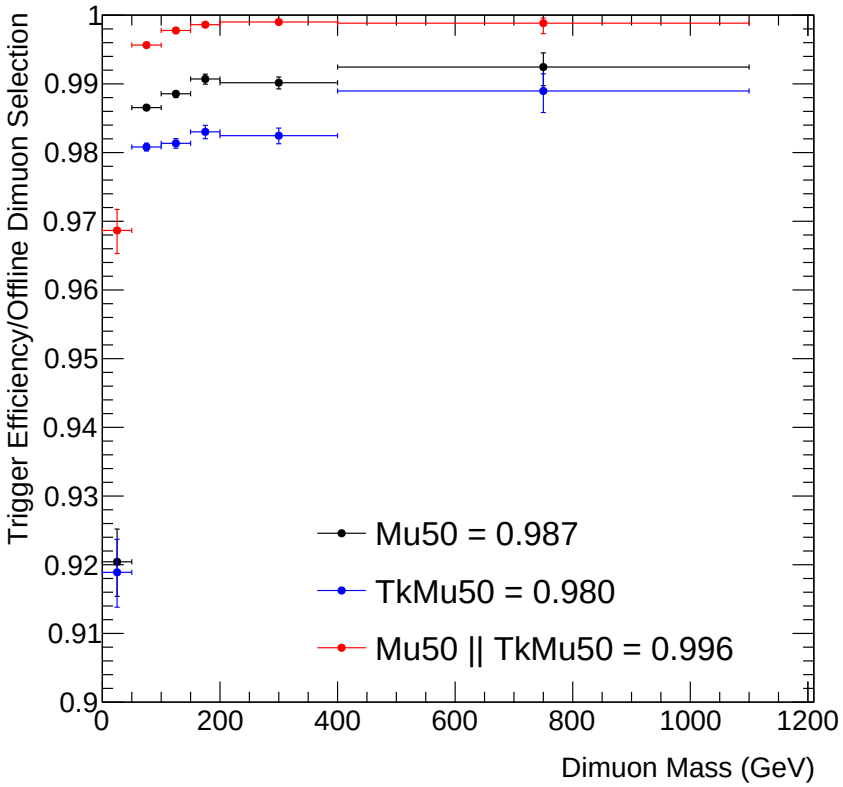

FIGURE 6.1: Individual and combined efficiencies of the single-muon triggers HLT_Mu50 and HLT_TkMu50 as a function of the dimuon invariant mass [102]. The efficiencies have been measured for individual muons and are then translated into a combinatorial efficiency for events with two muons by simulating the respective trigger performances.

The foundation both HLT_Mu50 and HLT_TkMu50 build upon is the L1 seed given by L1_SingleMu22 linked with L1_SingleMu25 by a logical "or". This configuration was chosen to ensure a stable yield, should the need arise to prescale the former to maintain a manageable rate of events. In this context, it should be noted that the commissioning of the new L1 muon trigger system (see Sec. 4.4) overlapped with the data-taking period, which caused temporary suboptimal conditions [102]. Neglecting minor issues, this overlap resulted in the late incorporation of RPC measurements into the L1 system and a misconfiguration of the endcap muon track finder (EMTF). As discussed in section 4.2.4, RPCs contribute primarily through their precise timing information. These were only

evaluated at the L1 stage for a small fraction[2] of the data-taking period of 2016. In the first half of this period, the misconfiguration of the EMTF lead to the trigger firing only once for two muons in the same section of the endcap. While this behavior only has a minor impact on the overall single-muon trigger efficiency for events with two muons, it has to be taken into consideration when calculating the efficiency using the "tag-and-probe" method with Lorentz-boosted Z bosons. On average, larger boosts imply a decreasing spatial separation of the Z boson decay products. The misconfiguration of the EMTF would therefore appear as an inefficiency if events where both muons are located in the endcaps and have a small angular distance ($\Delta\phi < 0.7$) were included in the aforementioned calculation.

The suboptimal conditions of the L1 trigger have prompted multiple studies of its performance when recording muon-centric events. One major concern is the contamination of the muon system measurement through additional hits due to showers induced by muons with large momenta (Sec. 5.1). This may hinder the reconstruction of an L1 candidate or lower its momentum estimate, resulting in the candidate not passing the required threshold. A comparison of measured and simulated muons which are both isolated and meet the high-p_T selection criteria (Sec. 7.3 & 7.4) has shown the respective amount of hits in the muon stations to be in agreement between momenta of 200 to 800 GeV [102]. In the first and last muon station, slight excesses have been observed. Given the possibility of hadronic remnants passing through the solenoid and contributions by neutrons, these observations are within expectations. The agreement of recorded and simulated data for the amount of muon system hits translates into a well-modeled decrease of the L1 efficiency with a rising number of showers. This efficiency has been measured using muon candidates which are matched to L1 tracks within a cone of radius $\Delta R < 0.2$. As a function of the transverse momentum, this efficiency is given in figure 6.2. One observes a decline in the measured and simulated distributions as the momentum increases, with the corresponding slopes being compatible within the expected statistical variation.

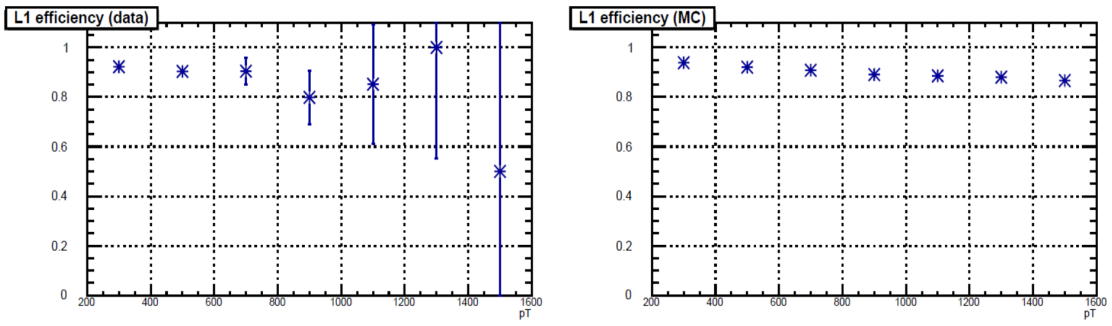

FIGURE 6.2: Efficiency of the L1 single-muon trigger as a function of the muon transverse momentum [102].

A second study has evaluated the L1 performance with respect to the assignment of measured segments to bunch crossings [102]. The design of the detector only allows for an efficient recording of events which are spaced at least 75 ns apart. This requirement is implemented as part of the L1 logic, suppressing triggers for two consecutive bunch crossings following the event candidate. To limit the occupancy of its silicon cells and strips, the operation of the inner tracking system dictates that it becomes inefficient for recording hits in the neighboring four events. In combination with a "prefiring" of the L1 trigger, originating from erroneous assignments of measured segments to

[2]Run 282917 to 282924 and 283820 to 284078; thus, only part of the 2016Hv3 era.

bunch crossings preceding their original one, this often results in the event failing subsequent trigger stages. Given the comparatively long drift times in the DTs, their measurements are most prone to result in a misidentification of events to which the segments belong. The fraction of muons with segments assigned to bunch crossings preceding the triggered event by 25 ns is shown in figure 6.3 for all four muon stations in the barrel region. Simulated muons with a flat transverse momentum distribution are used for the comparison to the measured data. A similar behavior with a slight increase of the fraction toward large momenta is observed in both distributions. The same qualitative behavior with an even lower fraction has also been observed for a 50 ns difference.

Given this compatibility, the simulated sample of muons is used to study the performance of the barrel muon track finder (BMTF) using muon tracks reconstructed in-time and out-of-time with respect to the correct bunch crossing. Two spatially compatible out-of-time segments in the muon system, generally a rare occurrence, are necessary for the BMTF to trigger an L1 prefiring. Only considering events where the L1 candidate has a transverse momentum larger than 22 GeV and is compatible with a fully reconstructed muon (Chap. 5) within a window of $|\Delta\phi| < 0.3$ and $|\Delta\eta| < 0.5$, the efficiency of the global muon trigger (and correspondingly the L1 trigger) is shown in figure 6.4 for different timing scenarios. The orange distributions represent the efficiency for out-of-time candidates and show the expected low probability of a successful reconstruction. On the other hand, the presence of these candidates has almost no impact on the reconstruction of in-time ones. This is illustrated by the near identical efficiencies for the total in-time distributions compared to the in-time distributions in the absence of any out-of-time candidates, respectively represented in blue and green.

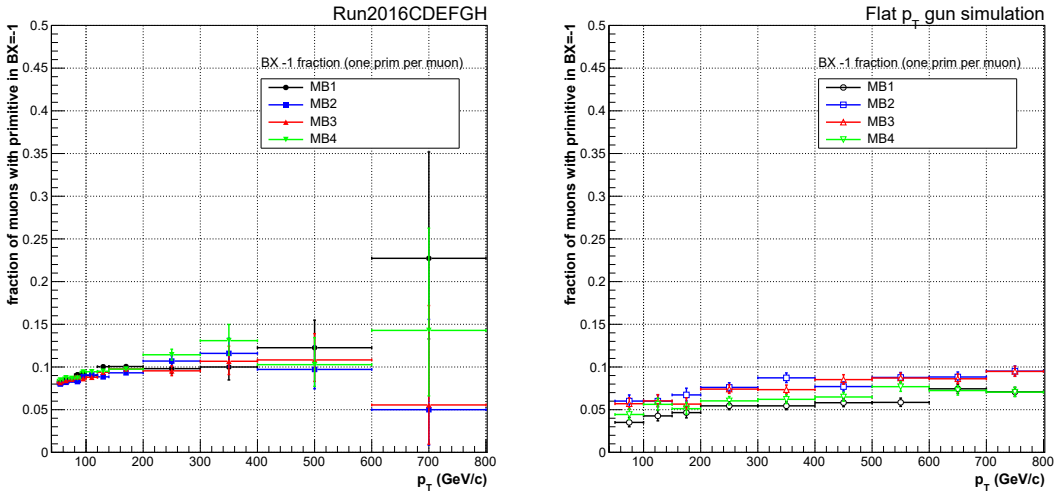

(a) (b)

FIGURE 6.3: Fraction of reconstructed muons with segments in the barrel muon stations assigned to bunch crossings (BXs) preceding the triggered one by 25 ns [Adapted from 102]. Measured and simulated data are shown in (a) and (b), respectively.

Both studies lend confidence to the performance of the underlying L1 seed. While building upon the same seed, the aforementioned two HLTs differ in their preliminary muon reconstruction strategy. The approach of HLT_Mu50 follows the sequential data processing of the trigger path from Level-1 to Level-2 and Level-3 (L3) to produce a muon track. Available from run 274954 onward, HLT_TkMu50 instead builds a track by

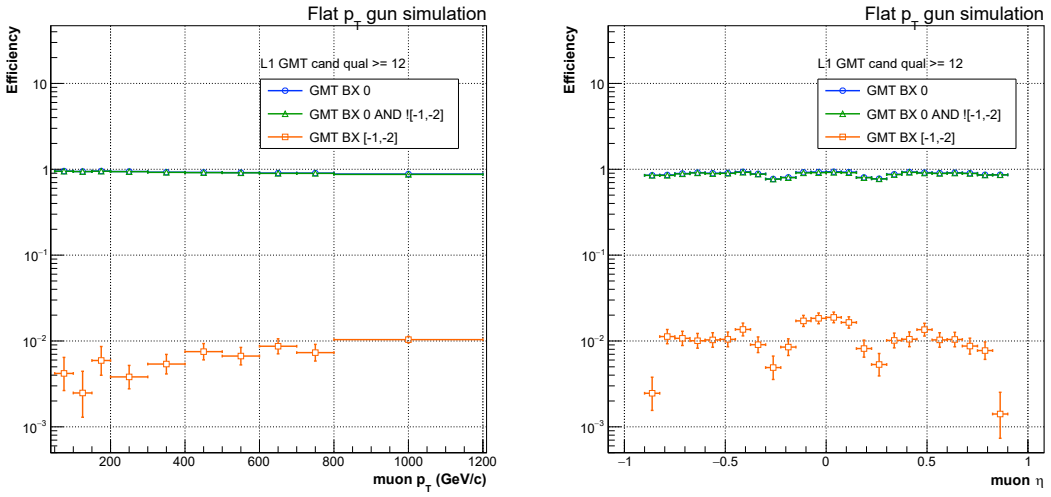

(a) (b)

FIGURE 6.4: Simulated efficiency of the global muon trigger for muons which are out-of-time (orange), in-time (blue) and for in-time scenarios where there are no out-of-time candidates (green) [Adapted from 102]. In (a) and (b) as a function of the transverse momentum and pseudorapidity, respectively.

iterative extrapolation around the L1 seed. Their combination yields an improvement of about 1 % with respect to the individual trigger efficiencies. Overall, the observed performance encourages using the datastream based on single-muon triggers.

6.2 Muon Datastream

Table 6.1 provides a summary of all "eras", denoted by capital letters B to H, into which the single-muon trigger datastream of the 2016 data-taking period has been divided. Each era is further subdivided into a threefold hierarchy of incrementing identification integers. This partitioning is generally driven by the detector conditions. While these conditions can change drastically between eras, they are stable for a single "run", which is the first subdivision. The subsequent ones are "lumisections", parts of a run where the instantaneous luminosity remains roughly constant, and the identification numbers of individual events. In the third column of the table, the integrated luminosity for the respective run range is given. These values correspond to events certified for utilization in analyses exclusively concerned with muon final states. As the reconstruction of muons only depends on the performance of the inner tracker and muon system, assuming a stable magnetic field, events where other subsystems may have performed poorly can therefore pass this certification and be included in the analysis. A dictionary in the JSON data format [103] detailing the included runs and lumisections is centrally provided and bears the following name:

`Cert_271036-284044_13TeV_23Sep2016ReReco_Collisions16_JSON_MuonPhys.txt`

The luminosities have been determined via pixel cluster counting (PCC) [104], which has proven to be the most accurate method as it benefits from the high granularity of the silicon pixel tracker. Given the mean number of pixel clusters per event $\langle N_{\text{Cluster}} \rangle$

and bunch orbit frequency f, the luminosity is given by

$$\dot{\mathcal{L}} = \frac{\langle N_{\text{Cluster}} \rangle \, f}{\sigma_{\text{vis}}^{\text{PCC}}}. \tag{6.1}$$

For PCC, the visible cross section $\sigma_{\text{vis}}^{\text{PCC}}$ is determined by the mean number of interactions per cluster multiplied by the minimum-bias cross section[3] of proton-proton collisions.

Data Set	Run range	$\mathcal{L}$ / fb^{-1}
/SingleMuon/Run2016**B**-23Sep2016-v3/MINIAOD	273150–275376	5.8
/SingleMuon/Run2016**C**-23Sep2016-v1/MINIAOD	275656–276283	2.6
/SingleMuon/Run2016**D**-23Sep2016-v1/MINIAOD	276315–276811	4.3
/SingleMuon/Run2016**E**-23Sep2016-v1/MINIAOD	276831–277420	4.0
/SingleMuon/Run2016**F**-23Sep2016-v1/MINIAOD	277932–278808	3.1
/SingleMuon/Run2016**G**-23Sep2016-v1/MINIAOD	278820–280385	7.7
/SingleMuon/Run2016**H**-PromptReco-v2/MINIAOD	281613–284035	8.6
/SingleMuon/Run2016**H**-PromptReco-v3/MINIAOD	284036–284044	0.2
Total	273150–284044	36.3

TABLE 6.1: Eras of the single-muon datastream recorded by the CMS detector during 2016. The integrated luminosities $\mathcal{L}$ correspond to the events certified for muon physics.

As implied by the "ReReco" tag in contrast to the "Prompt" one of the last two eras, a secondary reconstruction of the events recorded in eras B to G has been performed. Its primary purpose is to address the degradation of the inner track quality present in most of these subdivisions of the datastream, which has become known as the analog pipeline voltage (APV) issue. Optimizing the reconstruction algorithms for eras B to F has facilitated a partial recovery of this degradation while the APV settings have been adjusted from era G onward. The efficacy of the latter measure can be seen in figure 6.5, where the L3 over L1 efficiency is shown as a function of the instantaneous luminosity. While this ratio shows a clear dependence on the luminosity before the settings have been adjusted, it becomes effectively flat afterwards.

All used data sets are reconstructed based on the asymptotic alignment (see Sec. 4.3). For the first time in the CMS Collaboration, the corresponding alignment position errors (APEs) of the muon chambers are taken into account when reconstructing muons [102]. Weighting the individual inner tracker and muon system hits according to their positional uncertainties allows for the best possible momentum estimate when applying the Kalman filter. Figure 6.6 showcases the muon momentum resolution for varying alignment scenarios with and without the inclusion of APEs. The displayed resolutions correspond to the tracks reconstructed by the picky algorithm; pink markers show the performance of the tracker-only reconstruction. One can see that the best (realistic) scenario over the entire spectrum is given by the asymptotic alignment, while accounting for APEs becomes increasingly important for high momenta.

[3]Whereas a zero-bias trigger records events at random, a minimum-bias trigger requires a minimal amount of detector activity to record events while still attempting to remain unbiased toward any particular final state. The corresponding cross section is then referred to as the minimum-bias cross section.

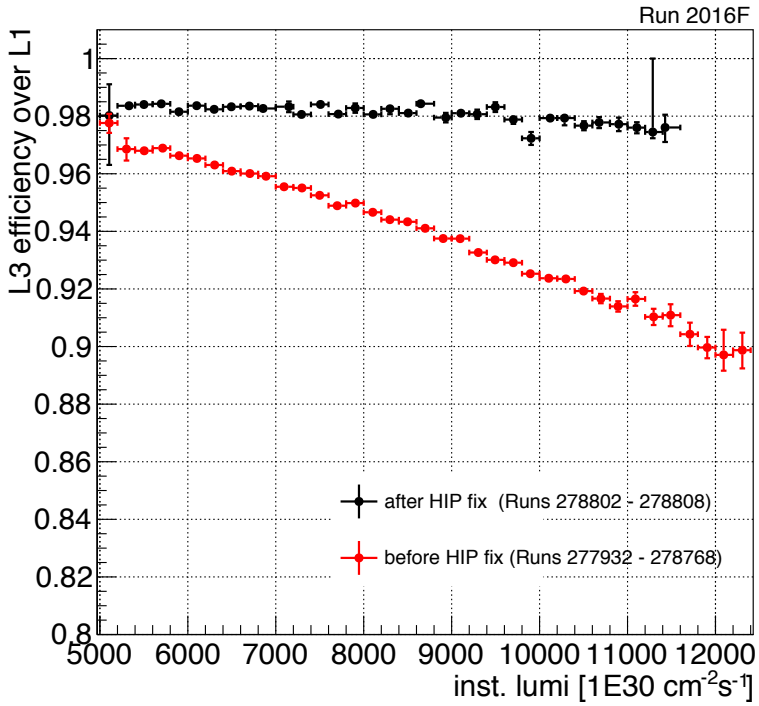

FIGURE 6.5: Efficacy of the APV adjustment to address the degrading L3 over L1 efficiency [102]. Red data points correspond to the 2016F era, which ends with the adjustment of the APV settings, while black data points illustrate the difference using six subsequent runs. The legend refers to "high-ionizing particles" (HIPs) which were initially believed to be the sole cause of the degradation.

6.3 Standard Model Background Simulation

For an eventual statistical analysis of the measured data, a null hypothesis describing the standard model expectation needs to be formulated. This is primarily done via simulation of SM processes, however, a certain subset of interactions does not adequately lend itself to such a description. Backgrounds where at least one of the muons originates from a jet are simulated but an accurate modeling of these contributions is expected to be difficult.

For the simulation of particle interactions, the Monte Carlo (MC) method is applied. Its overarching goal is to provide a probabilistic description of the underlying processes. Given the multitude of degrees of freedom in such interactions, MC methods often constitute the only practical approach to obtain this description. The progress from two colliding protons to a detector response mirroring the measured data is structured into a multi-step process. While there are various approaches to many of the individual steps, a general overview can be given with respect to the issues they aim to address. The starting point are descriptions of the parton distribution functions (see Sec. 2.3). Multiple competing sets of PDFs are available, which can be accessed and interpolated via the LHAPDF 6 [106] software. According to their models, based on experimental input, partons with varying fractions of the proton momenta enter the respective interaction. The theory-driven description of these interactions is given by perturbatively calculated matrix elements, whose accuracy depends on the loop and radiative corrections that are taken into account. Particle cascades produced by the emission of quarks and gluons are modeled via parton showering [107]. Further subsummation of these shower constituents to physical particles is described by hadronization [107]. At this stage,

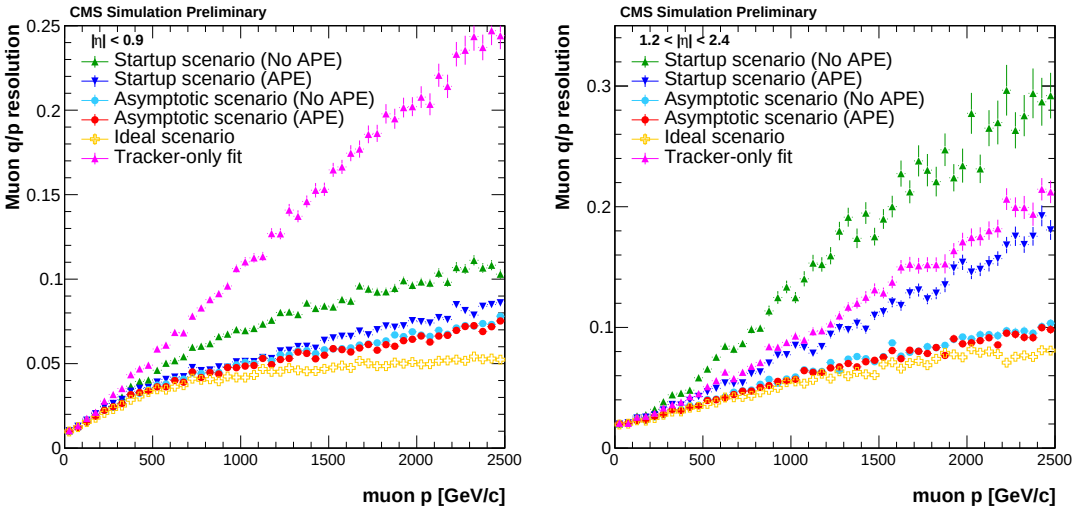

FIGURE 6.6: Muon momentum resolution of the picky algorithm in two $|\eta|$ regions for various alignment scenarios [105]. The resolution corresponding to the tracker muon algorithm is shown for comparison. For reconstruction of muons recorded in 2016, the alignment position errors (APE) of the asymptotic scenario are taken into account.

particles and their properties are described by what is referred to as generator-level quantities. It is also the stage where one transitions from event generation to detector simulation. Simulating the propagation of particles through the detector material is performed using the GEANT 4 [108–110] toolkit. In the subsequent step, known as "digitization", the response of the detector readout electronics is modeled using dedicated libraries of CMSSW [96]. By retracing the steps of the particle reconstruction discussed in the preceding chapter, one receives the reconstruction-level quantities which can be compared against the measurement.

Having outlined the general method for simulating events to approximate parity with the measurement, the process-specific settings for the respective data sets can be discussed. All considered simulated background data sets have been centrally produced by the CMS Collaboration during the `RunIISummer16MiniAODv2` campaign. The corresponding alignment scenario for the reconstruction matches the asymptotic one of the measured data. An overview of all considered processes is given in table 6.2.

Drell–Yan

The most important SM background to simulate, as mentioned in section 2.4, is the Drell–Yan $q\bar{q} \to Z/\gamma^* \to \mu\mu$ process. It contributes roughly 80 % of the total background event yield at high invariant masses at the final stage of this analysis (see Tab. 10.2). Given the similarity of DY and virtual graviton exchange processes, the contribution of the former is difficult to reduce without simultaneously affecting the signal yields. As a direct consequence, a reliable prediction by the simulation becomes all the more important. For the production of the baseline DY data set POWHEG BOX V2 [111–114] has been used. This particular event generator provides a common framework for process specific implementations following the eponymous POWHEG method. Its major advantage is the complete separation of generating hard radiation and subsequent application of parton shower models. The former allows for an accurate prediction of the DY process up to NLO in perturbative QCD (pQCD) by POWHEG BOX V2, while parton showering and hadronization is handled by PYTHIA 8.2 [115]. For the description of the PDFs,

Sample	σ / pb	Precision
ZToMuMu_NNPDF30_13TeV-powheg_M_50_120	1.98×10^{3}	NLO
ZToMuMu_NNPDF30_13TeV-powheg_M_120_200	1.93×10^{1}	NLO
ZToMuMu_NNPDF30_13TeV-powheg_M_200_400	2.73	NLO
ZToMuMu_NNPDF30_13TeV-powheg_M_400_800	2.41×10^{-1}	NLO
ZToMuMu_NNPDF30_13TeV-powheg_M_800_1400	1.68×10^{-2}	NLO
ZToMuMu_NNPDF30_13TeV-powheg_M_1400_2300	1.39×10^{-3}	NLO
ZToMuMu_NNPDF30_13TeV-powheg_M_2300_3500	8.95×10^{-5}	NLO
ZToMuMu_NNPDF30_13TeV-powheg_M_3500_4500	4.14×10^{-6}	NLO
ZToMuMu_NNPDF30_13TeV-powheg_M_4500_6000	4.56×10^{-7}	NLO
ZToMuMu_NNPDF30_13TeV-powheg_M_6000_Inf	2.06×10^{-8}	NLO
DYJetsToLL_M-50_TuneCUETP8M1_13TeV-madgraphMLM-pythia8	5.77×10^{3}	NNLO
TTTo2L2Nu_TuneCUETP8M2T4_13TeV-powheg	8.73×10^{1}	NNLO
TTTo2L2Nu_MLL_500To800_TuneCUETP8M2T4_13TeV-powheg	3.26×10^{-1}	NNLO
TTTo2L2Nu_MLL_800To1200_TuneCUETP8M2T4_13TeV-powheg	3.26×10^{-2}	NNLO
TTTo2L2Nu_MLL_1200To1800_TuneCUETP8M2T4_13TeV-powheg	3.05×10^{-3}	NNLO
TTTo2L2Nu_MLL_1800ToInf_TuneCUETP8M2T4_13TeV-powheg	1.74×10^{-4}	NNLO
ST_tW_top_5f_inclusiveDecays_13TeV-powheg-pythia8	3.56×10^{1}	app NNLO
ST_tW_antitop_5f_inclusiveDecays_13TeV-powheg-pythia8	3.56×10^{1}	app NNLO
ZZ_TuneCUETP8M1_13TeV-pythia8	1.65×10^{1}	NLO
WZ_TuneCUETP8M1_13TeV-pythia8	4.71×10^{1}	NLO
WWTo2L2Nu_TuneCUETP8M1_13TeV-powheg	1.22×10^{1}	NNLO
WWTo2L2Nu_Mll_200To600_TuneCUETP8M1_13TeV-powheg	1.39	NNLO
WWTo2L2Nu_Mll_600To1200_TuneCUETP8M1_13TeV-powheg	5.67×10^{-2}	NNLO
WWTo2L2Nu_Mll_1200To2500_TuneCUETP8M1_13TeV-powheg	3.56×10^{-3}	NNLO
WWTo2L2Nu_Mll_2500ToInf_TuneCUETP8M1_13TeV-powheg	5.40×10^{-5}	NNLO
WJetsToLNu_TuneCUETP8M1_13TeV_madgraphMLM-pythia8	6.15×10^{4}	NNLO
QCD_Pt-15to20_MuEnrichedPt5_TuneCUETP8M1_13TeV_pythia8	3.82×10^{6}	LO
QCD_Pt-20to30_MuEnrichedPt5_TuneCUETP8M1_13TeV_pythia8	2.96×10^{6}	LO
QCD_Pt-30to50_MuEnrichedPt5_TuneCUETP8M1_13TeV_pythia8	1.65×10^{6}	LO
QCD_Pt-50to80_MuEnrichedPt5_TuneCUETP8M1_13TeV_pythia8	4.38×10^{5}	LO
QCD_Pt-80to120_MuEnrichedPt5_TuneCUETP8M1_13TeV_pythia8	1.06×10^{5}	LO
QCD_Pt-120to170_MuEnrichedPt5_TuneCUETP8M1_13TeV_pythia8	2.52×10^{4}	LO
QCD_Pt-170to300_MuEnrichedPt5_TuneCUETP8M1_13TeV_pythia8	8.65×10^{3}	LO
QCD_Pt-300to470_MuEnrichedPt5_TuneCUETP8M1_13TeV_pythia8	7.97×10^{2}	LO
QCD_Pt-470to600_MuEnrichedPt5_TuneCUETP8M1_13TeV_pythia8	7.90×10^{1}	LO
QCD_Pt-600to800_MuEnrichedPt5_TuneCUETP8M1_13TeV_pythia8	2.51×10^{1}	LO
QCD_Pt-800to1000_MuEnrichedPt5_TuneCUETP8M1_13TeV_pythia8	3.65	LO
QCD_Pt-1000toInf_MuEnrichedPt5_TuneCUETP8M1_13TeV_pythia8	1.62	LO

TABLE 6.2: Overview of the simulated SM background data sets. Refer to the text for more information on the individual processes.

the set provided under the label NNPDF 3.0 [19] has been used. Its parameters are trained via neutral networks to minimize the global χ^2 test statistic using theory input up to NNLO in QCD as well as electroweak corrections. With the probability density to generate an event decreasing exponentially with rising interaction scales, an accurate probabilistic description up to high invariant masses can be obtained by restricting the phase space during event generation. This restriction is achieved by dividing the data set into 10 individual regions with respect to the invariant mass itself. The production then starts from $m_{\mu\mu} > 50\,\text{GeV}$ and closes with a final, unrestricted bin from 6 TeV onward. Corrections to the differential cross section will be discussed in section 8.3.

Contributions by the production of τ leptons via the complementary $q\bar{q} \to Z/\gamma^* \to \tau\tau$ process and the subsequent decay into muons are expected to be small. Assuming two three-body decays, corresponding to branching fractions of $\Gamma(\tau \to \nu_\tau \mu \nu_\mu) = (17.39 \pm 0.04)\,\%$ [64], they amount to less than 3 % of the total event yield. These contributions are accounted for by filtering a lepton-inclusive DY data set for the desired tau pairs[4] on generator-level. Also employing the NNPDF 3.0 PDF set, this data set is produced via MadGraph5 aMC@NLO [116, 117]. The main feature of this generator is its capability to dynamically generate any SM process, requiring no specialized code. While this is possible up to NLO in pQCD, this DY data set is generated at LO to take advantage of higher jet multiplicities and larger amount of produced events. The corresponding cross section is calculated using Fewz 3.1b2 [118] under consideration of perturbative NNLO QCD and NLO EW corrections. As the name "Fully Exclusive W, Z production" (FEWZ) implies, high-precision calculations of W and Z boson production cross sections are its sole purpose.

Top Quarks

Using the same combination of Powheg Box V2, NNPDF 3.0 and Pythia 8.2, both the production of top-antitop pairs and single top quarks with an associated W boson are simulated. With top quark almost exclusively decaying via $t \to bW$, the pair production process has a branching fraction to a dimuon final state of about 1.6 % [64]. Given its comparatively large cross section, it is expected to provide the second largest contribution to the background. Applying a filter to select the leptonic decay channel of the associated W boson allows for maintaining a statistically precise description with a reasonable number of generated events. Furthermore, following the example of the $Z/\gamma^* \to \mu\mu$ simulation, multiple regions with respect to the invariant dilepton mass are produced separately. The description for masses below 500 GeV is obtained by truncating the corresponding inclusive data set accordingly. Using Top++ [119], the cross sections for the production of top pairs and single top quarks with an associated W boson are calculated up to NNLO and approximate NNLO in pQCD, respectively.

Potential contamination by the semileptonic decay channel of the $t\bar{t}$ process, either via particle misreconstruction or the production of real muons, have been shown to be smaller than 1 % [102]. This has been tested with both a filtered inclusive and a dedicated semileptonically decaying $t\bar{t}$ data set. An evaluation of the dimuon invariant mass spectrum under the requirement of two b quark jets, see table 6.3, confirms that the fully leptonic decay channel provides an adequate description.

Vector Boson Pairs

The second considered group of prompt SM backgrounds are vector boson pair production processes. Here, the WW process is again generated using Powheg Box V2

[4] This filtering ensures that the muon channel contribution is only taken into account once.

Mass range / GeV	Observed	Total Bkg.	Ratio
120–200	7126	7069 ± 84	1.008 ± 0.012
200–400	5270	5448 ± 74	0.970 ± 0.012
400–800	602	611 ± 25	0.990 ± 0.044
800–2000	20	22 ± 5	0.910 ± 0.173

TABLE 6.3: Event yields for different regions of the dimuon invariant mass spectrum under the requirement of two opposite sign muons satisfying the high-p_T selection criteria (Sec. 7.2–7.4) and two b quark jets with $p_T > 35\,\text{GeV}$ [102]. Background contributions are given by $t\bar{t}$, tW and vector boson pair production processes; those of the Z + jets process have been subtracted. The quoted uncertainty represents the expected statistical variation.

under utilization of NNPDF 3.0, with PYTHIA 8.2 being responsible for parton showering and hadronization. Both WZ and ZZ processes have been simulated with the general purpose LO event generator PYTHIA 8.2 using the LO PDF set NNPDF 2.3 [120]. All corresponding cross sections have been determined up to NLO in QCD via MCFM [121].

Jet Backgrounds

Backgrounds where at least one of the two muons originates from a jet, therefore is not produced promptly, are mostly given by two processes. In the production of W bosons with associated jets, one muon can be provided by the decay of the boson while the other one must be sourced from one of the jets. The corresponding data set has been generated with MADGRAPH5 aMC@NLO at LO using NNPDF 3.0. It is scaled to a NNLO QCD, NLO EW cross section calculated with FEWZ 3.1b2 under utilization of the NNPDF 3.0 PDF set. Primarily hadronic interactions of quarks are subsumed under the label "QCD" and are accounted for by a set of 13 LO samples which have been produced using PYTHIA 8.2 with NNPDF 2.3. The high total cross section of these processes necessitates a division into $\hat{p}_T$-ranges alongside a filtering for events containing muons with a transverse momentum larger than 5 GeV to obtain a suitable description over a wide range of interaction scales. While these two background data sets are used to illustrate the performance of the event selection, their modeling of nonprompt muons requires further evaluation; this is discussed in section 8.1.

6.4 Coinciding Proton-Proton Interactions

A corollary to the tightly focused beams and high instantaneous luminosities of the LHC are multiple proton-proton interactions per bunch crossing. A mean number of 27 interactions per bunch crossing [78] poses a considerable experimental challenge, which the CMS detector meets with its granular segmentation. At the same time, this so-called "pileup" of interactions also has to be accounted for in the simulation. Since the actual conditions during data taking are not known ahead of time, the introduction of minimum-bias events into the simulation has to follow an estimated distribution. All used data sets have been produced using the same assumed conditions carrying the tag `PUMoriond17`. Both the estimated distribution and the corresponding measurement for the 2016 data-taking period are shown in figure 6.7.

The normalized data distribution for events certified for muon-based analyses has been created using the measured minimum-bias cross section of 69.2 mb [122]. While one observes a reasonable agreement of measurement and simulation up to about 35

interactions, the distributions diverge beyond that point. Using the ratio of the two to weight the generated events according to their simulated pileup allows for a more accurate description. The corresponding improvement can be seen by comparing the distributions of the number of vertices per event given in figure 6.8. It should be noted that one would not expect the reconstruction of high-energy muon tracks to have a strong dependence on the mean number of interactions. This expectation will be quantified by estimating the impact of the uncertainty in the minimum-bias cross section measurement (Sec. 9.3).

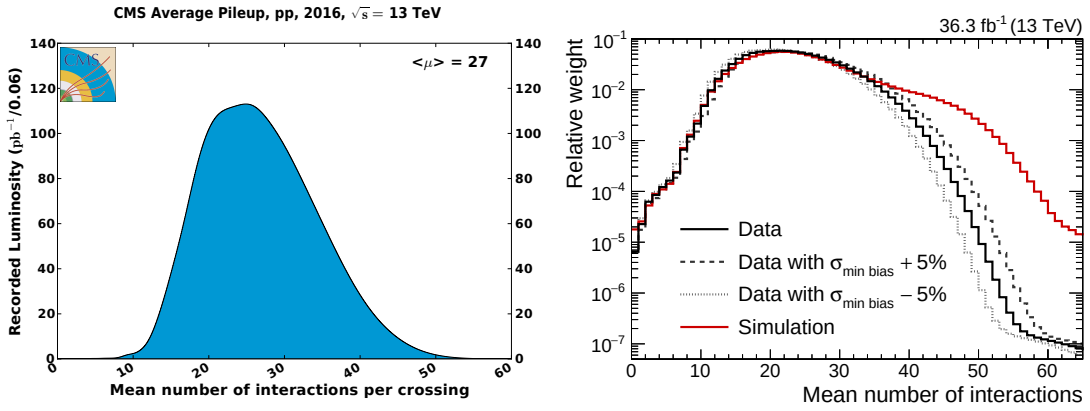

(a) (b)

FIGURE 6.7: Mean number of interactions per bunch crossing, also referred to as the pileup distribution, measured during the 2016 data-taking period. In (a) for all proton-proton collisions [78] and in (b) for all events certified for muon-based analyses. The latter figure also contains variations of the measured distribution with respect to the uncertainty in the minimum-bias cross section value. Distributions in (b) are normalized to unity.

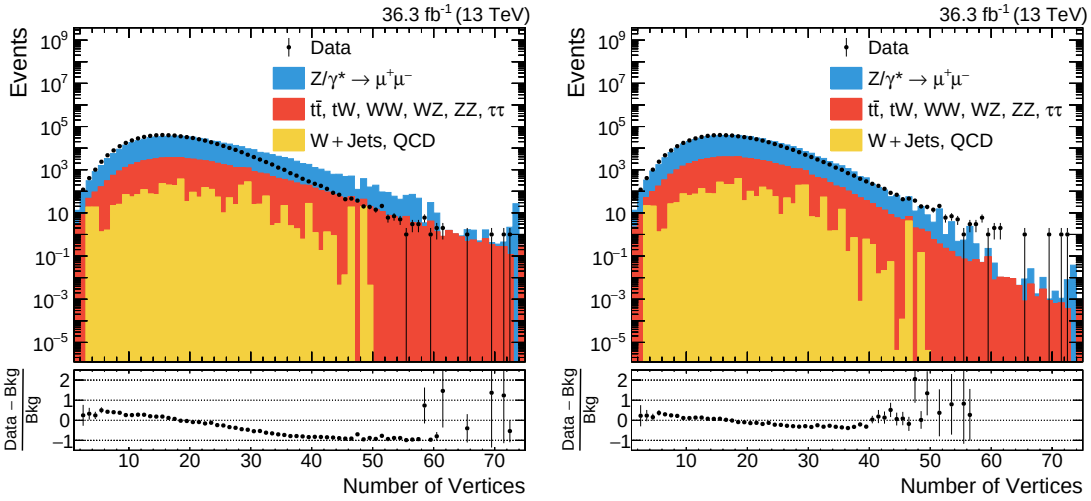

(a) (b)

FIGURE 6.8: Number of reconstructed vertices per event at an advanced stage of the analysis. In (a) without correcting for the measured pileup distribution and in (b) with the correction applied.

6.5 Graviton Signal Simulation

Both MadGraph5 aMC@NLO [123] and Sherpa 2 [124, 125] have have been considered as event generators for the simulation of the signal process in order to obtain NLO predictions in pQCD. Ultimately, the most robust results with a consistent behavior at $\hat{s} \simeq M_D$ and beyond, allowing for a dynamic truncation of contributions, are provided by Pythia 8.2. Offering a LO description of the virtual exchange of gravitons in interference with the DY process, it also accounts for differences in the angular dependencies (e.g., Tab. 3.2). As the production of samples is based on the settings of the `RunIISummer16MiniAODv2` campaign, they are also generated with the "Monash" tune. Formally labeled `CUETP8M1-NNPDF2.3LO` [126], this tune implies the usage of NNPDF 2.3 as the PDF set. While the ADD scenario for the model of LED has a dedicated implementation in Pythia 8.2 [127], one for LED in the AS scenario for quantum gravity is not included by default. The utilized extension which enables Pythia 8.2 to generate events for this combination has been developed and kindly provided by the colleagues of the High Energy & Particle Theory Group of the Technical University Dortmund [63].

Large Extra Dimensions

Using the described setup, a set of 13 samples with increasing values of the GRW convention parameter Λ_T has been generated including the full detector simulation. Starting from an initial value below the lower bound on the UV cutoff for the dilepton channel of $\Lambda_T > 4\,\text{TeV}$ (see Sec. 3.5), the goal is to cover values of Λ_T well above what the presented analysis would be able to distinguish. By squaring equation (3.16) to derive $\sigma \sim 1/\Lambda_T^8$ and assuming this cross section to scale linearly with the parton luminosity[5] (Fig. 6.9), the limit on Λ_T can be extrapolated to $\sqrt{s} = 13\,\text{TeV}$ yielding values between 6–7 TeV. Based on these thresholds, a range of 3.5 to 10 TeV has been chosen. An accompanying granularity of 500 GeV (1 TeV between the last two points) ensures that any differences in terms of kinematics or efficiencies can be taken into account.

Table 6.4 summarizes all centrally produced signal data sets. For the identification and subtraction of DY process contributions, a corresponding data set has been generated locally using Pythia 8.2 under identical conditions. The resulting DY cross section of $(1.171 \pm 0.001)\,\text{fb}$ has been subtracted from all signal cross sections listed in the third column. For a more granular interpolation of the cross section with respect to Λ_T, additional generator-level data sets are produced. Using the same parameters as in the central production campaign, 300 000 events for every 100 GeV in Λ_T have been generated using the computing resources available in Aachen. The resulting cross section curve is used and shown in later chapters (Chap. 11 & 12).

As the signal samples are generated in interference with the DY process, an inclusive production would lead to a predominant simulation of DY interactions at energy scales far below the region of interest. This is circumvented by introducing a generator-level invariant mass threshold of $m_{\ell\ell} > 1.7\,\text{TeV}$. The difference between signal and background in this restricted phase space is shown in figure 6.10 alongside a sketch of

[5] The cross section for a given process initiated by two partons a, b can often be expressed in relation to $1/s \times \mathrm{d}L_{ab}/\mathrm{d}\tau$ [128] where s denotes the center-of-mass energy, L_{ab} the parton luminosity and $\tau \equiv x_1 x_2$ the product of the parton momentum fractions. This term characterizes the dependence on the parameters of the collider experiment. The parton luminosity is defined with respect to the parton distribution functions $f_{x/X}$ by [128]

$$\tau \frac{\mathrm{d}L_{ab}}{\mathrm{d}\tau} = \frac{1}{1+\delta_{ab}} \int \mathrm{d}x_1\, \mathrm{d}x_2 \left(f_{a/A}(x_1, \mu_F^2) f_{b/B}(x_2, \mu_F^2) + [1 \leftrightarrow 2] \right) \delta(\tau - x_1 x_2).$$

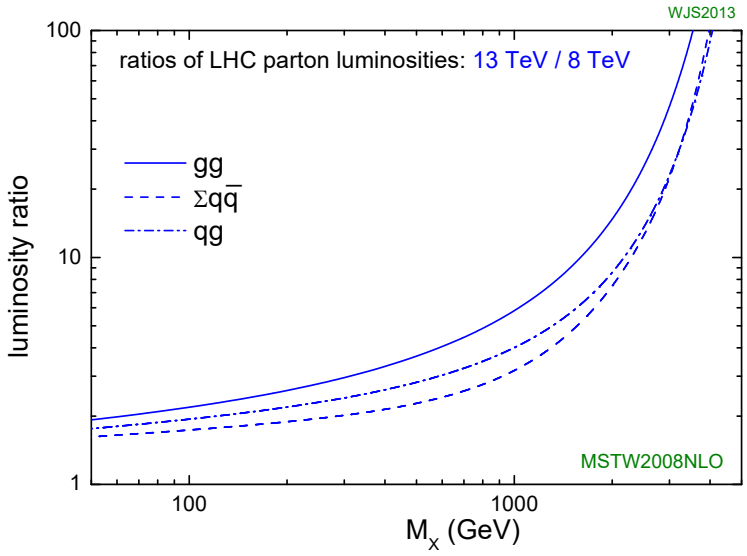

FIGURE 6.9: Ratio of parton luminosities corresponding to two center-of-mass energies of the LHC [129]. The predicted luminosities are based on the MSTW2008NLO PDF set.

Signal Data Set	Λ_T / TeV	σ / fb
ADDGravToLL_LambdaT-3500_M-1700_13TeV-pythia8	3.5	51.2
ADDGravToLL_LambdaT-4000_M-1700_13TeV-pythia8	4.0	17.6
ADDGravToLL_LambdaT-4500_M-1700_13TeV-pythia8	4.5	6.87
ADDGravToLL_LambdaT-5000_M-1700_13TeV-pythia8	5.0	2.95
ADDGravToLL_LambdaT-5500_M-1700_13TeV-pythia8	5.5	1.38
ADDGravToLL_LambdaT-6000_M-1700_13TeV-pythia8	6.0	0.691
ADDGravToLL_LambdaT-6500_M-1700_13TeV-pythia8	6.5	0.365
ADDGravToLL_LambdaT-7000_M-1700_13TeV-pythia8	7.0	0.203
ADDGravToLL_LambdaT-7500_M-1700_13TeV-pythia8	7.5	0.118
ADDGravToLL_LambdaT-8000_M-1700_13TeV-pythia8	8.0	0.072
ADDGravToLL_LambdaT-8500_M-1700_13TeV-pythia8	8.5	0.045
ADDGravToLL_LambdaT-9000_M-1700_13TeV-pythia8	9.0	0.031
ADDGravToLL_LambdaT-10000_M-1700_13TeV-pythia8	10.0	0.013

TABLE 6.4: Summary of all ADD signal data sets for which a detector simulation has been performed. Cross sections are inversely proportional to Λ_T^8. The listed values correspond to the cross sections calculated by the generator with the Drell–Yan contribution subtracted.

the expected impact by the virtual graviton exchange process. One observes a more pronounced differentiation between the two processes toward high invariant masses of muon pairs, which translates to a larger fraction of SM DY events produced at low masses. This observation holds true for increasing values of Λ_T, but the point at which the graviton signal contribution becomes significant shifts toward larger masses. The sketch acts as a visual summary of the signal shape discussion given in section 3.2. It shows the diverging signal as a series of individual graviton KK modes, which are exaggerated both in peak height and distance. Given the high density of graviton modes, expressed in equation (3.12) as the difference in mass between adjacent modes, measurements with current detector technologies would result in nonresonant excesses.

This expected behavior is replicated in the simulated distribution.

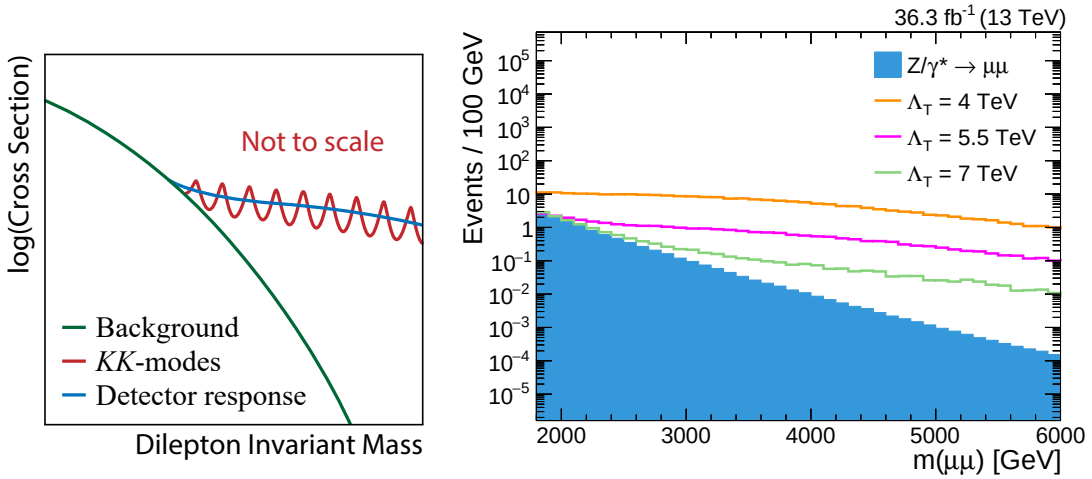

FIGURE 6.10: Sketch and simulation of the Drell–Yan background and graviton signal in the dimuon invariant mass spectrum. The former aims to summarize the discussion in section 3.2. Distance and height of the individual mass peaks of the graviton KK modes are exaggerated to illustrate the difference between underlying structure and measurement.

As the graviton directly transfers its momentum to the daughter particles, one expects to observe a similar difference between the signal and SM processes in the corresponding distributions. This can be seen in the simulations shown in figures 6.11a and 6.11b for the leading and subleading muon in terms of the transverse momentum, respectively. Both distributions show the same qualitative scaling with respect to the inverse of Λ_T. As the mass threshold for the generation of events has been set to $m_{\mu\mu} > 1700\,\text{GeV}$, only transverse momenta above 900 GeV are shown in order to avoid both the regimes of boosted muons and "turn-on" effects. The associated pseudorapidity distributions can be seen in figure 6.11c and 6.11d. In addition to differences in the mediator spin quantum number and the introduction of the gluon fusion production channel (Sec. 3.2), a larger fraction of muons with high transverse momenta is present in the graviton signals compared to the DY background. As a consequence, the distributions corresponding to the former process are expected to be more central with respect to the detector geometry than those of the background. The simulation matches this expectation and also exhibits the decreasing pronunciation of that difference toward larger values of Λ_T, which corresponds to larger fractions of DY events.

Given the distinct dependencies of the process cross sections on the CS angle, compared in table 3.2, one also expects to observe a difference in the corresponding angular distribution. The equations dictate that the opening angle between the negatively charged muon and the axis given by the incoming parton momenta is more perpendicular for the decay products of the graviton than the ones of the DY process. Figure 6.12 shows the cosine of the CS angle for both processes, confirming that the simulation takes into account the different spins of the mediator particles. In addition to the clear distinction between signal and background, the well-known asymmetry inherent to the DY process can also be seen. Toward larger values of Λ_T, implying a smaller fraction of graviton contributions to the overall spectrum, the signal distribution approaches the asymmetric one of the DY background. To conclude, one can summarize that all expected features of the signals have been observed and are modeled by the simulation.

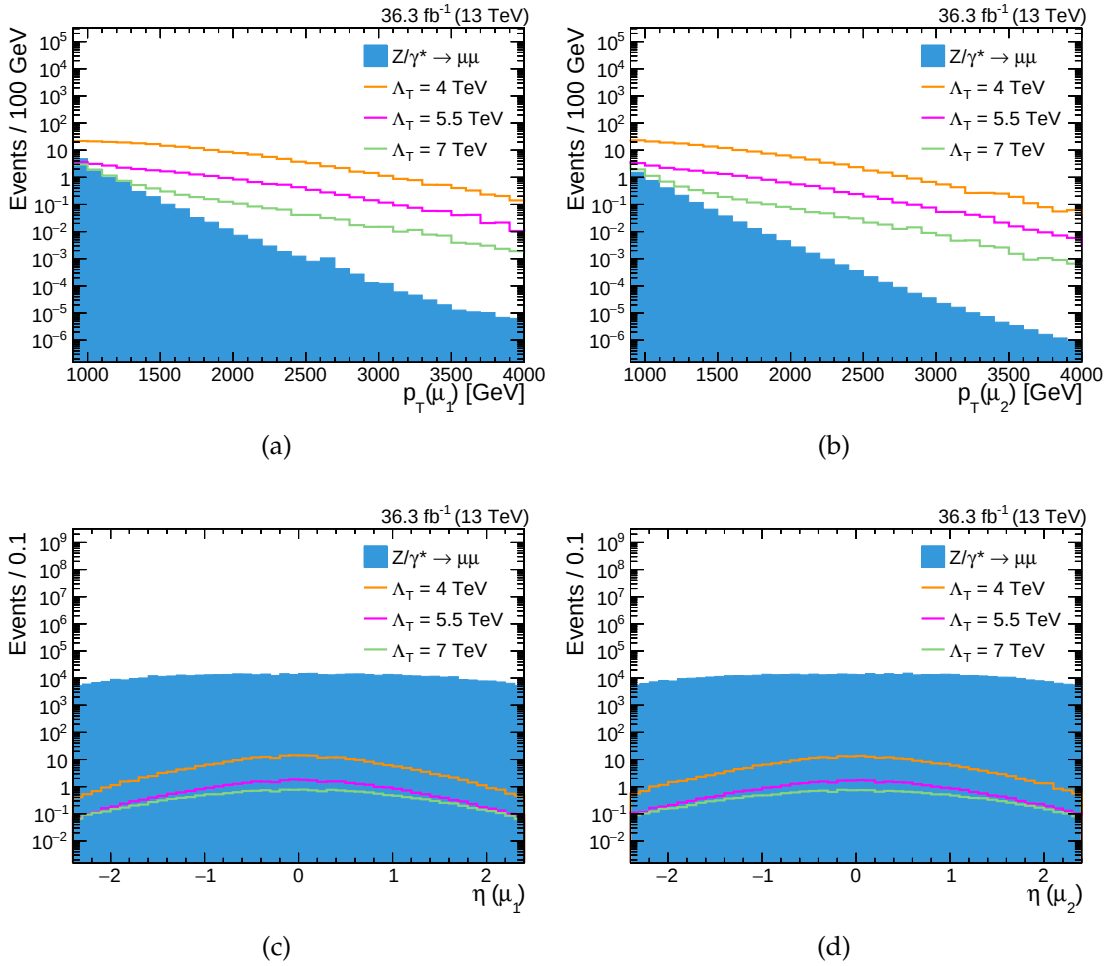

FIGURE 6.11: Transverse momentum and pseudorapidity of the leading (left) and subleading muon (right) with respect to transverse momentum. Given the production threshold of $m_{\mu\mu} > 1700\,\text{GeV}$ with which the data sets have been generated, the transverse momenta distributions only show $p_\text{T} > 900\,\text{GeV}$. Muons of all available momenta are included in the pseudorapidity distributions. Background fluctuations toward higher values in the momentum spectrum of the leading muon are due to individual events with large associated weights. They have been produced in boosted topologies as part of simulated Drell–Yan samples covering lower dimuon invariant mass ranges.

Large Extra Dimensions in the Asymptotically Safe Scenario

While the signals for the ADD model have been produced as part of the central CMS simulation campaign, the ones for LED in the AS scenario are generated using the available computing resources in Aachen. To evaluate potential deviations of the reconstruction and selection with respect to the AS signal samples, a full simulation of the detector has been performed for three of them. They are chosen as representative parameter points for the considered phase space and are generated under the same conditions as the ADD model signals. Since the three approximations for the transition between the IR and UV regime have the most drastic impact on the shape of the spectra, they are varied while the other parameters are kept constant. Between the three data sets, summarized in table 6.5, all approximations are covered.

The corresponding dimuon invariant mass spectra are shown in figure 6.13a. Each distribution shows a clear relation to the approximated evolutions of the anomalous

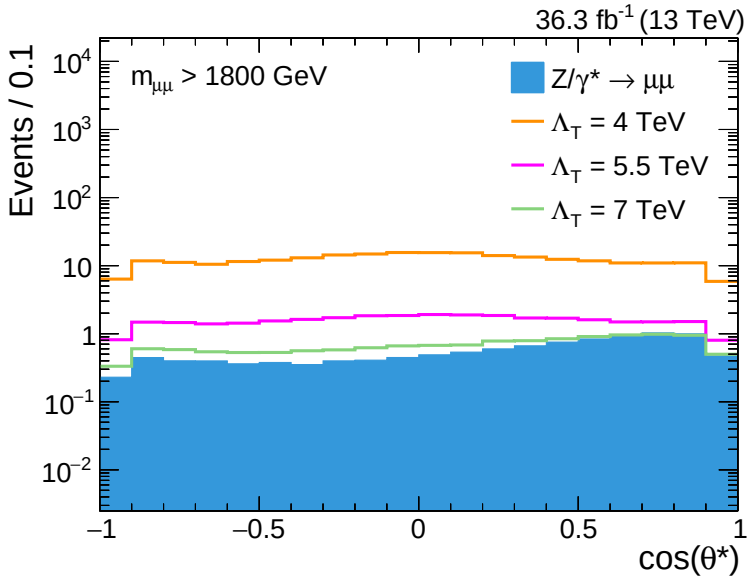

FIGURE 6.12: Cosine of the Collins–Soper angle θ^* for prompt muons produced in the DY and virtual graviton exchange processes. The reduced event yields in the outer two bins corresponds to the limited geometric acceptance of $|\eta| < 2.4$.

Signal Data Set	Transition	σ / fb
ASADDGravToLL_n-4_MD-6000_LambdaT-5000_Approx-0	Quenched	0.458
ASADDGravToLL_n-4_MD-6000_LambdaT-5000_Approx-1	Linear	0.228
ASADDGravToLL_n-4_MD-6000_LambdaT-5000_Approx-2	Quadratic	0.275

TABLE 6.5: Summary of all data sets for LED in the AS scenario for which a full detector simulation has been performed. To reduce the length of the data set names, the production threshold $m_{\ell\ell} > 1700\,\text{GeV}$, center-of-mass energy $\sqrt{s} = 13\,\text{TeV}$ and generator PYTHIA 8.2 have been omitted here. Each integer value of the approximation mode corresponds to the descriptive title given in the second column. The listed cross section values correspond to the ones calculated by the generator with the Drell–Yan contribution subtracted.

dimension η and wave function renormalization factor Z that have been discussed in section 3.4 and are displayed in figure 3.4. Following these predicted evolutions, all signals show a behavior similar to the one of a comparable ADD signal but diverge from it for larger interaction scales. The decreasing gravitational coupling results in a suppression of the differential cross section, setting in abruptly for the quenched approximation and continuously for both the linear and quadratic approximations. While the distributions of the latter two exhibit a similar shape, one can still observe the quadratic one resulting in slightly larger cross sections at lower masses. As the amount of produced events does not allow for a statistically stable prediction at high interaction scales, small differences in the shapes cannot be distinguished in this region of phase space. Overall, the disparity between the linear and quadratic approximation appears to be minuscule but accumulates to the larger total cross section given in table 6.5. The impact of varying the transition scale $\Lambda_{\text{Transition}}$ can be seen in figure 6.13b. As this scale serves as an indicator of the phase-space region where the transition between the IR and UV regime takes place, it effectively determines the strength of the aforementioned cross section suppression. The lower the value of $\Lambda_{\text{Transition}}$, the earlier the onset of the transition and associated suppression with respect to the energy scale. This dependency

is reflect by the simulation as shown by the distributions.

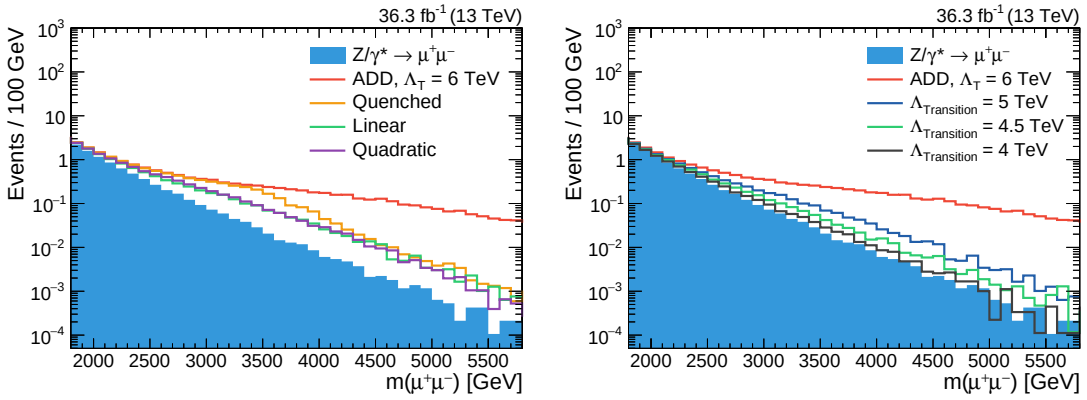

(a) (b)

FIGURE 6.13: Generator-level invariant mass spectra of muon pairs for simulated signals of LED in the AS scenario for quantum gravity. In (a) for varying approximations of the transition between the IR and UV regime and in (b) for multiple values of the transition scale using the linear approximation. To allow for a visual comparison, an ADD model signal is shown as well.

Given the suppression discussed in the paragraph above, one would consequently expect a similar feature to manifest in the momentum distributions. For the pseudorapidity spectra, no significant impact is expected as the cross section is mostly suppressed toward larger interaction scales. The distributions of two quantities for the leading and subleading muon with respect to the transverse momentum are shown in figure 6.14. A behavior matching the formulated expectation is observed, which concludes this analysis of the signal distributions. All discussed phenomena of the AS scenario, given LED, are present in the corresponding simulated samples. Consequently, one can confidently utilize them to perform an experimental search for this well-motivated, more advanced model.

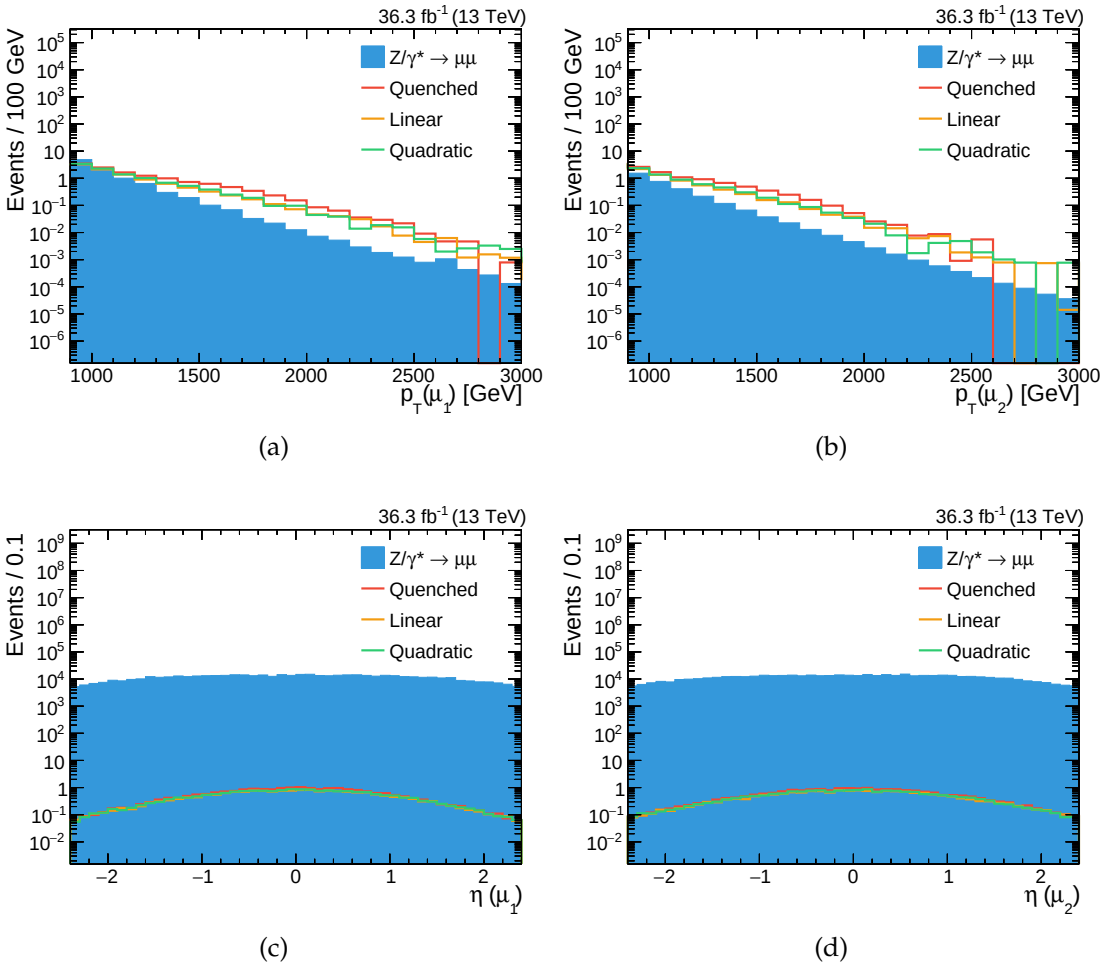

(a) (b)

(c) (d)

FIGURE 6.14: Transverse momenta and pseudorapidities of leading and subleading muon, respectively in (a) and (b) as well as (c) and (d), for simulated signals of LED in the AS scenario.

Chapter 7

Event Selection

Having defined the data sets and quantities with which to perform the analysis—most importantly the single-muon triggers and muon tracks—the quality of the object reconstruction has to be judged for each event. This is done in successive steps, requiring the variables in question to meet predefined criteria. A tabular summary of the categorized criteria is given in table 7.1. Figure 7.1 and table 7.2 provide overviews of the total amount of events satisfying each set of requirements. In the following sections, these sets will be discussed in detail. As most of them scrutinize multiple quantities with varying degrees of correlation, "$n-1$ distributions" will be used to showcase the impact of individual criteria. In this context, "$n-1$" refers to the number of requirements the object in question satisfies. For a given distribution corresponding to a criterion, the object meets the remaining $n-1$ criteria of the set.

Quantity	Requirement
Trigger & Acceptance	
Recorded with trigger	HLT_Mu50 or HLT_TkMu50
Muon transverse momentum p_{T}	>53 GeV
Muon pseudorapidity $\lvert\eta\rvert$	<2.4
Track Preselection	
Global muon track	Valid
Tracker muon track	Valid
Muon selection	
Tracker layers with measurements	>5
Hits in pixel detector	>0
Matched muon stations criterion	Valid
Hits in muon system	>0
Transverse impact parameter d_{xy}	<0.2 cm
Relative transverse momentum uncertainty $\Delta p_{\mathrm{T}}/p_{\mathrm{T}}$	<0.3
Relative track isolation	<0.1
Dimuon selection	
Sign of electric charges $\mathrm{sign}(\mu_1) \times \mathrm{sign}(\mu_2)$	-1
Conic distance ΔR of either muon to HLT object	<0.2
Opening angle between muons $\cos \measuredangle(\mu_1, \mu_2)$	> -0.9998
Common vertex fit χ^2/dof	<20

TABLE 7.1: Summary of all selection criteria. Refer to the respective sections of chapter 7 for discussions of each set of requirements.

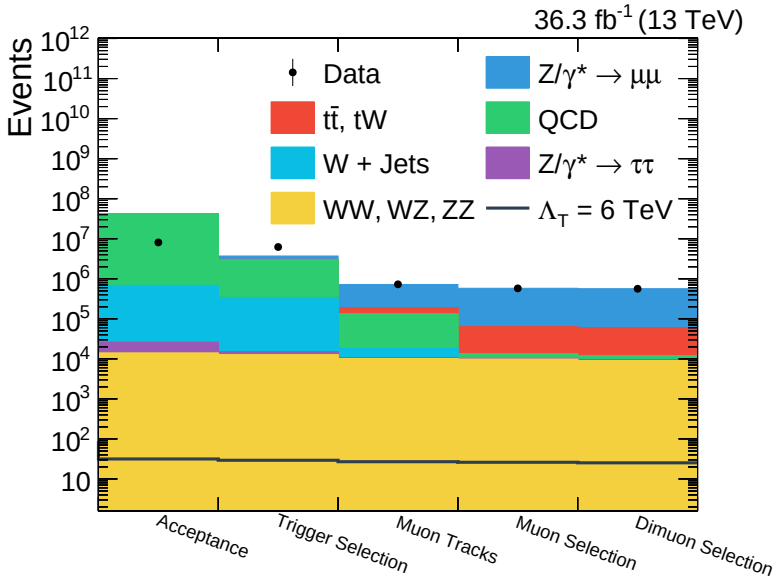

FIGURE 7.1: Total amount of events after successive steps in the event selection. Each bin corresponds to the number of events with at least one remaining pair of muons after the criteria corresponding to the bin label have been applied. Conditions between simulation and measurement are comparable after the trigger selection is performed. The event yields are also summarized in table 7.2.

7.1 Primary Vertex Selection

The precise alignment of the LHC proton beams and consequent definition of the nominal interaction point within the CMS detector constrains the position of primary vertices. Following the recommendation of the CMS Collaboration's analysis team (colloquially referred to as a physics object group or POG) concerned with the reconstruction of jets and missing transverse momentum [130], a primary vertex is required to satisfy three criteria. It has to have a minimum of four associated tracks and a distance with respect to the nominal interaction point in radial as well as longitudinal direction of $r < 2\,\text{cm}$ and $|z| < 24\,\text{cm}$, respectively. In combination, these criteria strongly favor vertices originating from bunch crossings while rejecting those created by interactions with particle remnants of the beam or the gas. Additionally, the requirements also guard against incidental measurements of muons produced by cosmic rays[1] passing through the detector volume, assuming that their trajectory is incompatible with the nominal interaction point. While a comparison of measured to simulated data is not meaningful before the trigger requirements have been matched, the individual fractions of discarded events can be studied. For the chosen subset of measured data, the fraction of discarded events amount to 2×10^{-4}. With the corresponding number for the simulated data sets being 3×10^{-8}, one can conclude that the vast majority of primary vertices are well reconstructed.

[1]Muons produced by cosmic rays, often abbreviated as cosmic muons, passing through the central region of the CMS detector traverse both the top and bottom half of its volume. As collisions are assumed to originate from the interaction point, the corresponding halves of the trajectory are often reconstructed as two individual muons of opposite electric charge.

Processes	Acceptance	Trigger Selection	Muon Tracks	Muon Selection	Dimuon Selection
ADD, $\Lambda_T = 6\,\text{TeV}$	3.15×10^1	2.92×10^1	2.69×10^1	2.60×10^1	2.52×10^1
$Z/\gamma^* \to \mu\mu$	6.93×10^5	6.63×10^5	5.30×10^5	5.15×10^5	5.05×10^5
$t\bar{t}, tW$	8.30×10^4	7.79×10^4	5.89×10^4	4.89×10^4	4.73×10^4
QCD	4.10×10^7	2.61×10^6	1.14×10^5	2.79×10^3	2.44×10^3
W + Jets	6.53×10^5	3.24×10^5	7.16×10^3	5.34×10^2	2.66×10^2
$Z/\gamma^* \to \tau\tau$	1.19×10^4	2.48×10^3	5.82×10^2	4.33×10^2	3.30×10^2
WW, WZ, ZZ	1.38×10^4	1.26×10^4	1.02×10^4	9.72×10^3	9.04×10^3
Total Background	4.25×10^7	3.69×10^6	7.18×10^5	5.78×10^5	5.64×10^5
Observed	8.06×10^6	6.20×10^6	7.25×10^5	5.75×10^5	5.62×10^5

TABLE 7.2: Total amount of events after successive steps in the event selection. Each column corresponds to the number of events with at least one remaining pair of muons after the criteria corresponding to the column title have been applied. Conditions between simulation and measurement are comparable after the trigger selection is performed. The event yields are also visualized in figure 7.1.

7.2 Acceptance & Trigger Selection

The definition of the acceptance is closely related to the configuration of the trigger. All used single-muon triggers include the entire geometric coverage of the muon system up to $|\eta| < 2.4$. Their efficiency is measured using the "tag-and-probe" procedure, with the "tagging" muon being accepted by the HLT_IsoMu24 trigger. The corresponding distributions as a function of the transverse momentum and pseudorapidity of the "probe" muon are shown in figure 7.2. One can generally observe high efficiencies of around 90 % for single muons, resulting in the aforementioned combinatorial efficiency of 99 % for two muons discussed in section 6.1. The most notable feature of the distribution for the combination of both $p_\text{T} > 50\,\text{GeV}$ triggers is the plateau they reach for transverse momenta above 53 GeV. In order to avoid event topologies corresponding to unstable trigger efficiencies[2], this value is used as the muon transverse momentum threshold for the kinematic acceptance.

Introducing a requirement for two muon candidates whose Tune-P tracks satisfy $p_\text{T} > 53\,\text{GeV}$ and $|\eta| < 2.4$ to both the measured and simulated data sets yields the amount of events shown in the first bin of figure 7.1. As the trigger conditions between measurement and simulation have not yet been matched, only a very rough agreement between the observation and prediction can be expected at this stage. For events to be part of the chosen single-muon datastream, they need to be recorded via at least one single-muon trigger while no such prerequisite exists for the simulated data sets. To obtain consistent trigger conditions, observed and generated events are required to be recorded via at least one of the two triggers corresponding to the respective labels HLT_Mu50 and HLT_TkMu50. This consistency, alongside the constraints of

[2]The steep incline of the efficiency near the transverse momentum threshold (instead of a step function) is caused by comparing different momentum estimates. While the distribution is shown as a function of the Tune-P momentum, the HLT applies the p_T requirement based on its preliminary track reconstruction.

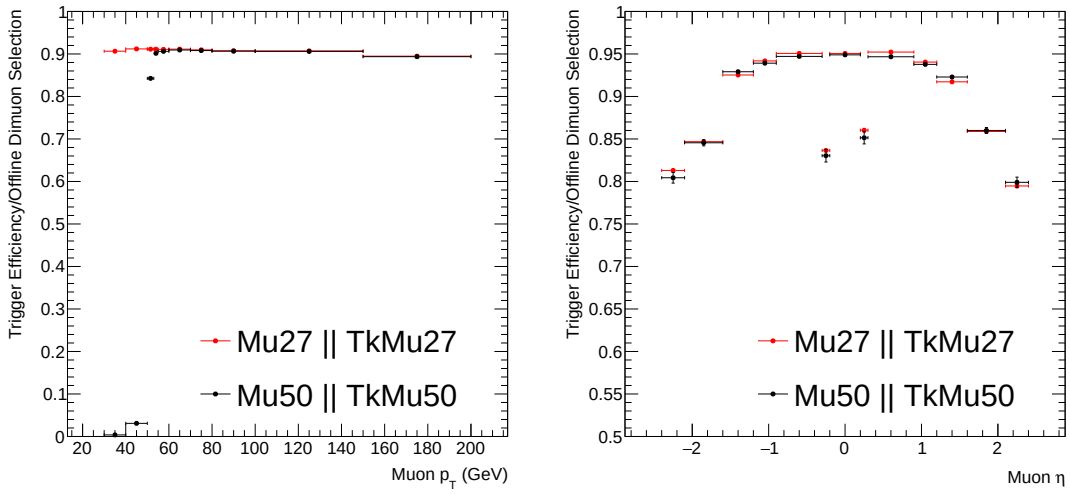

(a) (b)

FIGURE 7.2: Measured trigger efficiency as a function of the transverse momentum in (a) and pseudorapidity in (b) for the combination of HLT_Mu50 and HLT_TkMu50 compared to the one of HLT_Mu27 and HLT_TkMu27 [102]. The latter two will be used in section 8.4 to derive the overall normalization.

the preliminary HLT track reconstruction, results in a noticeable improvement of the agreement as shown in the second bin of figure 7.1.

7.3 Track Preselection

Following the acceptance and trigger requirements, a set of criteria for the selection of muon candidates with high transverse momenta is applied. They are developed and maintained by the muon reconstruction analysis team and focus on the quality of the fitted tracks [102, 131]. While all included criteria pertain to individual muon candidates, the hierarchical dependence of the variables necessitates a preselection step. In this step, it is ensured that the tracker muon and global muon algorithms (Sec. 5.3) have succeeded in reconstructing tracks for the candidates. Satisfying both conditions implies that an independent reconstruction of the respective hits recorded in the inner tracking system and muon chambers has resulted in self-consistent tracks.

The amount of muon candidates for which the respective reconstruction algorithms have yielded a valid track can be seen in figure 7.3 using the aforementioned $n - 1$ format. Incorporating the Tune-P track into the preselection shows that being able to reconstruct tracker or global muon tracks does indeed guarantee the success of the Tune-P algorithm. On the other hand, one can also see that it is possible to have a candidate without a tracker muon track even though the global muon track algorithm has succeeded. Given that the latter takes hits of the inner tracking system into account, one may naively expect otherwise. Following the discussion of the two approaches in section 5.3, it can be seen that their differences (e.g., the direction of the fit) allow for this scenario. If two muon candidates have tracker and global muon tracks, the event is recorded in the third bin of figure 7.1. The observed agreement between measurement and simulation supports the reliance on these algorithms as the basis of identifying muon signatures.

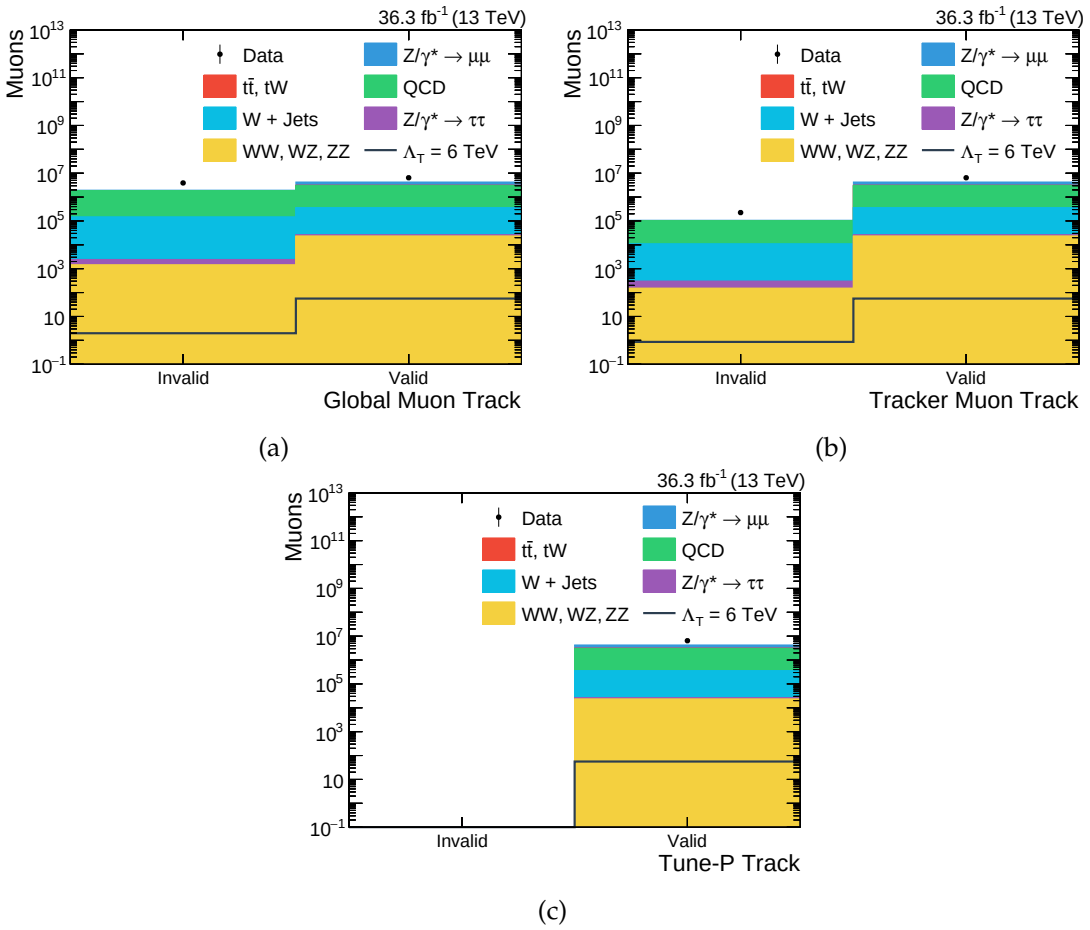

FIGURE 7.3: Amount of all muon candidates for which the different reconstruction algorithms have succeeded in reconstructing a track.

7.4 Muon Selection

Having ensured that each muon candidate is reconstructed as a tracker and global muon, further demands are posed to the properties of the corresponding tracks as part of the high-p_T muon selection. The overarching goal is to reject candidates which may not have originated from muons or whose track reconstruction is unreliable. Each criterion and its motivation as well as performance is discussed in the following paragraphs, with the latter being on display as $n-1$ distributions in figures 7.6 and 7.7.

Tracker layers with measurements As it provides the most precise spatial information of the CMS detector, the contribution of the inner tracking system to the muon track reconstruction is essential. Demanding the inner track to be based on at least five silicon layer measurements ensures that it can provide a reasonable estimate for the corresponding momentum. Additionally, this requirement also suppresses contributions from muons produced by "in-flight" meson decays. In these cases, the corresponding displaced vertex may not allow for a sufficient number of tracker layers to be hit. This expectation matches the observation of jet-based backgrounds in the excluded region of figure 7.6a.

Valid hits in the pixel detector Following the same reasoning discussed for the tracker layer requirement, the inner track of the candidate needs to have at least one hit in

the pixel detector. This provides further suppression with respect to muons originating from mesons decaying "in flight". Figure 7.6b shows the same qualitative behavior that has been observed in the tracker layer hit distribution, with backgrounds where muons have to be produced in jets having significant contributions in the hereby excluded region.

Number of matched muon stations Posing requirements to the number of muon stations which have measured segments that are compatible with the global track of the muon candidate aims to prevent two types of scenarios: On the one hand, hadronic remnants "punching through" the HCAL and solenoid resulting in hits in the closest muon station. On the other hand, accidental matches between inner tracks and segments in individual stations due to weak spatial constraints.

Previous iterations of the high-p_T muon quality criteria only allowed for muons with segments in at least two muon stations (2MS) to serve the aforementioned purpose [e.g. 73]. While this matches the trigger logic, it leads to minor inefficiencies due to gaps between the barrel wheels and the two "chimneys" for service cables (Fig. 7.4a). Adding two alternative criteria allows for recovering most of the otherwise valid muon candidates (Fig. 7.4b). Both require only a single muon station to match, either demanding that it is not part of the first layer (Not 1st) or, if it is, two compatible RPC measurements (2RPC).

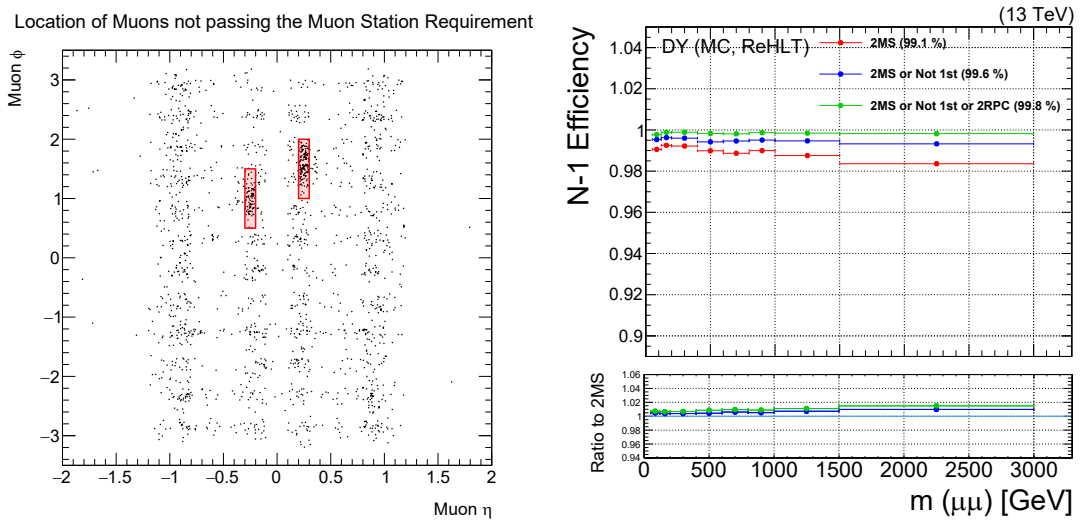

(a) (b)

FIGURE 7.4: Recovery of a minor inefficiency originating in the requirement of muon station measurements contributing to the track reconstruction [Adapted from 102]. The correlation between the inefficiency of the requirement and gaps between the barrel wheels can be seen in (a). Two red boxes indicate the location of the "chimneys" for service cables, corresponding to a comparatively larger inefficiency. The performance after introducing the two alternative criteria discussed in the text is shown in (b).

The final performance of this three-part criterion can be seen in figure 7.6c. One observes a sizable fraction of W + jets and QCD events not satisfying the requirement, matching the expectation with respect to their hadronic contributions.

Valid hits in the muon system The motivation to require at least one hit in the muon system to be incorporated into the global muon track fit is twofold. As mentioned in the discussion of the track reconstruction for muons (Sec. 5.3), the momentum

estimate benefits significantly from the first hit in the muon chambers extending the fitted arc. Should the global track reconstruction consider all standalone hits to be incompatible with the fit, the preliminary match between them and those of the inner tracking system may have been accidental. The muon system measurements could instead have originated from hadronic activity. When evaluating the corresponding distribution shown in figure 7.6d, this requirement is observed to suppress the aforementioned unreliable contributions located in the first bin. While one may argue that the threshold for the amount of hits could also be raised to 2 or 3, the given distribution shows that this would have no significant impact on the event yields.

Transverse impact parameter Demanding the transverse impact parameter d_{xy}, i.e., point of closest approach of the extrapolated Tune-P track to the primary vertex in the x-y plane to be smaller than 0.2 cm targets muons produced by cosmic rays and those stemming from heavy flavor quark decays. For the former, the transverse impact parameter distribution is expected to be distinctly flat as cosmic muons have no dependence on the primary vertex. While this would correspond to an excess of measured event yields with respect to the simulated ones toward larger impact parameter values, this is not observed in figure 7.6e; in fact, within the statistical uncertainty, the simulated yields exceed the measured ones for $d_{xy} > 0.2\,\text{cm}$. Past studies of the CMS Collaboration [132] have determined that a vast majority of cosmic muons are rejected by the given requirement on the transverse impact parameter. Thus, by inverting the requirement, the contamination of cosmic muons in the dimuon invariant mass spectrum can be estimated. The corresponding distribution where all other criteria up to and including those of this section are applied is shown in figure 7.5a. Very few measured "pairs" of muons and even fewer simulated ones are observed to meet the inverted criterion. This suggests that (individual) muons of cosmic origin—which are not described by the simulation—have been measured and that their overall contribution at this stage of the analysis is too small to be distinguished in figure 7.6e.

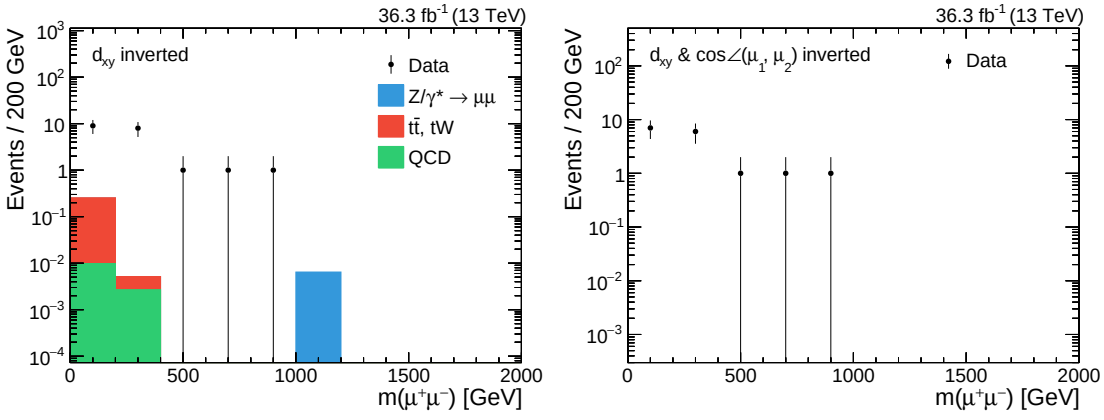

(a) (b)

FIGURE 7.5: Estimated contamination of cosmic muons in the dimuon invariant mass spectrum. In (a) determined by applying all selection criteria up to and including those for individual muons (Sec. 7.1–7.4) with the transverse impact parameter requirement inverted to $d_{xy} > 0.2\,\text{cm}$. Determined in (b) by applying the full set of selection criteria with the respective requirements posed to the transverse impact parameter and the opening angle between the two muons inverted to $d_{xy} > 0.2\,\text{cm}$ and $\cos \measuredangle(\mu_1, \mu_2) < -0.9998$. No simulated events fulfill the selection criteria for (b).

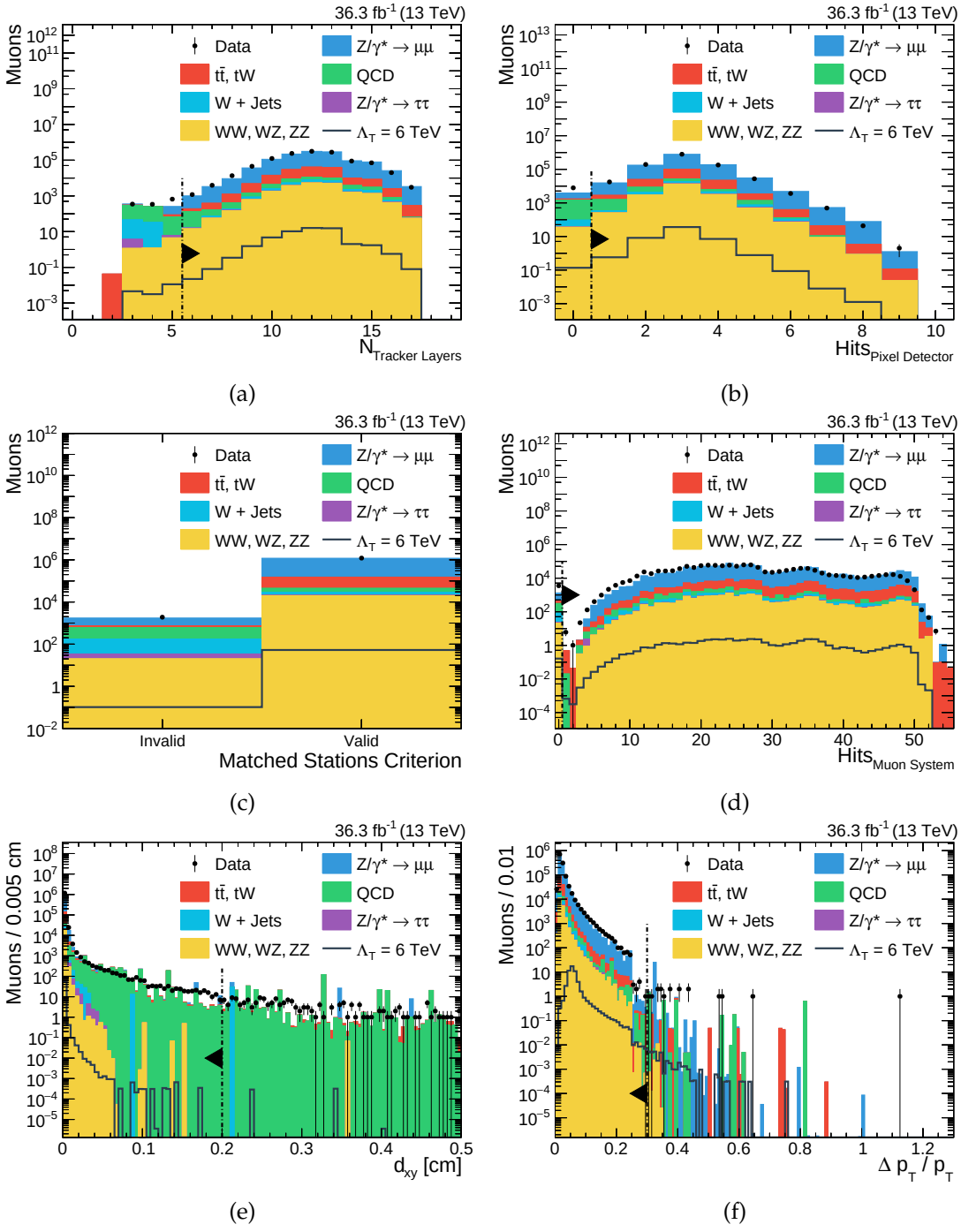

FIGURE 7.6: High-p_T muon selection $n-1$ distributions for all muon candidates fulfilling the discussed selection criteria up to section 7.4. Where applicable, dashed black lines indicate the respective requirement with the arrow pointing toward the remaining region of phase space. The relative isolation, displayed in figure 7.7, is also part of the n considered selection criteria. Shown are the number of tracker layers with measurements associated to the inner track in (a) and its amount of valid pixel hits in (b). The matched stations criterion is displayed in (c). In (d), the valid hits included in the global muon track reconstruction are given. The transverse impact parameter of the Tune-P track and its relative transverse momentum uncertainty are shown in (e) and in (f), respectively.

In contrast, the suppression of muons produced in heavy flavor quark decays can be clearly seen in the distribution. The observed behavior toward larger distances also hints at the inadequate simulation of muon contributions by QCD processes. While the measurement provides a stable yield of muon candidates, the QCD description fluctuates because the amount of generated events does not suffice.

Relative uncertainty of the transverse momentum The Tune-P algorithm requires the relative uncertainty in the transverse momentum, as estimated by the track fits, to be lower than 25 % unless all considered reconstructed tracks exceed this threshold (Sec. 5.3). As a consequence, a majority of the Tune-P tracks provide reliable estimates of the transverse momentum. However, some outliers still persist (Fig. 7.6f). They are rejected by requiring the relative uncertainty to be smaller than 30 %.

Relative isolation in the inner tracking system In addition to the baseline given by the high-p_T muon selection criteria, the candidate is also required to be isolated. The isolation parameter is defined with respect to the scalar sum of transverse momenta of all tracks surrounding the inner track of the muon candidate in a cone of $\Delta R < 0.3$. Evaluated relative to the transverse momentum of the candidate itself, the parameter is not allowed to exceed 10 %. This requirement primarily targets muons produced within jets against whom it proves to be a strong discriminator as shown in figure 7.7.

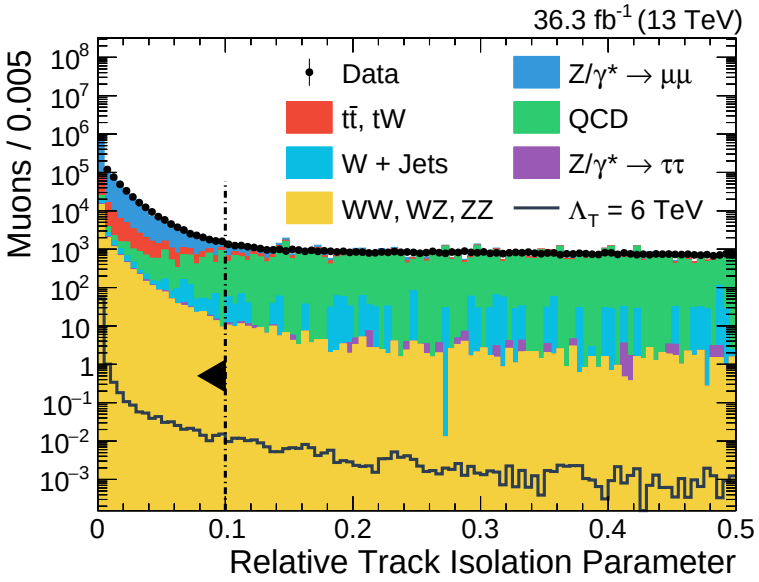

FIGURE 7.7: Relative isolation parameter of the inner track for all muon candidates satisfying the discussed selection criteria up to section 7.4. The quantity is shown as an $n-1$ distribution in combination with the requirements of figure 7.6. Note that the parameter denotes a scalar sum of transverse momenta surrounding the muon track in question and thus lower values imply a more isolated candidate.

Overall, one can conclude from the observed agreement between data and simulation that the latter accurately models the detector response. Summarizing the performance of the high-p_T muon selection requirements, the second to last bin of figure 7.1 shows the amount of events where at least two muons satisfy all criteria up to this point. Matching the preceding discussion of the individual requirements, one observes a good agreement between measurement and simulation alongside a significant reduction of QCD contributions.

7.5 Dimuon Selection

For the remaining muon candidates in each event, all possible pairwise combinations are considered as dimuon objects. Further constraints are imposed on these pairs, focusing on the consistency with the expected signature and corresponding event reconstruction. All $n-1$ distributions are shown in figure 7.8.

Opposite sign charge As the virtual graviton exchange process does not violate the conservation of (electric) charge, the muon candidates of a pair are required to have charges of opposite sign. Matching this expectation, one observes the vast majority of signal (and DY) muon pairs to be reconstructed with opposite sign charges in figure 7.8a. Studies based on cosmic muons have determined the probability for mismeasuring the charge of a muon with the CMS detector to range from below 0.01 % at transverse momenta of 10 GeV up to about 1 % at 500 GeV [133]. Given these results, the impact of such a mismeasurement on this selection criterion is taken to be negligible.

Match to trigger object With the trigger decision being based on the reconstruction of single muons, one of the candidates is required to be spatially compatible with the reconstructed HLT object within in a cone of $\Delta R < 0.2$. The corresponding distribution can be seen in figure 7.8b. While one observes that most dimuon objects satisfy this condition, contributions by QCD processes are suppressed by it. Given the increased hadronic activity, the probability that the preliminary HLT reconstruction performs as well as the more sophisticated ones is low. As a consequence, frequent spatial incompatibilities between the two objects are observed.

Opening angle between muons As discussed before, tracks corresponding to cosmic muons are reconstructed as two opposite sign muon candidates. These candidates appear to be produced back-to-back with respect to the opening angle between the two. Their contribution can be further reduced by requiring a minimum threshold of $\pi - 0.02$ for the opening angle, translating to $\cos \measuredangle(\mu_1, \mu_2) > \cos(\pi - 0.02) \simeq -0.9998$. While this does indeed remove a slight excess of measured muons as shown in figure 7.8c, better observed in the enhanced view of figure 7.8d, this phase space also coincides with the high-mass regime. Given the minuscule amount of rejected events corresponding to less than 1 % of all signal contributions, the rejection of cosmic muons still warrants applying this criterion.

Inverting both the current requirement and the one on the transverse impact parameter, in addition to applying all other selection criteria, yields the dimuon invariant mass distribution shown in figure 7.5b. Compared to figure 7.5a, the introduction of muon pair selection requirements (with $\cos \measuredangle(\mu_1, \mu_2) < -0.9998$) is observed to have little impact on the measurement while it removes all simulated contributions. This supports the aforementioned suggestion that the measured muons are of cosmic origin; it also leads to the conclusion that their contamination is negligible after the application of all selection criteria, matching the corresponding observation in the search for BSM physics at high dilepton invariant masses with the CMS experiment at $\sqrt{s} = 8$ TeV [73].

Quality of common vertex fit As the considered signal process predicts both muons to be immediate daughter particles to the virtual graviton, their tracks are expected to be compatible with a common vertex. Performing a Kalman filter vertex fit

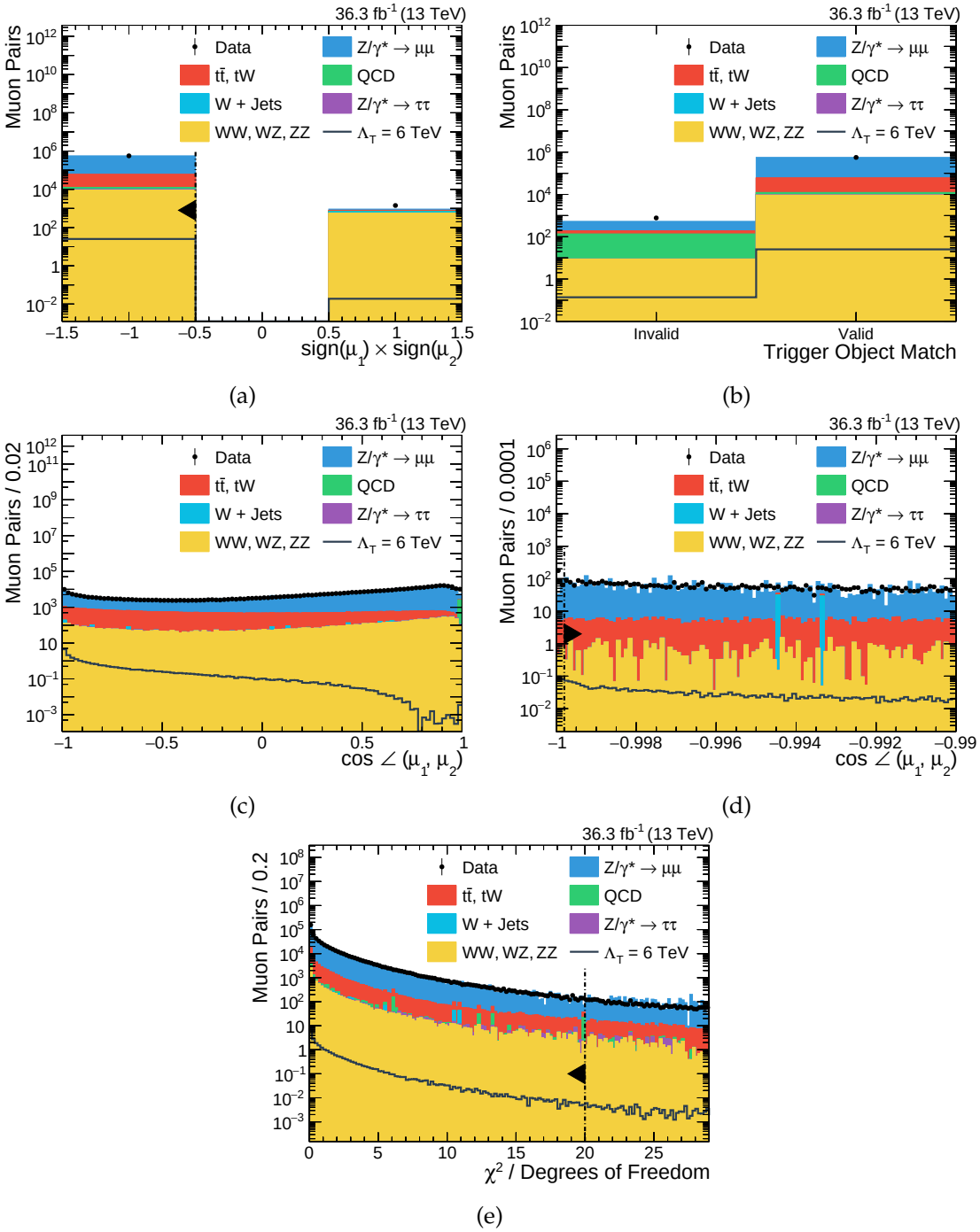

FIGURE 7.8: Muon pair selection $n-1$ distributions for all muon pair candidates which satisfy the discussed selection criteria up to section 7.5. Where applicable, dashed black lines indicate the respective requirement with the arrow pointing toward the remaining region of phase space. Shown are the distributions of the multiplied muon charges in (a), the muon pairs where one muon is spatially compatible with the HLT object in (b), the cosine of the 3D opening angle between the muons in (c) and (d), as well as the χ^2/dof of the common vertex fit in 7.8e.

under the constraint of a common origin for both tracks—elaborated on in section 8.2—provides an estimator for their compatibility in the form of the χ^2 test statistic (Fig. 7.8e). Given the inherent uncertainty in the reconstruction of tracks, only dimuon candidates with a $\chi^2/\text{dof} > 20$ are rejected, which corresponds to about 1–2 % of all muon pair candidates at this stage.

By applying the full set of requirements, including the ones discussed in this section, one arrives at the last bin of figure 7.1. Overall, one observes an agreement between measurement and simulation with only minor differences with respect to the previous bin. As the muon pair requirements mostly reject outliers, this is expected. Having considered all pairwise combinations of muon candidates, the dimuon object with the highest invariant mass is chosen if more than one satisfies all criteria.

7.6 Performance

To evaluate the performance of the event selection for LED processes, its efficiency is determined using the simulated data sets. In figures 7.9a and 7.9b, the efficiency for events satisfying the acceptance requirements with respect to all analyzed events is shown as a function of the generator-level dimuon invariant mass. The phase space below the production threshold of $m_{\mu\mu} > 1.7\,\text{TeV}$ is omitted. The more central production of muons with respect to the detector geometry via the virtual exchange of gravitons leads to slightly larger efficiencies at lower invariant masses. Lower values of the UV cutoff parameter Λ_T, corresponding to larger contributions of graviton-mediated events, enhance this effect. Once the graviton contributions dominate, the efficiency becomes effectively mass-independent at $(95 \pm 1)\,\%$. As higher masses generally favor a more central production, the difference between the DY and signal processes diminishes in this region of phase space. The efficiency of applying the full set of selection criteria with respect to all events satisfying the acceptance requirements is shown in figures 7.9c and 7.9d. Beyond the "turn-on" at low masses, a high efficiency of about 90 % with a similar performance for both the DY and signal processes is observed. As the differing angular dependencies could only affect the opening angle between the two muons and the corresponding amount of rejected events is small, this similarity is expected.

Using equidistant bins of 50 GeV each, the invariant mass distribution of muon pairs after all selection criteria have been applied is shown in figure 7.10. The signal is drawn in front of all simulated background processes, which displays its contributions below the production threshold $m_{\mu\mu} > 1.7\,\text{TeV}$. When generating events with Pythia 8.2,

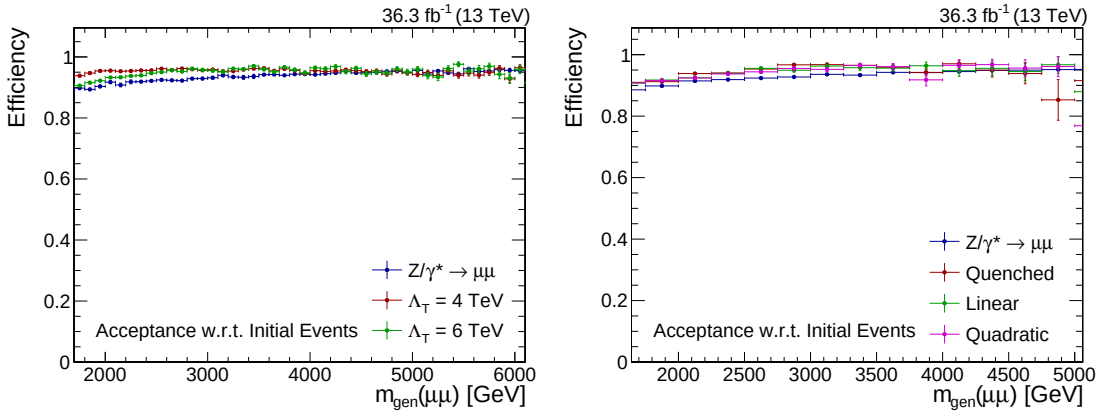

(a) (b)

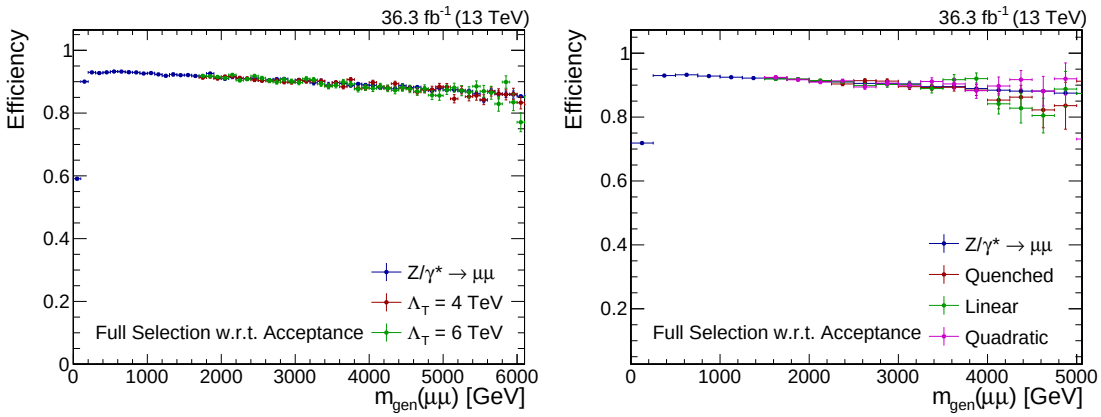

(c) (d)

FIGURE 7.9: Efficiency of the event selection for LED and DY events as a function of the generator-level dimuon invariant mass. The first pair of distributions shows the efficiency of the acceptance requirements with respect to the initial events above the production threshold of $m_{\mu\mu} > 1.7\,\text{TeV}$ and the second one shows the efficiency of the full selection with respect to the acceptance requirements. In (a) and (c) for the ADD model signals and in (b) and (d) for those of the AS scenario. The other parameters of the latter signals are set to $n = 4$, $M_D = 6\,\text{TeV}$ and $\Lambda_{\text{Transition}} = 5\,\text{TeV}$. Signal contributions below their generator invariant mass threshold are omitted.

this threshold is applied with respect to the mass of the particle mediating the $2 \to 2$ process. As a consequence, the invariant mass of the two leptons can still be reduced via radiative emission of energy; its value also depends on the simulation of the detector response. While one does observe contributions by processes where at least one of the muons is produced as part of a jet, the fluctuating description is indicative of an insufficient amount of generated events. The inherent complexity of modeling these contributions further exacerbates the difficulty of obtaining an accurate description via simulation. Replacing jet-based backgrounds is one of the outstanding improvements to the process descriptions discussed in the following chapter.

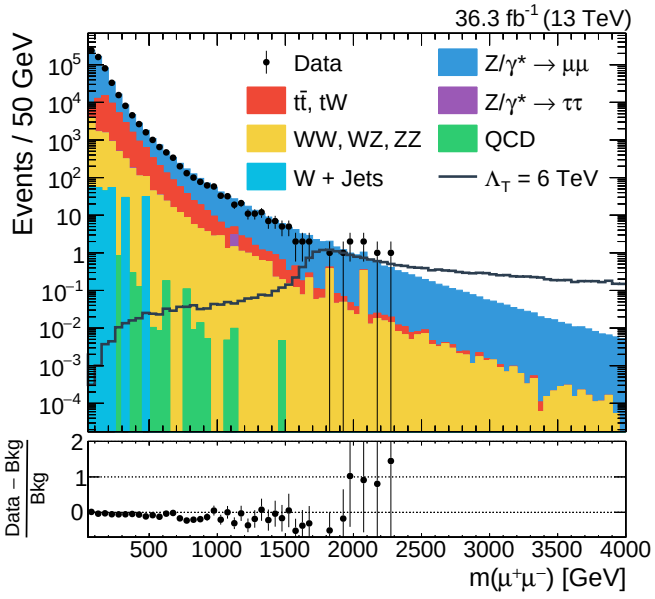

FIGURE 7.10: Invariant mass of muon pairs after the full set of selection criteria have been applied.

Chapter 8

Jet Background Estimate & Corrective Measures

In addition to the reevaluation of jet-based backgrounds motivated in the last section of the event selection (Sec. 7.6), three other options to improve the process modeling are discussed in this chapter. The utilization of the invariant mass provided by the common vertex fit, an approximation of higher order differential cross sections for the DY and signal processes, and using the measured data to derive the overall normalization.

As different detection systems of the CMS experiment are responsible for the measurement of muons in the barrel region and endcaps (Sec. 4.2.3 & 4.2.4), two pseudorapidity categories are introduced to treat events separately where appropriate. Those events with both muons measured in the barrel region $|\eta| < 1.2$ constitute the "barrel-barrel" (BB) category, whereas all other events with at least one muon measured in the endcaps $1.2 < |\eta| < 2.4$ are subsumed under the "barrel-endcap" (BE) label.

8.1 Data-driven Jet Background Estimate

While the object reconstruction and selection (Chap 5 & 7) put strict requirements on what is ultimately considered to be a muon track, they are not infallible. Objects misreconstructed as prompt muons satisfying the entire set of requirements are often referred to as "fake" muons. Even though they are expected to be rare (by design of the criteria), their contribution to the background also needs to be taken into account. The primary source of these misreconstructed muons are jets. Leptonic decays of heavy flavor quarks or mesons, e.g., b quarks and B or D mesons, can produce a real muon surrounded by hadronic activity. In this scenario, the muon would originate from a secondary vertex and be part of a jet; the latter implies a poor spatial isolation. Two other options are real muons produced "in flight" as a result of kaon or pion decays, and cosmic muons passing through the detector at an inopportune time. It is also possible that hadrons "punch through" both the HCAL and solenoid, prompting a detector response in the muon system. Given a coincidentally matching set of hits in the inner tracker, they may combine to a seemingly valid muon track. It should be noted that most of these scenarios involve real muons and only the latter would semantically be considered a fake one. However, in this section and context in general, the term is to be understood as defined with respect to *prompt* muons.

Given the rare occurrence of these phenomena (and their nontrivial simulation), the utilized simulated data sets do not describe these processes adequately (see Fig. 7.10). An alternative way to estimate their contribution is the data-driven "fake factor" (or "fake rate") method. It can be described as a sequence of three steps:

1. Replacing part of the reconstruction and selection requirements with looser criteria to create a region of phase space enriched with potentially misreconstructed

muons. From this point onward, the latter are referred to as misreconstruction candidates.

2. Measuring the probability that a misreconstruction candidate meets the high-p_T selection criteria, termed the "fake factor" P_{ff}, in an independent control region.

3. Applying this probability P_{ff} to subsamples of events in order to evaluate their contribution of misreconstructed muons to the final state.

Starting with the first step, an overview of the loose criteria is given in table 8.1. The candidates are still required to have a successfully reconstructed global and tracker muon track as well as a Tune-P track that is compatible with the primary vertex. In addition, all candidates also have to spatially match the HLT object and satisfy the high-p_T requirements for hits in the inner tracker. On the other hand, in line with the discussion of the origin of misreconstructed muons, isolation and muon system criteria are removed. There is also no requirement posed to the relative uncertainty in the transverse momentum measurement.

Quantity	Requirement
Global muon track	Valid
Tracker muon track	Valid
Longitudinal impact parameter d_z	<1.0
Transverse impact parameter d_{xy}	<0.2
Tracker layers with measurement	>5
Valid pixel hits	>0
Conic distance ΔR to HLT object	<0.2

TABLE 8.1: Criteria defining the region of phase space enriched with misconstruction candidates [102].

The control region in which the fake factor is measured is defined by selecting events satisfying the criteria listed in table 8.2. Individual muons still have to fulfill the trigger requirements, but events where more than one muon satisfies all high-p_T selection requirements are vetoed in order to ensure the aforementioned independence of the region. Introducing a threshold for the transverse mass of the leading muon with respect to its p_T and the missing transverse momentum

$$m_T = \sqrt{2 p_T p_T^{miss} (1 - \cos \Delta\phi)} < 35\,\text{GeV}, \tag{8.1}$$

prevents major contributions by μ + jets final states produced at the Jacobian peak of the W + jets process. Here, $\Delta\phi$ refers to the polar angle between the leading muon and the missing transverse momentum.

Quantity	Requirement
Muon transverse momentum p_T	>53 GeV
Muon pseudorapidity $\lvert\eta\rvert$	<2.4
Muons meeting high-p_T selection criteria	<2
Transverse mass $m_T(\mu, p_T^{miss})$	<35 GeV

TABLE 8.2: Criteria defining the control region in which the probability that a misreconstruction candidate satifies the high-p_T requirements is measured [102].

With the control region defined, the fake factor P_{ff}, i.e., the probability that a misreconstruction candidate satisfies the high-p_{T} selection requirements can be determined. After subtracting the electroweak contamination, it is measured as a function of the muon transverse momentum in the two pseudorapidity categories. The corresponding distributions are shown in figure 8.1. For intermediate transverse momenta, low values of P_{ff} are observed. While the statistical uncertainty does not allow for a precise evaluation toward high muon momenta, the fake factor is generally observed to be larger in this region of phase.

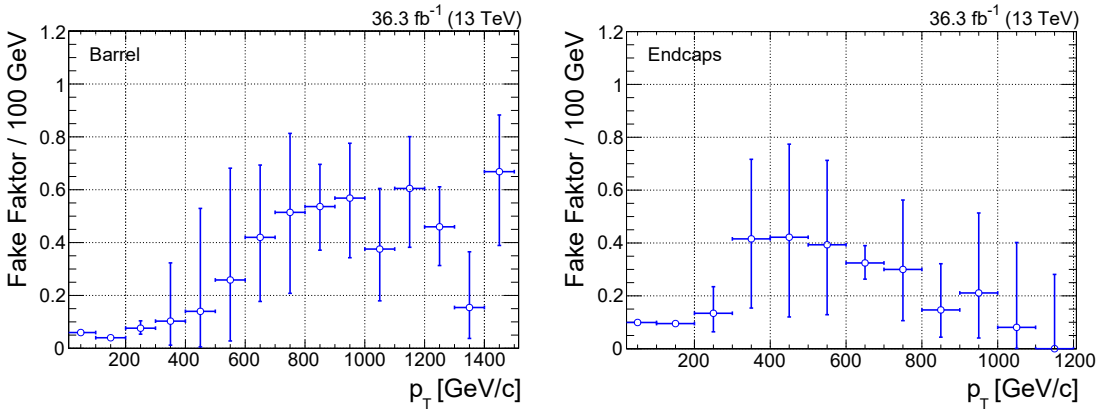

(a) (b)

FIGURE 8.1: Measured probability that a misreconstruction candidate satisfies the high-p_{T} selection requirements, referred to as the "fake factor", as a function of the muon transverse momentum [Adapted from 102]. Shown in (a) for the barrel region and in (b) for the endcaps. The displayed uncertainty is the statistical one.

Based on the measured fake factor P_{ff}, estimates for the contribution of misreconstructed muons can be derived. One differentiates between two subsamples for this purpose. The events of the respective subsample contain either one or two misreconstruction candidates which satisfy the loose criteria of table 8.1 while not satisfying the high-p_{T} selection criteria. Weighting these subsamples with $P_{\text{ff}}/(1 - P_{\text{ff}})$ per candidate yields the initial estimates with

$$N_{2\,\text{misreco.}\,\mu} = \sum \frac{P_{\text{ff}}(\mu_1)}{1 - P_{\text{ff}}(\mu_1)} \times \frac{P_{\text{ff}}(\mu_2)}{1 - P_{\text{ff}}(\mu_2)} \quad \text{and} \quad N_{1\,\text{misreco.}\,\mu} = \sum \frac{P_{\text{ff}}(\mu)}{1 - P_{\text{ff}}(\mu)}. \tag{8.2}$$

Subtracting the electroweak contributions from this initial estimate for two misreconstructed muons yields the corresponding final prediction with an enhanced purity of the QCD multijet content. Considering that either of the two misreconstruction candidates of this prediction could have met all selection criteria, their contribution contaminates the initial estimate for a single misreconstructed muon. In order to formulate a separate prediction for the latter, this contamination is subtracted.

An overview of both resulting event yields in comparison to the total observed yield is provided in tables 8.3 and 8.4 alongside the assigned statistical and systematic uncertainties. While multiple sources of systematic uncertainty have been taken into consideration, the dominant one is given by the dependence on jet kinematics. This also constitutes an aspect in which the control region differs from the search region. The impact of the dependence is estimated by introducing a requirement for a jet which satisfies loose selection criteria including a transverse momentum threshold of 30 GeV. The observed variations of the event yield range from 30 to 50 % [102]. While the overall prediction for contributions by misreconstructed muons is not precise, the

corresponding event yields are also much smaller than those of other SM backgrounds as indicated by the comparison to the total observed number of events.

Mass range / GeV	Total Obs.	Barrel-Barrel	Barrel-Endcap
120–400	244 269	$79.10 \pm 4.54 \pm 39.55$	$99.40 \pm 4.90 \pm 49.70$
400–600	5912	$1.80 \pm 0.68 \pm 0.90$	$5.00 \pm 1.10 \pm 2.50$
600–900	1311	$0.98 \pm 0.50 \pm 0.49$	$0.86 \pm 0.45 \pm 0.43$
900–1300	244	$0.36 \pm 0.30 \pm 0.18$	$0.33 \pm 0.29 \pm 0.17$
1300–1800	41	$0.0 \pm 0.0 \pm 0.0$	$0.10 \pm 0.12 \pm 0.05$
>1800	8	$0.90 \pm 0.50 \pm 0.45$	$0.01 \pm 0.06 \pm 0.01$

TABLE 8.3: Comparison of the total observed event yield to the data-driven prediction of the background contribution by events with two misreconstructed muons [102].

Mass range / GeV	Total Obs.	Barrel-Barrel	Barrel-Endcap
120–400	244 269	$205.20 \pm 11.74 \pm 61.56$	$440.71 \pm 21.80 \pm 132.21$
400–600	5912	$10.56 \pm 2.66 \pm 3.17$	$31.87 \pm 5.86 \pm 9.56$
600–900	1311	$7.62 \pm 2.26 \pm 2.29$	$13.99 \pm 3.88 \pm 4.20$
900–1300	244	$3.54 \pm 1.54 \pm 1.06$	$3.14 \pm 1.84 \pm 0.94$
1300–1800	41	$0.0 \pm 0.0 \pm 0.0$	$2.04 \pm 1.48 \pm 0.61$
>1800	8	$0.0 \pm 0.0 \pm 0.0$	$0.30 \pm 0.57 \pm 0.09$

TABLE 8.4: Comparison of the total observed event yield to the data-driven prediction of the background contribution by events with one misreconstructed muon in addition to a prompt one [102].

8.2 Correction of the Invariant Mass

Expanding upon the discussion of muon trajectories and their compatibility with a common vertex in section 7.5, Kalman filter tracks can be expressed as a propagation from an estimated vertex of origin [134]. With the introduction of a common vertex constraint to both muon tracks, an iterative minimization of the sum of squared residuals or "least-squares minimization" is performed. At each step, the transverse and longitudinal impact parameters of the muon tracks, their points of closest approach to the vertex in the respective planes, are updated according to their current trajectory fit. Should they remain incompatible after a given number of iterations, the minimization will not converge and the muon pairs do not satisfy the dimuon selection criteria. For converging fits, the degree of compatibility is given by their χ^2/dof ratio. The properties corresponding to the common vertex are then calculated based on the updated trajectories, e.g., the invariant mass of the vertex is determined by the sum of four-momenta of the associated tracks.

In figure 8.2, the performance of this invariant mass is compared to the one determined by the sum of the muon four-momenta reconstructed via the Tune-P algorithm (Sec. 5.3). Using simulated DY events in an invariant mass range of 800 to 4500 GeV, the residuals of the reconstructed masses relative to the respective values have been approximated using a Gaussian distribution. The associated standard deviations are shown in figure 8.2a as a function of the vertex fit χ^2/dof. An improvement of the mass resolution is observed when using the result of the constrained vertex fit compared

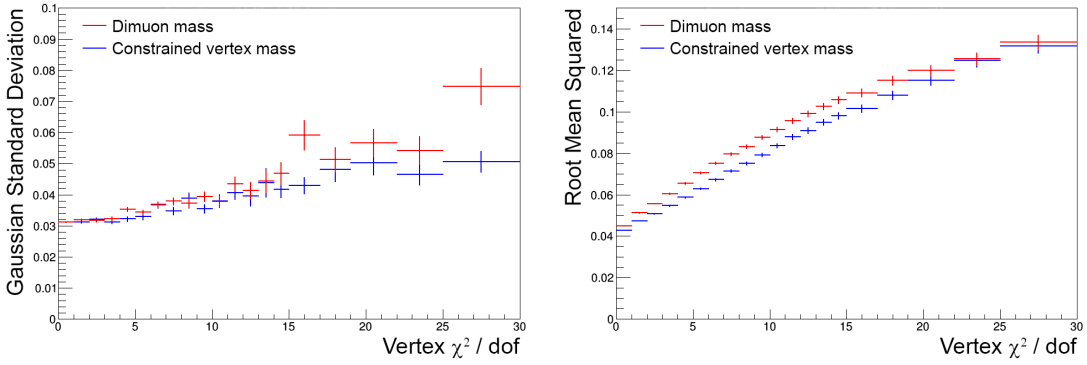

(a) (b)

FIGURE 8.2: Spread of the residuals associated to the Tune-P dimuon mass and constrained vertex mass relative to the respective masses themselves [Adapted from 102]. As opposed to the determination of constrained vertex mass, the Tune-P dimuon mass is determined without a common vertex constraint. The spread is shown in (a) as the standard deviation of a Gaussian fit to the relative dimuon mass residuals as a function of vertex χ^2/dof and in (b) as the root mean square of the relative dimuon mass residuals for events that are rejected by this ratio.

to the mass given by the two reconstructed Tune-P tracks. For events rejected by this requirement, allowing for a more stable statistical evaluation, the root mean squared (RMS) of the relative mass residuals is shown in figure 8.2b. One can see that the chosen threshold of χ^2/dof < 20 is well motivated as the RMS shows little difference between the two approaches beyond that value. Given the observed performance of the fit and in order to be consistent with the expected signal signature, the constrained common vertex mass is used for final dimuon invariant mass distributions.

8.3 Higher Order Contributions to Cross Sections

Recent calculations of the DY and ADD process cross sections have yielded higher order predictions (compared to the utilized event generators) as a function of the interaction scale. By applying the results of these studies as correction factors, also referred to as "K factors", their predicted behavior can be approximated.

Drell–Yan Process

For the DY process, the study includes orders up to NNLO in QCD as well as NLO in EW [135] and is based on FEWZ 3.1b2. The calculations have been performed following the G_μ scheme where the input parameters are given by the W and Z boson mass, the fermion masses, and the eponymous Fermi constant G_μ as measured in muon decays. For the strong coupling constant, the reference value of $\alpha_s(M_Z) = 0.118$ with respect to the Z boson mass M_Z is used. Expanding upon earlier studies [136], photon-induced or photon-initiated processes are also taken into account. By using LUXqed_plus_PDF4LHC15 [137] as the PDF Set, the corresponding photonic contributions are included in the recommended PDF set for the evaluation of Run 2 data referred to as PDF4LHC15 [138]; the latter averages the NNPDF 3.0, CT14 [139] and MMHT14 [140] PDF sets.

Significant negative corrections for large invariant dilepton masses are observed (see Fig. 8.3), which are consistent with the results of past studies concerning NLO EW contributions [e.g. 141]. They are mostly given by "Sudakov logarithms" of the

form $\alpha_V^2 \ln^2\left(\hat{s}/M_V^2\right)$. In this expression, V represents the W and Z boson, the respective masses are denoted by M_V and α_V stands for $\alpha_W = \alpha_{\text{em}}/\sin^2\theta_W$ and $\alpha_Z = \alpha_W/\cos^2\theta_W$ with the electromagnetic coupling parameter α_{em} and weak mixing angle θ_W. While not large enough to compensate the negative EW corrections, contributions by terms introduced by NNLO QCD corrections and photon-initiated processes are positive. Dependencies on the choice of the PDF set, the associated uncertainties and the uncertainties corresponding to the strong coupling constant as well as the factorization and renormalization scale have been evaluated as part of the study. At NNLO in QCD, the impact of the latter three has proven to be small compared to variations both within the PDF uncertainties and between different sets.

For the given simulation of the DY process produced with Powheg Box V2 and NNPDF 3.0, a mass dependent K factor based on the studies performed with Fewz 3.1b2 and LUXqed_plus_PDF4LHC15 is utilized. It has been calculated within the defined acceptance (Sec. 7.2) and the aforementioned pseudorapidity categories. The resulting evolution with respect to the invariant mass is shown in figure 8.3. Alongside the results for the transverse momentum threshold of 53 GeV, corresponding ones are shown for a threshold of 30 GeV. The latter ones are used for the normalization of the simulation to the measured data, which is discussed in section 8.4. A similar behavior is observed for both scenarios including the aforementioned decline toward high masses due to NLO EW corrections. An exception to this agreement can be seen in the low-mass region where only Z bosons with large Lorentz boosts can satisfy the higher transverse momentum requirement. The ratios are parametrized using a fourth-order polynomial, which allows for an individual application per muon pair. Labeled according to the pseudorapidity categories, these parametrizations for muons within the acceptance are given by

$$K_{BB} = 1.036 - 1.441 \times 10^{-4} M + 5.068 \times 10^{-8} M^2 - 7.581 \times 10^{-12} M^3, \tag{8.3}$$

for events with both muons in the barrel region and

$$K_{BE} = 1.052 - 1.471 \times 10^{-4} M + 5.903 \times 10^{-8} M^2 - 9.037 \times 10^{-12} M^3, \tag{8.4}$$

for the category where at least one is located in the endcaps. Here, the variable M is directly related to the dimuon mass via $M = m_{\mu\mu}\,/\,\text{GeV} - 400$ and allows for an extrapolation up to $m_{\mu\mu} < 5500\,\text{GeV}$. For dimuon objects with masses beyond this threshold—their overall contributions being small because of the steeply falling spectra—the value at $m_{\mu\mu} = 5500\,\text{GeV}$ is used. Corresponding parametrizations for muon transverse momenta larger than 30 GeV, determined for the Z boson mass peak region, read

$$K_{BB}^{p_T > 30\,\text{GeV}} = 1.003 - 2.904 \times 10^{-4} M + 3.281 \times 10^{-6} M^2 - 5.258 \times 10^{-9} M^3, \tag{8.5}$$

for the barrel-barrel category and

$$K_{BE}^{p_T > 30\,\text{GeV}} = 1.012 - 1.607 \times 10^{-3} M + 8.796 \times 10^{-7} M^2 - 1.401 \times 10^{-6} M^3. \tag{8.6}$$

for barrel-endcap events. Their variable is defined as $M = m_{\mu\mu}\,/\,\text{GeV} - 130$. In conclusion, per-event application of the former two functions allows for an approximate description of the DY dimuon invariant mass spectrum up to NNLO in QCD and NLO in EW, including contributions by photon-initiated processes. Given the importance of the DY background and the focus on high invariant masses, taking the large and overall negative corrections into account is essential for an accurate probabilistic evaluation. The latter two functions are applied analogously but are only used to account for the

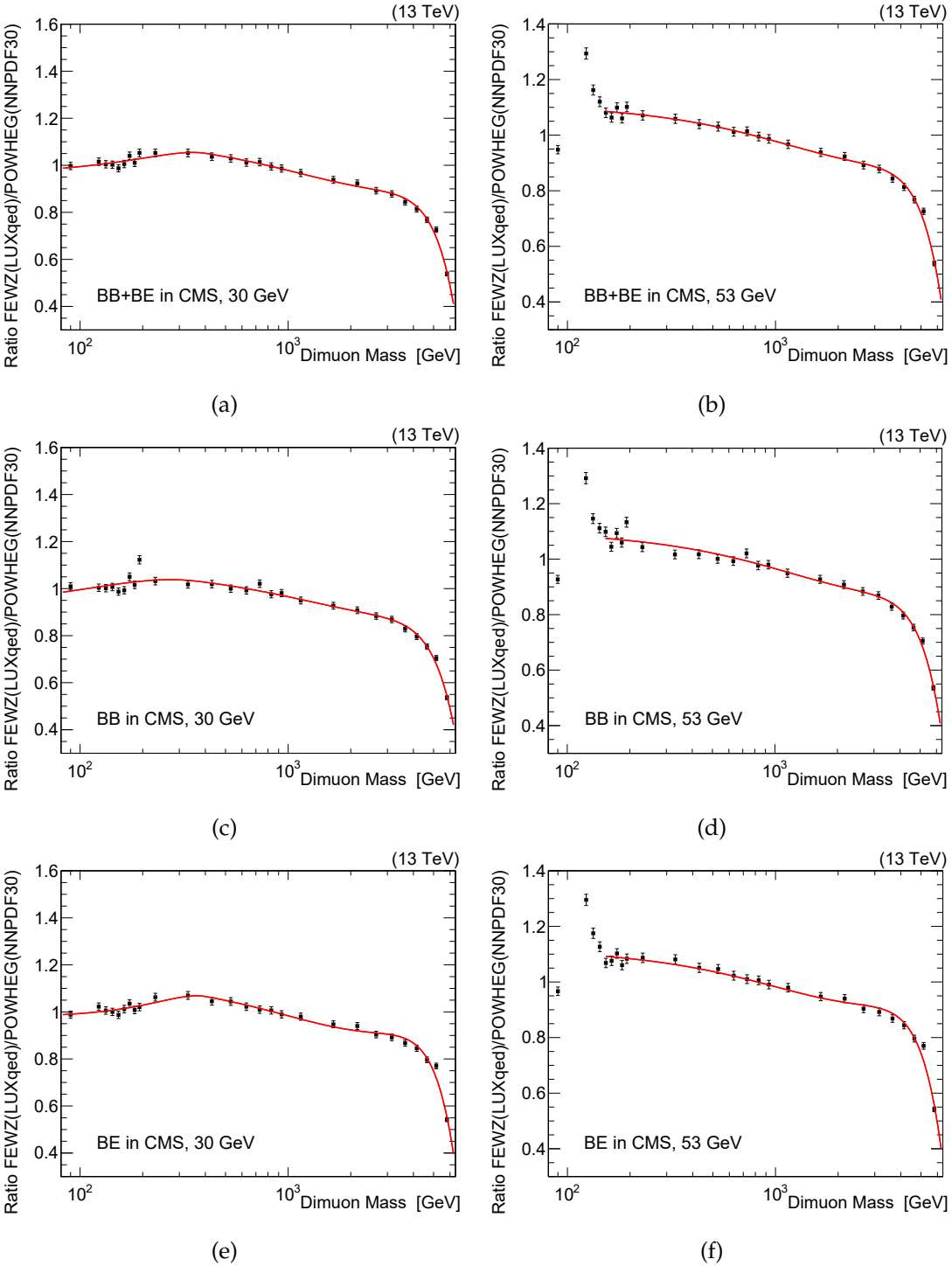

FIGURE 8.3: Correction factors for the approximation of the behavior of the Drell–Yan process up to NNLO in QCD and NLO in EW calculations [Adapted from 102, 135]. On the left for muons with transverse momenta larger than 30 GeV and on the right for the 53 GeV equivalent. Contributions by photon-initiated processes are also included in these correction factors. Red lines indicate the general mass-dependence of the correction factors.

corrections when deriving the overall normalization (Sec. 8.4).

Virtual Graviton Exchange

An initial study of the virtual exchange of gravitons in the dilepton channel up to NLO in QCD [142] has shown a significant increase of the differential cross section by factors of about 1.6 with respect to the LO prediction. Complementary studies have evaluated the impact of those corrections with respect to angular distributions [143] and the dependence on the choice and uncertainties of PDF sets [144]. Expanding upon these results, a similar behavior is observed for calculations up to NNLO in QCD [145]. This is shown in figure 8.4a for different values of the HLZ ultraviolet cutoff parameter M_S and for a varying number of extra dimensions n in figure 8.4b. For these two distributions (and as its general baseline), the study employs the respective LO, NLO and NNLO PDFs of the MSTW2008 set and the corresponding values of α_s. A total of $n_f = 5$ quark flavors are considered; the fine structure constant and weak mixing angle are set to $\alpha(M_Z) = 1/128$ and $\sin^2\theta_W = 0.227$, respectively. The same authors have also kindly provided the distribution shown in figure 8.4c as an extension of their study. Here, the K factor is shown for larger invariant masses and $M_S = 7\,\text{TeV}$ using the NNPDF 3.0 PDF set. All distributions display a behavior consistent with the predictions of the NLO QCD calculations, with figure 8.4c representing the simulated signals and their region of phase space most closely.

Following the discussion of the DY correction factor, NLO EW contributions are expected to reduce the differential cross section toward high invariant masses. However, given the additional gluon fusion production channel $gg \to G^* \to \mu\mu$, their overall impact is expected to be diminished. With respect to this expected reduction of the correction factor and to allow for a direct comparison with the current results of the CMS Collaboration [73], a mass-independent K factor of 1.3 is used for the produced ADD model signals. The distributions have shown that this value constitutes a conservative choice as it is safely exceeded for all numbers of extra dimensions given sufficiently large interaction scales.

8.4 Z Boson Mass Peak Normalization

The individual simulated samples shown in the presented distributions have been normalized by weighting them according to

$$f = w\frac{\sigma\mathcal{L}}{N}, \tag{8.7}$$

where σ, N and w denote the predicted total cross section, number of generated events and additional weight corresponding to the process, respectively. While these three quantities determine the relative importance of the contribution by a given process, the overall normalization which allows for a comparison to the measured data is governed by the integrated luminosity $\mathcal{L}$. An alternative method of deriving this normalization is the evaluation of measured data and simulated backgrounds in a well understood region of phase space. A prime candidate for this phase space in the presented analysis is a narrow invariant mass region centered around the Z boson mass peak at $(91.1876 \pm 0.0021)\,\text{GeV}$ [64]. Providing the probabilistic interpretation at large invariant masses with respect to the ratio of measurement to simulation in this mass region eliminates many dependencies at their lowest order and leaves only residual, mass-dependent

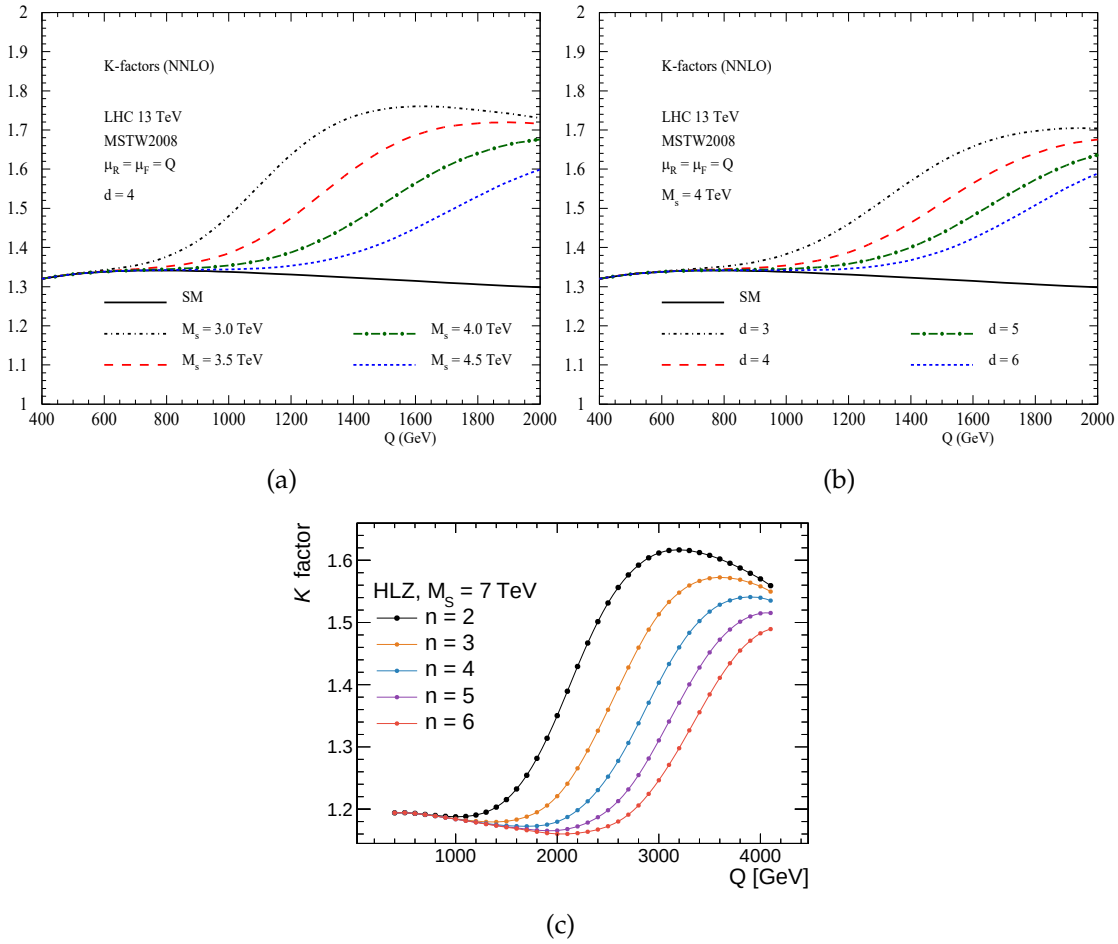

FIGURE 8.4: Correction factors for the approximation of virtual graviton exchange processes producing lepton pairs at NNLO in QCD. In (a) and (b) for varying values of the HLZ convention parameters M_S and n, respectively [145]. Figure (c) shows the NNLO correction factor for a larger value of M_S utilizing the NNPDF 3.0 PDF set [146].

terms to be accounted for. This applies to all differences between the measured and simulated efficiencies of the acceptance, trigger, reconstruction and selection requirements. Given the overlap of the data-taking period and commissioning of the new L1 trigger system, corresponding to measurements with varying trigger conditions (Sec. 6.1), this approach offers a more robust way to normalize.

As mentioned in section 8.3, dimuon objects produced at the Z boson mass peak require Lorentz boosts to satisfy the trigger transverse momentum threshold of 50 GeV. To avoid introducing a bias with respect to these kinematic properties when measuring the ratio, a secondary set of single-muon triggers is utilized. Otherwise analogously configured to HLT_Mu50 and HLT_TkMu50, HLT_Mu27 and HLT_TkMu27 lower the transverse momentum threshold for muons to 27 GeV, which is raised to 30 GeV in order to avoid the "turn-on" of the efficiency curve (Fig. 6.1). To be able to offer such low thresholds, the rate at which events are recorded has to be reduced via prescaling (see Sec. 6.1). The event yield at the Z boson mass peak is nonetheless roughly two orders of magnitude larger than the one obtained when requiring transverse momenta larger than 50 GeV [102]. Table 8.5 shows the ratios of measurement to background simulation in a 60 GeV window around the mass peak for subsets of integrated luminosities

corresponding to fixed prescale factors. With respect to the total integrated luminosity of $36.3\,\mathrm{fb}^{-1}$, one observes the measured data to be in agreement with the simulation up to 3.6 % on average. This value is used to correct the overall normalization of the simulated background.

			Ratio for respective category / %		
Period	Prescaling	$\mathcal{L}$ / pb^{-1}	BB	BE	BB + BE
1	14	11	94.8 ± 7.6	96.4 ± 6.5	95.7 ± 4.9
2	35	59	99.3 ± 5.2	107.1 ± 4.6	103.8 ± 3.4
3	40	48	94.9 ± 6.0	95.1 ± 5.1	95.0 ± 3.9
4	70	1455	96.4 ± 1.5	98.1 ± 1.3	97.4 ± 1.0
5	100	7065	98.1 ± 0.8	98.2 ± 0.7	98.1 ± 0.5
6	120	479	100.0 ± 3.4	98.2 ± 2.9	98.9 ± 2.2
7	140	4516	98.5 ± 1.2	98.8 ± 1.0	98.6 ± 0.8
8	150	4828	93.7 ± 1.2	94.8 ± 1.0	94.3 ± 0.8
9	160	2738	99.3 ± 1.6	98.1 ± 1.4	98.6 ± 1.1
10	170	3081	94.7 ± 1.6	89.9 ± 1.3	91.9 ± 1.0
11	180	518	102.1 ± 4.1	98.7 ± 3.4	100.0 ± 2.6
12	200	3719	94.1 ± 1.5	92.8 ± 1.3	93.3 ± 1.0
13	230	3299	97.0 ± 1.8	93.4 ± 1.5	94.8 ± 1.1
14	250	1010	97.9 ± 3.4	93.2 ± 2.8	95.1 ± 2.1
15	260	2345	98.6 ± 2.2	91.7 ± 1.8	94.5 ± 1.4
16	290	1828	95.6 ± 2.6	94.5 ± 2.2	94.8 ± 1.7
17	320	196	91.5 ± 8.3	95.8 ± 7.2	93.9 ± 5.4
Average		36 295	96.88 ± 0.42	96.10 ± 0.35	96.38 ± 0.20

TABLE 8.5: Ratios of measured to simulated data corresponding to different periods of static prescale factors based on the combination of HLT_Mu27 and HLT_TkMu27 [Adapted from 102]. The comparison is given with respect to the total integrated luminosity of $36.3\,\mathrm{fb}^{-1}$.

Chapter 9

Systematic Uncertainties

A key component to a meaningful interpretation of the measurement with respect to its simulation is the evaluation of all relevant systematic uncertainties. As mentioned before, the properties of a muon are determined via the reconstruction of its trajectory. The quantification of potential biases, inefficiencies and spatial resolutions alongside the respective systematic uncertainties is therefore also specific to a given type of track. Consequently, propagating these quantities to the adjusted trajectories from which the invariant mass of the common vertex is derived is nontrivial. To allow for a consistent treatment and avoid potential correlations introduced by the fit, all mass-dependent uncertainties are evaluated using the invariant mass of the selected muon pair. As the background is normalized using the ratio of measured to simulated events in a window around the Z boson mass peak (Sec. 8.4), dependencies of this ratio on the uncertainties are accounted for at the lowest order. The impacts of mass-dependent uncertainties are therefore evaluated after accounting for the relative difference they cause in the normalization.

9.1 Global Uncertainties

This section summarizes general uncertainties whose evaluation is identical for all simulated processes but are unrelated to the reconstruction of muons.

Starting with the generation of events, a major source of uncertainty is given by the extrapolation of the PDFs (Sec. 2.3) into unexplored regions of phase space. In the presented analysis, this corresponds to the high-energy regime where large invariant masses are produced in rare interactions where both partons carry a large fraction x_i of the proton momenta. The utilized sets of PDFs have been determined using an MC method which yields one central value of the PDFs as well as multiple variations corresponding to MC replica of the data. While the considered processes have been simulated with the former, representing the best estimate of the set, the other members characterize the uncertainty in the determination of the PDFs. Following the recommended procedure to evaluate the impact of PDF uncertainties [138], each event has to be reevaluated with respect to the weights predicted by these other members. Based on the properties of the colliding partons $f_{a/A}$, their fraction of the proton momentum x_i and the overall exchanged momentum Q^2, the weight which corresponds to a given member can be calculated using LHAPDF 6. By rescaling all events according to these weights, one obtains a set of mass spectra characterizing the dependence on the PDFs. A bin-by-bin evaluation of the respective 68 % confidence interval yields a mass-dependent estimate for the impact of the PDF uncertainty. As a function of the differential cross section, its computation can be expressed as

$$\delta\sigma = \frac{\sigma^{(84)} - \sigma^{(16)}}{2} \tag{9.1}$$

using the 16 and 84 % quantiles $\sigma^{(i)}$. For the sum of all background processes, the impact of this uncertainty on the total event yield ranges from less than 1 % at low masses to 20 % beyond invariant masses of 4 TeV. It should be noted that large differences, roughly factors of 5, between the impacts for individual processes are possible. The uncertainty is particularly large for processes generated at LO and those with substantial contributions by gluon-gluon fusion. While this would also apply to the produced signal samples, only the experimental impact, i.e., the one on the acceptance is taken into account for them.

As described in section 6.4, the correction of the simulated pileup scenario depends on the measured minimum-bias cross section of 69.2 mb. Variations within the corresponding uncertainty in this measurement of 5 % [122] affect the pileup distribution as shown in figure 6.7b. Performing the analysis with the two shifted distribution allows for evaluating the impact of this uncertainty on the event yield. With differences smaller than 1 %, one can conclude that the measurement of high-p_{T} muons is mostly insensitive to given pileup scenario and the corresponding uncertainty.

The efficiency of triggering events using individual muons has been measured to be above 90 % as shown in figure 7.2. By simulating the trigger performance using a random number generator, this result has been translated to a combinatorial efficiency for events containing two muons of more than 99 % (Fig. 6.1). When comparing the efficiencies determined in the respective measured and simulated data sets, both shown in figure 9.1, one observes a similar trigger performance with a slighty higher efficiency in the simulated data set. This behavior has been cross-checked with corresponding studies conducted as part of the search for high-mass resonances in lepton and missing transverse momentum final states [147]. As only minor differences between the two distributions are observed, no correction is applied. This difference is instead accounted for as a mass-independent uncertainty of 0.3 % and 0.7 % on the event yield in the respective BB and BE category. For the combination of the two categories, this uncertainty averages to 0.4 %.

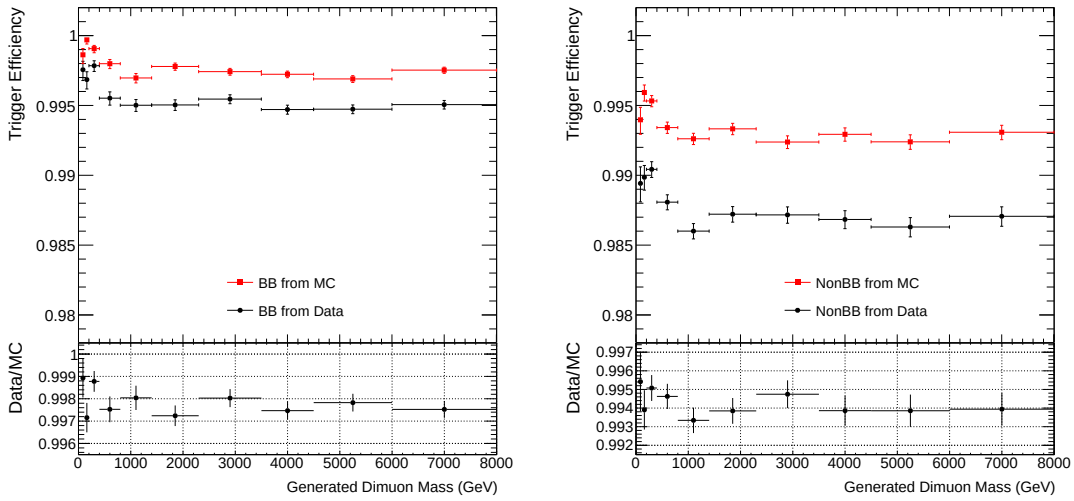

(a) (b)

FIGURE 9.1: Combined efficiency of HLT_Mu50 and HLT_TkMu50 as a function of the dimuon invariant mass for measured and simulated data sets [102]. In (a) for the BB category and in (b) for the BE category. The respective trigger efficiencies have been determined for individual muons and are combined by simulating the trigger performance for events with two muons. The resulting statistical uncertainty for each data point is also shown.

While dedicated, mass-binned, simulated data sets can be used to ensure that a sufficient amount of events is available toward large invariant masses, the necessary samples are not available for all considered processes (Tab. 6.2). As the generation of events follows the probability distribution given by the differential cross section, the description at high interaction scales is therefore sometimes given by individual events. Their assigned weight becomes disproportionally large as dictated by the normalization described in equation (8.7). The corollary to this statistically inadequate description are large Poissonian uncertainties. Evaluated in sufficiently wide bins, the relative impact of this uncertainty generally amounts to 1 % or less for the dominant DY process. For the other simulated processes, it can reach values of about 10 % in the same mass ranges.

9.2 Muon Reconstruction Uncertainties

As discussed in section 4.3, the reconstruction of muon tracks depends on the relative alignment of the detector components. An inaccurate modeling of this alignment may result in biases in the curvature of the measured muon tracks. At the lowest order, this can be expressed as a constant term added to the charge over momentum ratio

$$\frac{q}{p'_{\mathrm{T}}} \to \frac{q}{p_{\mathrm{T}}} + \kappa_b. \tag{9.2}$$

Measuring κ_b as a function of the pseudorapidity and polar angle of the muon allows for quantifying the bias in a given detector region. While the evaluation of this bias has been solely based on cosmic muons using the custom-developed "endpoint" method [85, 132] at $\sqrt{s} = 8\,\mathrm{TeV}$, these muons pass primarily through the barrel region of the detector and therefore do not allow for an accurate measurement in the endcaps. A generalized version of this method is applied to prompt muon pairs of the full 2016 data set collected via single-muon triggers [14]. As part of this method, a curvature bias κ_b is injected additively on top of an unbiased geometry for the simulated reconstruction of muons with a transverse momentum larger than 200 GeV. Using a χ^2 minimization, its value is optimized for the best possible agreement between measured and simulated data in the charge over transverse momentum ratio.

Figure 9.2a shows this ratio for the barrel region of the detector $|\eta| < 1.2$ with the corresponding χ^2 distribution given in figure 9.2b. Integrated over the polar angle, one observes a value of κ_b compatible with 0 and therefore no bias. This observation holds true when splitting the barrel region into three ϕ components as shown in figure 9.3. However, significant differences are observed in the endcaps. At the time of writing, this is assumed to be the result of a "weak mode" affecting the alignment of the tracker endcaps (TEC). Weak modes refer to systematic shifts of detector modules, e.g., rotations or deformations, which have little impact on the χ^2 test statistic of the track reconstruction and are thus difficult to eliminate. The aforementioned weak mode affecting the TEC is planned to be addressed in a reprocessing campaign preparing the data recorded in 2016 for analyses of the complete set of measurements at a center-of-mass energy of 13 TeV [149].

In order to determine the values of κ_b in the endcaps with a sufficient amount of muons, the aforementioned transverse momentum threshold of 200 GeV has been lowered to 110 GeV for $|\eta| > 2.1$. Given the diminishing number of muons with high transverse momenta—in particular toward larger pseudorapidities—a reliable estimate of κ_b for high interaction scales is not possible. As a consequence, no correction for the measured biases in the muon momentum scale is applied and their impact on the dimuon invariant mass spectrum is instead evaluated as a systematic uncertainty. For

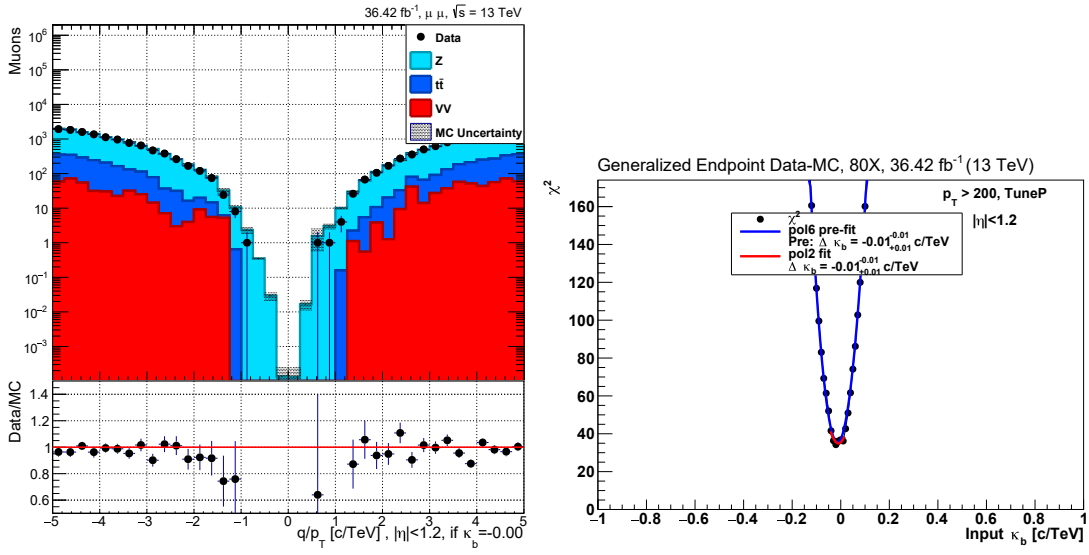

(a) (b)

FIGURE 9.2: Charge over transverse momentum ratio for $\kappa_b = 0$ in (a) and curvature bias minimization for muons in the barrel region in (b) [Adapted from 148].

this evaluation, with respect to equation (9.2), a bias is introduced into the transverse momentum estimate for each muon of the pair based on its (η, ϕ) coordinates and charge. Since the measurements in the barrel region are compatible with a vanishing bias, the respective central values and uncertainties are taken to be $\kappa_b = 0$ and $\sigma_{\kappa_b} = 0.025$. For the application per muon, each bias is then modeled using a Gaussian distribution with the mean given by κ_b and the standard deviation by σ_{κ_b}. As the majority of the observed decays result in each muon carrying roughly half the momentum and their charges are explicitly required to be of opposite sign, the introduced biases often compensate each other. The overall impact on the event yields of the dimuon invariant mass spectrum amounts to variations of 1 to 4 %.

Complementary studies of the uncertainty in the muon transverse momentum resolution have been performed using boosted Z bosons [102]. Splitting the simulated and measured spectra into multiple regions of muon transverse momenta ranging from 72 to 800 GeV, the width of the Z boson mass peak is fitted using a Gaussian function with exponential tails. For the BB category, the standard deviation of this combined function can be seen in figure 9.4a. Toward high transverse momenta, a slightly better resolution is observed for the simulation when compared against the measurement. The same trend, although slightly worse, is also observed for the BE category. With the simulated detector resolution determined by comparing the residuals of the generated and reconstructed mass, it is possible to approximate the resolution of the measurement by introducing an additional Gaussian smearing of 5–10 % as well as 10–20 % to the simulation in the BB and BE category, respectively. If introduced to generated DY events using the respective conservative values, this smearing results in the dimuon invariant mass resolution shown in figure 9.4b. However, as a nonresonant signal is generally insensitive to small variations of the momentum resolution, this correction is not applied and its impact is only evaluated as a systematic uncertainty. Following the recommended procedure, the evaluation differentiates between the barrel and endcap regions as well as three energy regimes. In each event, the transverse momenta of both selected muons are smeared individually according to the pseudorapidity and transverse momentum of the respective muon using a Gaussian distributed random variable whose standard

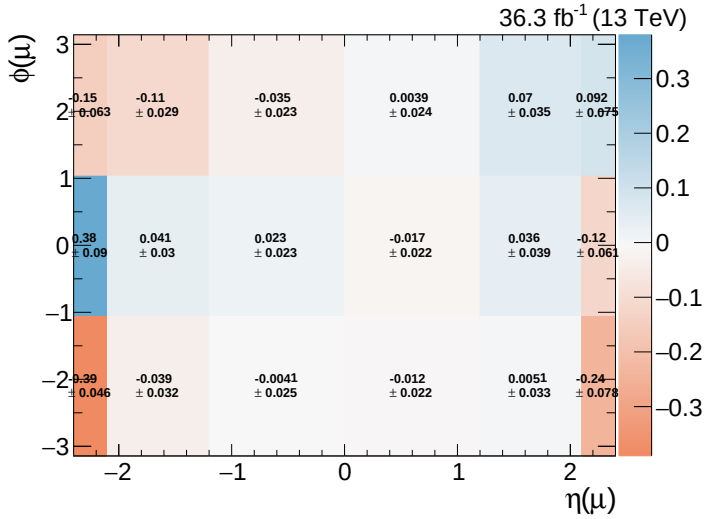

FIGURE 9.3: Muon transverse momentum scale bias κ_b per TeV in p_T as a function of η and ϕ [150]. With the exception of the forward region, the values are determined for muon transverse momenta larger than 200 GeV. In order to include a sufficient amount of muons in the region where $|\eta| > 2.1$, the momentum threshold is lowered to $p_T > 110$ GeV.

deviation is given by the percentages listed in table 9.1. This corresponds to variations of the event yields in the dimuon invariant mass spectrum of roughly 1 %.

	Transverse Momentum Range		
Detector Region	<200 GeV	200–500 GeV	>500 GeV
Barrel	0.3 %	0.5 %	1 %
Endcaps	0.6 %	1.0 %	2 %

TABLE 9.1: Uncertainty in the muon transverse momentum resolution for the barrel and endcap regions in three respective ranges of transverse momenta [150].

To evaluate the performance of the reconstruction and selection of muons with high momenta, a dedicated study utilizing the "tag-and-probe" method has been conducted [102]. As the probability to induce electromagnetic showers for a muon passing through the detector material primarily depends on its momentum p, the study is performed with respect to this quantity. The corresponding selection focuses on the rejection of events not produced via the DY process while avoiding kinematic requirements that bias the sample or heavily reduce the total amount of events.

In the iteration over all events, a muon which causes the trigger to fire "tags" the event for further investigation. This muon is also required to satisfy the selection requirements discussed in sections 7.3 and 7.4[1]. Additional muons that are part of the event are then used to "probe" the performance of the reconstruction and selection. To ensure that this evaluation is based on well reconstructed muons, their inner tracks need to satisfy a stringent set of criteria (Tab. 9.2). In addition to all aforementioned requirements, the inner tracks of both the "tag" and "probe" muon have to be well isolated. Following the definition of the relative track isolation parameter given in section 7.4, the scalar sum of momenta associated to all tracks surrounding the muon within a cone of radius

[1]A more stringent requirement for the relative track isolation will be discussed and applied, which supersedes the one introduced in Sec. 7.4.

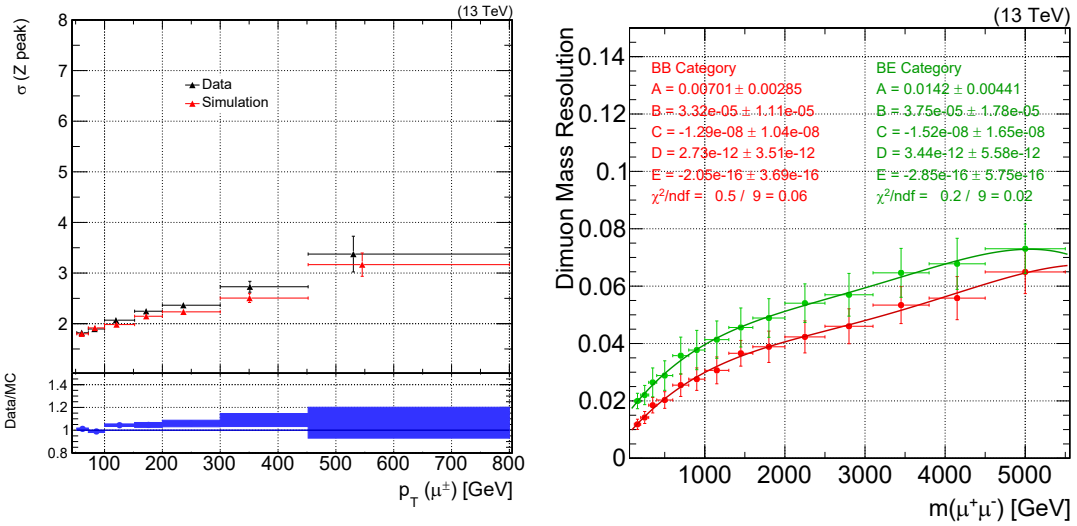

(a) (b)

FIGURE 9.4: Resolutions of the dimuon invariant mass measurement [Adapted from 102]. The Gaussian width of the mass peak for boosted Z bosons as a function of the muon transverse momentum for measured and simulated data in (a). In (b), the mass resolution for simulated DY events, which, for this distribution, has been smeared to match the measured resolution. The red and green data points and parametrizations represent the BB and BE category, respectively.

$R = 0.3$ is calculated. It is required to be smaller than 5 % of the muon momentum. The corresponding absolute value of the isolation parameter must also be below 15 GeV and the relative uncertainty in the transverse momentum estimate by the inner track has to be less than 50 %. Pairs of muons that meet these criteria are further required to be spatially separated by at least $\Delta R > 0.6$ but must not have an opening angle larger than $\pi - 0.02$. The latter would be indicative of a cosmic muon passing through the detector. To ensure that the muons are compatible with a common vertex of origin, the $\chi^2/\text{dof} < 20$ criterion is applied alongside a $|d_z(\text{tag}) - d_z(\text{probe})| < 0.05\,\text{cm}$ requirement. Should more than one pair of muons remain, the pair with the smallest χ^2/dof is chosen.

The "probe" muons are then used to quantify the efficiencies of subsequent reconstruction and selection steps factorized as

$$\epsilon = \epsilon_{\text{Standalone}} \times \epsilon_{\text{Global}} \times \epsilon_{\text{Muon Selection}}. \tag{9.3}$$

Each efficiency is defined as the fraction of these muons fulfilling the given requirements with respect to those which satisfy the preceding ones. With the baseline defined in the previous paragraph, the first efficiency is calculated as the fraction of "probe" muons which are also reconstructed as standalone muons. Subsequent efficiencies refer to the respective fraction of muons with a valid global muon track and those which meet the selection criteria corresponding to measurements in the muon system discussed in section 7.4. The resulting distributions are shown in figure 9.5 for both the barrel and overlap ($|\eta| < 1.6$) as well as endcap regions ($1.6 < |\eta| < 2.4$) of the detector. As a function of the muon momentum, a decline of the efficiency toward larger values is observed in both regions with the distributions associated to the endcaps exhibiting the steeper slope. The study has determined that the source of this decline is primarily given by the failing standalone track reconstruction for the selected "probe" muons. Considering that the amount of data toward large momenta is insufficient for a statistically reliable prediction, the given inefficiencies are only taken into account as a

systematic uncertainty in the following two ways.

While the goal is to account for the difference between measurement and simulation, only muons with momenta of up to 1 TeV have been observed in the barrel and overlap region. Within its uncertainty, the slope of the corresponding linear fit is also compatible with 0. As a consequence, instead of the ratio between the parametrizations of measured and simulated data, only the one of the simulation is used in this region. In contrast, measurements of muons are available up to momenta of 3.6 TeV in the endcaps, which allows for the utilization of the aforementioned ratio as it provides a meaningful quantification of the difference between measurement and simulation. The two discussed parametrizations for the respective regions are shown in the second row of figure 9.5. To only take the residual mass-dependency of the inefficiency into account, each function is applied with respect to a reference value of the muon momentum. These values are given by $p(\mu) = 100\,\text{GeV}$ for the $|\eta| < 1.6$ region and $p(\mu) = 200\,\text{GeV}$ for $1.6 < |\eta| < 2.4$. Adjusting the event weights based on these parametrizations for each of the two simulated muons according to their momenta results in variations of the predicted event yields between less than 1 % to more than 5 %.

Quantity	Requirement
Transverse momentum p_T	>50 GeV
Pseudorapidity $\lvert\eta\rvert$	<2.4
Tracker Layers with Measurements	>5
Lost Hits	0
Transverse Impact Parameter d_{xy}	<0.2 cm
Longitudinal Impact Parameter d_z	<0.5 cm

TABLE 9.2: Criteria which the "probe" muon has to satisfy [102]. All quantities refer to the properties of the inner track.

9.3 Process Specific Uncertainties

As all signals are normalized using the total integrated luminosity determined via the pixel cluster counting (PCC) method (Sec. 6.1), the precision of the measurement of 2.5 % [104] is also assigned as the accompanying mass-independent uncertainty in the signal event yields. The normalization of the background is derived from the ratio of measured to simulated events within a window around the Z boson mass peak (Sec. 8.3), which also determines the associated uncertainty. Averaged over the entire data-taking period, this ratio has been determined to be 96.38 % with a statistical uncertainty of only 0.20 %. However, the observed fluctuations for different prescale factors are significantly larger as shown in table 8.5. To take both the frequent changes of the prescale factor as well as the varying trigger system conditions into account, a flat uncertainty of 5 % is assigned to the background normalization [131]. This value is motivated by the largest observed variations of the ratio. While it also exceeds the uncertainty corresponding to the PCC measurement, one still benefits from the elimination of uncertainties at their lowest order.

For the sum of all simulated background processes, excluding the DY interaction, an uncertainty of 7 % on the cross sections [131] is assigned. This value accounts for uncertainties originating from theory calculations, the choice of the renormalization and factorization scales as well as the dependency on the strong coupling constant. The cross section of the DY process has been determined to a high degree of precision with

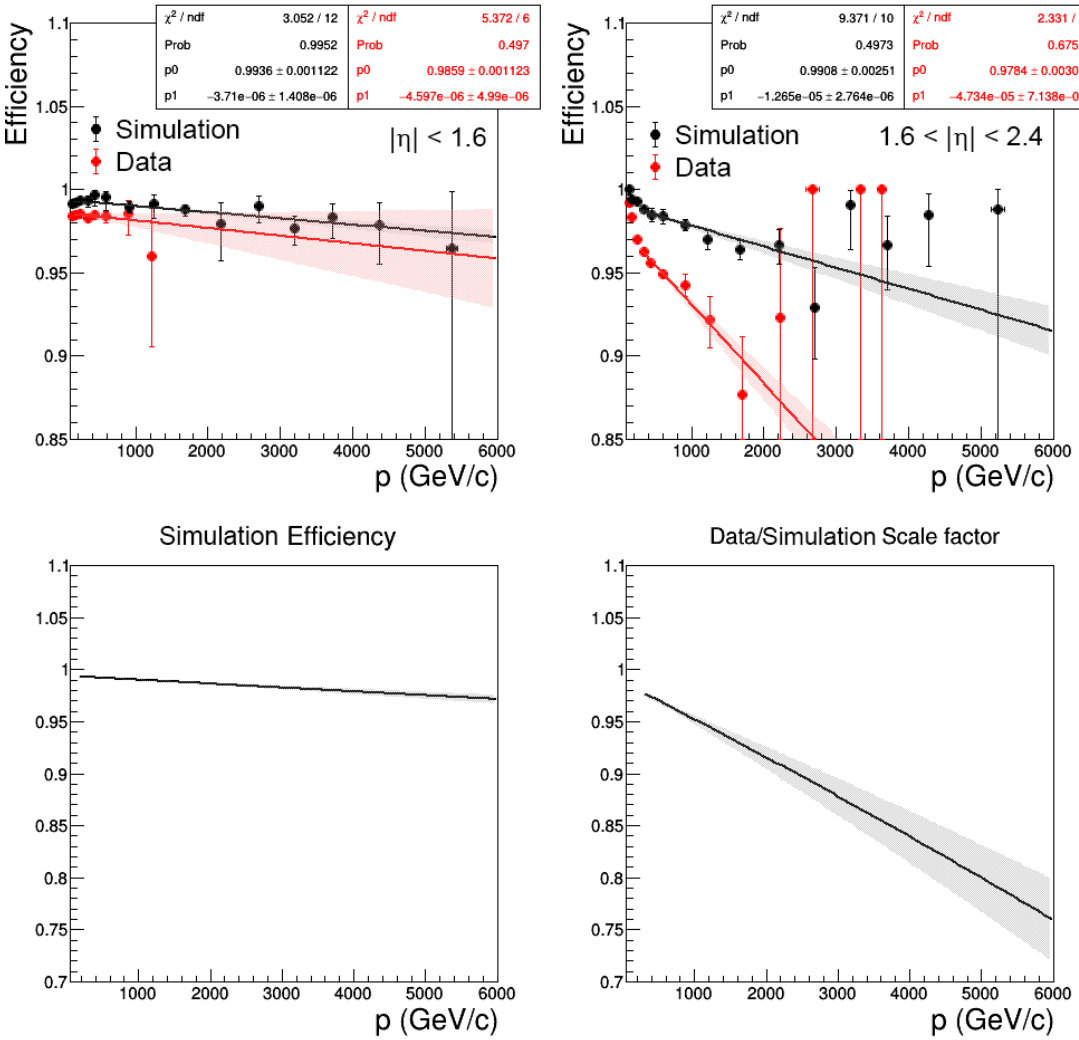

FIGURE 9.5: Efficiency of the reconstruction and selection of muons with high momenta for two pseudorapidity regions [Adapted from 102]. In the top row, simulated and measured muons are compared as a function of their momentum. Intercept and slope of the linear parametrizations are represented by $p0$ and $p1$ in the legend. The bottom row shows the (ratios of) parametrizations which are used for the estimation of the systematic uncertainty.

an approximation of the behavior up to NNLO in QCD and NLO in EW, including contributions by photon-initiated processes. As mentioned in the discussion of the correction factor with which this approximation has been achieved (Sec. 8.3), the impact of other sources of uncertainty in the calculation of the cross section is small compared to the dependence on the PDFs. Therefore, with the uncertainty corresponding to the determination of the PDFs already for (Sec. 9.1), no additional uncertainties are assigned to the DY cross section.

While most of the discussed uncertainties also apply to the simulated processes used in the estimation of the jet-based background, the dominant one is still given by the dependence on jet kinematics. As discussed in section 8.1 and shown in tables 8.3 and 8.4, this dependence can result in variations of 30 to 50 %. Taking the conservative value of 50 % as the total uncertainty in the predicted event yields of the jet-based backgrounds ensures that this dependency on jet kinematics inherent to the data-driven

method is accounted for.

9.4 Relative Impact of Uncertainties

With all considered sources of uncertainty summarized, their relative importance as a function of the dimuon invariant mass can be discussed. By definition, the impacts of all mass-independent uncertainties on the event yields are fixed while the ones of mass-dependent uncertainties evolve with respect to the aforementioned observable. This evolution is shown in figure 9.6 for both the dominant SM background and the sum of all subdominant backgrounds as well as one simulated signal.

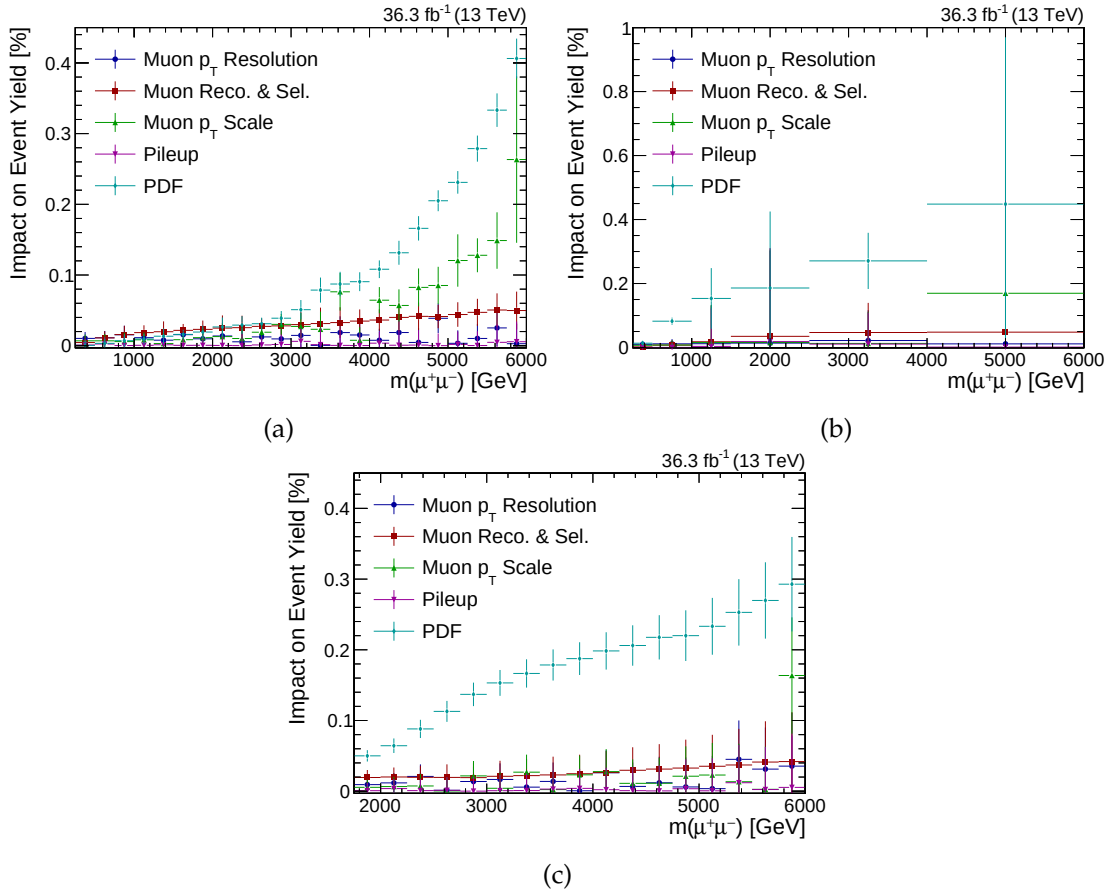

FIGURE 9.6: Impact of the mass-dependent uncertainties as a function of the dimuon invariant mass. In (a) and (b) for the Drell–Yan background and the sum of all other simulated backgrounds, respectively. Subfigure (c) shows the impact for an ADD model signal with $\Lambda_T = 6\,\text{TeV}$ in the phase space above its production threshold of $m_{\mu\mu} > 1.7\,\text{TeV}$.

For the DY process, the largest mass-independent uncertainty is given by the Z boson mass peak normalization with an impact of 5 %. As shown in figure 9.6a, the total impact of all mass-dependent ones becomes comparable to this value toward masses of 2 TeV. While an additional cross section uncertainty of 7 % has to be taken into account for the remainder of all simulated background processes, the increased PDF uncertainty already results in comparable impacts for both uncertainty types at around 1 TeV. Using the simulated signal with $\Lambda_T = 6\,\text{TeV}$ as an example, figure 9.6c shows the dominance of the PDF uncertainty if calculated identically to the other processes. However, as mentioned before, only the impact of this uncertainty on the acceptance is taken into

account which generally amounts to less than 1 %. As a result, the 2.5 % uncertainty associated to the normalization of the signals remains relevant for a large part of the mass spectrum. A numerical overview of the composition of the total uncertainty for two mass regions is given in the following chapter in table 10.1.

Chapter 10

Results

Both the properties of the two selected muons and those of the corresponding dimuon object are presented in this chapter. The invariant mass distribution of the latter constitutes the primary result and is used for the statistical analysis detailed in chapter 11.

10.1 Kinematic Distributions

The kinematic distributions of the individual muons after applying all event selection criteria and corrections to the simulated processes are shown in figure 10.1. As the data-driven jet background has been determined as a function of the invariant mass, the W + jets and QCD processes are not replaced in these distributions. Quantities of the leading muon with respect to the transverse momentum are displayed on the left and those associated to the subleading one on the right. The distributions of the transverse momentum itself are displayed in the top row while the bottom row shows the corresponding pseudorapidity spectra. For the latter, only events with dimuon invariant mass larger than 1 TeV are included as the spectra would otherwise be dominated by low-energy contributions. In order to allow for a straightforward visual comparison, the generator-level production threshold of the ADD model signal is also lowered to $m_{\mu\mu} > 1$ TeV. The cross section for this signal sample is given by (16.25 ± 0.01) fb times the mass-independent correction factor of 1.3, which has been discussed in section 8.3. While the SM background is normalized with respect to the ratio of measured to simulated events around the Z boson mass peak (Sec. 8.4), the normalization of the signal is determined by the integrated luminosity of 36.3 fb^{-1} that has been measured with the PCC method.

A general agreement between measurement and background simulation of 5 to 10 % is observed in all distributions, lending confidence to the description of processes with dimuon final states. When comparing the two transverse momentum spectra, the contributions by the subdominant processes toward larger values are observed to decline more rapidly in the distribution of the subleading muon. While pairs of muons are produced directly and thus back-to-back (with respect to the dimuon rest frame) in the $Z/\gamma^* \rightarrow \mu\mu$ process, the production through secondary decays in the other processes allows for less balanced kinematic distributions. With respect to the observed momentum spectra, this direct production of muons in the DY process implies that the associated transverse momenta are generally of similar magnitude[1] and therefore result in similar distributions. As the total momentum is divided among all produced particles in the subdominant processes, it becomes more likely that the momenta of the two muons are not balanced. This causes the aforementioned difference between the declines of DY and other SM background contributions toward higher transverse momenta in the distributions of the leading and subleading muons.

[1] Larger differences can occur in boosted topologies if the two muons are produced along and against the direction of the Lorentz boost, respectively.

The angular dependencies associated with the different SM background production mechanisms also result in dissimilar distributions in the pseudorapidity spectra. Compared to the the direct production via the DY process, muons produced via secondary interactions are observed to be less central with respect to the detector geometry. Following the discussion in the introduction of the virtual graviton exchange process (Sec. 3.2) and the evaluation of the corresponding data sets (Sec. 6.5), a more pronounced centrality of the signal compared to the DY background is expected and also observed. However, the restriction to high interaction scales results in a comparatively small difference between the predictions for the two processes.

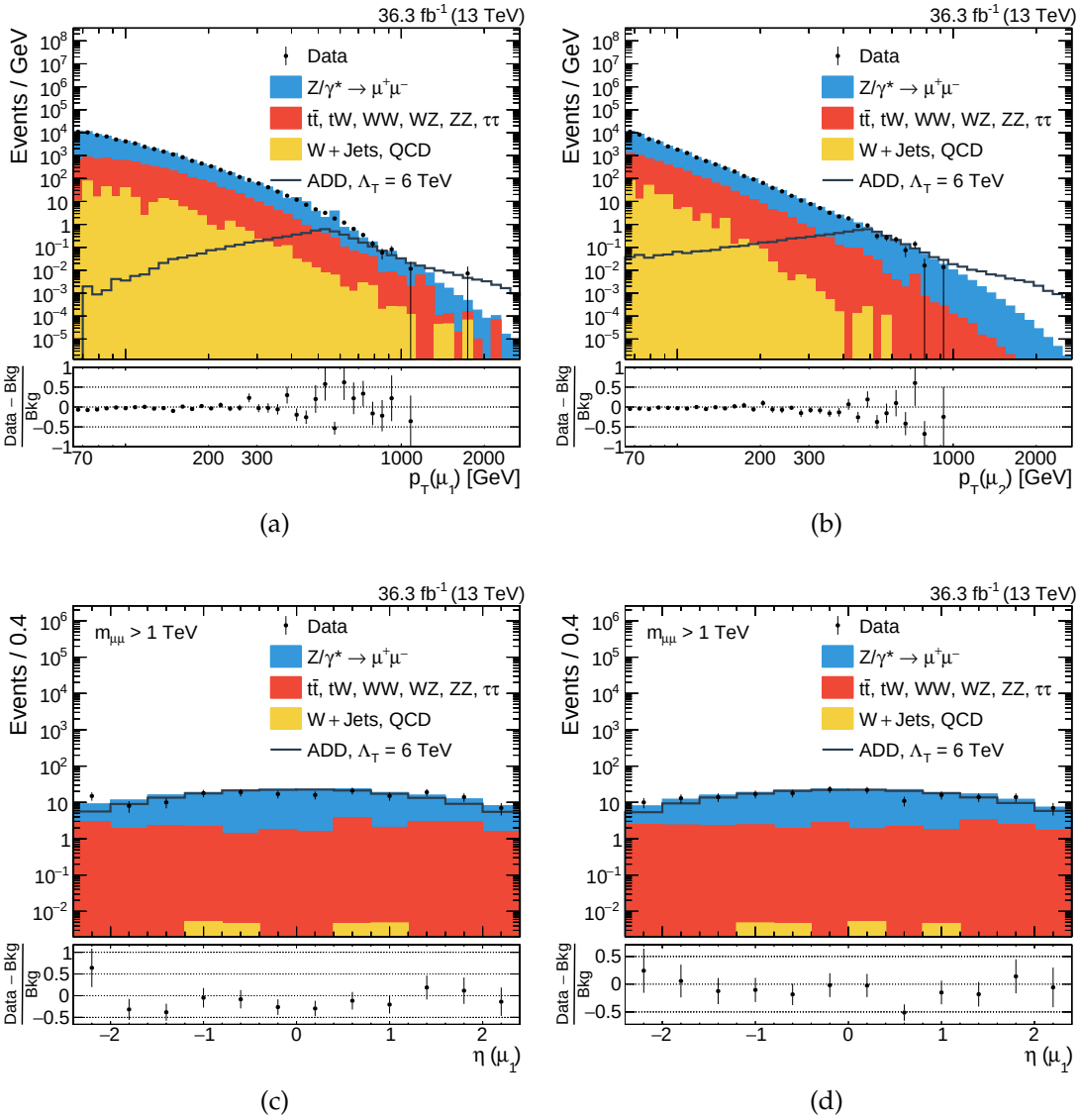

FIGURE 10.1: Transverse momentum and pseudorapidity distributions of the selected pair of muons. In (a) and (c) the properties of the leading muon with respect to the transverse momentum and in (b) and (d) those of the subleading muon. For both pseudorapidity distributions, only events with invariant masses larger than 1 TeV are included. The signal is also produced with a mass threshold of $m_{\mu\mu} > 1$ TeV.

10.2 Invariant Mass Distribution

Using an equidistant binning on a logarithmic scale, the invariant mass of the two selected muons is shown in multiple variations in figures 10.2 and 10.3. As discussed in section 8.2, this mass is determined via the reconstruction of the common vertex. What is referred to as "Jets" in the legend denotes the data-driven jet background estimate, which replaces both the simulated W + Jets and QCD process descriptions. In figures 10.2a and 10.2b, the respective distributions corresponding to the BB and BE category are shown. The displayed signal of the ADD scenario for the model of LED has its DY contribution subtracted and is stacked on top of all backgrounds. With the generator-level production threshold being reduced to $m_{\mu\mu} > 1\,\text{TeV}$, a continuous decline of the relative signal contribution toward lower invariant masses is ensured. Matching the observation in the pseudorapidity spectra, the centrality of the signal with respect to the detector geometry results in a slightly larger amount of events in the BB category compared to the BE one. Within the uncertainties, represented by the colored band in the ratio distributions, no significant deviations of the measurement from the simulated SM background are observed. As each of the histogram bins has been evaluated individually for the presented background uncertainty band, one observes fluctuations toward large invariant masses. These correspond to individual events contributed by the LO description of the WZ and ZZ processes as well as the jet background estimate with its uncertainty in the event yield of 50 %. The composition of the total uncertainty is summarized in table 10.1 for two invariant mass thresholds which characterize the high-energy regime. Given the importance of the DY process in the background description, the normalization uncertainty is the dominant one for low invariant masses with the PDF uncertainty becoming increasingly important and eventually dominant toward high invariant masses. With respect to the chosen signal sample, one can see a large difference in the statistical uncertainty of the simulation between the two regions. For $m_{\mu\mu} > 1\,\text{TeV}$, the subtraction of the DY background from signals with large values of Λ_T results in small signal contributions accompanied by comparatively large statistical uncertainties in the lowest bins. As UV cutoff parameters up to 10 TeV are taken into consideration, this will affect signal predictions in search regions focusing on lower invariant masses. However, with signal event yields close to zero, these search regions also have no substantial impact on the result of the statistical analysis.

While the measurement and simulation are in agreement within the uncertainties, one does observe a slight deficit of measured events toward the tail end of the BB mass spectrum when comparing it to the one of the BE category. Combining both categories yields the invariant mass distribution shown in figure 10.3a and its cumulative counterpart given in figure 10.3b. In the latter, the aforementioned deficit is most prominent. For dimuon invariant masses larger than 1.6 TeV, the number of predicted events in the BB category amounts to $10.4 \pm 0.4\,(\text{stat}) \pm 0.7\,(\text{syst})$ while only 2 are measured. This discrepancy gets reduced to a prediction of $22.1 \pm 0.6\,(\text{stat}) \pm 1.7\,(\text{syst})$ events compared to a measured number of 13 for the combination of both categories. Evaluating these two observations under the assumption of a Poisson distributed measurement around the predicted value yields a difference of 2.5 and 1.8 standard deviations, respectively. To account for experimental sources that could lead to the observed deficit, the performance of each individual analysis step has been discussed within this document. However, scrutinizing the efficiencies associated to the L1 trigger (Sec. 6.1), the HLT (Sec. 9.1) as well as the event reconstruction and selection (Sec. 9.2) has given no indication of an experimental source which could cause this discrepancy. If one assumes a yet undiscovered process such as the virtual exchange of gravitons to be the source, it

Uncertainty Source	Impact on event yield / %			
	ADD, $\Lambda_T = 6\,\text{TeV}$	$Z/\gamma^* \to \mu\mu$	$t\bar{t}, tW, VV, \tau\tau$	Jets
	$m_{\mu\mu} > 1\,\text{TeV}$			
Luminosity	2.5	–	–	–
Normalization	–	5.0	5.0	–
Cross section	–	–	7.0	–
Simulation stat.	11.1	0.5	7.7	–
Pileup	0.2	0.2	0.5	–
PDF	0.1[a]	1.2	15.6	–
Muon reco. & sel.	2.1	1.9	2.0	–
Muon p_T scale	1.9	0.8	1.5	–
Muon p_T resolution	1.0	1.1	1.2	–
Data-driven estimate	–	–	–	50
	$m_{\mu\mu} > 3\,\text{TeV}$			
Luminosity	2.5	–	–	–
Normalization	–	5.0	5.0	–
Cross section	–	–	7.0	–
Simulation stat.	0.7	0.8	11.8	–
Pileup	0.2	0.3	2.3	–
PDF	0.1[a]	7.6	30.6	–
Muon reco. & sel.	2.9	3.2	6.0	–
Muon p_T scale	0.2	3.6	4.1	–
Muon p_T resolution	<0.1	1.2	0.2	–
Data-driven estimate	–	–	–	50

TABLE 10.1: Composition of the total uncertainty for two dimuon invariant mass ranges. Here, VV refers to the W and Z boson pair production processes.
[a] As the PDF uncertainty in the normalization of the signal yield (roughly 20 % above 3 TeV) is considered a theoretical uncertainty, only its impact on the acceptance is taken into account.

would have to interfere negatively with the background. While the Hewett parameter convention allows for the interference term between the ADD signal and the DY process to be negative, the positive contribution by the quadratic graviton exchange term always leads to excesses at large invariant masses. Given that this behavior does not match the observation, the ADD model is not able to explain the deficit.

10.3 Scrutiny of High Mass Events

To further quantify the observed and predicted invariant mass spectra with respect to the deficit, the event yields for consecutive mass ranges are given in table 10.2. Assuming the measurement to be Poisson distributed around the background prediction, the observed and expected yields in the given ranges are generally compatible within 1 to 2 standard deviations. The numerical comparison of the individual background contributions also highlights the importance of the DY process. With the description of the latter being approximated up to NNLO in QCD and NLO in EW including photon-initiated processes (Sec. 8.3), no large deviations from the given yields are expected with respect to future cross section calculations.

For a visual assessment of the detector performance, schematic representations of the two events with the highest invariant masses are shown in figures 10.4 and 10.5, respectively. Individual measurements are highlighted with inner tracks being denoted by green lines, jets by yellow cones and muon tracks by red lines[2]. Entries in the CSCs and DTs are also indicated in red if they are part of the respective reconstructed global muon track and in blue if they are not. Stacked colored bars around the inner tracker represent calorimetric measurements and the estimated missing transverse momentum is given by the (very small) red arrow in the $\eta = 0$ direction. Neither event shows a significant amount of hadronic activity with all jets having transverse momenta of 40 GeV or less. Missing transverse momenta of around 50 GeV also imply an accurate reconstruction of the muons whose properties are given in tables 10.4c and 10.5c, respectively. The quoted uncertainties correspond to those provided by the track or vertex fits. All isolated entries in the muon system, most likely indicating charged and neutral hadronic activity depending on the distance of the muon station to the nominal interaction point, are not reconstructed as muons. In the measurement of the event with the second highest dimuon invariant mass, one additional muon is reconstructed in the forward direction. Its trajectory has been colored purple and can be seen most easily in figure 10.5b. Given its low momentum of roughly 8 GeV, it does not even satisfy the kinematic part of the acceptance requirements and thus no impact on the event reconstruction is expected. Overall, these visualizations are prime examples of excellent measurements by the CMS experiment, lending further confidence to its performance.

$m_{\mu\mu}$ / GeV	Observed	Predicted	$Z/\gamma^* \to \mu\mu$	$t\bar{t}, tW, VV, \tau\tau$	Jets
		BB Category			
120–400	103 667	107 400 ± 5700	87 800 ± 4500	19 400 ± 1700	280 ± 140
400–600	1869	2020 ± 110	1480 ± 77	531 ± 48	12.4 ± 6.2
600–1000	470	505 ± 29	417 ± 22	78.6 ± 8.8	10.0 ± 5.0
1000–1400	50	64.2 ± 4.3	55.6 ± 2.9	6.0 ± 1.9	2.5 ± 1.3
1400–1800	12	12.34 ± 0.69	11.91 ± 0.65	0.42 ± 0.06	0 ± 0
>1800	0	6.32 ± 0.69	4.97 ± 0.29	0.42 ± 0.35	0.92 ± 0.46
		BE Category			
120–400	140 602	153 500 ± 8200	131 000 ± 6900	22 000 ± 1900	540 ± 270
400–600	4043	4370 ± 260	2880 ± 150	1450 ± 140	37 ± 18
600–1000	955	1059 ± 73	757 ± 44	285 ± 40	16.9 ± 8.4
1000–1400	98	101.3 ± 7.3	82.1 ± 5.0	17.2 ± 3.4	2.0 ± 1.0
1400–1800	11	18.8 ± 1.7	14.8 ± 1.0	2.53 ± 0.68	1.51 ± 0.75
>1800	8	5.89 ± 0.64	4.87 ± 0.38	0.69 ± 0.36	0.32 ± 0.16
		Total			
120–400	244 269	261 000 ± 14 000	219 000 ± 11 000	41 300 ± 3600	820 ± 410
400–600	5129	6390 ± 370	4360 ± 230	1990 ± 190	50 ± 25
600–1000	1425	1565 ± 98	1170 ± 65	364 ± 48	26 ± 13
1000–1400	148	165 ± 11	137.7 ± 7.7	23.2 ± 4.6	4.6 ± 2.3
1400–1800	23	31.2 ± 2.2	26.7 ± 1.6	2.96 ± 0.74	1.51 ± 0.75
>1800	8	12.2 ± 1.1	9.84 ± 0.64	1.12 ± 0.50	1.24 ± 0.62

TABLE 10.2: Observed and predicted event yields in different mass ranges as well as pseudorapidity categories. Statistical and systematic uncertainties have been added in quadrature.

[2]The track of a third, low-energy muon muon has been colored purple.

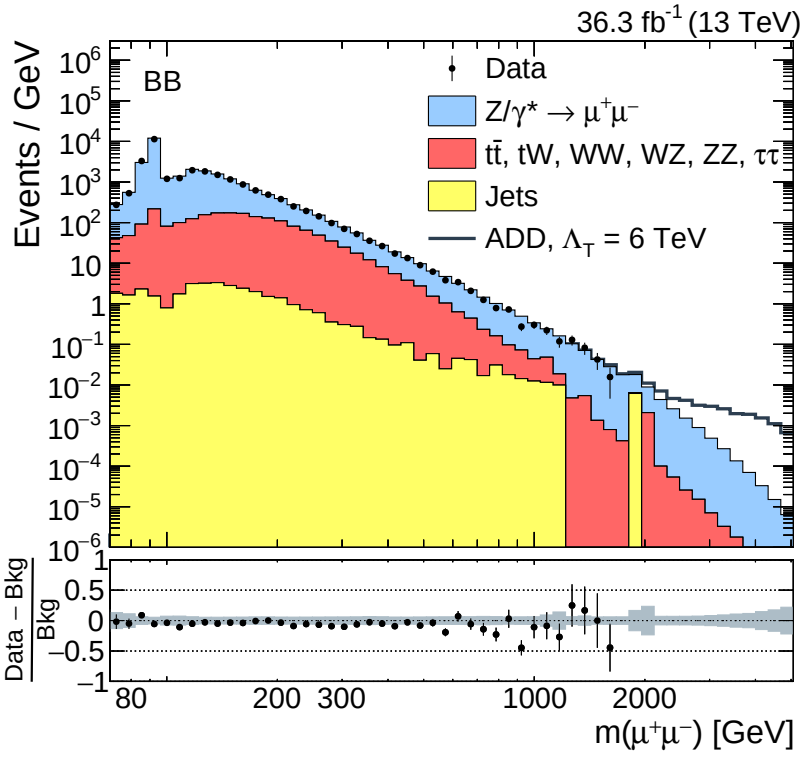

(a)

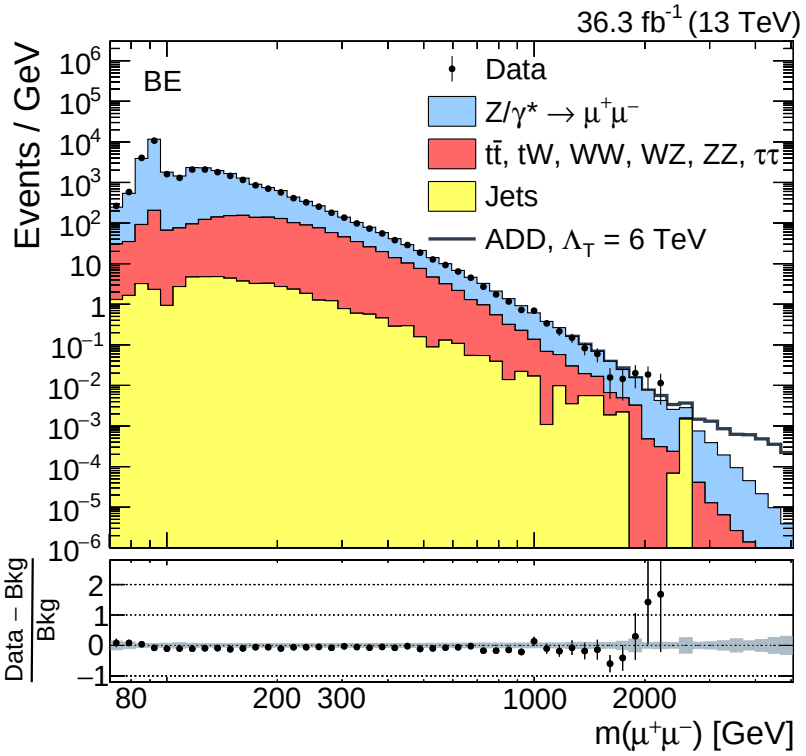

(b)

FIGURE 10.2: Dimuon invariant mass distribution for the BB and BE category in (a) and (b), respectively. The ADD model signal has its DY contribution subtracted and is stacked on top of the backgrounds.

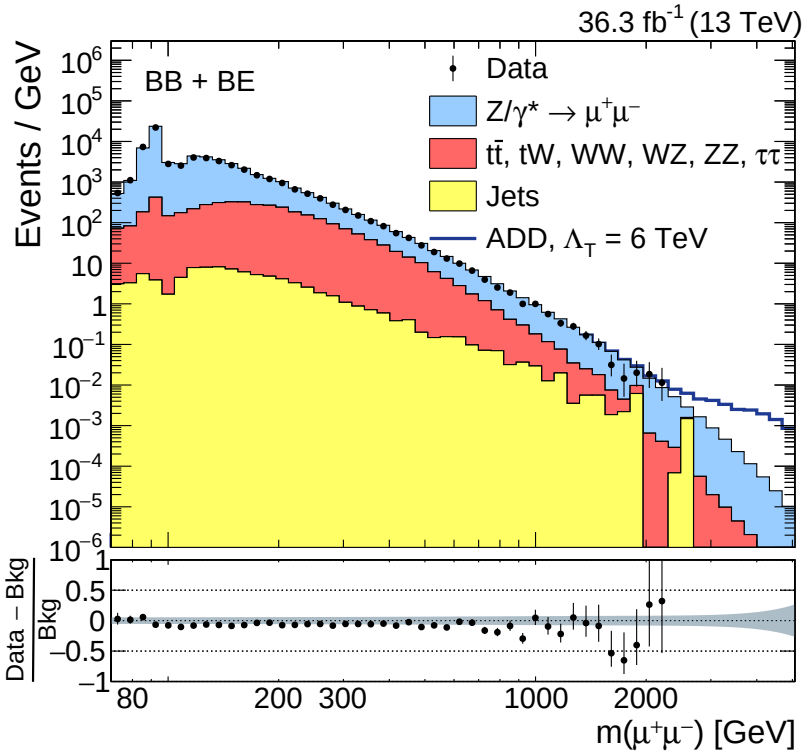

(a)

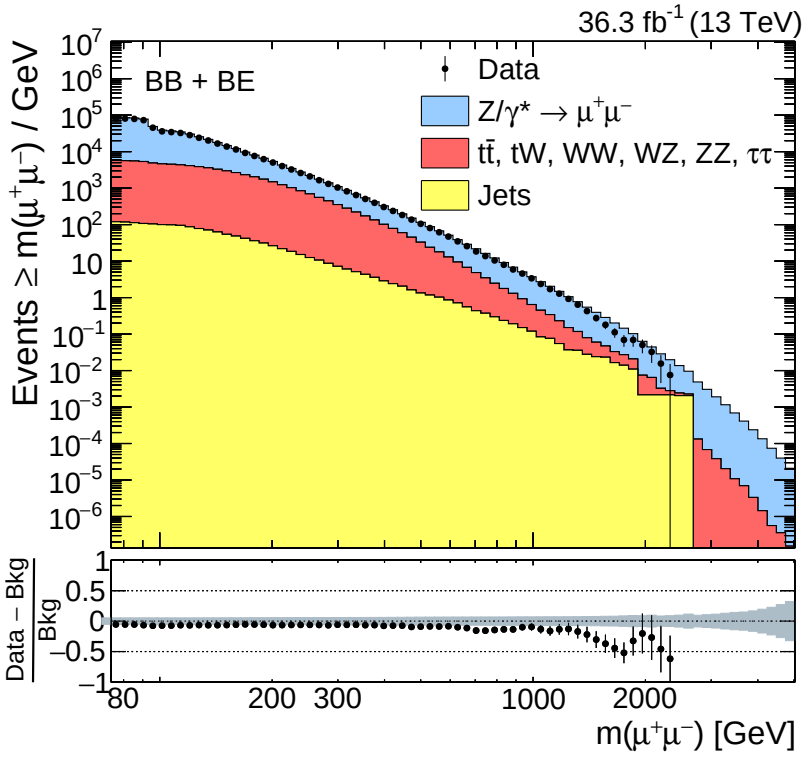

(b)

FIGURE 10.3: Dimuon invariant mass distribution for the combination of both pseudorapidity categories and its cumulative counterpart in (a) and (b), respectively. The signal is stacked on top of the background in (a) but is omitted in (b) as its predictions are only reliable up to 6 TeV.

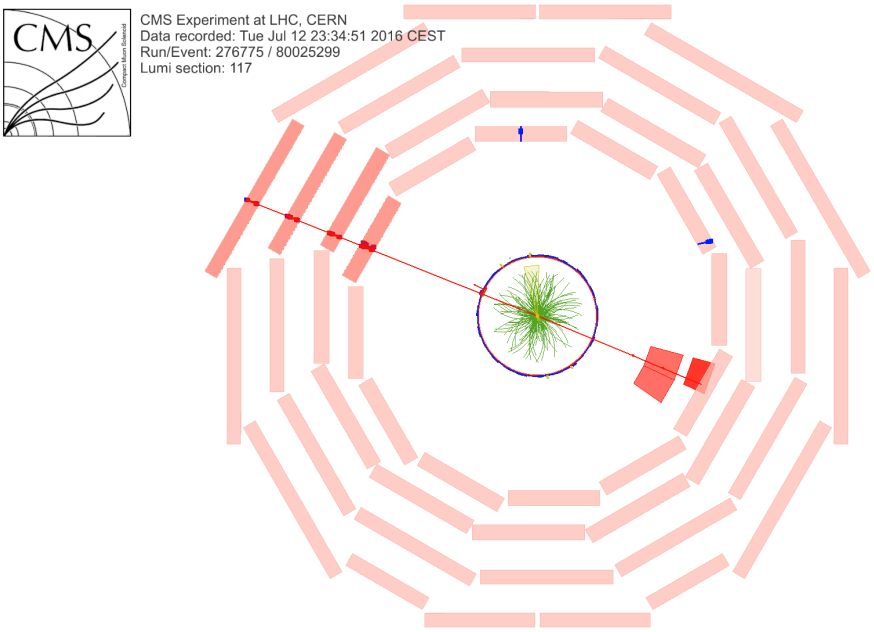

(a)

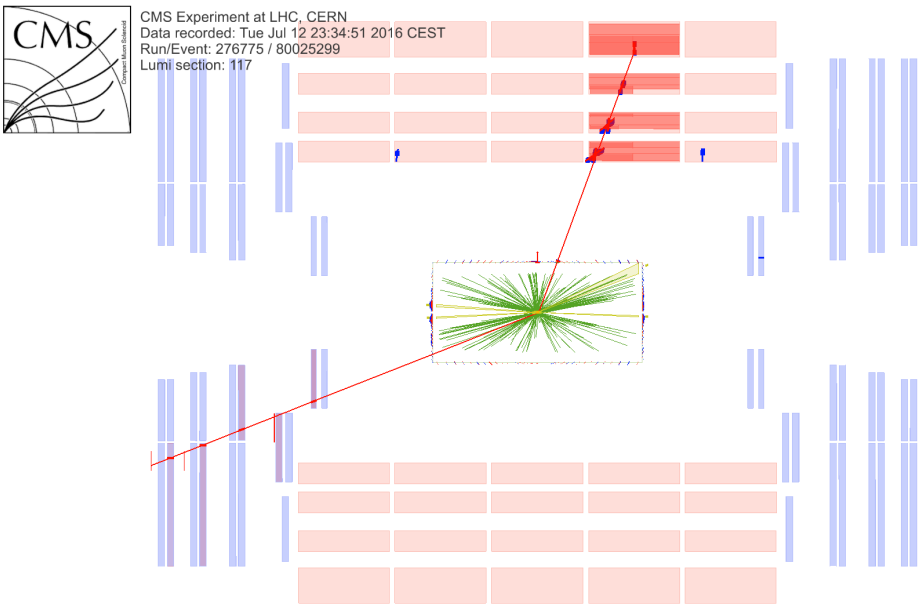

(b)

Muon		Antimuon			
p_T / GeV	(η, ϕ)	p_T / GeV	(η, ϕ)	$m(\mu^+\mu^-)$ / GeV	m_{Vertex} / GeV
748 ± 71	$(-1.66, -0.40)$	704 ± 33	$(0.36, 2.77)$	2256 ± 239	2273 ± 122

(c)

FIGURE 10.4: Schematic representation of the event with the largest observed dimuon invariant mass. In (a) and (b) projected into the r-ϕ and r-z plane, respectively. The corresponding particle properties are given in (c).

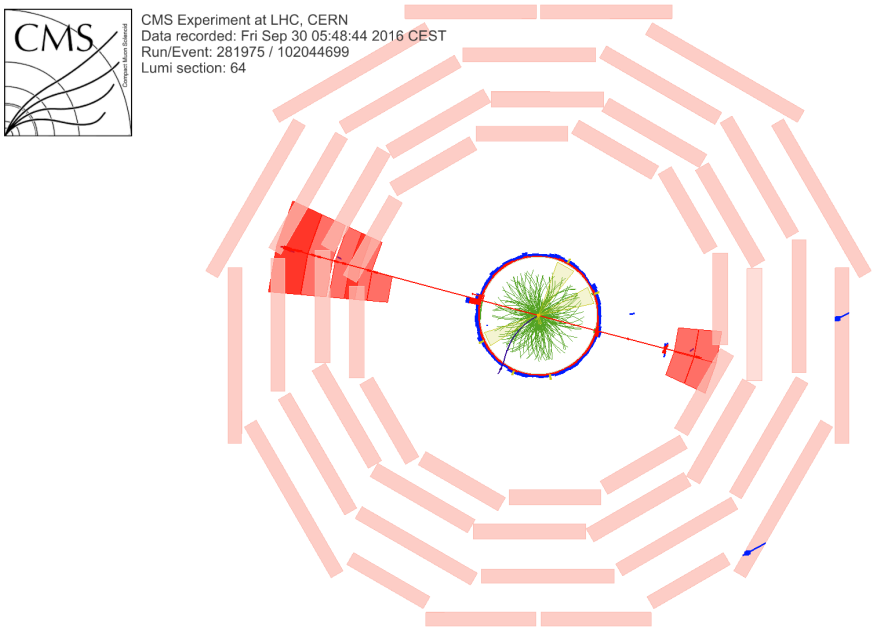

(a)

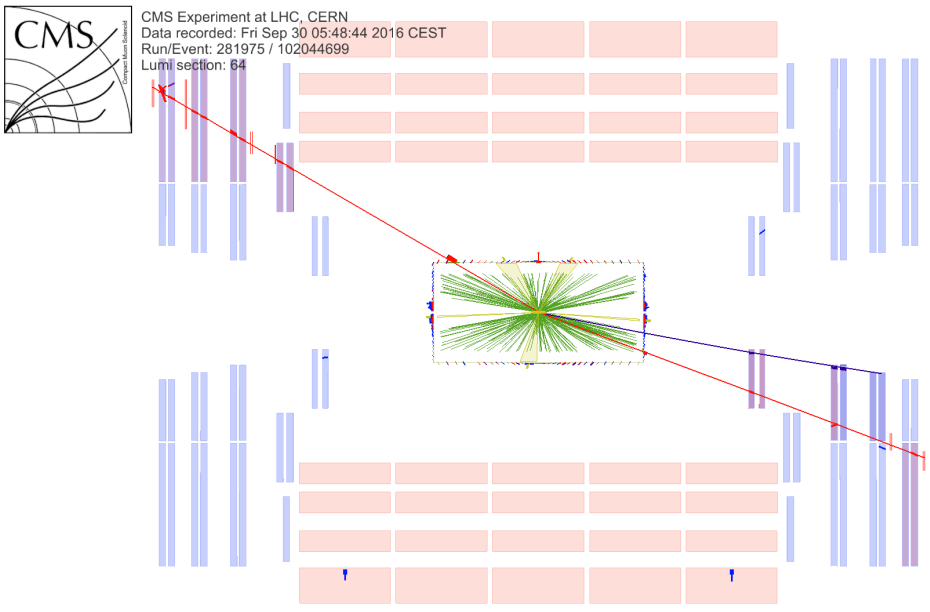

(b)

Muon		Antimuon			
p_T / GeV	(η, ϕ)	p_T / GeV	(η, ϕ)	$m(\mu^+\mu^-)$ / GeV	m_{Vertex} / GeV
521 ± 36	(1.70, −0.27)	413 ± 23	(−1.31, 2.89)	2193 ± 195	2191 ± 97

(c)

FIGURE 10.5: Schematic representation of the event with the second largest observed dimuon invariant mass. In (a) and (b) projected into the r-ϕ and r-z plane, respectively. The corresponding particle properties are given in (c). Purple curves represent the track of an additional muon with a momentum of roughly 8 GeV.

Chapter 11

Statistical Analysis

In the following sections, a probabilistic interpretation of the results that have been discussed in chapter 10 is presented. The two competing approaches to formulate this interpretation in the context of high-energy physics are the *frequentist* and *Bayesian* ones. Whereas the former defines probability as the fraction of outcomes of a repeatable experiment, the latter evaluates the *degree of belief* or subjective probability of a hypothesis in light of a given measurement. In practice, both approaches yield comparable results. A review of their properties and application in high-energy physics, the reference upon which the following sections are based, is provided by the Particle Data Group [64]. To allow for a direct comparison to previous results [73], Bayesian inference is chosen for the evaluation of the signal and background hypotheses with respect to the measurement. As no significant deviation from the SM expectation has been observed, bounds are set on the model cross sections and parameters.

The quantification of the probabilistic interpretation relies on the COMBINE framework [151], originally developed for the discovery of the Higgs boson. It is based on the libraries for statistical analysis provided as part of the ROOSTATS package [152].

11.1 Statistical Inference

Evaluating the *posterior* probability of a model using Bayes' theorem is based on two antecedents. The first one is the likelihood function $P(n \mid \nu)$ describing the probability to observe an amount (or vector) of data n for a given hypothesis parametrized by ν. This likelihood function for n observed events follows the Poisson distribution

$$\frac{x^n}{n!}e^{-x} \quad \text{with} \quad x = s + b \tag{11.1}$$

for the counting experiment at hand. Here, the number of predicted signal and background events are denoted by s and b, respectively. To exploit dependencies of the model prediction on the observable in question, the corresponding distribution can be split into multiple search regions to increase the sensitivity. The overall likelihood is then given by the product of likelihoods associated to the i individual channels

$$P(n \mid \nu) = \prod_i P_i(n_i \mid \nu). \tag{11.2}$$

When combining different search regions, in particular those of different decay channels, correlations between the variables of each channel have to be taken into consideration. The second antecedent is the initial degree of belief in or *prior* probability of the hypothesis $\pi(\nu)$. In Bayesian statistics, no general recipe to derive the prior probability is provided and it may depend on earlier measurements or be otherwise theoretically

motivated. The dependence of the posterior probability density function on this subjective quantity is an often criticized aspect of this approach to inference. A common choice in high-energy physics is to remain unbiased toward any particular values of the model parameters. This corresponds to a "flat" or, to be more precise, constant prior probability density function with respect to the signal strength given by the cross section. For the ADD model, the cross section is inversely proportional to Λ_T^8 (Sec. 3.2). Using these expressions for the likelihood and prior, the posterior probability density function can be written as

$$p(\nu \mid n) = \frac{P(n \mid \nu) \times \pi(\nu)}{P(n)} = \frac{P(n \mid \nu)\pi(\nu)}{\int P(n \mid \nu')\pi(\nu')\,\mathrm{d}\nu'}, \tag{11.3}$$

where the normalization is given by the integral over all possible model configurations.

To take uncertainties in the measurement into account, they are included as nuisance parameters θ in both the likelihood and prior distributions. Given the multiplicative types of uncertainties at hand, a suitable approximation of their probability density functions is given by a random variable whose natural logarithm is normal-distributed. This log-normal distribution allows for a continuous description down to its lower bound of zero whereas a corresponding Gaussian distribution would have to be truncated at that point. The relative impact of the uncertainty on the event yield, discussed in chapter 9 and section 10.2, determines the width of the log-normal distribution. What is referred to as "marginalitazion" describes the integration over all nuisance parameters in order to evaluate the posterior probability density function

$$p(\nu \mid n) = \int p(\nu, \theta \mid n)\,\mathrm{d}\theta \sim \int P(n, \theta \mid \nu)\pi(\theta, \nu)\,\mathrm{d}\theta\,. \tag{11.4}$$

As is common practice in high-energy physics, the experimental result of the presented analysis is reported as a best estimate of the parameter of interest $\hat{\nu}$. This applies to both the expected result based on the predicted number of events and the observed result based on the corresponding measurement. Alongside the best estimate for the expected result, an interval around this value describing the expected variation for the given probabilistic model with respect to the considered nuisance parameters is provided. In general, Bayesian or *credible* intervals of the parameter of interest $[\nu_{\mathrm{low}}, \nu_{\mathrm{up}}]$ containing the fraction $1 - \alpha$ of the posterior probability are determined as

$$1 - \alpha \stackrel{!}{=} \int_{\nu_{\mathrm{low}}}^{\nu_{\mathrm{up}}} p(\nu \mid n). \tag{11.5}$$

Adhering to the convention which most analyses in high-energy physics follow, the probabilistic interpretation is given as an upper bound at a *credibility* level (CL) defined as a single-sided integral

$$\mathrm{CL} = 1 - \alpha = \int_{-\infty}^{\nu_{\mathrm{up}}} p(\nu \mid n) = \frac{\int_{-\infty}^{\nu_{\mathrm{up}}} P(n \mid \nu)\pi(\nu)\,\mathrm{d}\nu}{\int_{-\infty}^{\infty} P(n \mid \nu')\pi(\nu')\,\mathrm{d}\nu'}. \tag{11.6}$$

These upper bounds on the number of predicted signal events s are often expressed as a multiplicative signal strength μ corresponding to $x = \mu s + b$ in the Poisson distribution (Eq. 11.1). Comparable intervals of the frequentist approach are referred to as confidence intervals and confidence levels. As suggested by the same convention and inspired by the relative width covered by two standard deviations of the Gaussian distribution, the presented results are given at 95 % CL and accordingly $\alpha = 5\,\%$. The

chosen Bayesian approach at 95 % CL matches the statistical analysis performed in the search for LED in the dilepton channel based on LHC data at a center-of-mass energy of $\sqrt{s} = 8\,\text{TeV}$ [73], allowing for a quantitative comparison.

11.2 Markov Chain Monte Carlo Integration

As the number of integrals rises with each additional considered channel and nuisance parameter, the only practical way to evaluate the posterior probability (Eq. 11.6) in the given scenario is the application of Monte Carlo integration techniques. Because of the high-dimensional nature of the integral, basic techniques such as inverse transform sampling or rejection sampling are inadequate. The former relies on the being able to invert the cumulative distribution function of the variable while the latter becomes increasingly inefficient for higher dimensions. As one is only interested in the result of the total integral, a suitable numerical approximation can be achieved through Markov chain Monte Carlo (MCMC) methods. When applying MCMC methods, the posterior probability density function is sampled via a "random walk". Based only on the state at a given iteration step, the probability for potential subsequent states is evaluated. Once one with a sufficiently high probability is chosen, it is added to the integral.

The Metropolis–Hastings algorithm employed by the RooStats libraries generates these *correlated* random numbers for a given probability density function $p(x)$ via a sequential proposal and rejection or acceptance of states. Given few enough parameters x, proposing new states according to a uniform probability density function suffices, but the present scenario necessitates more advanced densities to retain a high acceptance. A product of orthogonal Gaussian distributions corresponding to the respective nuisance parameters is used to ensure this high acceptance [151]. The standard deviation of each distribution is given by a fifth of the associated nuisance parameter range. By varying only a single coordinate between subsequent states, an even more robust generation of new states with respect to the aforementioned acceptance is achieved. Having defined the proposal probability density function, the algorithm starts from an arbitrary point x_t with $t = 0$ and iterates over the following four steps:

1. A candidate state x is randomly generated according to the proposal probability density function $q(x, x_t)$.
2. Its acceptance probability is calculated via $\mathcal{A}(x, x_t) = \min\left[1, \dfrac{p(x)q(x_t, x)}{p(x_t)q(x, x_t)}\right]$.
3. Comparing the result to a randomly generated value u, uniformly distributed between 0 and 1, the state is accepted if $u \leq \mathcal{A}(x, x_t)$ and rejected in case $u > \mathcal{A}(x, x_t)$.
4. Should the randomly generated state have been accepted, the subsequent iteration uses $x_{t+1} = x$. Otherwise the old state is kept and $x_{t+1} = x_t$. After incrementing the iteration counter $t = t + 1$, the algorithm returns to the first step.

A large number of iterations is necessary to ensure a wide range of the sample space corresponding to the posterior probability density function is covered by the saved states x_t. After discarding the initial few hundred steps of the Markov chain to become independent of the arbitrary starting seed, upwards of 10 000 iterations are performed. This is further multiplied by tens to hundreds of repetitions of generating these chains with different seeds, resulting in a single averaged state being saved. As the distribution of states x_t approaches that of $p(x)$, it allows for approximating the integral of the latter and thus the estimation of the posterior probability.

11.3 Bounds in the ADD Scenario

In the ADD scenario for the model of LED, limits are set on the UV cutoff parameter Λ_T of the GRW convention. As discussed in section 3.2, the cross section of the virtual graviton exchange process depends on this parameter with $\sigma_{\mathrm{ADD}} \sim 1/\Lambda_T^8$. Expressions for the translation between Λ_T of the GRW convention and the respective parameters of the HLZ and Hewett conventions have also been given in the same section. To determine the limits, two types of strategies are pursued. The first one focuses only on one individual search region, representing the most basic approach. This procedure mirrors the one used in the preceding analysis based on proton-proton collisions recorded at a center-of-mass energy of 8 TeV. In the second approach, multiple search regions are considered and combined according to equation (11.2). While the additional regions are less sensitive individually, incorporating them by combining all likelihoods is expected to improve upon the bounds derived with the first strategy. Following the discussion in section 3.2, all signal contributions at invariant masses above the respective value of the UV cutoff parameter Λ_T are set to 0.

In collaboration with the School of Particles and Accelerators from the Institute for Research in Fundamental Sciences in Teheran, the results of the dimuon and dielectron channel analyses are combined [153]. These channels are the two most sensitive ones for leptonic decays of virtual gravitons. While the considered model does not favor the decay into a particular lepton flavor, the experimental challenges differ. With the reconstruction of electrons relying primarily on measurements by the ECAL, the corresponding coverage determines the geometric acceptance for the dielectron channel. As the components in the barrel and endcap regions are separated by a small gap, clusters of energy deposited by the electron in the calorimeter cells are required to be located within $|\eta_C| < 1.4442$ or $1.566 < |\eta_C| < 2.5$. These two ranges also define the respective barrel-barrel and barrel-endcap categories analogously to the those of the dimuon analysis (with the exception of events where both electrons are located in the endcaps, which are rejected). The dielectron search is based on a trigger requiring an event signature containing two electrons, resulting in transverse momentum thresholds of only 33 GeV per electron. In combination with reconstruction and selection of electrons, the aforementioned gap and utilization of a double-electron trigger result in slightly (~10 %) lower efficiencies in the selection of events. For the analysis of the dielectron invariant mass spectrum, the following sources of uncertainty are the most important ones in the high-energy regime ($m_{ee} > 3$ TeV). With respect to the calorimetric measurement, the uncertainty in the energy scale has an impact of 14 % on the event yields while the one in the energy resolution is negligible. The overall uncertainty in triggering, reconstructing and selecting electrons at high energies has been determined to result in variations of the event yields of 6 %. Both the uncertainty in the PDFs and the subdominant SM background cross sections result in impacts similar to the ones they have in the dimuon channel (Tab. 10.1). It should be noted that, while the background is also normalized by comparing measurement and prediction in a window around the Z boson mass peak, the corresponding uncertainty benefits from the lower transverse momentum thresholds of the double-electron trigger. This uncertainty has an impact of 5 % in the presented analysis (Sec. 9.3) but is reduced to 1 % in the dielectron channel.

By utilizing the results of the complementary analysis focusing on photon pair final states [72], even more stringent bounds can be set on the ADD model parameters. The graviton decay width for the production of photon pairs is comparable to the sum of the dimuon and dielectron decay widths; thus, the sensitivity which the diphoton channel offers is similar to the one provided by the combination of the two lepton channels. With its experimental challenges centered around the ECAL, the photon pair

analysis also differentiates between the two pseudorapidity categories. Using multiple search regions with respect to the diphoton invariant mass and pseudorapidity, 95 % CL exclusion limits have been set using Bayesian inference. As the chosen statistical approach is identical to the one of the leptonic channels, a methodologically consistent combination is possible.

Single Search Region

In order to set the best possible limit on the UV cutoff parameter of the ADD model based on a single search region, the corresponding invariant mass range needs to be optimized. As signal and background event yields decline for rising dimuon invariant masses, the ratio between the two has been observed to improve (see Fig. 6.10 and 10.3). This suggests that the best possible limit is set beyond a lower mass threshold toward the tail end of the spectrum. However, while the signal-to-background ratio improves, the overall signal yield decreases with respect to rising values of Λ_T. Consequently, the model can only be excluded up to a specific value of the UV cutoff parameter. Neglecting efficiency losses and utilizing the Bayesian approach, setting limits at 95 % CL corresponds to a minimum of about three events that can be excluded in scenarios where no background events are expected. With the strategy outlined, the search region is defined with respect to a lower invariant mass threshold where $m_{\mu\mu} > M_{\text{min}}$ and the resulting bounds are evaluated for increasing M_{min}. Figure 11.1 shows the expected limit on Λ_T as function of the lower mass threshold M_{min} evaluated in steps of 100 GeV. As the predicted background yield decreases with rising lower mass thresholds, the displayed expected limit is observed to become more stringent at masses of 2.4, 2.6 and 2.8 TeV. Each improvement corresponds to a reduction of the median background yield from two to one to zero events (Tab. 11.1). In between and beyond the last of the invariant mass thresholds where the median is lowered, raising the threshold further only reduces the signal yield without affecting the median. Consequently, the limit on Λ_T becomes weaker. Based on these observations, one can conclude that the best expected limit is given by the search region where $M_{\text{min}} = 2.8$ TeV.

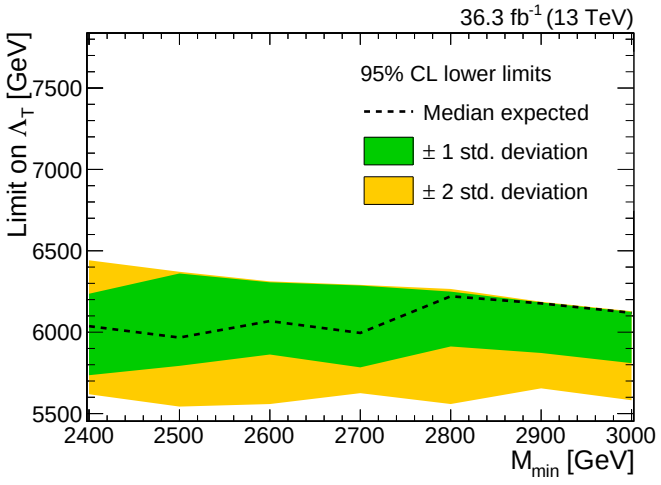

FIGURE 11.1: Expected limit on the ADD model UV cutoff parameter Λ_T as a function of the lower dimuon invariant mass threshold M_{min} in a search region defined as $m_{\mu\mu} > M_{\text{min}}$. The dependence is evaluated in steps of 100 GeV in M_{min}.

With the search region defined, the corresponding data can be used to evaluate the performance of the employed COMBINE limit calculation framework. Generating toy data based on the predicted signal and background yields allows for inferring whether

$m_{\mu\mu}$ / GeV	$\Lambda_T = 6\,\text{TeV}$	Total Bkg.	$Z/\gamma^* \to \mu\mu$	$t\bar{t}, tW, VV, \tau\tau$	Jets
>2400	7.24 ± 0.27	2.10 ± 0.21	1.74 ± 0.13	0.056 ± 0.017	0.30 ± 0.15
>2600	6.66 ± 0.25	1.047 ± 0.090	1.020 ± 0.084	0.028 ± 0.008	0 ± 0
>2800	5.98 ± 0.23	0.624 ± 0.060	0.609 ± 0.057	0.015 ± 0.005	0 ± 0
>3000	5.29 ± 0.21	0.374 ± 0.040	0.367 ± 0.038	0.007 ± 0.003	0 ± 0

TABLE 11.1: Predicted event yields above different dimuon invariant mass thresholds. Serving as an example for the ADD model signal samples, the event yields for the data set with $\Lambda_T = 6\,\text{TeV}$ are shown in the second column. As discussed in section 10.3, no measurements are available above invariant masses of 2.3 TeV. Statistical and systematic uncertainties have been added in quadrature.

the inserted signal or absence thereof is accurately reconstructed. This is quantified using maximum likelihood fits [151] for the signal strength parameter. In figure 11.2, the best fit for the signal strength parameter $\hat{\mu}$ and its confidence intervals are shown based on 10 000 toys for each signal model in two types of scenarios. On the left, the fit is performed for toy data generated without signal contributions. For a wide range of the considered Λ_T values, the predicted signal yields would be large and thus the fit remains close to 0. As the expected signal contribution decreases with rising Λ_T, so does the potential for it to be hidden within the background-only toy events. Beyond $\Lambda_T = 8\,\text{TeV}$, even contributions scaled to their full signal strength are too small to be distinguished in this search region, implying that these models cannot be excluded. In the second scenario, a signal is assumed to be present and the toy data is generated for the combined background plus signal expectation. Performing the fits based on this data yields the distribution shown on the right. While structurally similar to the result of the first scenario, the interpretation of the fitted signal strength parameter differs. When evaluating the best fit under the assumption that a signal is present, one observes the signal contributions for low values of Λ_T to be distinguishable from the background for signal strengths matching the model prediction. This corresponds to values of $\hat{\mu} = 1$. As the yield becomes smaller for increasing Λ_T, signal strengths larger than 1 are necessary for the predicted excess to remain distinguishable in this search region. The departure from baseline prediction of 1 is located between 6 and 7 TeV, providing an estimate for the expected limit compatible with the prediction formulated in section 6.5.

With the optimal dimuon invariant mass threshold for a single search region determined, the 95 % CL exclusion limit can be calculated. The aforementioned compatibility of the indicated bound determined via the signal strength study also lends confidence to the selected region. Figure 11.3a shows both the observed and expected limits on the cross section as function of the model parameter Λ_T, with green and yellow bands corresponding to the 68 % and 95 % credibility intervals of the expected limit, respectively. As no events have been measured beyond the lower mass threshold of 2.8 TeV and the median predicted background yield matches this measurement, observed and expected limit coincide. Differences between the event reconstruction and selection efficiencies of various signal samples have been observed to be statistically insignificant (Sec. 7.6) and thus no dependence of the limit on the UV cutoff parameter can be seen. The two dashed blue curves represent the excess in terms of the cross section predicted by the ADD model with contributions above invariant masses larger than Λ_T set to 0. While both curves are based on the LO prediction, the one depicted with nonuniform dashes is obtained by applying a mass-independent correction factor of 1.3. Intersections of the curves with the observed and expected cross section limits yield the respective 95 %

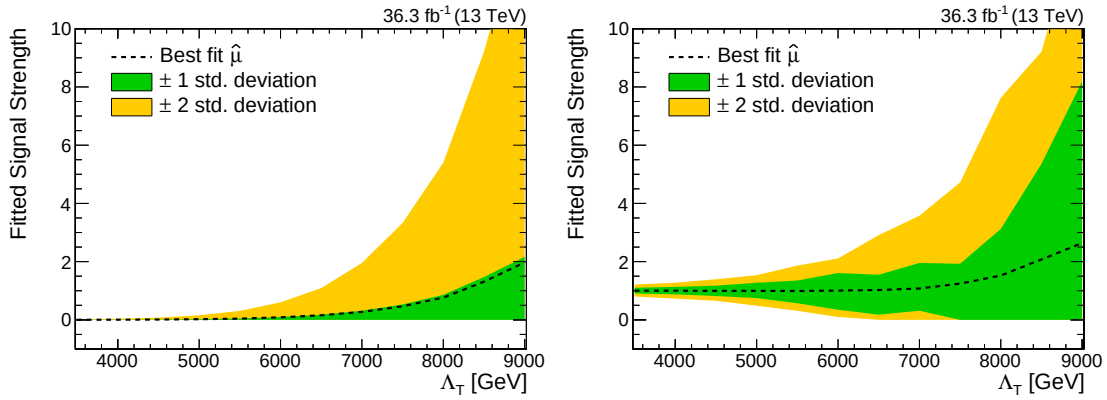

FIGURE 11.2: Best estimate for the signal strength parameter $\hat{\mu}$ based on maximum likelihood fits in the search region defined by $m_{\mu\mu} > 2.8\,\text{TeV}$. In (a) for toy events generated for a background-only expectation and in (b) for toy events generated under the assumption that a signal is present and thus a combined background plus signal expectation.

CL exclusion bound on the model parameter. With the presented approach, Λ_T values of 6.2 TeV (LO) and 6.5 TeV (LO × 1.3) for the ADD scenario for the model of LED are excluded. Combining the results of the dimuon and dielectron channel and performing an analogue optimization of the lower dilepton invariant mass threshold yields the distribution shown in figure 11.3b. All uncertainties—summarized in table 10.1 for the dimuon channel and discussed in the introduction of section 11.3 for the dielectron one—not pertaining to the specific lepton flavor are assumed to be fully correlated between the two channels. The distribution with its threshold of $m_{\ell\ell} > 3\,\text{TeV}$ exhibits no structural differences compared to the one of the dimuon channel. As lepton universality is not violated by the considered virtual graviton exchange process, an improvement by roughly a factor of 2 with respect to the excluded signal cross section is expected and observed. The corresponding bounds on the UV cutoff parameter are given by $\Lambda_T > 6.6\,\text{TeV}$ (LO) as well as 6.8 TeV (LO × 1.3) and extend those of the dimuon channel by about 6 %. A summary of all results for individual search regions, including the translations from the GRW parameter convention to the Hewett and HLZ conventions, is given in table 11.2.

Order	GRW Λ_T / TeV	Hewett M_S / TeV	HLZ M_S / TeV					
			$n=2$	$n=3$	$n=4$	$n=5$	$n=6$	$n=7$
$m_{\mu\mu} > 2.8\,\text{TeV}$, $\sigma_{\mu\mu,\,\text{excl.}} > 0.10\,\text{fb}$ (0.10 fb expected) at 95 % CL								
LO	6.2 (6.2)	5.6 (5.6)	6.4 (6.3)	7.4 (7.4)	6.2 (6.2)	5.6 (5.6)	5.2 (5.2)	5.0 (4.9)
LO × 1.3	6.5 (6.4)	5.8 (5.7)	6.7 (6.7)	7.7 (7.6)	6.5 (6.4)	5.8 (5.8)	5.4 (5.4)	5.1 (5.1)
$m_{\ell\ell} > 3\,\text{TeV}$ for ee and $\mu\mu$, per channel $\sigma_{\ell\ell,\,\text{excl.}} > 0.055\,\text{fb}$ (0.058 fb expected) at 95 % CL								
LO	6.6 (6.5)	5.9 (5.8)	6.8 (6.7)	7.8 (7.8)	6.6 (6.5)	5.9 (5.9)	5.5 (5.5)	5.2 (5.2)
LO × 1.3	6.8 (6.8)	6.1 (6.1)	7.1 (7.1)	8.1 (8.1)	6.8 (6.8)	6.2 (6.1)	5.7 (5.7)	5.4 (5.4)

TABLE 11.2: Summary of the 95 % CL exclusion limits on the respective model parameters of the ADD scenario for the model of large extra dimensions. Observed bounds are followed by expected bounds in parentheses.

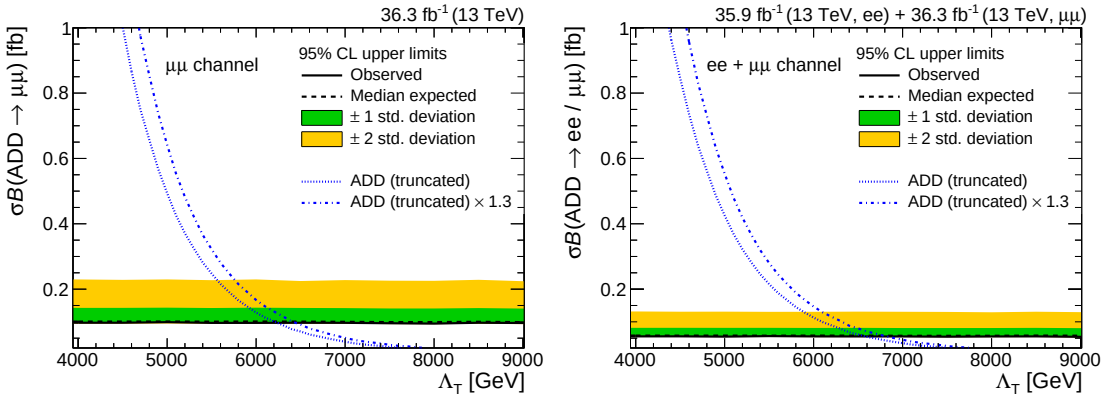

(a) (b)

FIGURE 11.3: Exclusion limit at 95 % CL for a single search region defined via a lower dilepton invariant mass threshold. In (a) for the dimuon channel with $m_{\mu\mu} > 2.8\,\text{TeV}$ and in (b) for the combination of the dimuon and dielectron [153] channel where $m_{\ell\ell} > 3\,\text{TeV}$.

Multiple Search Regions

With the most sensitivity search region evaluated, the goal is to improve upon the determined exclusion limits by combining individual likelihoods of various invariant mass ranges. To exploit the centrality of the signal with respect to the detector geometry (Fig. 10.2), all search regions are split into the BB and BE pseudorapidity categories. Beginning with the optimal dilepton invariant mass threshold of 3 TeV, multiple widths for additional mass ranges down to invariant masses of 1.8 TeV have been considered. The lower bound for the width is given by the dimuon mass resolution (Fig. 9.4b), which corresponds to values between 200 and 300 GeV in this region. While limited by increasingly large statistical uncertainties toward widths of 200 GeV and becoming less sensitive to the distribution of the signal for values beyond 500 GeV, the intermediate options yield similar results. Choosing a width of 400 GeV, the boundaries between the individual search regions are given by 1.8, 2.2, 2.6 and 3 TeV per pseudorapidity category. The last region beyond 3 TeV includes all contributions up to invariant masses equal to Λ_T. Using the signal sample with $\Lambda_T = 6\,\text{TeV}$ as an example, the correspondingly binned invariant mass distributions are shown in figure 11.4. The virtual graviton exchange process is stacked on top of the background and bin heights are not scaled to their width, which allows for a visual comparison of event yields. A tabular summary of the predicted background and measured event yields is also provided in appendix A.

Since the uncertainties are considered to be fully correlated between the respective search regions, their nuisance parameters may be constrained during the determination of the integral. To avoid inadvertently optimistic or pessimistic constraints, a comparison of the nuisance parameters before and after fitting the prediction to the data within the given uncertainties serves as an estimate of the expected variation. The states prior to and after performing the fit are also referred to as pre- and postfit in this context. It should be emphasized that this fit is not performed as part of the Bayesian approach implemented in the COMBINE framework and is only used for this estimate. The differences between the central values of the nuisance parameters are given in figure 11.5a and the ratios of the respective standard deviations in figure 11.5b. Both visualizations are based on the event yields of the search regions corresponding to a model parameter of $\Lambda_T = 6\,\text{TeV}$. No substantial differences between the pre- and postfit values are observed. Among the considered quantities, only the conservative estimate

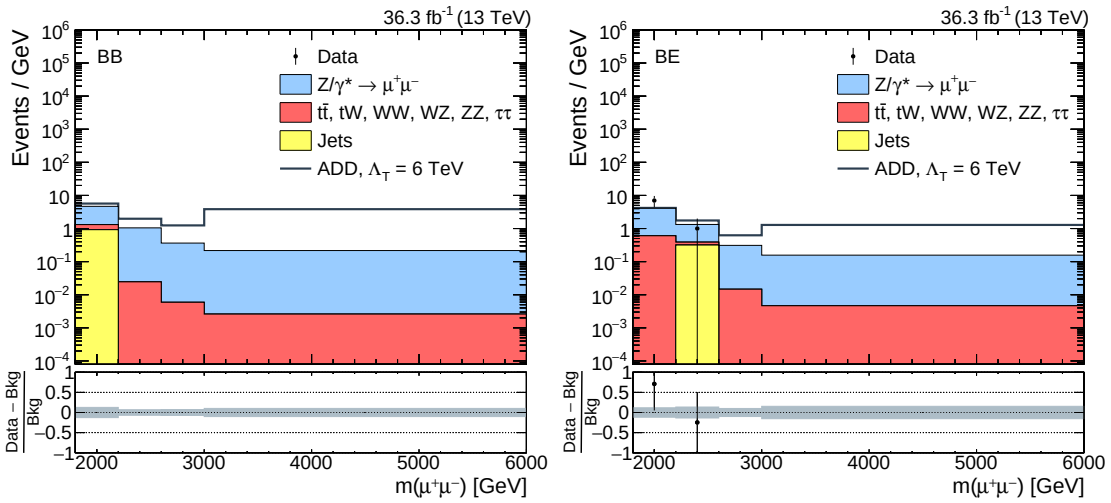

(a) (b)

FIGURE 11.4: Dimuon invariant mass distributions where the individual bins correspond to the considered search regions. In (a) and (b) for the BB and BE pseudorapidity category, respectively. Bin heights are not scaled to their widths to allow for a visual comparison of event yields.

for the uncertainty in the determination of the jet background estimate has received any notable reduction. However, given the comparatively minor contribution to the total background yield alongside the large initial uncertainty assigned to it, this has little to no impact on the overall result.

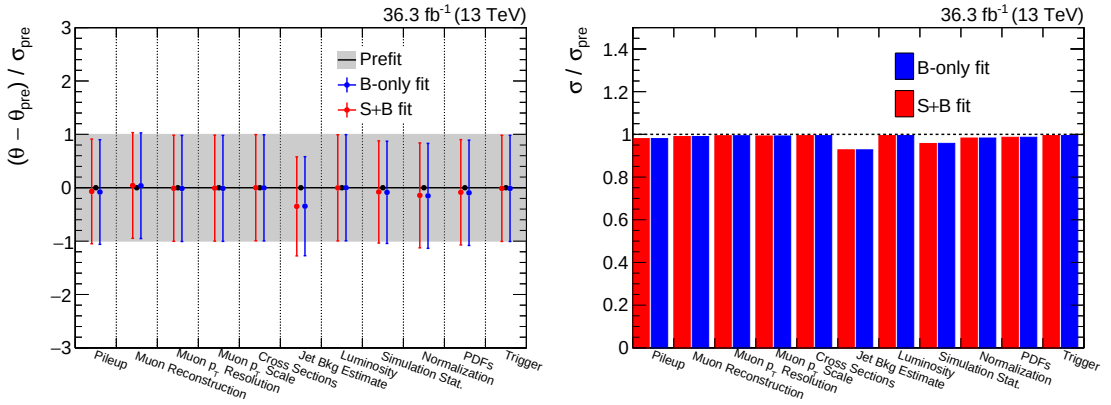

(a) (b)

FIGURE 11.5: Comparison of pre- and postfit nuisance parameters serving as an estimate for potential constraints in the marginalization through the assumed correlation between search regions. The differences of the central values and the ratios of the standard deviations are shown in (a) and (b), respectively. These fits have been performed with the measured and predicted event yields corresponding to the search regions for the model parameter $\Lambda_T = 6\,\text{TeV}$.

With the search regions defined and potential concerns regarding the calculation of bounds within them addressed, the corresponding 95 % CL exclusion limit is calculated and given in figure 11.6a. Between model parameters of 4 to 6.5 TeV, the resulting distribution shows a steady improvement of the bound on the cross section. As observed for the limit based on a single search region, different values of Λ_T do not lead to statistically significant variations of the reconstruction and selection efficiency. However,

the signal contributions are shifted toward search regions with lower background yields for rising values of the UV cutoff parameter, causing the observed improvement. Beyond $\Lambda_T \simeq 7\,\text{TeV}$, the signal yields in search regions with lower dilepton masses become small and their statistical uncertainty rises, which corresponds to likelihoods with a low significance. Consequently, the lower bound on the cross section becomes weaker for these model parameters. As a larger range of invariant masses is considered, the measured deficit with respect to the predicted background yield in the dimuon channel, discussed in sections 10.2 and 10.3, results in the observed limit being consistently below and thus more stringent the expected one. For the largest considered value of Λ_T, observation and expectation are more compatible as the signal contributions are further shifted toward search regions with even lower predicted background yields. In terms of the model parameter Λ_T at LO, an improvement of roughly 300 GeV or 5 % for the expected limit and 500 GeV or 8 % for the observed one can be seen between the isolated evaluation of the most significant search region and the combination of multiple ones. A similar improvement of the expected limit in the combination of both leptonic channels can be observed in figure 11.6b. However, in contrast to the measured deficit in the dimuon channel, the dielectron analysis has observed 9 events compared to a predicted background yield of 7.5 ± 1.1 for $m_{ee} > 1.8\,\text{TeV}$. With opposing fluctuations in the measurements, the combined observed limit improves only by 200 GeV. A visualization of the bounds on Λ_T obtained in the dimuon channel and the combination of the two leptonic channels as well as their translation to the other parameter conventions are given in figure 11.7.

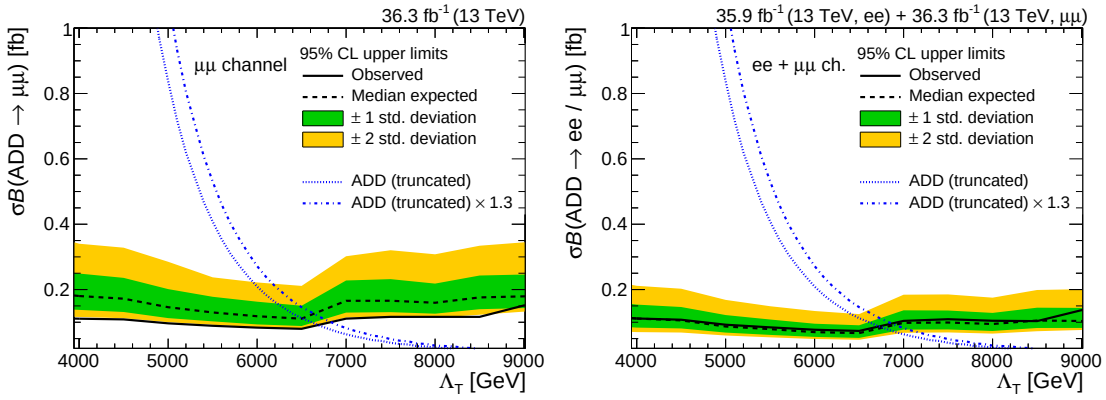

(a) (b)

FIGURE 11.6: Exclusion limits at 95 % CL for the combination of multiple search regions. The regions correspond to dilepton invariant mass ranges of 1.8 to 3 TeV in steps of 400 GeV and one additional region from 3 TeV to the respective value of Λ_T. In (a) for the dimuon channel and in (b) for the combination of the dimuon and dielectron channels.

To illustrate the dependence of the 95 % CL exclusion limit of the dimuon channel on the total uncertainty, it is recalculated in four additional scenarios. For the first one, representing the ideal case, no uncertainties are taken into account. In the other three, a hypothetical source of uncertainty with an impact of 10, 20 and 30 % is introduced in addition to the determined uncertainty for both the signal and DY background in each search region, respectively. Figure 11.8 shows the expected limit for all four scenarios in comparison to the one of the presented analysis. Overall, the excluded value of Λ_T is observed to be robust with respect to the total uncertainty. All pessimistic test scenarios correspond to variations of the limit on the UV cutoff parameter between 100

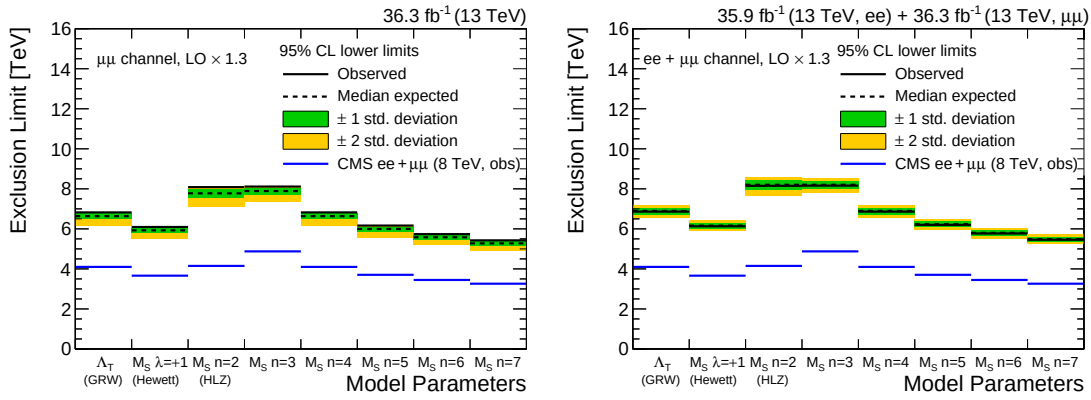

(a) (b)

FIGURE 11.7: Visualization of the 95 % CL exclusion limits for the combination of multiple search regions. The regions correspond to dilepton invariant mass ranges of 1.8 to 3 TeV in steps of 400 GeV and one additional region from 3 TeV to the respective value of Λ_T. In (a) for the dimuon channel and in (b) for the combination of the dimuon and dielectron channels. Limits of the preceding analysis by the CMS Collaboration at $\sqrt{s} = 8$ TeV [73] are shown for comparison.

to 200 GeV. The bound derived in the presented analysis is also observed to be close to the one corresponding to the ideal scenario.

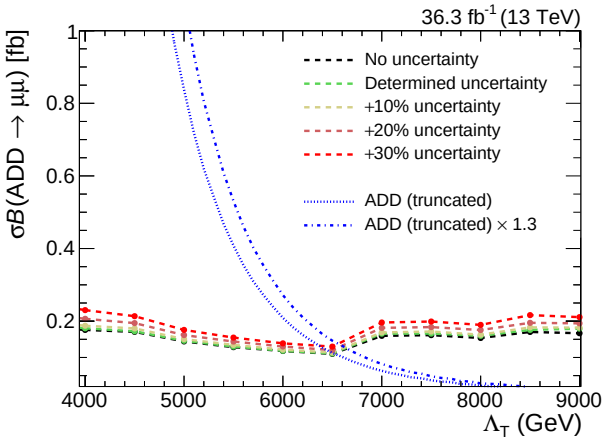

FIGURE 11.8: Dependence of the 95 % CL exclusion limit for the combination of multiple search regions on the total uncertainty. The "determined uncertainty" denotes the limit corresponding to the presented analysis.

Utilizing the aforementioned results obtained in the analysis of the complementary diphoton channel [72], it is possible to further improve the determined exclusion limits. While the combination is performed using the THETA framework for statistical inference [154], the calculation is still based on the discussed Bayesian approach. As the considered invariant mass ranges differ, $m_{\ell\ell} > 1.8$ TeV and $m_{\gamma\gamma} > 500$ GeV, the nuisance parameters are assumed to be uncorrelated between the two channels[1]. The resulting expected and observed 95 % CL exclusion limits are shown in figures 11.9a and 11.9b, respectively. To allow for a direct comparison, the individual diphoton and dilepton bounds as well as the corresponding results for the latter channel obtained

[1]Alternatively, one could perform a detailed evaluation of the correlations. This ensures that one does not introduce unexpected constraints, but no substantial gain is expected given the observed performance of the chosen approach (Fig. 11.8).

at $\sqrt{s} = 8\,\text{TeV}$ are included in this visualization. In summary, the exclusion limits determined in the analysis of the individual dimuon channel already improve upon those of the 8 TeV dilepton analysis and the combination of all three channels extend these bounds by about 80 %. While the expected limits highlight the benefit of the combination, the diphoton analysis yields more stringent observed limits as a deficit has been measured with respect to the SM prediction. This deficit—while still within the expected variation—has resulted in a difference of 700 GeV between the expected and observed bound on Λ_T in the diphoton channel, with the latter being given by 7.8 TeV. All discussed bounds for the combination of multiple search regions are also numerically summarized in table 11.3.

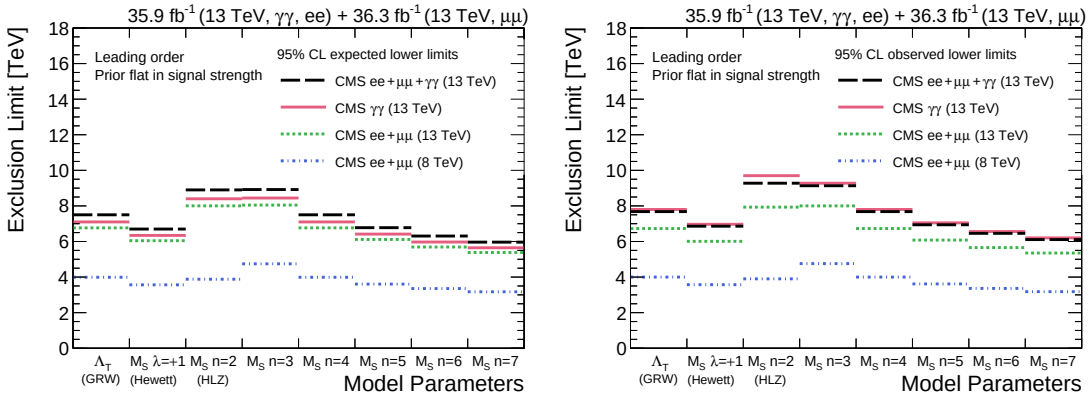

(a) (b)

FIGURE 11.9: Exclusion limits at 95 % CL for the combination of the muon, electron and photon pair decay channels of the virtual exchange of gravitons. The results of the individual channels and those of dilepton channel at a center-of-mass energy of $\sqrt{s} = 8\,\text{TeV}$ are shown for comparison. While the expected limits show that the most sensitive analysis is given by the combination of all three channels, the deficit that has been measured with respect to the SM prediction in the diphoton channel results in slightly more stringent observed limits.

In conclusion, the 95 % CL exclusion limits of the combined dielectron, dimuon and diphoton channels constitute the world's most sensitive nonhadronic search for large extra dimensions in the ADD scenario. With hadronic channels benefiting from substantially larger cross sections, the overall most stringent limit of $\Lambda_T > 10.1\,\text{TeV}$, determined in the dijet analysis of the CMS Collaboration [71], exceeds the one of the nonhadronic search by more than 2 TeV.

11.4 Bounds in the Asymptotically Safe Scenario

Based on the discussions of the model and produced signals in sections 3.4 and 6.5, the characteristics of the virtual graviton exchange process cross section for the model of LED in the AS scenario for quantum gravity can be summarized as follows. For a given number of extra dimensions and approximation of the transition between the IR and UV regime, the cross section depends on two free parameters. It scales inversely with increasing values of the fundamental scale of gravity M_D, similar to the UV cutoff parameter of the ADD model, but also becomes larger with rising transition scales $\Lambda_{\text{Transition}}$. The latter dependency is exhibited in figure 3.4, where the gravitational coupling parameter and thus the cross section becomes (gradually) suppressed toward and beyond $\Lambda_{\text{Transition}}$. Following this characterization, limits can be set in a two-dimensional plane spanned by the fundamental scale of gravity M_D and the transition

Order	GRW Λ_T / TeV	Hewett M_S / TeV	HLZ M_S / TeV					
			$n = 2$	$n = 3$	$n = 4$	$n = 5$	$n = 6$	$n = 7$
$m_{\mu\mu} > 1.8\,\text{TeV}$								
LO	6.7 (6.5)	6.0 (5.8)	7.9 (7.6)	7.9 (7.7)	6.7 (6.5)	6.0 (5.9)	5.6 (5.5)	5.3 (5.2)
LO × 1.3	6.8 (6.6)	6.1 (5.9)	8.1 (7.8)	8.1 (7.9)	6.8 (6.6)	6.2 (6.0)	5.7 (5.6)	5.4 (5.3)
$m_{\ell\ell} > 1.8\,\text{TeV}$ for ee and $\mu\mu$								
LO	6.7 (6.8)	6.0 (6.0)	7.9 (8.0)	8.0 (8.0)	6.7 (6.8)	6.1 (6.1)	5.7 (5.7)	5.4 (5.4)
LO × 1.3	6.9 (6.9)	6.1 (6.2)	8.2 (8.2)	8.2 (8.2)	6.9 (6.9)	6.2 (6.2)	5.8 (5.8)	5.5 (5.5)
$m_{\ell\ell} > 1.8\,\text{TeV}$ for ee and $\mu\mu$ combined with $m_{\gamma\gamma} > 500\,\text{GeV}$								
LO	7.7 (7.5)	6.9 (6.7)	9.3 (8.9)	9.1 (8.9)	7.7 (7.5)	6.9 (6.8)	6.5 (6.3)	6.1 (6.0)

TABLE 11.3: Summary of the 95 % CL exclusion limits on the respective model parameters of the ADD scenario for the model of large extra dimensions for the combination of multiple search regions. Observed limits are followed by expected limits in parentheses. As no higher order correction factor for the cross section has been considered in the analysis of the diphoton channel, limits for the combination of all channels could also only be determined at LO.

scale $\Lambda_{\text{Transition}}$ for each approximation and number of additional dimensions. This approach has also been pursued in the reinterpretation of the dilepton channel results at a center-of-mass of $\sqrt{s} = 8\,\text{TeV}$ (Fig. 3.5), allowing for a direct comparison.

In order to set the best possible limits in the AS scenario, the high multiplicity of the parameters necessitates an excessive amount of signal data sets. To determine one point of an M_D-$\Lambda_{\text{Transition}}$ exclusion curve, a granular analysis of the $\Lambda_{\text{Transition}}$ parameter space for a given value of M_D is required. The resulting amount of samples for one curve then scales multiplicatively with both the considered approximations of the transition as well as the number of extra dimensions n. While a wide range of M_D-$\Lambda_{\text{Transition}}$ values has been explored in the reinterpretation, transition scales beyond M_D can lead to a violation of unitarity [155]. The allowed ratio of $\Lambda_{\text{Transition}}$ to M_D can be large (a factor of 5) but also depends on the number of extra dimensions. By conservatively restricting the parameter space to be explored, using the respective value of M_D as an upper bound for $\Lambda_{\text{Transition}}$, unitarity is ensured. A practical approach to reducing the necessary computational effort to probe this restricted parameter space is to set model-independent limits for spin-2 gravitons using averaged efficiencies for the selected search regions. While this scenario still requires generating the necessary samples, it avoids simulating the detector response and calculating the exclusion limits corresponding to the individual data sets. Within the current limitations of readily available computing resources, the former prolongs the process by roughly one order of magnitude while the duration of the latter is comparable to the one of the event generation itself.

When defining search regions for the model-independent limits, signal contributions toward lower invariant masses have to be taken into consideration as they are significant for a large fraction of the considered parameter space. By including invariant mass ranges down to $m_{\mu\mu} > 400\,\text{GeV}$, these contributions are accounted for. Below this threshold, aspects like the determination of uncertainties have to be reevaluated as one leaves the high-p_{T} regime for muons. Since a combination of multiple search regions becomes sensitive to the shape of the respective signals, the chosen model-independent approach focuses on two sets of individual regions with different widths. Based on the

discussion in the previous section, the dimuon invariant mass spectrum is divided into 400 GeV wide regions between 600 GeV and 3 TeV for the first set of bins. Two additional regions cover the mass ranges from 400 to 600 GeV and above 3 TeV. To create the second set, the same lower bounds of the individual bins are used cumulatively, e.g., having one region with $m_{\mu\mu} > 400\,\text{GeV}$ and one with $m_{\mu\mu} > 600\,\text{GeV}$. A visualization of the dimuon invariant mass spectrum for these bins is given in figure 11.10. Appendix A provides the corresponding predicted and measured event yields in tabular form. While the second set of regions is generally expected to be more sensitive to nonresonant signals, the first one covers edge cases with localized contributions for low transition scales. These edges cases mostly occur for the quenched approximation of the transition in the search region with the lowest invariant masses.

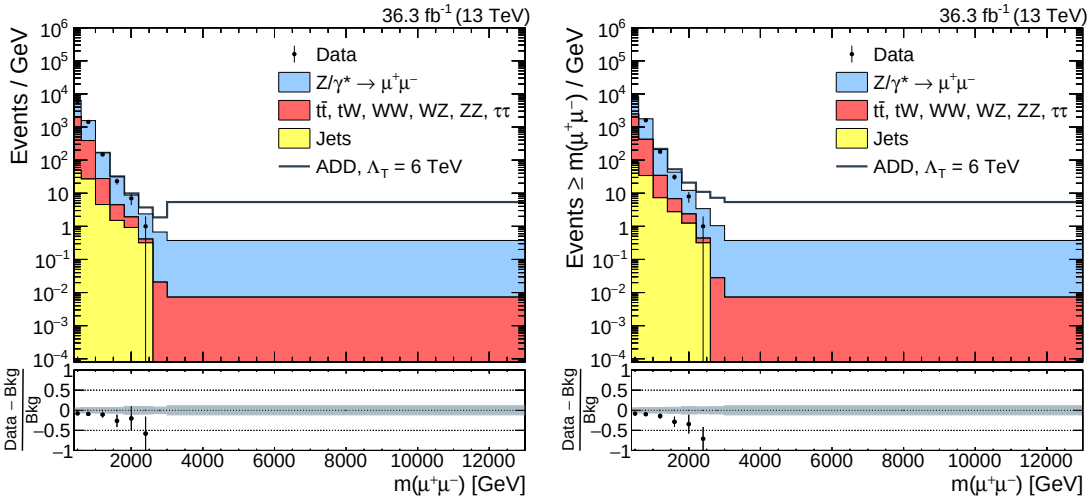

(a) (b)

FIGURE 11.10: Dimuon invariant mass spectrum for the search regions defined for large extra dimensions in the asymptotically safe scenario for quantum gravity. In (a) for the set of successive bins and in (b) for the cumulative ones.

With the search regions defined, the performance of the detector needs to be approximated for each considered mass range to be able to set model-independent limits for spin-2 gravitons. Starting with the efficiency to select signal events satisfying the acceptance requirements (Fig. 7.9), the data sets show little dependence on the invariant mass once the virtual graviton exchange process dominates. The efficiency is observed to be compatible with a mass-independent value of $\epsilon_{\text{Acceptance}} = (95 \pm 1)\,\%$. Using a signal sample of the AS scenario (with its DY contribution subtracted) as an example, figure 11.11 confirms that this compatibility holds true down to invariant masses of $m_{\mu\mu} > 400\,\text{GeV}$. The linear behavior shown by the efficiency of the full selection with respect to the events satisfying the acceptance requirements can be approximated by

$$\epsilon_{\text{Selection}} = 0.9404 \pm 0.0007 - (1.34 \pm 0.02) \times 10^{-5} m_{\mu\mu} / \text{GeV}. \tag{11.7}$$

While the product of the two efficiencies does depend on the shape of the signal, evaluating the parametrization at the center of each bin always provides a conservative estimate for monotonically falling spectra. With the exception of the statistical one, the impact of each considered source of uncertainty on the signal yield is minor (<5 %) as shown in table 10.1. The statistical uncertainty can become large, as discussed in the paragraph associated to the aforementioned table, when the predicted excess is small with respect to the DY contribution. By assigning a nuisance parameter of 10 % to the

signal hypothesis, this is taken into account.

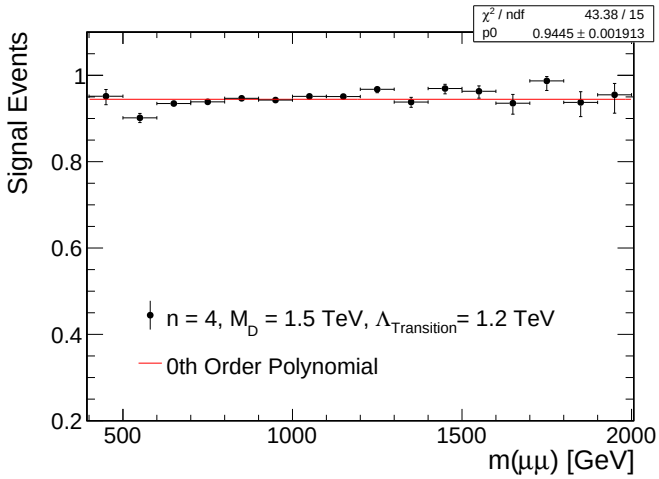

FIGURE 11.11: Selection efficiency of all produced events with respect to the acceptance requirements for low dimuon invariant masses. The signal sample of the AS scenario corresponds to the linear approximation of the transition between the infrared and ultraviolet regime and is produced with a dilepton invariant mass threshold of $m_{\ell\ell} > 300\,\text{GeV}$.

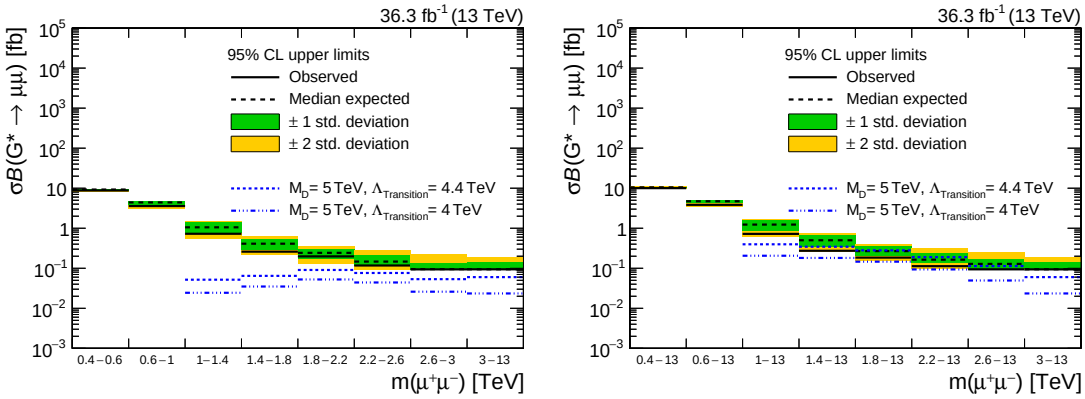

(a) (b)

FIGURE 11.12: Model-independent 95 % CL exclusion limits for spin-2 gravitons in the dimuon invariant mass ranges given on the x axis. In (a) for successive search regions and in (b) for cumulative ones. Signal contributions below their production threshold are omitted.

Having defined the selection efficiency and assigned an uncertainty, the model-independent 95 % CL exclusion limits for spin-2 gravitons can be calculated. They are shown in figure 11.12 for both sets of search regions alongside the predicted excess in terms of the cross sections for two parameter configurations. Following the discussion regarding the production of the ADD model data sets (Sec. 6.5), the signal samples are generated above a lower mass threshold to avoid a predominant production of DY events. This mass threshold is dynamically determined to ensure all relevant signal contributions are taken into account. Comparing the event yields predicted by the ADD model signals and the DY background in invariant mass bins of 50 GeV each, the first bin with significant signal contribution is shown in figure 11.13 as a function of Λ_T. In this context, a significant contribution is defined by a prediction constituting a relative excess of at least 2 % in the evaluated bin followed by an excess of 4 % or more in

the subsequent one. Given the observed similarity of the signals toward lower masses (Fig. 6.13), this approximately linear relation is used to estimate the lowest search region to be included in the evaluation. The final production threshold is given by the lower bound of the estimated region reduced by another 100 GeV to avoid "turn-on" effects.

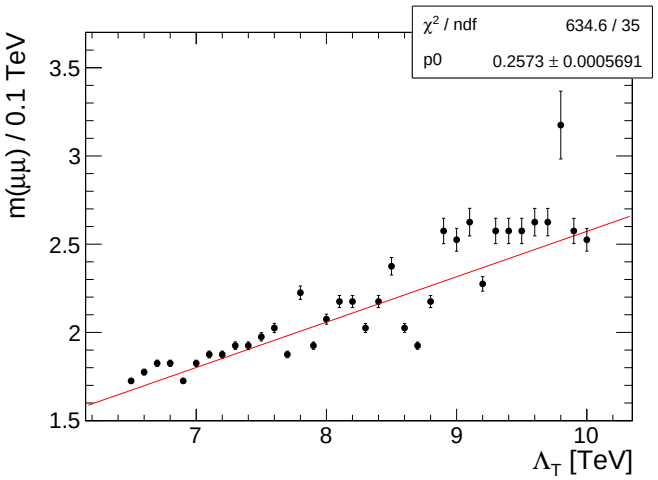

FIGURE 11.13: Center of the first bin with significant signal contributions determined using the simulated ADD model signals.

The two signal samples shown in figure 11.12 illustrate the procedure of finding the pair of transition scales between which the excluded value of $\Lambda_{\text{Transition}}$ lies for a fixed value of M_D. While the parameter point with the lower transition scale cannot be excluded in any search region, the other one can barely be excluded in two of them. Taking all transition scales in steps of 100 GeV up to (and slightly above) M_D into consideration, the search is chosen to start at an arbitrary value of $\Lambda_{\text{Transition}} \simeq 0.8 M_D$. By comparing the predicted cross section distribution of a given sample with the excluded values, the transition scale parameter space is iteratively narrowed down via a modified binary search algorithm. In case the predicted values exceed the excluded ones at any point, all considered transition scales larger than the current one are discarded. Conversely, all transition scales smaller than the current one are discarded should all predicted cross sections be lower than the excluded values. Using the central value of the remaining transition scales, allowing for slight biases depending on how large the differences between the predicted and excluded values are, the next sample is generated. The search concludes when only two values of $\Lambda_{\text{Transition}}$ remain. With respect to the relative difference of the predicted to the excluded cross sections, a linear interpolation between the two transition scales is performed to determine the final pair of M_D and $\Lambda_{\text{Transition}}$.

Based on the described approach, exclusion curves are determined in the two-dimensional M_D-$\Lambda_{\text{Transition}}$ plane. For each approximated behavior of the transition between the IR and UV regime, these curves are shown for 2 to 7 additional dimensions in figure 11.14. Following the discussion at the beginning of this section, the respective value of M_D serves as a guide for the largest considered transition scale. Each curve is therefore determined up to a value of the fundamental scale of gravity where the relation $M_D > \Lambda_{\text{Transition}}$ is no longer given. The dashed gray lines represent the threshold where both quantities are equal. Starting with low values of M_D, the 95 % CL exclusion curves are observed to be more stringent with respect to ascending numbers of extra dimensions n. This behavior matches both the theoretical prediction given in equation (3.16) and the limits for the ADD model (Tab. 11.3). However, as the window

for the transition widens for lower n (Sec. 3.4), its suppressive impact on the differential cross section also becomes more pronounced for lower interaction scales. The exclusion curves reflect this expectation as those corresponding to fewer extra dimensions become the least stringent ones for rising values of M_D; larger values of the latter imply a shift of signal contributions toward higher interaction scales, which enhances the impact of the suppression.

While the two-dimensional nature of the limits precludes a simple quantification of the improvement with respect to the exclusion curves obtained in the reinterpretation of the dilepton channel results at a center-of-mass of $\sqrt{s} = 8\,\text{TeV}$ (Fig. 3.5) [63], salient features can be compared. For the fundamental scale of gravity, the previously covered parameter space of $M_D > 2\,\text{TeV}$ is extended down to $M_D > 500\,\text{GeV}$. The delimiting threshold of the $M_D > \Lambda_{\text{Transition}}$ regime is exceeded at values of M_D between 3 to 4 TeV in the results of the reinterpretation. This is improved by 2 TeV in this analysis, extending the regime up to $M_D \simeq 5$–$6.5\,\text{TeV}$. The exclusion curves of the reinterpretation are also observed to be continuous because they are based on a single search region. As the presented statistical analysis takes multiple search regions into account (Fig. 11.12), slight variations can be seen in both the expected and observed limits. With the measurement being subject to statistical fluctuations, the corresponding variations are more pronounced. In conclusion, the derived 95 % CL exclusion limits benefit from the higher center-of-mass energy, larger integrated luminosity and the consideration of multiple search regions. Compared to the results of reinterpretation, they exhibit a larger curvature and are thus able to extend the existing bounds in the probed parameter space.

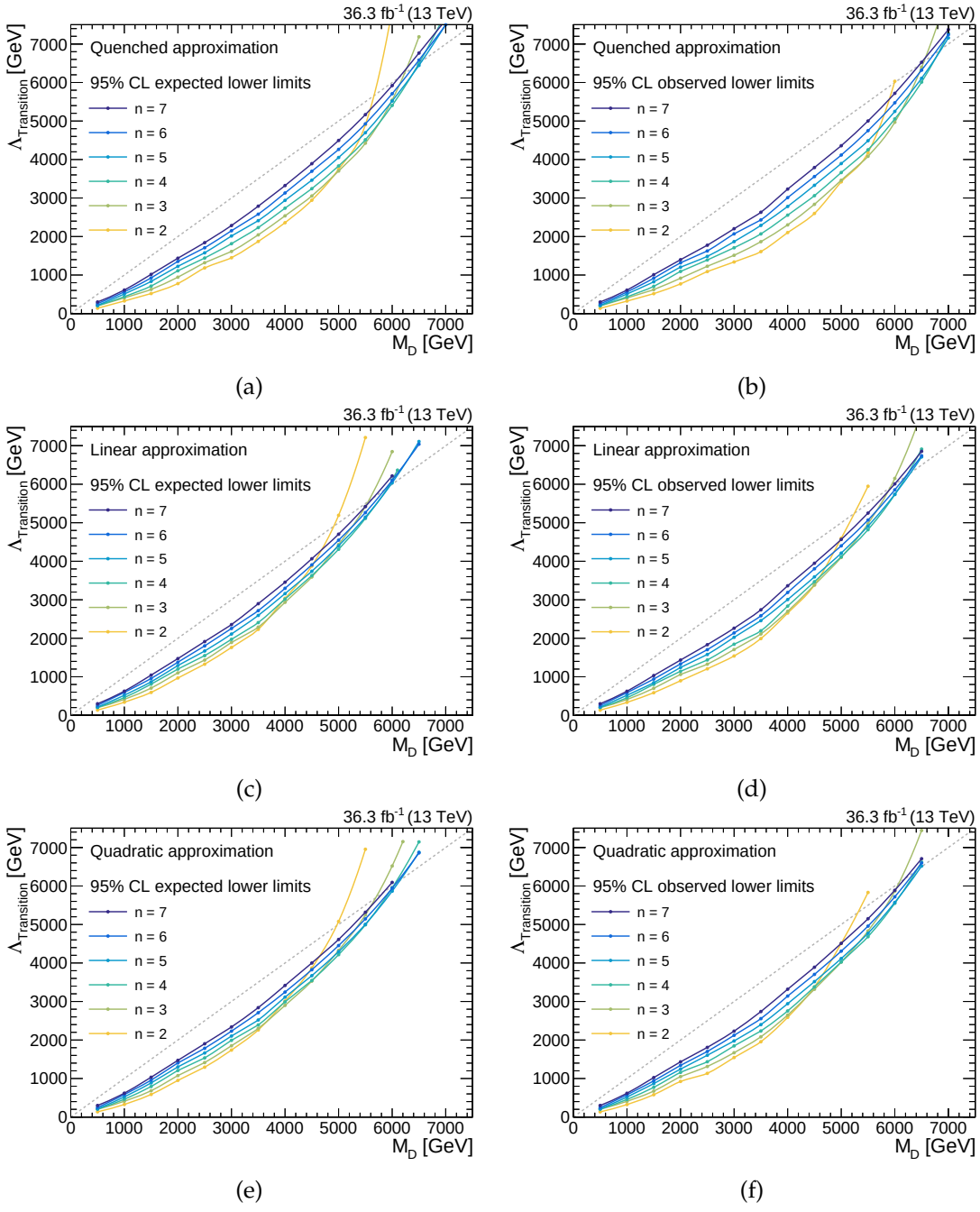

FIGURE 11.14: Exclusion curves at 95 % CL for the model of large extra dimensions in the asymptotically safe scenario for quantum gravity. The top row corresponds to the quenched approximation of the transition between the IR and UV energy regime, the middle row to the linear approximation and the bottom row to the quadratic one. Expected and observed exclusion curves are given in the left and right column, respectively.

Chapter 12

Future Prospects & Conclusion

In the final chapter of this analysis, a variety of additional studies are presented. They build upon the results of the preceding chapters, discussing the potential of searches for large extra dimensions in future measurements.

12.1 Discriminative Power of Angular Distributions

The difference between the angular distributions of the DY background and the virtual graviton exchange process of the ADD model has been highlighted in table 3.2 as well as depicted in figure 6.12 using the respective simulated data sets. Part of the discriminative power associated to the angular variables has already been exploited by evaluating the combination of multiple search regions in two pseudorapidity categories. Figure 12.1 shows the cosine of the CS angle split into the BB and BE category for dimuon invariant masses larger than 1.8 TeV to provide an overview of the remaining discriminative power. While it is possible to visually distinguish between the shapes of the signal and background distributions, it is a priori uncertain whether the difference is statistically significant. In order to quantify the potential impact of utilizing this angular variable to improve upon the limits derived by combining multiple likelihoods, the corresponding search regions are further subdivided. To minimize the impact of increasingly large statistical uncertainties, the division only differentiates between positive and negative values of $\cos\theta^*$. The resulting 95 % CL exclusion limit is displayed in figure 12.2. While minor differences are observed with respect to the bounds shown in figure 11.6a, most prominent toward high values of Λ_T, the excluded value of the UV cutoff parameter is unaffected within the statistical uncertainty of the limit calculation. Even though there is little benefit to further exploiting angular variables in the presented analysis, they still remain a valuable tool to test for deviations of the measurement from the SM prediction. Assuming that a sufficient amount of events will be recorded, they may also be used to differentiate between different types of mediator couplings (Sec. 3.2) in case of a discovery.

12.2 Extrapolations for Upcoming Measurements

Looking toward future measurements of proton–proton collisions provided by the LHC, two prominent benchmark scenarios exist. The first one marks the end of "Phase I", referring to the data-taking period which began in 2015 and for which a total integrated luminosity of 300 fb^{-1} is expected. After receiving numerous upgrades in preparation for the harsh conditions of the high luminosity LHC (HL-LHC), the experiments enter "Phase II" of data taking where a total integrated luminosity of 3000 fb^{-1} is expected to be reached. This constitutes the second benchmark scenario. While the experimental conditions are subject to change, in particular the increase of the center-of-mass energy

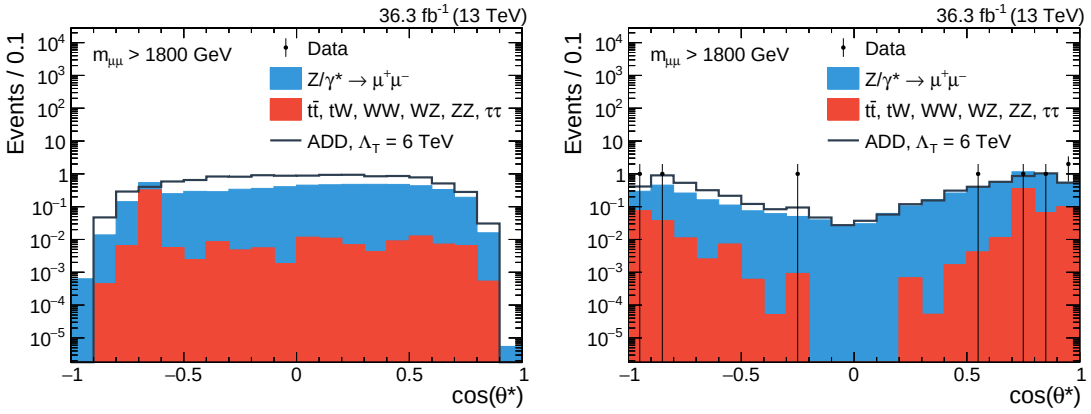

FIGURE 12.1: Cosine of the angle θ^* measured in the Collins–Soper frame for dimuon invariant masses above 1.8 TeV. In (a) and (b) for the BB and BE pseudorapidity category, respectively. No contributions of simulated jet-based backgrounds remain in the displayed phase space.

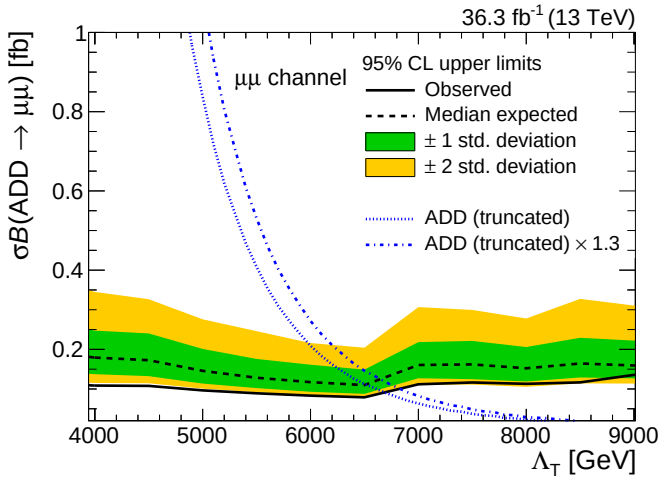

FIGURE 12.2: Exclusion limit at 95 % CL for the combination of multiple search regions split into two pseudorapidity and two Collins–Soper angle categories.

from 13 TeV to its initial design value of 14 TeV for the latter scenario, it is still worthwhile to provide rough extrapolations to quantify the expected sensitivities.

These sensitivities are expressed as expected limits determined with respect to the integrated luminosities of the two benchmark scenarios. As no sufficiently precise predictions are available, the detector conditions are assumed to remain comparable to the ones of the presented analysis for the sake of these studies. Starting with the first benchmark scenario, this assumption simplifies the extrapolation to scaling the predicted event yields with the expected luminosity of 300 fb^{-1} instead of the measured 36.3 fb^{-1}. To accommodate the increased yields, the considered combination of search regions is extended by an additional dedicated dimuon invariant mass region of 3 to 3.4 TeV. With an expected increase of 30 to 40 % in the differential cross section for masses above of 1.8 TeV[1], new data sets are necessary to facilitate a reliable extrapolation to $\mathcal{L} = 3000\,\text{fb}^{-1}$ at a center-of-mass energy of 14 TeV. These data sets are produced

[1]This estimate is the result of comparing the differential cross sections corresponding to the respective Drell–Yan invariant mass spectra generated via POWHEG BOX V2 and PYTHIA 8.2 above dimuon masses of 1.8 TeV at the two center-of-mass energies.

and restricted according to the acceptance requirements at generator-level. The detector response is then approximated by applying the measured and parametrized efficiency (Eq. 11.7). Their production threshold has been raised to $m_{\ell\ell} > 2.5\,\text{TeV}$ in order to, once again, avoid a predominant production of DY events and consequently ensure a statistically stable prediction. Adjusting the search regions accordingly, the mass range from 2.6 TeV to 4.2 TeV is divided in 400 GeV wide bins, with an additional bin covering masses from 4.2 TeV to the respective value of Λ_T. Both resulting estimates for the 95 % CL exclusion limits in the respective benchmark scenarios are shown in figure 12.3.

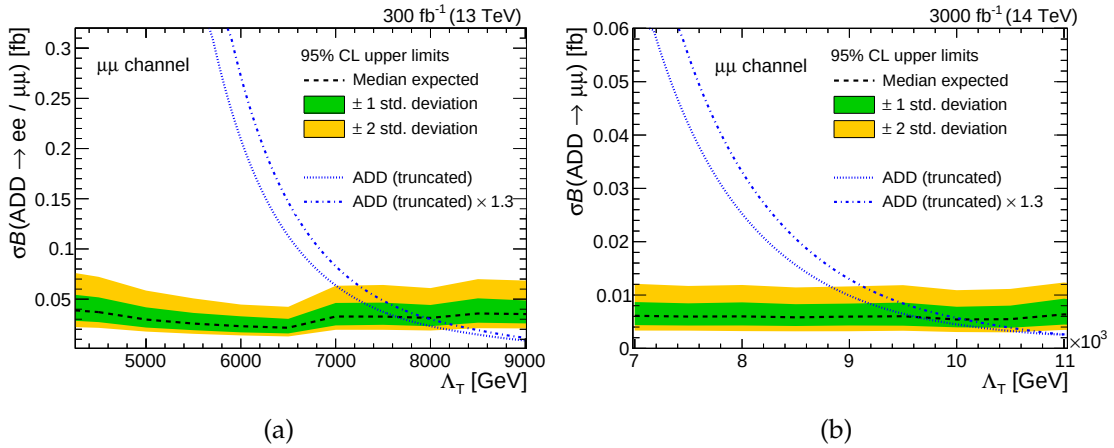

(a) (b)

FIGURE 12.3: Extrapolations of the 95 % CL exclusion limit based on the combination of multiple search regions. In (a) for an integrated luminosity of 300 fb^{-1} at $\sqrt{s}$ = 13 TeV and in (b) for 3000 fb^{-1} at $\sqrt{s}$ = 14 TeV.

Compared to the expected limit of the dimuon channel obtained in this analysis, the bound on Λ_T is expected to increase by 18 % to 7.7 TeV for the LO prediction in the 300 fb^{-1} scenario at $\sqrt{s}$ = 13 TeV. The corresponding estimate for 3000 fb^{-1} at $\sqrt{s}$ = 14 TeV predicts an improvement by 48 % to 9.6 TeV. With respect to the bound of $\Lambda_T > 7.5\,\text{TeV}$, determined in the combination of the dimuon, dielectron and diphoton channels (Tab. 11.3), the estimate for the dimuon channel in the 300 fb^{-1} scenario already constitutes a slight improvement. By raising both the center-of-mass energy and integrated luminosity in the second scenario, the aforementioned bound is expected to be extended by 28 % in the dimuon channel alone. In conclusion, even though the combination of multiple decay channels has not been taken into account, these estimates show that analyses at the given benchmark scenarios allow for a substantial expansion of the probed parameter space. While iterations of the analysis with small, incremental increases of the total integrated luminosity may not be considered worthwhile, one can summarize that at least two follow-up studies are necessary to fully utilize the potential of the LHC with respect to the ADD model.

12.3 Naturalness

In the context of high-energy particle physics, more specifically quantum field theories, the concept of "naturalness" is discussed with respect to the link between a low- and high-energy behavior of a theory. Proponents of naturalness claim that the parameters in the IR regime must not be (highly) sensitive to variations of those in the UV regime, with the latter being generally assumed to be more fundamental. This is also often referred to as a "decoupling" of the theory at high energies. As a corollary to the

descriptions being decoupled, the corresponding dimensionless coupling parameters of the theory are expected to be close to 1.

To quantify the fine-tuning of a particular observable O with respect to the parameters θ_i it depends upon, the Babieri–Giudice (BG) measure is one of the most intuitive and commonly used ones. It is defined as

$$\Delta_{\mathrm{BG}} = \max \left| \frac{\theta_i}{O} \frac{\mathrm{d}O}{\mathrm{d}\theta_i} \right|, \tag{12.1}$$

and can be applied to the expression for the Higgs boson mass given in equation (2.11) to provide numerical estimates of its fine-tuning. Using the global averages for boson and fermion masses as published by the Particle Data Group (Tab. 12.1), the fine-tuning as a function of the scale of BSM physics can thus be expressed as

$$\Delta_{\mathrm{BG}}\left(m_H^2\right) = \left| \frac{\Delta m_H^2}{m_H^2} \right| \simeq 3.3 \frac{\Lambda^2}{\mathrm{TeV}^2}. \tag{12.2}$$

Assuming the fundamental scale of gravity to be of the order of the HLZ convention UV cutoff parameter M_S, estimates of the fine-tuning for the respective number of extra dimensions n are given in table 12.2. Compared to the result corresponding to the Planck scale M_{Pl}, given in the caption of the table, a fundamental scale of gravity closer to the respective value of M_S would still be considered much more natural. However, specifying a threshold for Δ_{BG} below which a theory is considered to be natural is arbitrary. While more general and mathematically rigorous frameworks exist, e.g., Bayesian approaches to quantifying naturalness [156], declaring a model to be natural ultimately remains an aesthetic choice. This subjective element is an inherent aspect of the demand that parameters of the IR regime are supposed to remain insensitive to variations of those associated to the UV regime. The probability distribution according to which these variations would have to be evaluated is ultimately unknown.

Particle	Mass / GeV	
Top quark	173.0	± 0.4
Higgs boson	125.18	± 0.16
Z boson	91.1876	± 0.0021
W boson	80.379	± 0.012

Table 12.1: Masses of heavy bosons and fermions as published by the Particle Data Group [64].

Instances where the informal argument of naturalness could be used to successfully constrain the scale of BSM physics include the prediction of the positron and charm quark [157]. For the former, the argument arises when the estimated radius of the electron, derived by evaluating its electromagnetic energy in the particle rest frame, is compared against the measured upper bound. The observed disagreement could be due to a precise cancellation of the individual electromagnetic contributions or a modification of its potential (by the positron). While this deduction was formulated a posteriori to the discovery of the positron, the existence of the charm quark was predicted using measurements of the mixing between individual kaon states. An effective description of the mixing hinted at what is now known as the Glashow–Iliopoulos–Maiani (GIM) mechanism [158], describing suppressed flavor-changing neutral currents which require a fourth quark. On the other hand, quantum field theoretical predictions of the

	M_S					
Fine-tuning for channel	$n = 2$	$n = 3$	$n = 4$	$n = 5$	$n = 6$	$n = 7$
Δ_{BG} for $\mu\mu$	206	210	148	121	104	94
Δ_{BG} for $ee + \mu\mu$	209	212	150	123	106	95
Δ_{BG} for $ee + \mu\mu + \gamma\gamma$	285	277	196	160	138	124

TABLE 12.2: Quantification of the Higgs boson mass fine-tuning for different energy scales at which BSM physics processes are introduced. The observed 95 % CL exclusion bounds on M_S of the respective channels are used as representative values for the fundamental scale of gravity. For comparison, energy scales close to M_{Pl} correspond to $\Delta_{\mathrm{BG}} = 4.9 \times 10^{32}$.

vacuum energy density stand in stark contrast to the significantly lower experimentally observed value [157]. In the absence of solutions at energy scales compatible with the argument of naturalness, the aforementioned discrepancy illustrates that naturalness does not reliably predict the advent of new physics.

With respect to the scale dependence of the Higgs boson mass and the associated hierarchy problem, many theoretical approaches such as the introduction of large extra dimensions or supersymmetric extensions to SM physics were offering solutions at the TeV scale. Without discoveries to support these models, their parameter space becomes inadvertently restricted to values that would be considered unnatural. While offering a natural solution to the hierarchy problem does partly motivate the search for the existence of LED, the results of this thesis should not be used to discourage further studies given the discussed unreliability of this type of argument.

12.4 Conclusion

In summary, a search for large spatial extra dimensions in the ADD scenario and an asymptotically safe scenario for quantum gravity has been performed using the dimuon invariant mass spectrum. The search is based on proton-proton collisions produced by the LHC at a center-of-mass energy of $\sqrt{s} = 13\,\mathrm{TeV}$ and measured with the CMS experiment during the data-taking period of 2016. In total, the recorded amount of events corresponds to an integrated luminosity of $\mathcal{L} = 36.3\,\mathrm{fb}^{-1}$.

The expected background has been modeled to a high degree of precision, approximating the behavior of the dominant Drell–Yan process up to NNLO in QCD and NLO in EW, including photon-initiated contributions. Distinctive features of the signal models have been discussed; both theoretically and with respect to their simulation. Utilizing a dedicated set of selection criteria, the measured and simulated data sets have been pruned to ensure that only well reconstructed events are taken into account. The performance of the simulation, reconstruction and selection of events has been evaluated and the impacts of the corresponding sources of uncertainty on the event yields have been quantified.

As no excess with respect to the predicted background has been observed, bounds have been set on the signal cross sections and model parameters using Bayesian inference. By combining the results of the dimuon, dielectron and diphoton invariant mass spectrum analyses, the world's most sensitive analysis in nonhadronic decay channels of the ADD model has been performed. With respect to the bounds obtained in combination of the dimuon and dielectron channels at $\sqrt{s} = 8\,\mathrm{TeV}$, the 95 % CL exclusion limits on the model parameter have been improved by more than 80 %. Expressed in

the HLZ convention parameters, the bounds on M_S range from 9.3–6.1 TeV for 2 to 7 extra dimensions. Hadronic channels still provide the overall highest sensitivity for searches for large extra dimensions in the ADD scenario, with the CMS Collaboration's analysis of the dijet channel quoting the most stringent limits on M_S of 12 to 8.5 TeV in the same range of extra dimensions. In the asymptotically safe scenario for quantum gravity, two-dimensional bounds have been set in the plane spanned by the fundamental scale of gravity M_D and the transition scale $\Lambda_{\text{Transition}}$ for each approximation of the transition between the infrared and ultraviolet energy regime. The 95 % CL exclusion curves of the presented analysis improve upon those obtained in the reinterpretation of the results determined in the search for large extra dimensions at $\sqrt{s} = 8$ TeV in the considered $M_D > \Lambda_{\text{Transition}}$ regime. This regime is also extended by 60 % to values of the two quantities between 5–6.5 TeV for 2 to 7 additional dimensions. These bounds show that the fundamental scale of gravity in more complex models with large extra dimensions may be lower than suggested by the ADD model; in fact low enough to still be within the TeV range.

Two benchmark scenarios have been discussed to outline the parameter space to be explored in future analyses by extrapolating the ADD model bounds toward higher integrated luminosities. While part of the motivation to search for large extra dimensions is given by its more "natural" solution to the hierarchy problem, it has been reasoned that one should not be discouraged by the decreasing "naturalness" of the parameter configurations that have yet to be probed.

Appendix A

Event Yields of the Mass Spectrum

$m_{\mu\mu}$ / GeV	Observed	$Z/\gamma^* \to \mu\mu$	$t\bar{t}, tW, VV, \tau\tau$	Jets
Barrel-Barrel Category				
120–400	103 667	87 800 ± 4500	19 400 ± 1700	280 ± 140
400–600	1869	1480 ± 77	531 ± 48	12.4 ± 6.2
600–1000	470	417 ± 22	78.6 ± 8.8	10.0 ± 5.0
1000–1400	50	55.6 ± 2.9	6.0 ± 1.9	2.5 ± 1.3
1400–1800	12	11.91 ± 0.65	0.42 ± 0.06	0 ± 0
1800–2200	0	3.37 ± 0.19	0.39 ± 0.35	0.92 ± 0.46
2200–2600	0	1.023 ± 0.064	0.025 ± 0.006	0 ± 0
2600–3000	0	0.358 ± 0.023	0.006 ± 0.001	0 ± 0
>3000	0	0.214 ± 0.019	0.003 ± 0.001	0 ± 0
Barrel-Endcap Category				
120–400	140 602	131 000 ± 6900	22 000 ± 1900	540 ± 270
400–600	4043	2880 ± 150	1450 ± 140	37 ± 18
600–1000	955	757 ± 44	285 ± 40	16.9 ± 8.4
1000–1400	98	82.1 ± 5.0	17.2 ± 3.4	2.0 ± 1.0
1400–1800	11	14.8 ± 1.0	2.53 ± 0.68	1.51 ± 0.75
1800–2200	7	3.49 ± 0.26	0.60 ± 0.34	0 ± 0
2200–2600	1	0.941 ± 0.078	0.070 ± 0.023	0.32 ± 0.16
2600–3000	0	0.295 ± 0.027	0.015 ± 0.005	0 ± 0
>3000	0	0.153 ± 0.022	0.005 ± 0.002	0 ± 0
Total				
120–400	244 269	219 000 ± 11 000	41 300 ± 3600	820 ± 410
400–600	5129	4360 ± 230	1990 ± 190	50 ± 25
600–1000	1425	1170 ± 65	364 ± 48	26 ± 13
1000–1400	148	137.7 ± 7.7	23.2 ± 4.6	4.6 ± 2.3
1400–1800	23	26.7 ± 1.6	2.96 ± 0.74	1.51 ± 0.75
1800–2200	7	6.86 ± 0.43	1.00 ± 0.49	0.92 ± 0.46
2200–2600	1	1.96 ± 0.13	0.095 ± 0.027	0.32 ± 0.16
2600–3000	0	0.653 ± 0.047	0.021 ± 0.006	0 ± 0
>3000	0	0.367 ± 0.038	0.007 ± 0.003	0 ± 0

TABLE A.1: Number of dimuon events recorded with the CMS experiment in 2016 and their predicted counterparts in different invariant mass intervals. Events where both muons are measured in the barrel region are included in the barrel-barrel category; those where at least one muon is measured in the endcaps are part of the barrel-endcap one. All selection criteria and background corrections have been applied. Statistical and systematic uncertainties have been added in quadrature.

References

[1] Sheldon L. Glashow. "Partial Symmetries of Weak Interactions". In: *Nucl. Phys.* 22 (Feb. 1961), pp. 579–588. DOI: 10.1016/0029-5582(61)90469-2.

[2] Steven Weinberg. "A Model of Leptons". In: *Phys. Rev. Lett.* 19 (Nov. 1967), pp. 1264–1266. DOI: 10.1103/PhysRevLett.19.1264.

[3] Abdus Salam. "Weak and Electromagnetic Interactions". In: *Conf. Proc.* C680519 (May 1968), pp. 367–377.

[4] David J. Gross and Frank Wilczek. "Ultraviolet Behavior of Nonabelian Gauge Theories". In: *Phys. Rev. Lett.* 30 (June 1973), pp. 1343–1346. DOI: 10.1103/PhysRevLett.30.1343.

[5] H. David Politzer. "Reliable Perturbative Results for Strong Interactions?" In: *Phys. Rev. Lett.* 30 (June 1973), pp. 1346–1349. DOI: 10.1103/PhysRevLett.30.1346.

[6] Albert Einstein. "The Foundation of the General Theory of Relativity". In: *Annalen Phys.* 49.7 (1916), pp. 769–822. DOI: 10.1002/andp.19163540702. URL: http://dx.doi.org/10.1002/andp.200590044.

[7] Nima Arkani-Hamed, Savas Dimopoulos, and Gia Dvali. "Phenomenology, astrophysics and cosmology of theories with submillimeter dimensions and TeV scale quantum gravity". In: *Phys. Rev.* D59 (Mar. 1999), p. 086004. DOI: 10.1103/PhysRevD.59.086004. arXiv: hep-ph/9807344 [hep-ph].

[8] Nima Arkani-Hamed, Savas Dimopoulos, and Gia Dvali. "The Hierarchy problem and new dimensions at a millimeter". In: *Phys. Lett.* B429 (June 1998), pp. 263–272. DOI: 10.1016/S0370-2693(98)00466-3. arXiv: hep-ph/9803315 [hep-ph].

[9] Theodor Kaluza. "Zum Unitätsproblem der Physik". In: *Sitzungsber. Preuss. Akad. Wiss. Berlin (Math. Phys.)* 1921 (1921), pp. 966–972. arXiv: 1803.08616 [physics.hist-ph].

[10] Oscar Klein. "The Atomicity of Electricity as a Quantum Theory Law". In: *Nature* 118 (Oct. 1926), p. 516. DOI: 10.1038/118516a0.

[11] Oskar Klein. "Quantentheorie und fünfdimensionale Relativitätstheorie". In: *Zeitschrift für Physik* 37.12 (Dec. 1926), pp. 895–906. ISSN: 0044-3328. DOI: 10.1007/BF01397481.

[12] Ignatios Antoniadis and Karim Benakli. "Large dimensions and string physics in future colliders". In: *Int. J. Mod. Phys.* A15 (Oct. 2000), pp. 4237–4286. DOI: 10.1142/S0217751X00002170. arXiv: hep-ph/0007226 [hep-ph].

[13] Steven Weinberg. *Ultraviolet divergences in quantum theories of gravitation*. Ed. by Stephen Hawking and Werner Israel. Cambridge University Press, Aug. 1979. Chap. 16, pp. 790–831. ISBN: 9780521222853.

[14] CMS Collaboration. "Performance of the CMS muon detector and muon reconstruction with proton-proton collisions at $\sqrt{s}$ = 13 TeV". In: *JINST* 13.06 (June 2018), P06015. DOI: 10.1088/1748-0221/13/06/P06015. arXiv: 1804.04528 [physics.ins-det].

[15] David J. Griffiths. *Introduction to elementary particles*. Second edition. Wiley, 2008. ISBN: 9783527406012.

[16] Francis Halzen and Alan D. Martin. *Quarks and Leptons: An Introductory Course in Modern particle physics*. Wiley, 1984. ISBN: 9780471887416.

[17] Richard P. Feynman. "Space - time approach to quantum electrodynamics". In: *Phys. Rev.* 76 (Sept. 1949), pp. 769–789. DOI: 10.1103/PhysRev.76.769.

[18] John C. Collins, Davison E. Soper, and George F. Sterman. "Factorization of Hard Processes in QCD". In: *Adv. Ser. Direct. High Energy Phys.* 5 (July 1989), pp. 1–91. DOI: 10.1142/9789814503266_0001. arXiv: hep-ph/0409313 [hep-ph].

[19] Richard D. Ball et al. "Parton distributions for the LHC Run II". In: *JHEP* 04 (Apr. 2015), p. 040. DOI: 10.1007/JHEP04(2015)040. arXiv: 1410.8849 [hep-ph].

[20] Yuri L. Dokshitzer. "Calculation of the Structure Functions for Deep Inelastic Scattering and e+ e- Annihilation by Perturbation Theory in Quantum Chromodynamics." In: *Sov. Phys. JETP* 46 (1977). [Zh. Eksp. Teor. Fiz. 73, 1216], pp. 641–653.

[21] Vladimir N. Gribov and Lev N. Lipatov. "Deep inelastic e p scattering in perturbation theory". In: *Sov. J. Nucl. Phys.* 15 (1972). [Yad. Fiz. 15, 781], pp. 438–450.

[22] Guido Altarelli and Giorgio Parisi. "Asymptotic Freedom in Parton Language". In: *Nucl. Phys.* B126 (Aug. 1977), pp. 298–318. DOI: 10.1016/0550-3213(77)90384-4.

[23] Sidney D. Drell and Tung-Mow Yan. "Massive Lepton-Pair Production in Hadron-Hadron Collisions at High Energies". In: *Phys. Rev. Lett.* 25 (5 Aug. 1970), pp. 316–320. DOI: 10.1103/PhysRevLett.25.316. Erratum in "Massive Lepton-Pair Production in Hadron-Hadron Collisions at High Energies". In: *Phys. Rev. Lett.* 25 (13 Sept. 1970), pp. 902–902. DOI: 10.1103/PhysRevLett.25.902.2.

[24] CMS Collaboration. "Angular coefficients of Z bosons produced in pp collisions at $\sqrt{s}$ = 8 TeV and decaying to $\mu^+\mu^-$ as a function of transverse momentum and rapidity". In: *Phys. Lett.* B750 (Nov. 2015), pp. 154–175. DOI: 10.1016/j.physletb.2015.08.061. arXiv: 1504.03512 [hep-ex].

[25] John C. Collins and Davison E. Soper. "Angular distribution of dileptons in high-energy hadron collisions". In: *Phys. Rev. D* 16 (7 Oct. 1977), pp. 2219–2225. DOI: 10.1103/PhysRevD.16.2219.

[26] Erwin Mirkes and James Ohnemus. "W and Z polarization effects in hadronic collisions". In: *Phys. Rev.* D50 (Nov. 1994), pp. 5692–5703. DOI: 10.1103/PhysRevD.50.5692. arXiv: hep-ph/9406381 [hep-ph].

[27] CMS Collaboration. "Forward-backward asymmetry of Drell-Yan lepton pairs in pp collisions at $\sqrt{s}$ = 7 TeV". In: *Phys. Lett.* B718 (Jan. 2013), pp. 752–772. DOI: 10.1016/j.physletb.2012.10.082. arXiv: 1207.3973 [hep-ex].

[28] CMS Collaboration. "Measurement of the weak mixing angle using the forward–backward asymmetry of Drell–Yan events in pp collisions at 8 TeV". In: *Eur. Phys. J.* C78.9 (Sept. 2018), p. 701. DOI: 10.1140/epjc/s10052-018-6148-7. arXiv: 1806.00863 [hep-ex].

[29] Tom W. B. Kibble. "Symmetry Breaking in Non-Abelian Gauge Theories". In: *Phys. Rev.* 155 (5 Mar. 1967), pp. 1554–1561. DOI: 10.1103/PhysRev.155.1554.

[30] Peter W. Higgs. "Spontaneous Symmetry Breakdown without Massless Bosons". In: *Phys. Rev.* 145 (4 May 1966), pp. 1156–1163. DOI: 10.1103/PhysRev.145.1156.

[31] François Englert and Robert Brout. "Broken Symmetry and the Mass of Gauge Vector Mesons". In: *Phys. Rev. Lett.* 13 (9 Aug. 1964), pp. 321–323. DOI: 10.1103/PhysRevLett.13.321.

[32] Peter W. Higgs. "Broken symmetries, massless particles and gauge fields". In: *Physics Letters* 12.2 (Sept. 1964), pp. 132–133. ISSN: 0031-9163. DOI: 10.1016/0031-9163(64)91136-9.

[33] Peter W. Higgs. "Broken Symmetries and the Masses of Gauge Bosons". In: *Phys. Rev. Lett.* 13 (16 Oct. 1964), pp. 508–509. DOI: 10.1103/PhysRevLett.13.508.

[34] Gerald S. Guralnik, C. Richard Hagen, and Tom W. B. Kibble. "Global Conservation Laws and Massless Particles". In: *Phys. Rev. Lett.* 13 (20 Nov. 1964), pp. 585–587. DOI: 10.1103/PhysRevLett.13.585.

[35] CMS Collaboration. "Observation of a new boson at a mass of 125 GeV with the CMS experiment at the LHC". In: *Phys. Lett.* B716 (Sept. 2012), pp. 30–61. DOI: 10.1016/j.physletb.2012.08.021. arXiv: 1207.7235 [hep-ex].

[36] ATLAS Collaboration. "Observation of a new particle in the search for the Standard Model Higgs boson with the ATLAS detector at the LHC". In: *Phys. Lett.* B716 (Sept. 2012), pp. 1–29. DOI: 10.1016/j.physletb.2012.08.020. arXiv: 1207.7214 [hep-ex].

[37] CMS Collaboration. "Precise determination of the mass of the Higgs boson and tests of compatibility of its couplings with the standard model predictions using proton collisions at 7 and 8 TeV". In: *Eur. Phys. J.* C75.5 (May 2015), p. 212. DOI: 10.1140/epjc/s10052-015-3351-7. arXiv: 1412.8662 [hep-ex].

[38] CMS Collaboration. "Constraints on the spin-parity and anomalous HVV couplings of the Higgs boson in proton collisions at 7 and 8 TeV". In: *Phys. Rev.* D92.1 (July 2015), p. 012004. DOI: 10.1103/PhysRevD.92.012004. arXiv: 1411.3441 [hep-ex].

[39] CMS Collaboration. "Measurements of properties of the Higgs boson decaying into the four-lepton final state in pp collisions at $\sqrt{s}$ = 13 TeV". In: *JHEP* 11 (Nov. 2017), p. 047. DOI: 10.1007/JHEP11(2017)047. arXiv: 1706.09936 [hep-ex].

[40] Abdelhak Djouadi. "The Anatomy of electro-weak symmetry breaking. I: The Higgs boson in the standard model". In: *Phys. Rept.* 457 (Feb. 2008), pp. 1–216. DOI: 10.1016/j.physrep.2007.10.004. arXiv: hep-ph/0503172 [hep-ph].

[41] Edward Witten. "String theory dynamics in various dimensions". In: *Nucl. Phys.* B443 (June 1995), pp. 85–126. DOI: 10.1016/0550-3213(95)00158-O. arXiv: hep-th/9503124 [hep-th].

[42] Michael J. Duff. "M theory (The Theory formerly known as strings)". In: *Int. J. Mod. Phys.* A11 (Dec. 1996), pp. 5623–5642. DOI: 10.1142/S0217751X96002583. arXiv: hep-th/9608117 [hep-th].

[43] Thomas Appelquist, Hsin-Chia Cheng, and Bogdan A. Dobrescu. "Bounds on universal extra dimensions". In: *Phys. Rev.* D64 (June 2001), p. 035002. DOI: 10.1103/PhysRevD.64.035002. arXiv: hep-ph/0012100 [hep-ph].

[44] Lisa Randall and Raman Sundrum. "A Large mass hierarchy from a small extra dimension". In: *Phys. Rev. Lett.* 83 (Oct. 1999), pp. 3370–3373. DOI: 10.1103/PhysRevLett.83.3370. arXiv: hep-ph/9905221 [hep-ph].

[45] Hsin-Chia Cheng. "Introduction to Extra Dimensions". In: *Physics of the large and the small, TASI 09, proceedings of the Theoretical Advanced Study Institute in Elementary Particle Physics, Boulder, Colorado, USA, 1-26 June 2009*. Mar. 2011, pp. 125–162. DOI: 10.1142/9789814327183_0003. arXiv: 1003.1162 [hep-ph].

[46] Graham D. Kribs. "TASI 2004 lectures on the phenomenology of extra dimensions". In: *Physics in D >= 4. Proceedings, Theoretical Advanced Study Institute in elementary particle physics, TASI 2004, Boulder, USA, June 6-July 2, 2004*. May 2006, pp. 633–699. arXiv: hep-ph/0605325 [hep-ph].

[47] Gian F. Giudice, Riccardo Rattazzi, and James D. Wells. "Quantum gravity and extra dimensions at high-energy colliders". In: *Nucl. Phys.* B544 (Apr. 1999), pp. 3–38. DOI: 10.1016/S0550-3213(99)00044-9. arXiv: hep-ph/9811291 [hep-ph].

[48] Tao Han, Joseph D. Lykken, and Ren-Jie Zhang. "On Kaluza-Klein states from large extra dimensions". In: *Phys. Rev.* D59 (Mar. 1999), p. 105006. DOI: 10.1103/PhysRevD.59.105006. arXiv: hep-ph/9811350 [hep-ph].

[49] JoAnne L. Hewett. "Indirect collider signals for extra dimensions". In: *Phys. Rev. Lett.* 82 (June 1999), pp. 4765–4768. DOI: 10.1103/PhysRevLett.82.4765. arXiv: hep-ph/9811356 [hep-ph].

[50] Roberto Percacci. "A Short introduction to asymptotic safety". In: *Time and Matter: Proceedings, 3rd International Conference, TAM2010, Budva, Montenegro, 4-8 October, 2010*. Oct. 2011, pp. 123–142. arXiv: 1110.6389 [hep-th].

[51] Daniel F. Litim. "Fixed points of quantum gravity". In: *Phys. Rev. Lett.* 92 (May 2004), p. 201301. DOI: 10.1103/PhysRevLett.92.201301. arXiv: hep-th/0312114 [hep-th].

[52] Erik Gerwick, Daniel F. Litim, and Tilman Plehn. "Asymptotic safety and Kaluza-Klein gravitons at the LHC". In: *Phys. Rev.* D83 (Apr. 2011), p. 084048. DOI: 10.1103/PhysRevD.83.084048. arXiv: 1101.5548 [hep-ph].

[53] Roberto Franceschini et al. "LHC bounds on large extra dimensions". In: *JHEP* 05 (May 2011), p. 092. DOI: 10.1007/JHEP05(2011)092. arXiv: 1101.4919 [hep-ph].

[54] Robert Cousins et al. "Spin discrimination of new heavy resonances at the LHC". In: *JHEP* 11 (Nov. 2005), p. 046. DOI: 10.1088/1126-6708/2005/11/046.

[55] Cheng-Wei Chiang et al. "Discovery in Drell-Yan Processes at the LHC". In: *Phys. Rev.* D85 (Jan. 2012), p. 015023. DOI: 10.1103/PhysRevD.85.015023. arXiv: 1107.5830 [hep-ph].

[56] John F. Donoghue. "Introduction to the effective field theory description of gravity". In: *Advanced School on Effective Theories Almunecar, Spain, June 25-July 1, 1995*. Dec. 1995. arXiv: gr-qc/9512024 [gr-qc].

[57] Gerard 't Hooft and Martinus J. G. Veltman. "One loop divergencies in the theory of gravitation". In: *Ann. Inst. H. Poincare Phys. Theor.* A20 (1974), pp. 69–94.

[58] Marc H. Goroff and Augusto Sagnotti. "The Ultraviolet Behavior of Einstein Gravity". In: *Nucl. Phys.* B266 (Mar. 1986), pp. 709–736. DOI: 10.1016/0550-3213(86)90193-8.

[59] Martin Reuter. "Nonperturbative evolution equation for quantum gravity". In: *Phys. Rev.* D57 (Jan. 1998), pp. 971–985. DOI: 10.1103/PhysRevD.57.971. arXiv: hep-th/9605030 [hep-th].

[60] Christof Wetterich. "Exact evolution equation for the effective potential". In: *Phys. Lett.* B301 (Feb. 1993), pp. 90–94. DOI: 10.1016/0370-2693(93)90726-X. arXiv: 1710.05815 [hep-th].

[61] Tim R. Morris. "The Exact renormalization group and approximate solutions". In: *Int. J. Mod. Phys.* A9 (June 1994), pp. 2411–2450. DOI: 10.1142/S0217751X94000972. arXiv: hep-ph/9308265 [hep-ph].

[62] Alessandro Codello, Roberto Percacci, and Christoph Rahmede. "Ultraviolet properties of f(R)-gravity". In: *Int. J. Mod. Phys.* A23 (Jan. 2008), pp. 143–150. DOI: 10.1142/S0217751X08038135. arXiv: 0705.1769 [hep-th].

[63] Henning Sedello. "Collider physics in anticipation of new TeV-scale phenomena". PhD thesis. Technische Universität Dortmund, Mar. 2014. DOI: 10.17877/de290r-453.

[64] Particle Data Group. "Review of Particle Physics". In: *Phys. Rev.* D98.3 (Aug. 2018), p. 030001. DOI: 10.1103/PhysRevD.98.030001.

[65] Eric G. Adelberger et al. "Torsion balance experiments: A low-energy frontier of particle physics". In: *Prog. Part. Nucl. Phys.* 62 (Jan. 2009), pp. 102–134. DOI: 10.1016/j.ppnp.2008.08.002.

[66] Christoph Hanhart et al. "The Likelihood of GODs' existence: Improving the SN1987a constraint on the size of large compact dimensions". In: *Phys. Lett.* B509 (June 2001), pp. 1–9. DOI: 10.1016/S0370-2693(01)00544-5. arXiv: astro-ph/0102063 [astro-ph].

[67] Steen Hannestad and Georg G. Raffelt. "Supernova and neutron star limits on large extra dimensions reexamined". In: *Phys. Rev.* D67 (Apr. 2003), p. 125008. DOI: 10.1103/PhysRevD.67.125008. arXiv: hep-ph/0304029 [hep-ph]. Erratum in "Erratum: Supernova and neutron-star limits on large extra dimensions reexamined". In: *Phys. Rev. D* 69 (2 Jan. 2004), p. 029901. DOI: 10.1103/PhysRevD.69.029901.

[68] Ambreesh K. Gupta, Naba K. Mondal, and Sreerup Raychaudhuri. "Constraining large extra dimensions using dilepton data from the Tevatron collider". In: *arXiv e-prints* (Apr. 1999). arXiv: hep-ph/9904234 [hep-ph].

[69] CMS Collaboration. "Search for new physics in final states with an energetic jet or a hadronically decaying W or Z boson and transverse momentum imbalance at $\sqrt{s}$ = 13 TeV". In: *Phys. Rev.* D97.9 (May 2018), p. 092005. DOI: 10.1103/PhysRevD.97.092005. arXiv: 1712.02345 [hep-ex].

[70] ATLAS Collaboration. "Search for dark matter and other new phenomena in events with an energetic jet and large missing transverse momentum using the ATLAS detector". In: *JHEP* 01 (Jan. 2018), p. 126. DOI: 10.1007/JHEP01(2018)126. arXiv: 1711.03301 [hep-ex].

[71] CMS Collaboration. "Search for new physics in dijet angular distributions using proton-proton collisions at $\sqrt{s}$ = 13 TeV and constraints on dark matter and other models". In: *Submitted to Eur. J. Phys. C* (Mar. 2018). arXiv: 1803.08030 [hep-ex].

[72] CMS Collaboration. "Search for physics beyond the standard model in high-mass diphoton events from proton-proton collisions at $\sqrt{s}$ = 13 TeV". In: *Submitted to Phys. Rev.* (2018). arXiv: 1809.00327 [hep-ex].

[73] CMS Collaboration. "Search for physics beyond the standard model in dilepton mass spectra in proton-proton collisions at $\sqrt{s}$ = 8 TeV". In: *JHEP* 04 (Apr. 2015), p. 025. DOI: 10.1007/JHEP04(2015)025. arXiv: 1412.6302 [hep-ex].

[74] Maximilien Brice. "Aerial View of the CERN taken in 2008". July 2008. URL: https://cds.cern.ch/record/1295244.

[75] Lyndon Evans and Philip Bryant. "LHC Machine". In: *JINST* 3 (Aug. 2008), S08001. DOI: 10.1088/1748-0221/3/08/S08001.

[76] Esma Mobs. "The CERN accelerator complex. Complexe des accélérateurs du CERN". July 2016. URL: https://cds.cern.ch/record/2197559.

[77] Ezio Todesco et al. "Training Behavior of the Main Dipoles in the Large Hadron Collider". In: *IEEE Trans. Appl. Supercond.* 27.4 (Jan. 2017), p. 4702807. DOI: 10.1109/TASC.2017.2657504.

[78] CMS Luminosity Physics Object Group. *CMS Luminosity — Public Results*. 2016. URL: https://twiki.cern.ch/twiki/bin/view/CMSPublic/LumiPublicResults (visited on 08/19/2018).

[79] ALICE Collaboration. "The ALICE experiment at the CERN LHC". In: *JINST* 3 (Aug. 2008), S08002. DOI: 10.1088/1748-0221/3/08/S08002.

[80] LHCb Collaboration. "The LHCb Detector at the LHC". In: *JINST* 3 (Aug. 2008), S08005. DOI: 10.1088/1748-0221/3/08/S08005.

[81] CMS Collaboration. "The CMS Experiment at the CERN LHC". In: *JINST* 3 (Aug. 2008), S08004. DOI: 10.1088/1748-0221/3/08/S08004.

[82] ATLAS Collaboration. "The ATLAS Experiment at the CERN Large Hadron Collider". In: *JINST* 3 (Aug. 2008), S08003. DOI: 10.1088/1748-0221/3/08/S08003.

[83] Tai Sakuma and Thomas McCauley. "Detector and Event Visualization with SketchUp at the CMS Experiment". In: *Journal of Physics: Conference Series* 513.2 (2014), p. 022032. URL: http://stacks.iop.org/1742-6596/513/i=2/a=022032.

[84] Giovanni Abbiendi. "The CMS muon system in Run2: preparation, status and first results". In: *PoS* EPS-HEP2015 (2015), p. 237. DOI: 10.22323/1.234.0237. arXiv: 1510.05424 [physics.ins-det].

[85] CMS Collaboration. "The performance of the CMS muon detector in proton-proton collisions at sqrt(s) = 7 TeV at the LHC". In: *JINST* 8 (Nov. 2013), P11002. DOI: 10.1088/1748-0221/8/11/P11002. arXiv: 1306.6905 [physics.ins-det].

[86] CMS Collaboration. *CMS Technical Design Report for the Level-1 Trigger Upgrade*. Tech. rep. CERN-LHCC-2013-011. CMS-TDR-12. June 2013. URL: https://cds.cern.ch/record/1556311.

[87] CMS Collaboration. "The CMS Level-1 trigger system for LHC Run II". In: *JINST* 12.03 (Mar. 2017), p. C03021. DOI: 10.1088/1748-0221/12/03/C03021.

[88] Christoph Eck et al. *LHC computing Grid: Technical Design Report*. Technical Design Report LCG. Geneva: CERN, June 2005. URL: https://cds.cern.ch/record/840543.

[89] Giovanni Abbiendi et al. "Muon Reconstruction in the CMS Detector". 2008. URL: http://cms.cern.ch/iCMS/jsp/db_notes/noteInfo.jsp?cmsnoteid=CMS%5C%20AN-2008/097.

[90] Rudolf Frühwirth and Rudolf K. Bock. "Data analysis techniques for high-energy physics experiments". In: *Camb. Monogr. Part. Phys. Nucl. Phys. Cosmol.* 11 (2000). Ed. by Hartwig Grote, Dieter Notz, and Meinhard Regler, pp. 1–434.

[91] Hans Bethe. "Zur Theorie des Durchgangs Schneller Korpuskularstrahlen durch Materie". In: *Annalen der Physik* 397 (1930), pp. 325–400. DOI: 10.1002/andp.19303970303.

[92] Felix Bloch. "Zur Bremsung Rasch Bewegter Teilchen beim Durchgang durch Materie". In: *Annalen der Physik* 408 (1933), pp. 285–320. DOI: 10.1002/andp.19334080303.

[93] CMS Collaboration. "Description and performance of track and primary-vertex reconstruction with the CMS tracker". In: *JINST* 9.10 (Oct. 2014), P10009. DOI: 10.1088/1748-0221/9/10/P10009. arXiv: 1405.6569 [physics.ins-det].

[94] Rudolf Frühwirth. "Application of Kalman filtering to track and vertex fitting". In: *Nucl. Instrum. Meth.* A262 (Dec. 1987), pp. 444–450. DOI: 10.1016/0168-9002(87)90887-4.

[95] CMS Collaboration. *Technical Proposal for the Phase-II Upgrade of the CMS Detector*. Tech. rep. CERN-LHCC-2015-010. LHCC-P-008. CMS-TDR-15-02. Geneva, June 2015. URL: https://cds.cern.ch/record/2020886.

[96] CMS Collaboration. *CMS Offline Software*. 2018. URL: https://github.com/cms-sw/cmssw (visited on 07/18/2018). Restricted.

[97] CMS Collaboration. *CMS computing: Technical Design Report*. Technical Design Report CMS. Geneva: CERN, 2005. URL: https://cds.cern.ch/record/838359.

[98] CMS Calibration & Alignment Team. *Global Tags for Conditions Data*. 2018. URL: https://twiki.cern.ch/twiki/bin/view/CMSPublic/SWGuideFrontierConditions (visited on 07/18/2018). Restricted.

[99] Physics Institute III A, RWTH Aachen University. *TAPAS — Three A Physics Analysis Software*. 2018. URL: https://gitlab.cern.ch/aachen-3a (visited on 09/10/2018). Restricted.

[100] CMS Collaboration. "Search for resonant and nonresonant Higgs boson pair production in the $b\bar{b}\ell\nu\ell\nu$ final state in proton-proton collisions at $\sqrt{s} = 13$ TeV". In: *JHEP* 01 (Jan. 2018), p. 054. DOI: 10.1007/JHEP01(2018)054. arXiv: 1708.04188 [hep-ex].

[101] Sébastien Brochet et al. *Muons trigger efficiencies using T&P method for $HH \to bbWW \to bb\ell\ell\nu\nu$*. 2017. URL: https://indico.cern.ch/event/615185/#10-double-muon-trigger-efficie (visited on 09/10/2018). Restricted.

[102] CMS Collaboration. "Search for High-Mass Resonances Decaying to Muon Pairs in pp Collisions at $\sqrt{s} = 13$ TeV with the full 2016 data set of 37 fb and combination with 2015 result". 2016. URL: http://cms.cern.ch/iCMS/jsp/db_notes/noteInfo.jsp?cmsnoteid=CMS%5C%20AN-2016/391.

[103] Tim Bray. *The JavaScript Object Notation (JSON) Data Interchange Format*. RFC 8259. Dec. 2017. DOI: 10.17487/RFC8259.

[104] CMS Collaboration. *CMS Luminosity Measurements for the 2016 Data Taking Period*. Tech. rep. CMS-PAS-LUM-17-001. Geneva: CERN, 2017. URL: http://cds.cern.ch/record/2257069.

[105] CMS Collaboration. *Performance of muon reconstruction including Alignment Position Errors for 2016 Collision Data*. Tech. rep. CMS-DP-2016-067. Geneva: CERN, Nov. 2016. URL: https://cds.cern.ch/record/2229697.

[106] Andy Buckley et al. "LHAPDF6: parton density access in the LHC precision era". In: *Eur. Phys. J.* C75 (Mar. 2015), p. 132. DOI: 10.1140/epjc/s10052-015-3318-8. arXiv: 1412.7420 [hep-ph].

[107] Andy Buckley et al. "General-purpose event generators for LHC physics". In: *Phys. Rept.* 504 (July 2011), pp. 145–233. DOI: 10.1016/j.physrep.2011.03.005. arXiv: 1101.2599 [hep-ph].

[108] GEANT4 Collaboration. "GEANT4: A Simulation toolkit". In: *Nucl. Instrum. Meth.* A506 (July 2003), pp. 250–303. DOI: 10.1016/S0168-9002(03)01368-8.

[109] GEANT4 Collaboration. "Geant4 developments and applications". In: *IEEE Trans. Nucl. Sci.* 53 (Feb. 2006), p. 270. DOI: 10.1109/TNS.2006.869826.

[110] GEANT4 Collaboration. "Recent developments in Geant4". In: *Nuclear Instruments and Methods in Physics Research Section A: Accelerators, Spectrometers, Detectors and Associated Equipment* 835 (Nov. 2016), pp. 186–225. ISSN: 0168-9002. DOI: 10.1016/j.nima.2016.06.125.

[111] Paolo Nason. "A New method for combining NLO QCD with shower Monte Carlo algorithms". In: *JHEP* 11 (Dec. 2004), p. 040. DOI: 10.1088/1126-6708/2004/11/040. arXiv: hep-ph/0409146 [hep-ph].

[112] Stefano Frixione, Paolo Nason, and Carlo Oleari. "Matching NLO QCD computations with Parton Shower simulations: the POWHEG method". In: *JHEP* 11 (Nov. 2007), p. 070. DOI: 10.1088/1126-6708/2007/11/070. arXiv: 0709.2092 [hep-ph].

[113] Simone Alioli et al. "NLO vector-boson production matched with shower in POWHEG". In: *JHEP* 07 (July 2008), p. 060. DOI: 10.1088/1126-6708/2008/07/060. arXiv: 0805.4802 [hep-ph].

[114] Simone Alioli et al. "A general framework for implementing NLO calculations in shower Monte Carlo programs: the POWHEG BOX". In: *JHEP* 06 (June 2010), p. 043. DOI: 10.1007/JHEP06(2010)043. arXiv: 1002.2581 [hep-ph].

[115] Torbjörn Sjöstrand et al. "An Introduction to PYTHIA 8.2". In: *Comput. Phys. Commun.* 191 (June 2015), pp. 159–177. DOI: 10.1016/j.cpc.2015.01.024. arXiv: 1410.3012 [hep-ph].

[116] Johan Alwall et al. "The automated computation of tree-level and next-to-leading order differential cross sections, and their matching to parton shower simulations". In: *JHEP* 07 (July 2014), p. 079. DOI: 10.1007/JHEP07(2014)079. arXiv: 1405.0301 [hep-ph].

[117] Johan Alwall et al. "Comparative study of various algorithms for the merging of parton showers and matrix elements in hadronic collisions". In: *Eur. Phys. J.* C53 (Feb. 2008), pp. 473–500. DOI: 10.1140/epjc/s10052-007-0490-5. arXiv: 0706.2569 [hep-ph].

[118] Ye Li and Frank Petriello. "Combining QCD and electroweak corrections to dilepton production in FEWZ". In: *Phys. Rev.* D86 (Nov. 2012), p. 094034. DOI: 10.1103/PhysRevD.86.094034. arXiv: 1208.5967 [hep-ph].

[119] Michal Czakon and Alexander Mitov. "Top++: A Program for the Calculation of the Top-Pair Cross-Section at Hadron Colliders". In: *Comput. Phys. Commun.* 185 (Nov. 2014), p. 2930. DOI: 10.1016/j.cpc.2014.06.021. arXiv: 1112.5675 [hep-ph].

[120] Richard D. Ball et al. "Parton distributions with LHC data". In: *Nucl. Phys.* B867 (Feb. 2013), pp. 244–289. DOI: 10.1016/j.nuclphysb.2012.10.003. arXiv: 1207.1303 [hep-ph].

[121] John M. Campbell and R. Keith Ellis. "An Update on vector boson pair production at hadron colliders". In: *Phys. Rev.* D60 (Nov. 1999), p. 113006. DOI: 10.1103/PhysRevD.60.113006. arXiv: hep-ph/9905386 [hep-ph].

[122] CMS Physics Validation Team. *Utilities for Accessing Pileup Information for Data*. 2016. URL: https://twiki.cern.ch/twiki/bin/viewauth/CMS/PileupJSONFileforData (visited on 07/18/2018). Restricted.

[123] Rikkert Frederix et al. "Drell-Yan, ZZ, W^+W^- production in SM & ADD model to NLO+PS accuracy at the LHC". In: *Eur. Phys. J.* C74.2 (Feb. 2014), p. 2745. DOI: 10.1140/epjc/s10052-014-2745-2. arXiv: 1307.7013 [hep-ph].

[124] Tanju Gleisberg et al. "Event generation with SHERPA 1.1". In: *JHEP* 02 (Feb. 2009), p. 007. DOI: 10.1088/1126-6708/2009/02/007. arXiv: 0811.4622 [hep-ph].

[125] Tanju Gleisberg et al. "Helicity formalism for spin-2 particles". In: *JHEP* 09 (Sept. 2003), p. 001. DOI: 10.1088/1126-6708/2003/09/001. arXiv: hep-ph/0306182 [hep-ph].

[126] CMS Collaboration. "Event generator tunes obtained from underlying event and multiparton scattering measurements". In: *Eur. Phys. J.* C76.3 (Mar. 2016), p. 155. DOI: 10.1140/epjc/s10052-016-3988-x. arXiv: 1512.00815 [hep-ex].

[127] Stefan Ask et al. "Real Emission and Virtual Exchange of Gravitons and Unparticles in Pythia8". In: *Comput. Phys. Commun.* 181 (Sept. 2010), pp. 1593–1604. DOI: 10.1016/j.cpc.2010.05.013. arXiv: 0912.4233 [hep-ph].

[128] R. Keith Ellis, W. James Stirling, and Bryan R. Webber. "QCD and collider physics". In: *Camb. Monogr. Part. Phys. Nucl. Phys. Cosmol.* 8 (1996), pp. 1–435.

[129] Alan D. Martin et al. "Parton distributions for the LHC". In: *Eur. Phys. J.* C63 (Sept. 2009), pp. 189–285. DOI: 10.1140/epjc/s10052-009-1072-5. arXiv: 0901.0002 [hep-ph].

[130] CMS JetMET Physics Object Group. *MET Optional Filters*. 2016. URL: https://twiki.cern.ch/twiki/bin/viewauth/CMS/MissingETOptionalFilters (visited on 07/18/2018). Restricted.

[131] CMS Collaboration. "Search for high-mass resonances in dilepton final states in proton-proton collisions at $\sqrt{s}$ = 13 TeV". In: *JHEP* 06 (June 2018), p. 120. DOI: 10.1007/JHEP06(2018)120. arXiv: 1803.06292 [hep-ex].

[132] CMS Collaboration. "Performance of CMS muon reconstruction in pp collision events at $\sqrt{s}$ = 7 TeV". In: *JINST* 7 (Oct. 2012), P10002. DOI: 10.1088/1748-0221/7/10/P10002. arXiv: 1206.4071 [physics.ins-det].

[133] CMS Collaboration. "Performance of CMS Muon Reconstruction in Cosmic-Ray Events". In: *JINST* 5 (Mar. 2010), T03022. DOI: 10.1088/1748-0221/5/03/T03022. arXiv: 0911.4994 [physics.ins-det].

[134] Thomas Speer et al. *Vertex Fitting in the CMS Tracker*. Tech. rep. CMS-NOTE-2006-032. Geneva: CERN, Feb. 2006. URL: https://cds.cern.ch/record/927395.

[135] Dimitri Bourilkov. "Exploring the LHC Landscape with Dileptons". In: *arXiv e-prints* (Sept. 2016). arXiv: 1609.08994 [hep-ph].

[136] Dimitri Bourilkov. "Photon-induced Background for Dilepton Searches and Measurements in pp Collisions at 13 TeV". In: *arXiv e-prints* (June 2016). arXiv: 1606.00523 [hep-ph].

[137] Aneesh Manohar et al. "How bright is the proton? A precise determination of the photon parton distribution function". In: *Phys. Rev. Lett.* 117.24 (Dec. 2016), p. 242002. DOI: 10.1103/PhysRevLett.117.242002. arXiv: 1607.04266 [hep-ph].

[138] Jon Butterworth et al. "PDF4LHC recommendations for LHC Run II". In: *J. Phys.* G43 (Jan. 2016), p. 023001. DOI: 10.1088/0954-3899/43/2/023001. arXiv: 1510.03865 [hep-ph].

[139] Sayipjamal Dulat et al. "New parton distribution functions from a global analysis of quantum chromodynamics". In: *Phys. Rev.* D93.3 (Feb. 2016), p. 033006. DOI: 10.1103/PhysRevD.93.033006. arXiv: 1506.07443 [hep-ph].

[140] Lucian A. Harland-Lang et al. "Parton distributions in the LHC era: MMHT 2014 PDFs". In: *Eur. Phys. J.* C75.5 (May 2015), p. 204. DOI: 10.1140/epjc/s10052-015-3397-6. arXiv: 1412.3989 [hep-ph].

[141] Guido Bell, Johann H. Kuhn, and Jörg Rittinger. "Electroweak Sudakov Logarithms and Real Gauge-Boson Radiation in the TeV Region". In: *Eur. Phys. J.* C70 (Dec. 2010), pp. 659–671. DOI: 10.1140/epjc/s10052-010-1489-x. arXiv: 1004.4117 [hep-ph].

[142] Prakash Mathews et al. "Next-to-leading order QCD corrections to the Drell-Yan cross section in models of TeV-scale gravity". In: *Nucl. Phys.* B713 (May 2005), pp. 333–377. DOI: 10.1016/j.nuclphysb.2005.01.051. arXiv: hep-ph/0411018 [hep-ph].

[143] Prakash Mathews and Vajravelu Ravindran. "Angular distribution of Drell-Yan process at hadron colliders to NLO-QCD in models of TeV scale gravity". In: *Nucl. Phys.* B753 (Oct. 2006), pp. 1–15. DOI: 10.1016/j.nuclphysb.2006.06.039. arXiv: hep-ph/0507250 [hep-ph].

[144] Meduri C. Kumar, Prakash Mathews, and Vajravelu Ravindran. "PDF and scale uncertainties of various DY distributions in ADD and RS models at hadron colliders". In: *Eur. Phys. J.* C49 (Jan. 2007), pp. 599–611. DOI: 10.1140/epjc/s10052-006-0054-0. arXiv: hep-ph/0604135 [hep-ph].

[145] Taushif Ahmed et al. "NNLO QCD corrections to the DrellYan cross section in models of TeV-scale gravity". In: *Eur. Phys. J.* C77.1 (Jan. 2017), p. 22. DOI: 10.1140/epjc/s10052-016-4587-6. arXiv: 1606.08454 [hep-ph].

[146] Taushif Ahmed et al. Private Communication. 2018.

[147] CMS Collaboration. "Search for high-mass resonances in final states with a lepton and missing transverse momentum at $\sqrt{s} = 13$ TeV". In: *JHEP* 06 (June 2018), p. 128. DOI: 10.1007/JHEP06(2018)128. arXiv: 1803.11133 [hep-ex].

[148] Raffaella Radogna. *Muon Momentum Scale measurement at HighPt*. 2017. URL: https://indico.cern.ch/event/601852/#3-update-about-the-generalize (visited on 07/29/2018). Restricted.

[149] Elisabetta Manca. *Bias in the momentum scale of reconstructed muons in 2016 data*. 2018. URL: https://indico.cern.ch/event/723551/#9-bias-in-the-momentum-scale-o (visited on 10/01/2018). Restricted.

[150] CMS Muon Physics Object Group. *EXO-MUO Documentation for Run2*. 2018. URL: https://twiki.cern.ch/twiki/bin/viewauth/CMS/TWikiEXO-MUODocumentationRun2 (visited on 07/23/2018). Restricted.

[151] The ATLAS and CMS Collaborations and the LHC Higgs Combination Group. *Procedure for the LHC Higgs boson search combination in Summer 2011*. Tech. rep. CMS-NOTE-2011-005. ATL-PHYS-PUB-2011-11. Geneva: CERN, Aug. 2011. URL: https://cds.cern.ch/record/1379837.

[152] Lorenzo Moneta et al. "The RooStats Project". In: *13th International Workshop on Advanced Computing and Analysis Techniques in Physics Research (ACAT2010)*. PoS(ACAT2010)057. SISSA, 2010. arXiv: 1009.1003 [physics.data-an]. URL: http://pos.sissa.it/archive/conferences/093/057/ACAT2010_057.pdf.

[153] Ferdos Rezaei Hosseinabadi, Seyed Mohsen Etesami, and Mojtaba Mohammadi Najafabadi. Private Communication. 2018.

[154] Thomas Muller, Jochen Ott, and Jeannine Wagner-Kuhr. *theta - a framework for template-based modeling and inference*. Tech. rep. Karlsruhe: KIT, June 2010. URL: https://cds.cern.ch/record/1365033.

[155] Gudrun Hiller, Magdalena Zenglein, et al. Private Communication. 2018.

[156] Sylvain Fichet. "Quantified naturalness from Bayesian statistics". In: *Phys. Rev.* D86 (Dec. 2012), p. 125029. DOI: 10.1103/PhysRevD.86.125029. arXiv: 1204.4940 [hep-ph].

[157] Gian Francesco Giudice. "Naturally Speaking: The Naturalness Criterion and Physics at the LHC". In: *Perspectives on LHC Physics*. Ed. by Gordon Kane and Aaron Pierce. World Scientific Publishing Co, June 2008, pp. 155–178. ISBN: 9789812779762. DOI: 10.1142/9789812779762_0010. arXiv: 0801.2562 [hep-ph].

[158] Sheldon L. Glashow, John Iliopoulos, and Luciano Maiani. "Weak Interactions with Lepton-Hadron Symmetry". In: *Phys. Rev.* D2 (Oct. 1970), pp. 1285–1292. DOI: 10.1103/PhysRevD.2.1285.